Constraining the Flux and Cross Section Models using Carbon and Oxygen Targets in the Off-Axis Near Detector for the 2016 Joint Oscillation Analysis at T2K

by

Christine Nielsen

B.Sc. Physics, University of California Santa Barbara, 2010

A THESIS SUBMITTED IN PARTIAL FULFILLMENT
OF THE REQUIREMENTS FOR THE DEGREE OF

Doctor of Philosophy

in

THE FACULTY OF GRADUATE AND POSTDOCTORAL STUDIES
(Physics)

The University of British Columbia
(Vancouver)

March 2017

Abstract

The T2K experiment is a long baseline neutrino experiment designed to measure various neutrino oscillation parameters, particularly θ_{13} and θ_{23}, at world-leading precisions. T2K uses muon neutrino and antineutrino beams produced at the Japan Proton Accelerator Research Complex. The off-axis beam strikes near detectors 280 m from the source (ND280) and the water Cherenkov detector, Super-Kamiokande, 295 km away. The far detector performs the primary oscillation analysis, while ND280 provides cross-section and flux constraints to reduce uncertainties in the oscillation analyses. ND280 consists of several different detectors, with the main target mass being the Fine Grained Detectors, one of which provides an active carbon target and one which provides a combined water-carbon target. This thesis describes the fitting methods used for T2K's oscillation analyses and near detector constraints, with a focus on the near detector fit. The addition of water target data in the near detector fit improves cross-section uncertainties at both near and far detectors. The near detector fit is a maximum likelihood fit to observed neutrino interaction rates in ND280 to constrain the cross-section and flux at the far detector. Event cuts identify and separate charged-current neutrino interactions into topology-based samples, with selection uncertainties and correlations handled through extensive detector systematic studies. The near detector fit to data including a water target shows consistent fitted cross-section and flux with previous ND280 fits, and significantly reduces the uncertainty on the neutrino energy spectrum predictions at the far detector. In addition, nuclear model dependencies in the cross-section model used at T2K were investigated using the near detector fit, and the T2K model was shown to be sufficient in accounting for nuclear effects.

Preface

This dissertation is based on the experimental apparati and data of the T2K experiment, and was completed with the aid of other members of the T2K collaboration. The text of this dissertation has not been taken from previously published articles or other collaborative documents.

The detectors and selections described in Chapter 2 were designed and built by members of the T2K collaboration. The fit software used for the analysis at Super-Kamiokande in Chapter 3 was created and used by members of the T2K VALOR and p–Theta groups for both the previous results and the portion of the results in this thesis at SK. The first implementation of the near detector fit software was created by M. Hartz and the current software implementation using only FGD 1 was created by J. Myslik with some help from myself and optimization by M. Scott. The addition of the ability to run the fit using both FGD 1 and FGD 2, as well as allowing correlations between detector systematic parameters in toy parameter throws, was my work. The creation of the observable normalization parameter covariance matrix was done by myself, building on previous work by M. Scott, with the addition of detector systematic correlations being mine.

The reconstruction methods described in Chapter 4.4.1 were developed by the members of the various reconstruction groups on the T2K project. The inclusive charged event selection for the Forward Horn Current interactions was primarily developed by members of the ND280 Numu Analysis group. I personally did the initial selection migration, tuning and testing for the CC inclusive FGD 2 selection, adapting cuts originally developed for FGD 1. The FHC CC inclusive multi-pion samples and cuts were defined and developed by members of the ND280

NuMu analysis group. I personally developed and studied the current Michel electron cut used in defining the sample selections. The RHC CC inclusive samples and cuts for neutrino and antineutrino interactions were developed by the ND280 Numu Analysis group.

The systematics effects described in Chapter 5 were identified, studied and measured by members of the T2K ND280 Numu Analysis group. In addition, the correlations described in that Chapter were defined by M. Ravonel and implemented by myself. I personally measured the uncertainty associated with the purity of the Michel electron cut for the FHC multipion selection. The work and studies shown in Chapter 6 were done entirely by myself.

The analysis of the near detector fit using FGD 1 + FGD 2 shown in Chapters 7 and 8 is my original work. The prediction and prediction uncertainties at SK using the ND280 fit result were produced by the T2K VALOR group. The plots of the oscillation contours shown in this Chapter were also created by the T2K VALOR group. The model dependency studies in Chapter 8 was my original work, with the SK spectra and total event numbers produced by Raj Shah from the results.

Table of Contents

List of Tables

List of Figures

Glossary

2p-2h Two particle – two hole

APD Avalanche photodiode

ASIC Application-specific integrated circuit

ASUM Analog sum

CC Charged weak current

CCQE Charged-current quasi-elastic

CKM Cabibo-Kobayashi-Maskawa matrix

CMB Crate master board

CP Charge-parity

DCC Data concentrator card

ECal Electromagnetic Calorimeter

FEB Front End Board

FGD Fine Grained Detector

FHC Forward horn current mode in which positive particles are focused to produce the T2K beam. Also referred to as neutrino mode.

FPGA Field-programmable gate array

FSI Final state interaction

GEANT4 Simulation package for particle detectors and particle propagation and interaction

ID Inner detector

IH Inverted heirarchy

INGRID Interactive Neutrino GRID

J-PARC Japan Proton Accelerator Research Center

LINAC Linear accelerator

LPB Light pulser board

MC Monte Carlo

MPPC Multi-pixel Photon Counter

MR Main ring synchrotron

MSW Mikheyev-Smirnov-Wolfenstein effect

NC Neutral weak current

ND280 The Near Detector at 280 meters

NH Normal heirarchy

OD Outer detector

OOFV Out of fiducial volume

P0D Pi-0 Detector

PID Particle identification

PMNS Pontecorvo-Maki-Nakahata-Sakata matrix

PMT Photomultiplier tube

POT Protons on target

RCS Rapid-cycling synchrotron

RFG Relativistic Fermi Gas model

RHC Reverse horn current mode, in which negative particles are focused to produce the T2K beam. Also referred to as antineutrino mode.

ROOT C++ Libraries designed for use with data analysis and simulation

RPA Random phase approximation

SCA Switched capacitor array

SF Spectral function

SI Secondary interactions

SK Super-Kamiokande

SMRD Side Muon Range Detector

T2K The Tokai to Kamiokande Experiment

TPC Time Projection Chamber

WLS Wavelength shifting

Chapter 1

Physics of Neutrinos

1.1 Standard Model Neutrino Theory

The first suggestions of the existence of neutrinos came from experiments with β decay, where current theory predicted that the energy of the electron produced in the decay $A \rightarrow B + e$ would have a single constant value. Instead, the emitted electron energy was found to be a continuous spectrum of energies, lower than the predicted value[1]. This "missing energy" was in fact due to the production of a light neutral particle in the decay, now known to be the neutrino. The first to postulate the neutrino's existence was Pauli in 1930 as some additional neutral particle, and his theory was extended later by Fermi for β decay[1]. Direct experimental confirmation of the neutrino's existence came in 1953, from the work of Reines and Cowan[2]. A few years later in 1959, Davis and Harmer showed that the neutrino and antineutrino were distinct particles[1].

It was not until 1962 that the neutrino (and antineutrino) was discovered to come in more than one flavor; so far theories had assumed that all neutrinos were the same and the only distinction was between particle and antiparticle. An experiment at Brookhaven National Laboratory[3] had observed that neutrinos produced from muon decay would only go on to produce muons, rather than electrons. This indicated that there were at least two types of neutrino: the muon neutrino and the electron neutrino to match the two known charged leptons. Once the tau was discovered in 1975, the existence of the electron and muon neutrino sug-

gested that there should be a third neutrino, one related to the τ. Its existence was verified more recently by the DONUT collaboration, using data from 1997[4]. So far, there have only been three kinds of neutrino discovered, which is consistent both with the measurements of the cosmic microwave background and its constraints on the number of neutrino generations[5]. The measurements of the Z boson decay also suggest that there are only three neutrino flavors that can couple to the Z[6].

1.1.1 Basic Neutrino Formalism

The neutrino is part of the Standard Model, which describes the various types of fundamental particles and their interactions with each other. The Standard Model itself has been developed over the past century and serves as the theoretical description of the electroweak and strong interactions. The particles are composed of the fermions, with spin-$\frac{1}{2}$, and the bosons which mediate the various forces in the Standard Model[1].

The fermions are split into the lepton and quark sectors. In the lepton sector, there are three lepton flavors: the electron (e), the muon (μ) and the tau (τ) with negative (matter) or positive (antimatter) charge. Each lepton flavor is associated with a neutrino and antineutrino of the same flavor: ν_e, ν_μ and ν_τ for neutrinos and $\bar{\nu}_e$, $\bar{\nu}_\mu$ and $\bar{\nu}_\tau$ for antiparticles. Each flavor has its own lepton number ($+1$ for matter and -1 for antimatter), which is conserved in the weak interaction. The quark sector consists of six different flavours of quark: the up (u), charm (c) and top (t) quarks which have a charge of $+\frac{2}{3}$, and the down (d), strange (s) and bottom (b) quarks with charge of $-\frac{1}{3}$. The quarks interact with the charged leptons and neutrinos through the weak force[1]; quarks and charged leptons can also interact through the electromagnetic force.

Standard Model Basics

The Standard Model is built off of the principle of gauge invariance, and depends upon various symmetries. Gauge invariance means that the Lagrangian must remain invariant under transformations, which can be either global or local. In particular, the Standard Model rests on the

assumption of local gauge invariance, which imposes the symmetries from which we derive the properties of the gauge bosons.

To start, we look at the simple case of the Dirac equation, which is a quantum mechanical equation that satisfies the relativistic energy equation. The Dirac Lagrangian for a free particle is

$$\mathscr{L} = \overline{\Psi}(i\partial\!\!\!/ - m)\Psi \tag{1.1}$$

with $\overline{\Psi} = \Psi^\dagger\gamma^0$, $\partial\!\!\!/ = \gamma^\mu\partial_\mu$ and γ^μ are the Dirac matrices[1]. Solutions to the Dirac equation represent spin-$\frac{1}{2}$ particles such as the neutrino. This is invariant under the global transformation $\Psi \to e^{i\alpha}\Psi$, where α is any real number. This global invariance corresponds to a conserved current. However, we additionally require that the Lagrangian be invariant under local gauge transformations.

To guarantee invariance under local transformations

$$\Psi(x) \to e^{i\alpha(x)}\Psi(x) \tag{1.2}$$

a correction must be added to the derivative giving

$$\mathscr{L} = \overline{\Psi}(iD\!\!\!/ - m)\Psi \tag{1.3}$$

where the covariant derivative $D_\mu = \partial_\mu - iqA_\mu$, with A_μ being some new field that transforms as $A_\mu \to A_\mu + \partial_\mu q$. Local invariance additionally requires that A_μ be massless. A_μ is in fact the electromagnetic potential, generated through the requirement of local invariance. Invariance under the global phase transformation described previously also still holds; as $e^{i\alpha}$ is a unitary 1×1 matrix, the group of all such matrices is $U(1)$. With the addition of a kinetic term, we can then construct the QED Lagrangian[1]:

$$\mathscr{L}_{QED} = i\overline{\Psi}\partial\!\!\!/\Psi - m\overline{\Psi}\Psi - \frac{1}{4}F^{\mu\nu}F_{\mu\nu} + q\overline{\Psi}\gamma^\mu\Psi A_\mu \tag{1.4}$$

where $F^{\mu\nu} = \partial^\mu A^\nu - \partial^\nu A^\mu$.

This principle can be extended to SU(2) gauge group describing the weak force as well: starting with the Lagrangian for two spin-$\frac{1}{2}$ fields ψ_1 and ψ_2 with equal mass:

$$\mathscr{L} = i\hbar c\overline{\psi}\gamma^\mu \partial_\mu \psi - mc^2\overline{\psi}\psi \tag{1.5}$$

where $\psi = \begin{pmatrix} \psi_1 \\ \psi_2 \end{pmatrix}$ – this is just the sum of two Dirac Lagrangians. We can see this is invariant under the global transformation $\psi \to e^{i\tau\cdot\mathbf{a}}\psi$, where τ are the Pauli matrices τ_1, τ_2 and τ_3[1] and $\mathbf{a}$ is three real numbers a_1, a_2 and a_3. This is a global SU(2) gauge transformation and rotates the ψ_1 and ψ_2 fields into each other – meaning that the weak force acts equally on the ψ_1 and ψ_2 components. Much like with the initial Dirac case, we promote this to a local invariance:

$$\psi \to e^{-iq\tau\cdot\mathbf{a}(\mathbf{x})}\psi \tag{1.6}$$

As before, the Lagrangian is no longer invariant under this transformation and a correction must be added to the derivative:

$$\mathscr{D}_\mu = \partial_\mu + iq\tau\cdot\mathbf{A}_\mu \tag{1.7}$$

where $\mathbf{A}^\mu = (A_1^\mu, A_2^\mu, A_3^\mu)$. These A^μ are three gauge fields which transform such that

$$\mathscr{D}_\mu\psi \to e^{-iq\tau\cdot\mathbf{a}(\mathbf{x})}\mathscr{D}_\mu\psi \tag{1.8}$$

fulfilling the local gauge invariance. The three vector gauge fields are massless, just as with the U(1) case. These three gauge fields give rise to the W^+, W^- and Z^0 bosons, which acquire their masses through electroweak symmetry breaking. In moving from a simple SU(2) gauge theory to the electroweak, we can identify ψ_1 and ψ_2 with either the charged lepton – neutrino or up – down quark weak isospin doublets. In these pairs, the neutrino and up quark have a weak isospin of $+\frac{1}{2}$, while the lepton and down quark have a weak isospin of $-\frac{1}{2}$. The weak

isospin, often written as I_3, is the conserved charge of the weak interaction, and is assigned to only to left-handed particles.

To describe the electroweak Lagrangian, we want to combine the electromagnetic and SU(2) gauge symmetries. This leads to a Lagrangian composed of one part which describes interactions between the three SU(2) gauge bosons and the U(1) boson, and one which contains the kinetic terms for the fermions. This forms the electroweak group with $SU(2)_L \times U(1)_Y$ gauge symmetry, where the subscript L indicates that the SU(2) transformations are only on left-handed particles, and Y is hypercharge. There are four generators in total: one from U(1), corresponding to the hypercharge and three from SU(2). These correspond to massless gauge boson fields, as the mass term is not locally invariant. Of course, the bosons in the weak interaction – W^+, W^- and Z^0 – are massive; to correctly describe the electroweak Lagrangian, there needs to be some way to give the gauge bosons mass.

In order to generate the massive gauge boson fields in the electroweak theory, we employ the Higgs mechanism and spontaneous symmetry breaking. This allows the local gauge invariance to be preserved by way of choosing a vacuum ground state and expanding the fluctuations around it, with the addition of a gauge-invariant scalar field to the Lagrangian. In the case of the electroweak symmetries, this causes the original $SU(2) \times U(1)$ to be broken to $U(1)_{QED}$, the electromagnetic subgroup. This gives three massless Goldstone boson fields, which with a bit of math can be transformed away to generate the masses of the gauge bosons W^+, W^- and Z^0 as well as ending up with a single additional massive scalar. This is more specifically known as the Higgs mechanism, and also serves to give mass to the leptons and quarks[1].

From the electroweak Lagrangian we can find the various propagators and vertex factors which are used to describe the weak interactions. This includes both the vertex factors for the interaction of quarks and leptons with the gauge bosons as well as boson self-interaction vertices. For leptons and neutrinos, the vertex factor for the $W^{\pm}$[1] is:

$$-\frac{ig_W}{2\sqrt{2}}\gamma^\mu(1-\gamma^5) \tag{1.9}$$

where g_W is the weak coupling constant for the W. The quark coupling is similar with an additional factor from the Cabibo-Kobayashi-Maskawa (CKM) matrix which depends on the quark flavour. The vertex factor for the Z^0 interacting with a quark or lepton is

$$\frac{-ig_Z}{2}\gamma^\mu(c_V^f - c_A^f\gamma^5) \tag{1.10}$$

where c_V^f and c_A^f are constants that depend on the interacting particle, and g_Z is the weak coupling constant for the Z[1]. The propagator for both the W and the Z^0 is

$$\frac{-ig_{\mu\nu} - \frac{q_\mu q_\nu}{M^2}}{q^2 - M^2} \tag{1.11}$$

where $g_{\mu\nu}$ is the metric tensor, q_μ is the momentum transfer of the particles and M is the mass of the W or Z respectively. As M is very large, this propagator looks like $\frac{1}{M^2}$ at lower energies; this applies to many neutrino experiments such as T2K. This is why weak interactions are so much weaker than electromagnetic interactions, which have similar coupling constants but no mass term in the denominator of the propagator due to the photon being massless. This forms the basis of how we calculate neutrino interactions and cross-sections for free partons.

The Standard Model Neutrino

The Standard Model neutrino is represented by four-component spinors, and is generally assumed to be massless. The chiral representation of these bispinors is :

$$\Psi = \begin{pmatrix} \Psi_L \\ \Psi_R \end{pmatrix} \tag{1.12}$$

where Ψ_L is the left-handed Weyl spinor and Ψ_R is the right-handed Weyl spinor. Here left-handed and right-handed refer not to the helicity of the fields, which relates the particle spin and direction, but to the chirality of the particle. This means that ψ_L transforms under the left-handed representation of the Lorentz group, and ψ_R transforms under the right-handed

representation[7].

In the Glashow-Weinberg-Salam theory of weak interactions, the left-handed fermion fields are $SU(2)$ doublets:

$$\psi_L = \begin{pmatrix} \nu_{Ll} \\ l_L \end{pmatrix} \tag{1.13}$$

with the right-handed $U(1)$ singlet being l_R for each lepton-neutrino pair. The free-field Lagrangian for neutrinos is

$$\mathscr{L} = i(\bar{\Psi}_{Ll}\gamma^\mu \partial_\mu \Psi_{Ll} + \bar{\Psi}_{Rl}\gamma^\mu \partial_\mu \Psi_{Rl}) \tag{1.14}$$

and is invariant under $SU(2) \times U(1)$ symmetry[8].

The neutrino, as a neutral particle with no color, only interacts with other particles through the weak force. In the charged current interactions a neutrino and lepton of the same flavour couple to the $W^\pm$, and for the neutral current interactions a neutrino field couples to the Z boson without any change of flavor. However, due to chirality only left-handed neutrino fields and right-handed antineutrino fields participate in weak interactions. The coupling for the neutrino field and lepton field ψ_{ν_l} and ψ_l to the $W^\pm$ is :

$$-\frac{g_W}{2\sqrt{2}}(\bar{\psi}_{\nu_l}\gamma_\mu(1-\gamma^5)\psi_l)W^\mu \tag{1.15}$$

and the neutrino coupling to the Z boson is:

$$-\frac{g_W}{4\cos\theta_W}\bar{\psi}_{\nu_l}\gamma_\mu(1-\gamma^5)\psi_{\nu_l}Z^\mu \tag{1.16}$$

where $\cos\theta_W$ is the weak mixing angle. The $\frac{1}{2}(1-\gamma^5)$ ensures that only the left-handed fields participate in the weak interaction. Additionally, both types of weak interaction can be separated into vector (γ_μ) and axial ($\gamma_\mu\gamma^5$) current parts.

So far, we have assumed that the neutrino, as in the Standard Model formulation, is massless

– this avoids attempting to construct a mass term without evidence for a right-handed neutrino field. This assumption was also initially corroborated by the limits on the neutrino mass scale from cosmology[9] and maximal parity violation of the weak interaction. However, through the initial observations of neutrino flavor oscillation by the Super-Kamiokande collaboration[10] and the Sudbury Neutrino Observatory[11], as well as subsequent oscillation measurements, it is now evident that neutrinos do have some mass, however tiny. It is not yet know where the neutrinos derive their masses from, and there are various potential theories.

Neutrinos can gain mass in the Standard Model in a few ways: the first would be the assumption that like their partner leptons, neutrinos are Dirac particles and thus have Dirac mass terms[12]. This does require both that neutrinos and antineutrinos are distinct particles as well as requiring the existence of a right-handed neutrino field. This right-handed neutrino would be a "sterile neutrino" – unable to interact through the weak force or electromagnetic force – making it very difficult to observe. In addition, the neutrino mass scale would require a very weak Yukawa coupling, more than a million times smaller than that of the electron.

There is also the possibility for the neutrino to be a Majorana particle, and have its mass generated through a Majorana mass term. A Majorana particle is one which is its own antiparticle, requiring that there are no charges to be conserved[12]. While the neutrino is a neutral particle and does not carry electric charge, this would require that lepton number not be conserved. Unlike the Dirac neutrino, a Majorana neutrino does not need an additional right-handed sterile neutrino to generate a mass term, as the Majorana mass term only involves fields of the same chirality. The Majorana mass term also can be used to explain the small size of the neutrino masses by way of the seesaw mechanism. In the seesaw mechanism, light Majorana neutrinos are paired with extremely heavy neutrinos, with the observed neutrinos being superpositions of these[13].

1.2 Neutrino Oscillations

The discovery of massive neutrinos introduced a new effect to the Standard Model neutrino: oscillations similar to those seen in the quark sector. Because the flavor eigenstates and mass eigenstates are not part of the same basis, neutrinos propagate in mass states that are a mix of the flavor states that interact through the weak force. In experimental terms, this explains the "solar neutrino problem", where a deficit of ν_e was seen in the observed flux of neutrinos generated by the Sun, by allowing electron neutrinos to be converted into other flavors through interactions with matter, producing an observed deficit in electron neutrinos. Oscillation also explains the second big neutrino problem: the "atmospheric neutrino anomaly", where a deficit in atmospheric ν_μ was observed in two different experiments. While neutrino oscillations require that neutrinos do have mass, they do not give any indication to how that mass is generated.

1.2.1 Neutrino Oscillation Theory

Once neutrino mixing is included, the left-handed neutrino flavor states can be represented as linear combination of the mass eigenstates:

$$\nu_l(x) = \sum_{j=1}^{3} U_{lj}\nu_j(x) \tag{1.17}$$

where $l = e$, μ and τ, ν_l is the flavor eigenstate and ν_j is the mass eigenstate with mass $m_j \neq 0$[1]. U is the neutrino mixing matrix, shown in Equation 1.18. Current experimental evidence points towards 3-flavor mixing, and thus three mass states ν_1, ν_2 and ν_3 with differing masses. This does not exclude the possibility of more than three types of massive neutrino, such as in the case of potential sterile neutrinos, which do not interact through the weak force. The mixing between the three neutrino flavor states and the three mass eigenstates is described by a unitary mixing matrix called the Pontecorvo-Maki-Nakahata-Sakata (PMNS) matrix shown

[1] At least two of the three neutrino mass states must have non-zero mass. However, it is allowed for the lightest neutrino to be massless.

in Equation 1.18. This is analogous to the Cabibo-Kobayashi-Maskawa (CKM) matrix that governs mixing in the quark sector, and is characterized by the three mixing angles: θ_{13}, θ_{12} and θ_{23} and a Dirac phase δ_{CP}, which is a complex phase governing CP violation in the neutrino sector. It is written as the product of three rotation matrices, with the complex phase included in the matrix for the 1-3 plane rotation.

$$U = \begin{pmatrix} 1 & 0 & 0 \\ 0 & \cos\theta_{23} & \sin\theta_{23} \\ 0 & -\sin\theta_{23} & \cos\theta_{23} \end{pmatrix} \begin{pmatrix} \cos\theta_{13} & 0 & \sin\theta_{13}e^{-i\delta} \\ 0 & 1 & 0 \\ -\sin\theta_{13}e^{i\delta} & -0 & \cos\theta_{13} \end{pmatrix} \begin{pmatrix} \cos\theta_{12} & \sin\theta_{12} & 0 \\ -\sin\theta_{12} & \cos\theta_{12} & 0 \\ 0 & 0 & 1 \end{pmatrix} \tag{1.18}$$

which then can be written as :

$$U = \begin{pmatrix} U_{e1} & U_{e2} & U_{e3} \\ U_{\mu 1} & U_{\mu 2} & U_{\mu 3} \\ U_{\tau 1} & U_{\tau 2} & U_{\tau 3} \end{pmatrix} = \begin{pmatrix} c_{12}c_{13} & c_{13}s_{12} & s_{13}e^{-i\delta_{CP}} \\ -s_{12}c_{23} - c_{12}s_{13}s_{23}e^{i\delta_{CP}} & c_{12}c_{23} - s_{12}s_{13}s_{23}e^{i\delta_{CP}} & c_{13}s_{23} \\ s_{12}s_{23} - c_{12}s_{13}c_{23}e^{i\delta_{CP}} & c_{12}s_{23} - s_{12}s_{13}c_{23}e^{i\delta_{CP}} & c_{13}c_{23} \end{pmatrix} \tag{1.19}$$

where $s_{ij} = \sin\theta_{ij}$ and $c_{ij} = \cos\theta_{ij}$. From this, it is apparent that the CP violating phase δ_{CP} is associated here with $\sin\theta_{13}$ – meaning that if $\theta_{13} = 0$, there can be no CP violation in neutrino oscillations. However, the mixing matrix can be reparametrized such that δ_{CP} can be associated with any of the the three mixing angles, meaning that all three mixing angles must be non-zero for CP violation to occur. In the case that neutrinos are Majorana particles, with $\nu = \bar{\nu}$, there are two additional CP-violating phases that must be included to preserve invariance of the Majorana mass term: ϕ_{12} and ϕ_{13}. These comprise an additional diagonal matrix used in calculating U from the other rotation matrices[12], though they have no impact

on the neutrino oscillation probabilities:

$$U_{Majorana} = \begin{pmatrix} 1 & 0 & 0 \\ 0 & e^{i\phi_{21}/2} & 0 \\ 0 & 0 & e^{i\phi_{31}/2} \end{pmatrix} \tag{1.20}$$

1.2.2 Oscillation Probability

With the PMNS mixing matrix, and the understanding that the flavor neutrinos are superpositions of the mass eigenstates as in Equation 1.17, it is possible to find the probability that a neutrino will oscillate from one flavor to another over some known distance. Here we will take the assumption that the neutrinos can be approximated as plane waves – a fully complete description would require using a wave packet description – and that the neutrino is traveling in a vacuum.

The vacuum oscillation amplitude for a neutrino of flavor a to flavor b, traveling a distance L is :

$$A(\nu_a \rightarrow \nu_b) = \sum_k U_{bk} D_k U^{\dagger}_{ka} \tag{1.21}$$

where D_k is the function that describes the propagation of the neutrino mass state ν_k over a distance L:

$$D_k = e^{-iE_kT + ip_kL} \tag{1.22}$$

where T is the travel time, and E_k and p_k are the energy and momentum of the neutrino mass state[2]. To find the oscillation probability, we first assume that all mass eigenstates were generated with the same momentum p and different energies E_k. [3] As the neutrino is ultrarelativistic due to its very low mass, the propagation time, T, can be approximated as $\approx L/c$ and the time

[2]Here units are $\hbar = c = 1$

[3]Performing this calculation starting with equal energies E and differing momenta p_k provides the same answer.

dependence can be written out of D_k through Taylor expansion:

$$E_k T - p_k L \approx (E_k - \sqrt{E^2 - m_k^2})L \approx \frac{m_k^2}{2E} L \tag{1.23}$$

where E is the energy of the neutrino in the massless limit. The probability of oscillation can then simply be calculated as the oscillation amplitude squared:

$$P_{\nu_a \to \nu_b}(L) = |A(\nu_a \to \nu_b)|^2 = \left| \sum_k U_{bk}^* e^{-i m_k^2 L/2E} U_{ka} \right|^2 \tag{1.24}$$

This can then be simplified to:

$$P_{\nu_a \to \nu_b}(L,E) = \left| \sum_{j,k} U_{aj}^* U_{bj} U_{ak} U_{bk}^* e^{-i \frac{\Delta m_{jk}^2 L}{2E}} \right| \tag{1.25}$$

where $\Delta m_{ij}^2 = m_i^2 - m_j^2$. This means that the only intrinsic property, other than the mixing matrix itself, that the oscillation probability depends on is the square of the mass splittings. Expanding out the terms separates the probability into contributions from the real and imaginary terms, and makes apparent how the probability differs between neutrino and antineutrino oscillation:

$$P(\nu_a \to \nu_b) = \delta_{ab} - 2 \sum_{i>k} Re[U_{bi} U_{ai}^* U_{bk}^* U_{ak}] \left(1 - \cos\left(\frac{\Delta m_{ki}^2 L}{2E} \right) \right) \pm 2 \sum_{i>k} Im[U_{bi} U_{ai}^* U_{bk}^* U_{ak}] \sin\left(\frac{\Delta m_{ki}^2 L}{2E} \right) \tag{1.26}$$

where the third term is $+$ for neutrinos and $-$ for antineutrinos. The final term in this equation allows for the observation of CP violation in the lepton sector, so long as a and b are different flavors. By looking for the asymmetry between oscillation probabilities of neutrinos and antineutrinos, CP violation has the potential to be measured experimentally.

$$A_{CP}^{ab} = P(\nu_a \to \nu_b) - P(\bar{\nu}_a - \bar{\nu}_b) \tag{1.27}$$

With the probability given in Equation 1.26, this asymmetry depends only on the final term:

$$A_{CP}^{ab} = 4 \sum_{i>k} Im[U_{bi} U_{ai}^* U_{bk}^* U_{ak}] \sin\left(\frac{\Delta m_{ki}^2 L}{2E}\right) \tag{1.28}$$

To properly measure this asymmetry, the values and signs of the mass splittings must be known – while the magnitudes of Δm_{21}^2, Δm_{32}^2 and Δm_{31}^2 have been measured[14], only the sign of Δm_{21}^2 has been. This gives two potential orderings of the neutrino masses: the Normal Hierarchy (NH), with m_1 lightest and m_3 heaviest, and the Inverted Hierarchy (IH), with m_3 lightest and m_2 heaviest. Like CP violation, determining the mass ordering is the subject of current and future neutrino experiments.

1.2.3 Matter Effects

While the oscillation probability derived in Equation 1.26 assumes that the neutrino travels in a vacuum, this is generally not the case in neutrino experiments. Before detection, neutrinos may travel through the atmosphere or the Earth's crust, as in neutrino beam experiments. When a neutrino travels through matter, there is some probability of interaction before reaching its destination which can have an impact on the observed oscillations. These matter effects are referred to as the Mikheyev-Smirnov-Wolfenstein (MSW) effect[15]. The primary effect on oscillations comes from ν_e scattering elastically off of electrons, specifically through charged-current interactions. While the other types of neutrino interactions can and do occur, interactions with no neutrino in the final state will show no effect on oscillation measurements, and neutral current processes occur at equal rates for all of the neutrino mass eigenstates. However, as there are only e^- in ordinary matter, and no μ^- or τ^-, only ν_e and $\bar{\nu}_e$ can interact with matter through the $W^\pm$. This leads to an effect on the overall flavour composition during propagation.

This changes the Hamiltonian from the vacuum case, as the electron neutrino acquires an additional potential energy $V_{MSW} = \sqrt{2} G_F N_e(t)$, where N_e is the electron density. This change in the Hamiltonian leads to a difference in the mass eigenstates when propagating through matter, and thus differences in the effective mixing angles and oscillation probabilities due to

this effect. These matter effects have only a small impact on experiments such as T2K, where the baseline is not long enough to see major differences, but are important when considering neutrinos that propagate through the Earth's core or are produced in the Sun[15].

1.3 Previous Oscillation Experiments

The first observed effects of neutrino oscillation came in the form of the "solar neutrino problem" at Homestake in 1965. While the experiment was looking for electron neutrinos produced by the sun, the observed rate of ν_e was much less than expected: they only observed 0.5 events per day compared to predictions of 2 – 7 per day[16]. At the time, however, neutrinos were always assumed massless and neutrino oscillation unheard of. As a major unsolved problem in neutrinos, there were many various attempts to both reproduce the ν_e deficit and understand its source, including Bahcall's work on solar neutrino models[17]. However, it was not until the 1990s that progress was made on this "solar neutrino problem".

The experiment to first solve the solar neutrino problem was the Sudbury Neutrino Observatory (SNO), a 1 kton heavy water Cherenkov detector which was able to look at more than just the signal from ν_e. This, combined with the measurements from Super-Kamiokande[10], the follow-up to Kamiokande II, allowed SNO to both confirm the ν_e deficit as well as confirm that the solar neutrino flux also contained ν_μ and ν_τ in 2001[11] by using neutral current, elastic scattering and charged current interactions to determine the electron and nonelectron neutrino components of the flux – clear evidence of neutrino flavor change.

The "solar neutrino problem" was not the only historic issue that arose from neutrino oscillations: equally key in discovering them was the "atmospheric neutrino anomaly". In the 1980s, measuring the decay of protons had become experimentally viable. However, the predicted lifetime for the proton was very long, which required both a large detector volume with a large number of protons, and a low, well understood background. Part of this background comes in the form of muon and electron neutrinos produced by cosmic rays in the Earth's atmosphere, known as atmospheric neutrinos, which could then interact in the proton decay

detectors to produce a background.

This neutrino background could be predicted using the cosmic ray muon flux, and knowledge about the neutrino production processes in the atmosphere – both of which had been studied by then. This allowed the prediction of the muon neutrino to electron neutrino production ratio, as a function of energy – something that could be measured at these proton decay experiments. When the Kamioka Nucleon Decay Experiment (KamiokaNDE)[18], designed originally to measure proton decay in a large water Cherenkov detector, did so, it saw a significant deficit in ν_μ compared to predictions of the $\frac{\nu_\mu}{\nu_e}$ flux ratio.

As with the solar neutrino problem, the solution came later from measurements at Super-Kamiokande in 1998, which was able to both measure the ν_μ and ν_e flux along with direction of the outgoing lepton, which relates to the initial direction of the interacting neutrino[10]. This showed that there was an angular dependence to the difference between the measured ν_μ rate and predicted – which for atmospheric neutrinos gives a measure of the distance the neutrino has traveled, and can be related back to the distance and energy dependence in the neutrino oscillation probability.

Since then, there have been many different neutrino experiments that sought to measure the various neutrino oscillation parameters. Several of these are reactor experiments, which use $\bar{\nu}_e$ disappearance to probe neutrino oscillation, such as Chooz[19] in 2003 and Double Chooz[20] in 2011, RENO[21] in 2012, KamLAND[22] and Daya Bay[23]. Other neutrino experiments have used neutrino beams to look at both appearance and disappearance of various flavours of neutrinos. Some of these are short baseline, where the detectors are placed close to the neutrino source, such as the NOMAD[24] experiment. Other major short baseline experiments were LSND[25], and MiniBooNe[26][4]. Other neutrino beam neutrino experiments are long-baseline, where there is a detector is placed many kilometers from the beam source, such as K2K[27], MINOS[28], NOνA[29] and T2K[30]. The current measured values for the neutrino

[4]Both LSND and MiniBooNe saw some indications of neutrino oscillations. However, these results are controversial and are difficult to reconcile with the current neutrino model. As such, they will not be discussed further here.

Parameter	Value
$\sin^2\theta_{12}$	0.304 ± 0.014
$\sin^2\theta_{23}$ (NH)	0.50 ± 0.05
$\sin^2\theta_{13}$	$(2.19 \pm 0.12) \times 10^{-2}$
Δm^2_{21}	$(7.53 \pm 0.18) \times 10^{-5}$ eV^2
$\lvert\Delta m^2_{32}\rvert$	$(2.44 \pm 0.06) \times 10^{-3}$ eV^2

Table 1.1: Summary of current measured values for the various oscillation parameters. Values taken from [14] and are shown for the normal mass hierarchy. Δm^2_{32} is shown as an absolute value as the sign is not currently known.

oscillation parameters are summarized in Table 1.1.

1.4 Neutrino Interactions

1.4.1 Neutrino Interaction Modes

In the Standard Model, the neutrino only interacts with other particles through the weak force, which is mediated by the Z^0 and $W^\pm$ bosons. The Z^0 is a neutral particle of mass 91.1876 ± 0.0021 GeV/c^2 and the $W^\pm$ is a charged particle of mass 80.385 ± 0.015 GeV/c^2, with W^+ being positive and W^- negative. Interactions mediated by Z^0 are referred to as Neutral Current (NC) interactions, and interactions mediated by $W^\pm$ are referred to as Charged Current (CC) interactions. For the neutrino, neutral current interactions allow the neutrino to transfer energy and momentum to some other quark or lepton without any change of flavor. In Charged Current interactions, the neutrino interacts through the W to produce a lepton of the same flavour: $\nu_l + l \rightarrow \nu_l + l$, where the neutrino interacts with another lepton[5] , and $\nu_l + d \rightarrow l^- + u$, where it interacts with a quark. These produce a charged lepton in the final state, making them easier to detect than the Neutral Current interactions. Of course, quarks are not free particles in nature and instead exist in bound states inside of nucleons – p and n – and mesons. This complicates the possible interactions, and leads to classifying these interactions into multiple categories to better describe them.

Of particular interest are the CC interactions, specifically the charged-current quasi-elastic

[5] $\nu_l + l \rightarrow \nu_l + l$ can also be a neutral current process, with the lepton and neutrino scattering off each other.

interaction. The main charged-current interactions relevant to the T2K experiment are shown in Figure 1.1. These are Charged-current Quasi-elastic (CCQE), where only a lepton and outgoing nucleon are produced, the charged-current resonant pion production, where a pion is produced in the final state via Δ resonance, coherent pion production where the neutrino scatters off an entire nucleus and produces a single outgoing pion, and deep inelastic scattering, where the nucleon is broken into another nucleon and hadrons.

Understanding these various cross-sections is important to correctly model neutrino interactions in experiment. In particular, the choice of neutrino interaction model and measurements of the various model parameters has a significant impact on how well neutrino interaction rates – and interaction cross-sections – can be predicted. For this reason, there has been significant effort to measure various neutrino interaction cross-sections and underlying parameters, and to construct a sufficiently robust model of neutrino interactions on nuclei.

1.4.2 Nucleon-neutrino Interactions

Charged-current Quasi-elastic Scattering

Charged-current quasi-elastic neutrino scattering for nucleons is the simplest neutrino interaction, with simple two-body kinematics for the interaction:

$$\nu_l + n \rightarrow p + l^- \tag{1.29}$$

where ν_l and l are a neutrino and lepton of the same flavor. Because of its simplicity, the initial neutrino energy and momentum transfer can be determined using just the outgoing lepton's energy and angle as in Equation 1.30 (assuming the nucleon is initially at rest), making this type of interaction very useful for experiments. This is the primary signal interaction at T2K. The initial neutrino energy can be calculated as:

$$E_\nu = \frac{m_p^2 - m_n^2 - m_l^2 + 2m_n E_l}{2(m_n - E_l + p_l \cos\theta_l)} \tag{1.30}$$

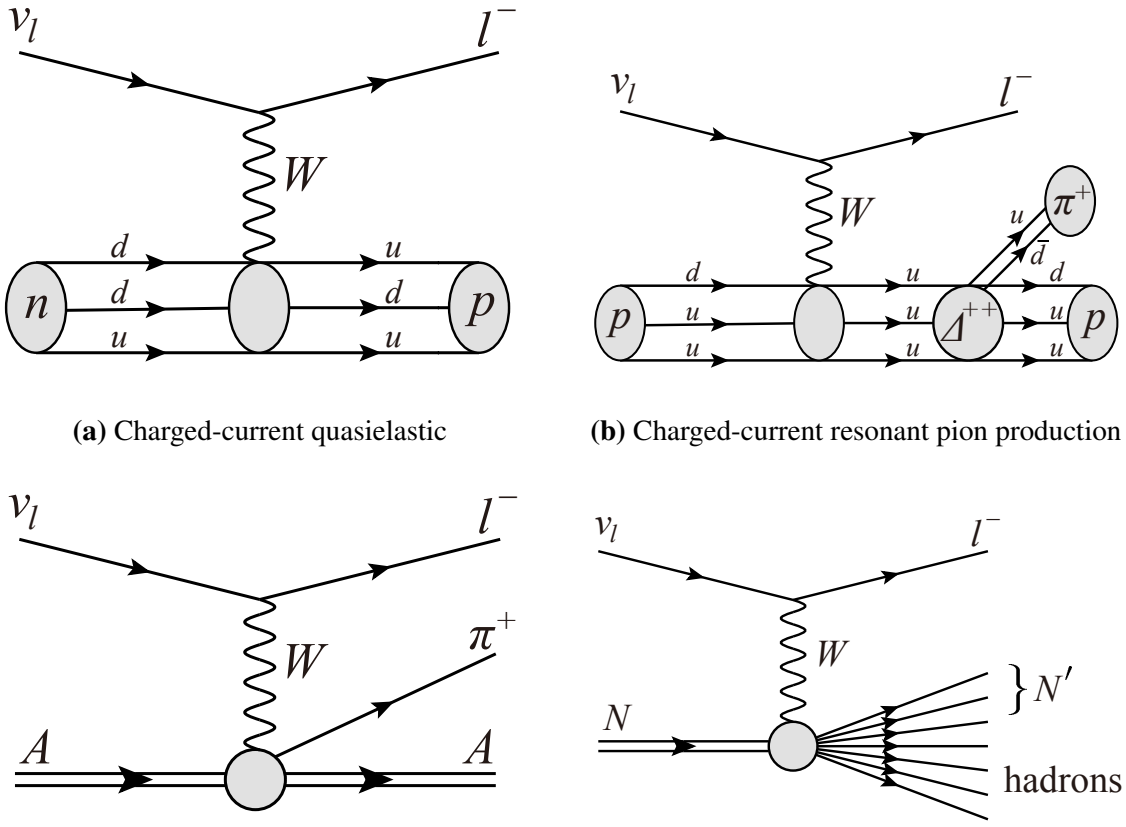

(a) Charged-current quasielastic

(b) Charged-current resonant pion production

(c) Charged-current coherent pion production

(d) Charged-current deep inelastic scattering

Figure 1.1: Diagrams for the primary charged-current interactions relevant to the T2K experiment[31].

Here m_p is the mass of the proton, m_n the mass of the neutron, m_l the mass of the outgoing lepton, which has an energy of E_l and momentum of p_l and travels at an angle θ relative to the direction of the incident neutrino.

The cross-section for this interaction can be calculated by contracting the hadron current with the lepton current, using the parton model for the quarks[32], and the vertex function for this interaction is written as a combination of a vector current and an axial current:

$$J^{\mu}_{QE} = V^{\mu}_{QE} - A^{\mu}_{QE} \tag{1.31}$$

with the vector current V^{μ}_{QE} and axial current A^{μ}_{QE}

$$V^{\mu}_{QE} = -F_1\gamma^{\mu} + \frac{F_2}{2M}i\sigma^{\mu\lambda}q_{\lambda} \tag{1.32}$$

$$A^{\mu}_{QE} = -F_A\gamma^{\mu}\gamma^5 - \frac{F_P}{M}q^{\mu}\gamma^5 \tag{1.33}$$

where $Q^2 = -q^2$, the four-momentum transfer, M is the mass of the nucleon, F_1 and F_2 the vector form factors, F_A the axial form factor and F_P the pseudoscalar form factor[33]. The vector current can be well measured using results from electron scattering experiments, as the form factors are directly related to the electromagnetic form factors[33]. The form factors for the axial current A^{μ}_{QE} are less well known as they are more difficult to measure experimentally, though the form factor F_P can be related to F_A by way of pion pole dominance[33]:

$$F_P(Q^2) = \frac{2M^2}{Q^2 + m_{\pi}^2}F_A(Q^2) \tag{1.34}$$

In general, the axial form factor is expressed as a dipole when modeling the CCQE interaction in experiments:

$$F_A(Q^2) = \frac{g_A}{(1 + \frac{Q^2}{M_A})^2} \tag{1.35}$$

The choice of the dipole approximation comes from the assumption that the weak axial charge follows an exponential distribution in the nucleus. Here the axial form factor shape is now determined only by the axial mass, M_A, as g_A can be experimentally measured from β-decay. So in the neutrino-nucleon case for the CCQE interaction, we only need to determine the value of M_A to calculate the interaction cross-section.

Charged-current Resonant Pion Production

In addition to the CCQE scattering, another important neutrino-nucleon interaction channel is the charged-current resonant pion production. Here the neutrino is high enough in energy, above 200 MeV, such that pion production through nucleon resonances becomes possible.

These resonances are mostly either spin-1/2 or spin-3/2. In particular, at experimental energies the spin-3/2 resonances where the pion is produced through delta resonances are dominant:

$$\nu_l + p \rightarrow l^- + \Delta^{++} \rightarrow l^- + \pi^+ + p \tag{1.36}$$

For the spin-1/2 resonances, the currents are the same form as the quasielastic interaction described previously for the nucleon in the CCQE interaction, though the incident neutrino energy cannot be calculated in the same way. However, the currents for the spin-3/2 resonances are more complicated in structure. Like the CCQE interaction, the vertex can be written as a combination of a vector current and an axial current. The axial current for the spin-3/2 resonance is

$$A^{\alpha\mu}_{3/2} = -(\frac{C^A_3}{M}(g^{\alpha\mu}\not{q} - q^\alpha\gamma^\mu) + \frac{C^A_4}{M^2}(g^{\alpha\mu}q\dot{p} - q^\alpha p^\mu) + C^A_5 g^{\alpha\mu} + \frac{C^A_6}{M^2}q^\alpha q^\mu) \tag{1.37}$$

where C^A_3, C^A_4, C^A_5 and C^A_6 are the axial $N-\Delta$ (Nucleus to Δ) transition form factors, q is the momentum transfer, $g^{\alpha\mu}$ is the metric tensor and M is the nucleon mass in the case of the free nucleon. The form factor $C^5_A(Q^2)$ can be expressed as a modified dipole:

$$C^A_5(Q^2) = C^A_5(0)\left(1 + \frac{Q^2}{M^2_{RES}}\right)^{-2}\left(1 + \frac{Q^2}{3M^2_A}\right)^{-1} \tag{1.38}$$

where M_{RES} is the axial mass for resonant processes. For the other form factors, we use the Adler model, where C^A_4 can be related back to C^A_5:

$$C^A_4(Q^2) = -\frac{C^A_5(Q^2)}{4} \tag{1.39}$$

and $C^A_3(Q^2)$ is equal to 0. For C^A_6, this form factor can be related back to C^A_5 through pion pole

dominance similar to the QE case[33], giving:

$$C_6^A(Q^2) = C_5^A(Q^2)\frac{M^2}{Q^2 + m_\pi^2} \tag{1.40}$$

where m_π is the mass of the pion and M is the mass of the nucleon. This allows there to only be one independent form factor, C_5^A, for the axial current for the Δ resonance. This is the Llewellyn-Smith formalism[32], and is the standard description used for neutrino-nucleon interactions in current neutrino generators. In this case there are two parameters that must be measured in order to determine the cross-section: the axial mass M_{RES}, and the form factor C_5^A.

1.4.3 CC-0π Neutrino Interactions on Nuclei

While the description of the charged-current neutrino scattering off of nucleons can be reduced to equations that depend only on a select few form factors and masses, these equations assume that the nucleon is free, and not bound in a nucleus. Just as quarks are found in bound states, the nucleons in neutrino experiments are bound in nuclei. So what needs to be considered is not just neutrino-nucleon interactions, but neutrino-nucleus interactions – introducing nuclear effects to the interaction cross-sections. Once a nucleon is bound in a nucleus, it becomes subject to various other effects which present various experimental problems. Interactions of the final state products (known as Final State Interactions or FSI), where the produced pions and nucleons interact in the nucleus itself, can lead to different particles leaving the nucleus than those from the original neutrino interactions – leading to difficulties in correctly identifying the interaction type.

To correctly calculate the cross sections for interactions with a nucleon inside a nucleus, other effects such as the Fermi motion of the initial nucleons, Pauli blocking of final nucleons and final state interactions, where produced particles continue to interact inside the nucleus, must be considered. Because of the complexity and variety of nuclear effects on the interactions, neutrino experiments use a variety of different models to account for these. In addition to modeling nuclear effects for the CCQE interaction, this section will also discuss modeling

multi-nucleon-neutrino interactions, also known as n particle – n hole. These interactions share the same observed final state topology as CCQE interactions, and therefore form an irreducible experimental background for a CCQE signal.

Relativistic Fermi Gas Model

The Relativistic Fermi Gas model (RFG) is the most commonly used model for simple CCQE interactions on nuclei in neutrino generators, and allows nuclear effects to be accounted for alongside the neutrino-nucleon dipole model described previously. The RFG model which is most commonly used by neutrino interaction generators is the Smith-Moniz model[34]. This model has been in use for several decades. The RFG model depends on just two nucleus-dependent parameters: the Fermi momentum p_F and the nucleon binding energy E_B. The nuclear ground state is thus modeled as a Fermi gas of non-interacting nucleons, both proton and neutron, as shown in Figure 1.2. The Fermi momentum and binding energy are global for all nucleons and constant for a given material. The effect on modeled cross-sections is shown for electron scattering in Figure 1.3, and is modeled the same as for neutrino interactions.

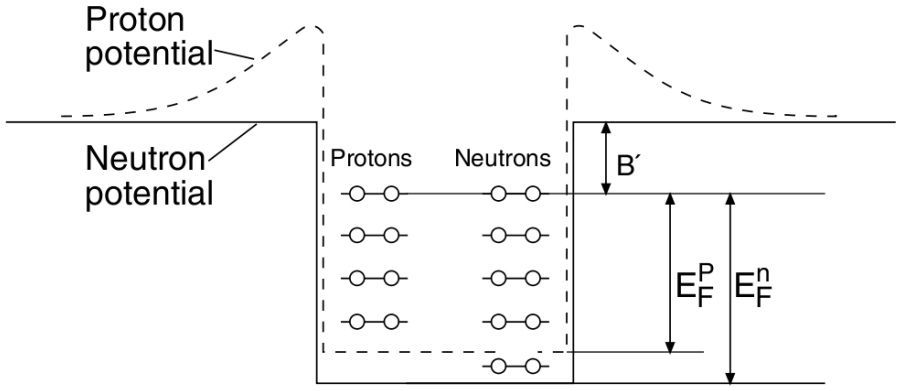

Figure 1.2: Diagram of protons and neutrons in a Fermi gas potential. Here E_F is the Fermi energy, related to the Fermi momentum p_F and B is the nucleon binding energy. The proton potential differs from the neutron potential due to electrostatic repulsion. Image reused from [35] with permission.

The RFG model is generally applied only for CCQE interactions, rather than also for CC resonant interactions. The reason for this is that the Fermi momentum and the binding energy

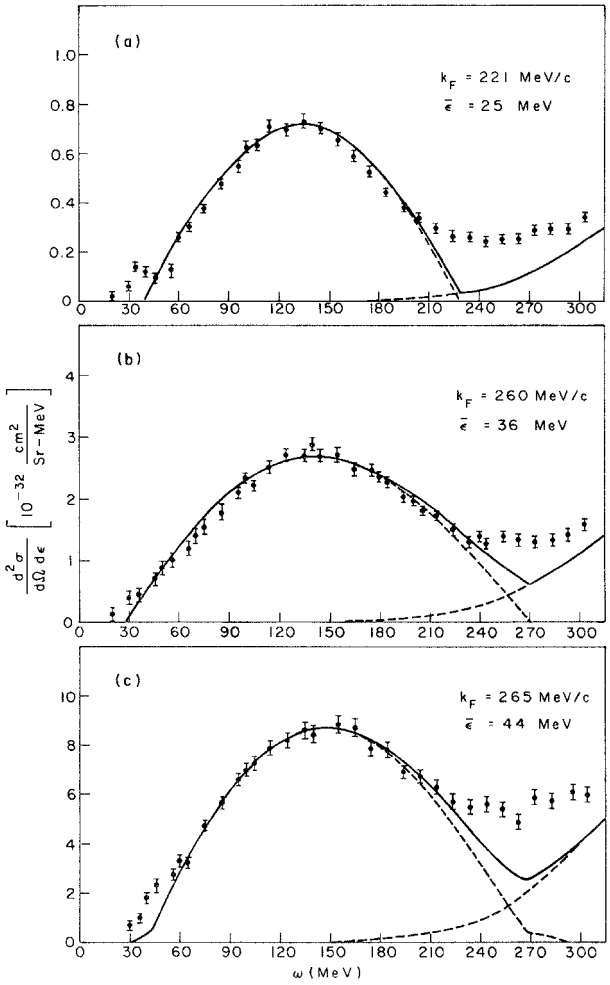

Figure 1.3: Plots of the cross-sections $d^2\sigma/d\Omega d\varepsilon$ for electron scattering on various targets versus electron energy loss $\omega = \varepsilon_1 - \varepsilon_2$, with solid line representing the Fermi gas model predictions. Plot a is on carbon, plot b is on nickel and plot c on lead. Diagrams taken from [36] with permission.

should have little effect on these types of interactions. In resonant interactions, the Fermi momentum would apply to the nucleon produced from the decay of the intermediate resonances. These nucleons are generally above the Fermi momentum, and thus are rarely affected by Pauli blocking[34]. Pauli blocking comes from the Pauli exclusion principle, which bars identical fermions (in this case neutrons and protons) from occupying the same quantum state in a nucleus. In practice, the Fermi gas model treats all of its possible particle states as filled, and any produced outgoing nucleon cannot occupy them. This gives a lower bound to the momentum of the outgoing nucleon, the Fermi momentum p_F. Additionally, the binding energy is much

smaller than the resonance mass, M_Δ, and so only has a small effect on the resonance decay.

Spectral Function Model

The RFG model, while simple to implement and use in generators, does not provide a very complete description of nuclear effects: it assumes the neutrino interacts with a single nucleon in the nucleus, without correlations to other nucleons. The spectral function (SF) model, where spectral function refers to some function that describes the momentum and energy distributions of the initial nucleons in the nucleus, is made to be a more physically motivated model. Like the RFG model, the SF model does depend on the target nucleus: separate spectral functions must be built for each target nucleus. Additionally, the SF model is used only for CCQE interactions. These functions are relatively easy to calculate for light nuclei, but for medium nuclei, such as carbon or oxygen, the spectral function will be an approximation[37].

The spectral functions are made up of two terms: a mean field term for single particles, and a term from correlated nucleon-nucleon pairs. This second term leads to a tail for the momentum and binding energy. Unlike the RFG model, where Pauli blocking arises from the Fermi momentum parameter p_F, the spectral functions used in the SF do not implicitly have Pauli blocking. While the correct way to include this would be to determine the cutoff using the local density, this is computationally impractical; instead a simple cutoff is applied to the spectral function at the appropriate energy, effectively forcing Pauli blocking. The spectral function is used as an alternative to the RFG model, and is presented here to give a more complete idea of the state of currently used neutrino models.

Random Phase Approximation

While the RFG model includes important nuclear effects such as Pauli blocking, it is still a somewhat basic model and does not cover many other nuclear effects, particularly those related to correlations between nucleons within a nucleus. At low and intermediate energies, one of these additional nuclear effects is that of long-range correlations between nucleons[38]. The CCQE peak energy lies in these energy regions, and therefore such long-range correlations can

have a significant effect on the shape of the differential cross-section for the neutrino.

The Random Phase Approximation (RPA) model specifically accounts for the nuclear-medium polarization effects on the 1 particle – 1 hole contributions and is used as a correction to the RFG nuclear model. The RPA model can be calculated using either relativistic or non-relativistic nucleon kinematics, with T2K and other neutrino experiments commonly using relativistic kinematics. At lower energies, relativistic and non-relativistic treatments of the kinematics shows similar behavior, In particular, adding the RPA effects reduces the CCQE cross-section at lower energies Additionally, while RPA models a nuclear effect, the corrections from the model do not depend strongly on the choice of nucleus[38].

Multi-nucleon Correlation Models

A major contributor to additional nuclear effects on the interaction cross-sections, and the observed topologies, are multi-nucleon-neutrino interactions,, where the incoming neutrino interacts with multiple nucleons simultaneously. These interactions are generally referred to as n particle – n hole (np-nh) interactions, as multiple particle-hole pairs are propagated in the nucleus. These models were introduced to help resolve the disagreement between the MiniBooNE cross-section results published in 2010 and its best-fit $M_A = 1.35 \pm 0.66$ GeV/c^2 [39], and the best-fit values from other experiments such as NOMAD, with a best fit $M_A = 1.05 \pm 0.02(stat) \pm 0.06(syst)$ GeV/c^2[24]. MiniBooNE was not the only experiment that measured a high value for M_A, as K2K had also measured the axial mass and found a value of $1.144 \pm 0.077(fit)^{+0.078}_{-0.072}(syst)$[40] although this was in better agreement with the global results. One possibility for these measurements is that otherwise unmodelled nuclear effects were being absorbed into other CCQE parameters, such as p_F, E_B or M_A. MiniBooNE did not use a multi-nucleon-neutrino interaction model, and was not able to subtract such events from the CCQE sample. However, the MiniBooNE data was found to agree with global M_A values when fit with a model using multi-nucleon-neutrino effects[41].

To predict the contribution from these interactions, the cross-sections can be computed with

a multi-body expansion of the weak propagator in the nuclear medium[42]. In this multi-body expansion, the first-order expansion gives the standard CCQE interaction, where one nucleon in involved in the interaction and there is a single hole in the nucleus. Once one looks at the second order terms, Feynman diagrams for two possible 2 particle – 2 hole (2p-2h) W-self energy interactions are shown in Figure 1.4. In Figure 1.4a, the W couples to a second nucleon, and in Figure 1.4b, the 2p2h process is driven by ρ exchange through short range correlations [42]. However, there are many more possible diagrams from the various types of 2p-2h interactions.

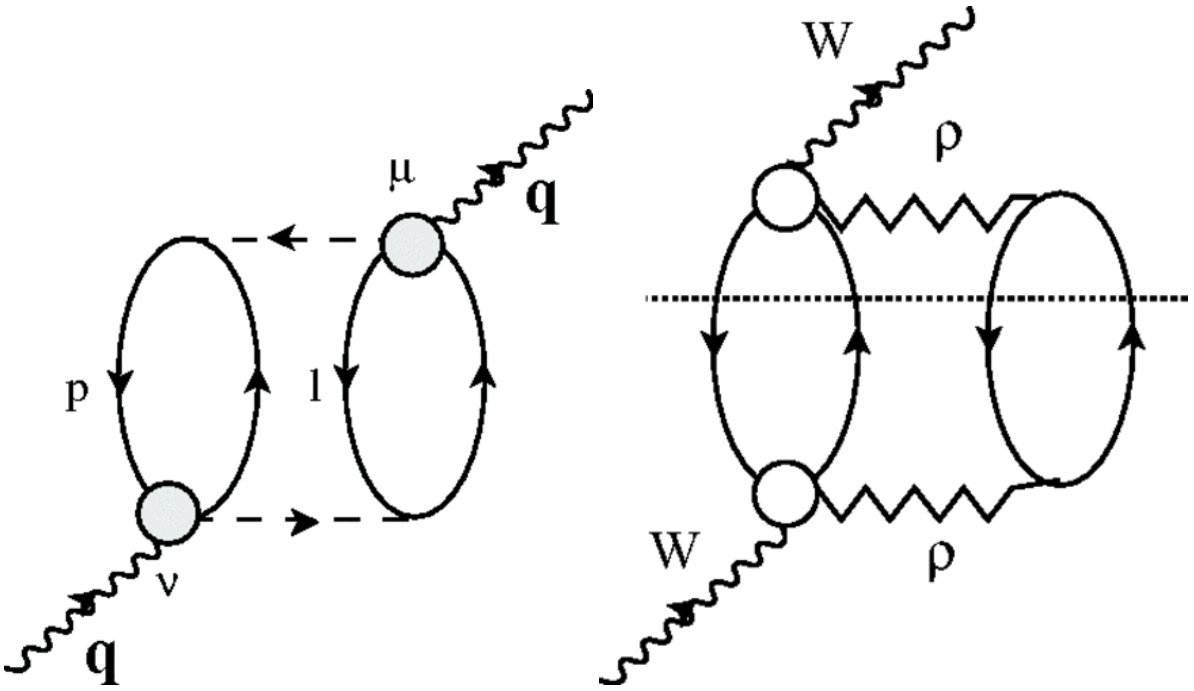

(a) Diagram of W-selfenergy from nucleon-nucleon correlations.

(b) Diagram of W-selfenergy driven by ρ exchange.

Figure 1.4: Example diagrams for 2 particle – 2 hole interactions in nuclear medium. Diagrams taken from [42] with permission.

These are not quasi-elastic interactions, as more than one nucleon is included in the interaction through correlations. This means that the CCQE neutrino energy calculation in Equation 1.30 is no longer applicable[42], and complete energy calculation requires more than just the outgoing lepton momentum. However, these multi-nucleon interactions still share the CC-0π final state topology with CCQE interactions and are a irreducible experimental background,

as the final state protons are both difficult to detect and can be affected by various final state interactions. Because of this, neglecting to model the higher order terms in the expansion can lead to bias in the reconstructed energy spectrum for CCQE events.

One frequently used model for 2p-2h interactions is the Nieves 2p-2h model[43], which is the model currently used in the T2K experiment. In the Nieves model, the many body expansion of the W-boson self energy contribution in the calculation for the differential cross-section for neutrino charged-current interactions, up to the third order terms. As this model is difficult to implement in generators, the hadronic level model parameters cannot be changed in a fit. Another major 2p-2h model is the Martini model[44]. Like the Nieves model, the Martini model uses a a multi-body expansion for the n particle – n hole terms. However, Nieves also accounts for higher order terms in the meson-exchange current (MEC) and axial-vector interference terms, which are not included in the Martini model.

1.4.4 Current state of Neutrino Interaction Modeling

The neutrino interaction models used today are by no means complete – because nuclear modeling is a complicated and difficult process, all models include significant assumptions that may not always be valid. Of course, a nuclear model with poor assumptions can have a negative effect on any oscillation measurements, as it can lead to incorrectly assigning energies to interactions and incorrectly predicting the relative amounts of the various interaction channels, among other things. In addition, it is difficult to simply scale the modeling of nuclear effects between different nuclei, which is a major source of uncertainty for experiments with differing near and far detector materials such as T2K.

In part, this is due to relatively few cross-section measurements on oxygen targets relative to carbon – as Figure 1.5 shows, most of the cross-section measurements for neutrinos have been on carbon and deuterium, rather oxygen. Outside of measurements at T2K and its predecessor K2K, only MINERνA has used a water target to study neutrino interactions. As the far detector target of T2K is oxygen[45], this presents some issues in using previous cross-section data to

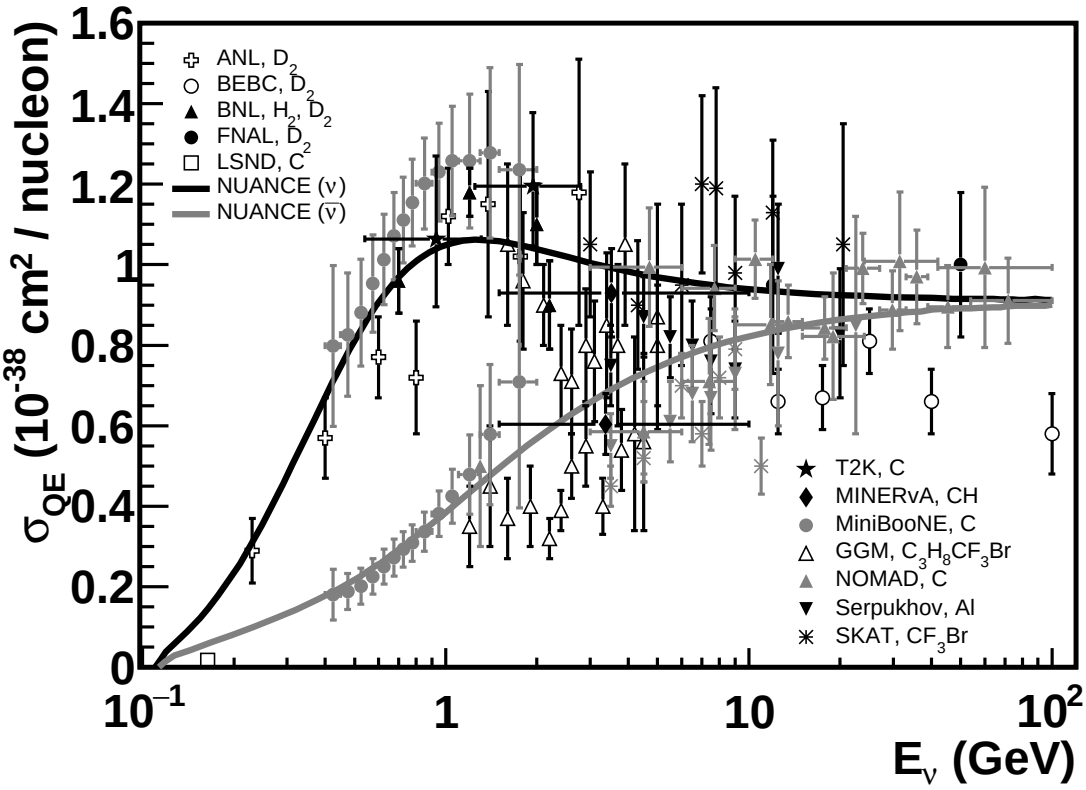

Figure 1.5: Measured CCQE neutrino cross-sections for neutrino (black) and antineutrino (grey). Plot taken from [14] with permission.

understand interaction rates at the far detector due to difficulty in scaling between targets. In practical terms, this means that oscillation measurements at T2K must either incorporate uncertainties due to potential differences in carbon and oxygen interactions or be able to provide some form of information on neutrino interactions on oxygen itself.

Chapter 2

The T2K Experiment

2.1 The History of T2K

The T2K experiment is a long-baseline neutrino oscillation experiment designed to study various neutrino oscillation parameters through ν_μ disappearance and ν_e appearance, using a ν_μ beam. T2K was built in order to measure the mixing angle θ_{13}, which had not been measured at the time. Additionally, the best limits on θ_{13} from the CHOOZ experiment[19] did not exclude $\theta_{13} = 0$. The design goal of T2K was to improve on these limits and achieve a sensitivity a factor of 20 better than that of the CHOOZ experiment. In addition to measurements of θ_{13}, T2K is designed to be able to study other oscillation parameters with the precision of $\delta(\Delta m^2_{23}) \sim 10^{-4}\text{eV}^2$ and $\delta(\sin^2 2\theta_{23}) \sim 0.01$ using ν_μ disappearance. As the T2K beam can run in either neutrino or antineutrino mode, δ_{CP} can also potentially be investigated. The T2K near detectors also provides for a variety of neutrino interaction studies and cross-section measurements.

The T2K experiment is made up of the neutrino beamline at Japan-Proton Accelerator Research Center (J-PARC), the near detectors 280 m from the beam source, and the far detector at Super-Kamiokande (SK), 295 km from the beam source. The far detector at SK has been operational since 1996 and both the T2K near detectors and the neutrino beamline were completed in 2009. T2K has been accumulating neutrino beam data since 2010; the total data collected

is counted in numbers of protons on target as that directly corresponds to the beam energy and number of spills collected. The T2K neutrino beam was run in neutrino mode from 2010 to the spring of 2013, and in antineutrino mode from 2014 to 2016. The total protons on target (POT) and running periods are shown in Figure 2.1.

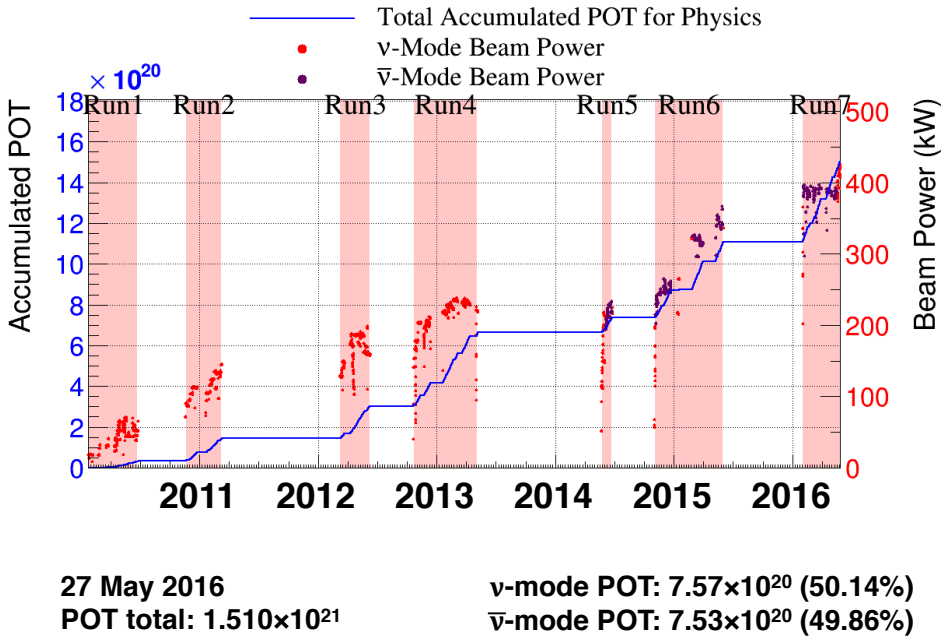

Figure 2.1: Plot showing the T2K beam run periods. Light red regions indicate periods where the T2K neutrino beam was being produced. Plot from [46].

Both the near detectors and far detector sit at 2.5° off-axis from the muon neutrino beam, which gives a narrow-band energy spectrum with a peak energy of 600 MeV. This energy is chosen to maximize the probability of ν_μ oscillation at the far detector 295 km away. This is possible due to the fact that the probability of oscillation, as described previously in Section 1.2.2, depends on the neutrino energy and distance traveled as $\sin^2 \frac{\Delta m^2_{ij} L}{4E}$, where $\Delta m^2_{ij} = m^2_i - m^2_j$ for the relevant neutrino flavors. Because the energy spectrum of the T2K neutrino beam has a broad spread from the energy of the parent pions, situating the detectors off-axis is necessary to achieve both a narrow energy band, and a peak energy around the oscillation maximum, as is discussed in Section 2.2.1. The near detectors are positioned close

enough to the beam source to have effectively no oscillations, allowing measurement of the unoscillated beam flux.

2.2 The Neutrino Beam at T2K

The T2K neutrino beam is produced using the 30 GeV proton beam produced at the Japan-Proton Accelerator Research Center (J-PARC). The beam facilities are located in Tokai, on the eastern coast of Japan. J-PARC comprises three proton accelerators for the beam: a linear accelerator (LINAC), a rapid-cycling synchrotron (RCS) and the main ring synchrotron (MR)[45]. The initial proton beam is produced by injecting H^- ions into the LINAC and accelerating them up to 400 MeV. The H^- beam is passed through charge stripping foils to produce a H^+ beam. This proton beam is then injected into the RCS, and accelerated to 3 GeV. The RCS has a 25 Hz cycle and has two bunches in each cycle. Around 5% of the beam bunches are supplied to the MR, with the rest used in the muon and neutron beamline at J-PARC. In the MR, the proton beam is accelerated to 30 GeV, its final kinetic energy. The MR beam has eight bunches and these are extracted in a single turn for use by the T2K neutrino beamline.

The neutrino beamline, where the proton beam is extracted from the MR, consists of a primary beamline and secondary beamline. The primary beamline transports and focuses the extracted proton beam. This is done in three separate sections: the preparation section, the arc section and the final focusing section. The preparation section is 54 m long, and tunes the extracted proton beam for the arc section using magnets. The arc section is 147 m long, and is where the beam is redirected towards Kamioka and the far detector. The tuned proton beam is bent by 80.7° with a 104 m radius of curvature using superconducting combined function magnets. The final focusing section is 37 m and serves to focus and guide the proton beam on the target, as well as aim the beam downwards by 3.637° with respect to the horizontal[45].

The secondary neutrino beam line consists of the target station, decay volume and the beam dump. The target station contains the proton beam target, a 91.4 cm long graphite tube

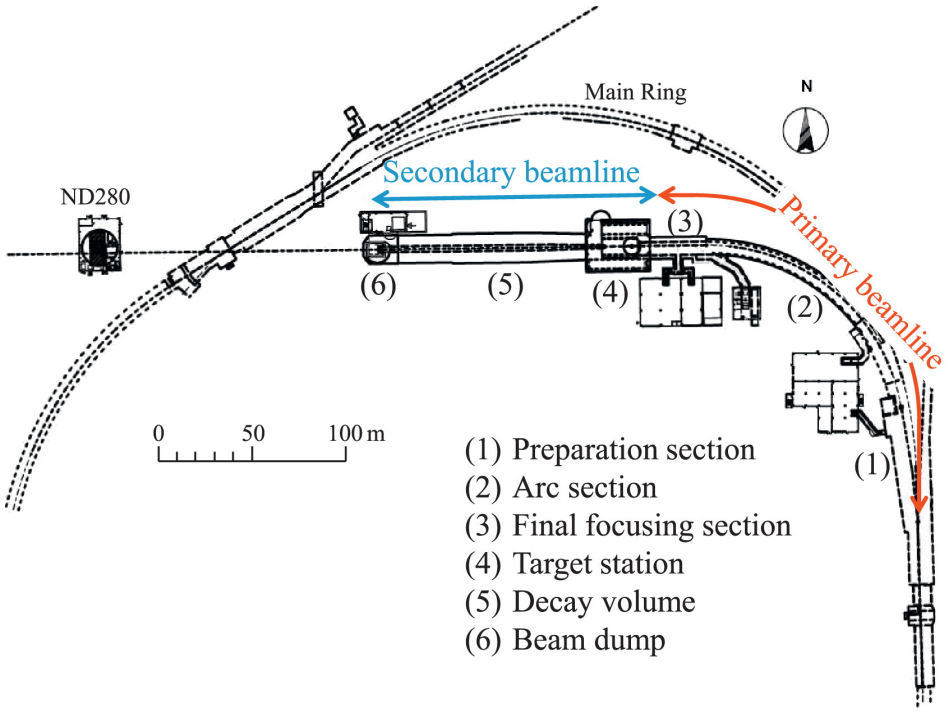

Figure 2.2: Overview of the T2K beamline. Figure taken from [45] with permission.

surrounded by another 2mm thick graphite tube in a titanium case, and three magnetic horns. The proton beam is incident on the target, producing primarily pions along with kaons, and the magnetic horns are used to collect and focus the pions. The horns can be run in Forward Horn Current (FHC) mode, which collects the π^+ to produce a neutrino beam, and in Reverse Horn Current (RHC) mode, which collects the π^- to produce an antineutrino beam. The pions go through the decay volume, which is a 96 m long steel tunnel filled with helium[47], and decay primarily into muons and muon neutrinos. The muons and other decay products are stopped by the beam dump, producing a muon neutrino beam.

2.2.1 The Off-Axis Neutrino Beam

In order to achieve a narrow-band neutrino beam, T2K uses the off-axis method to tune the neutrino beam energy spectrum. This places the detectors at an angle relative to the primary focusing axis for the beam. The neutrinos in the T2K beam are produced from two-body pion decay, where the energy of the emitted neutrino at a given angle relative to the direction of the

parent meson has a weak dependence on the parent momentum. While the neutrino energy has a linear relation to the parent pion energy when on-axis, at high off-axis angles, the produced neutrino energy instead levels out at higher pion energies [48]. This means that the neutrino energy spectrum has a strong angular dependence, and the energy peak and spread can be tuned by choice of angle relative to the primary beam focusing axis. On axis, the T2K neutrino beam peaks at around 1 GeV. At T2K, the off-axis angle is set to be 2.5°, setting the peak neutrino energy at around 0.6 GeV. This gives a neutrino spectrum peaked near the first oscillation maximum at SK, as shown in Fig. 2.3. The lower peak energy also reduces the background from non-CCQE processes at both the near and far detectors.

2.3 Super-Kamiokande

2.3.1 The Super-Kamiokande Detector

The Super-Kamiokande detector functions as the far detector for the T2K experiment, and is located in the Mozumi mine beneath Mt. Ikenoyama, 295 km from the beam source. The mountain provides 1000m of rock, equivalent to 2700 m water, mean overburden to reduce the background from cosmic ray muons [49]. The detector itself is a water Cherenkov detector, consisting of a stainless-steel tank 39 m in diameter and 42 m tall, with a total volume of 50 ktons. Inside the tank, there is a 55 cm thick stainless-steel framework 2.5 m inside the walls that support arrays of Photomultiplier Tubes (PMTs), which split the tank volume into the Outer Detector (OD) and Inner Detector (ID). These are optically isolated by two light-proof sheets on the surfaces of the stainless-steel framework, which is uninstrumented dead space, to prevent light leaking between the two volumes. A diagram of the SK detector and its placement is shown in Figure 2.4.

The OD is the volume from the outer edge of the tank to the PMTs and framework 2.5 m into the tank, and is instrumented with 1885 Hamamatsu 20 cm PMTs. These PMTs face outwards towards the wall of the SK tank. As the OD is sparsely instrumented, the walls of the volume are lined with a reflective coating of Tyvek[49] in order to improve the light collection

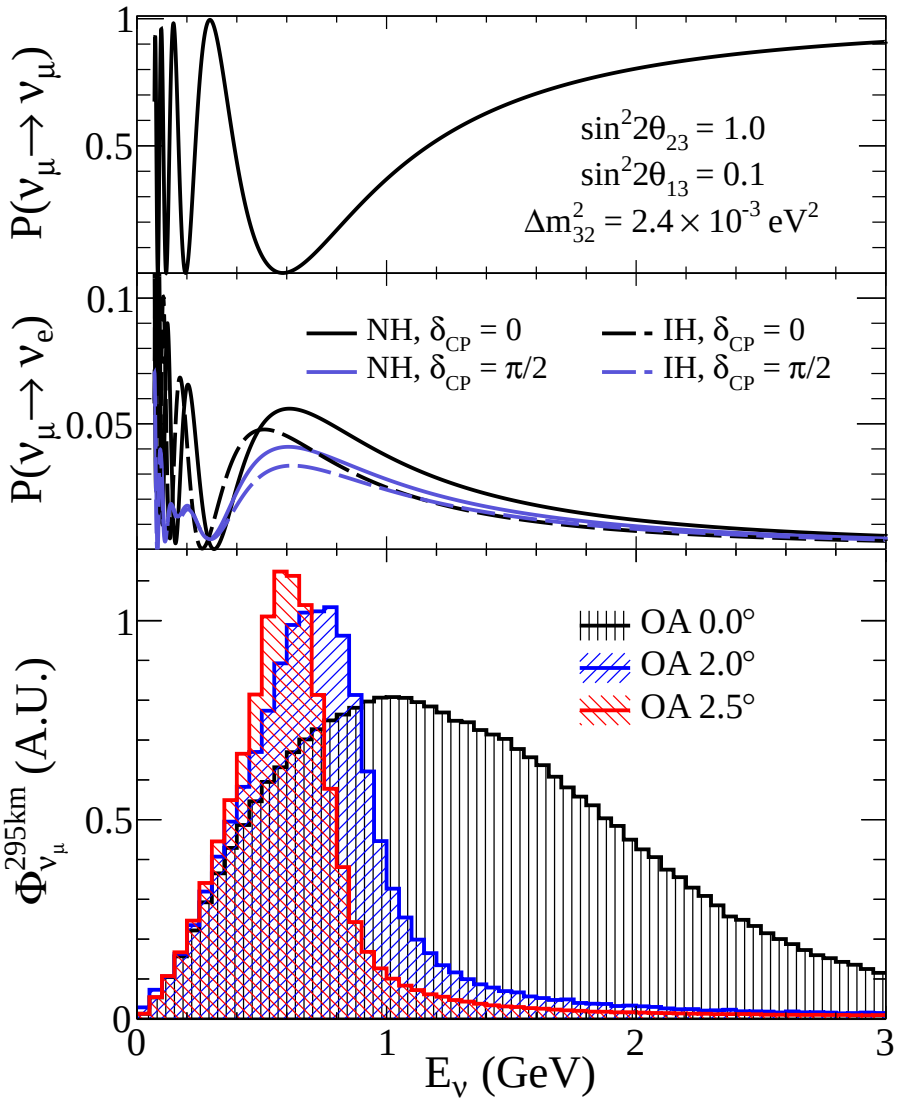

Figure 2.3: The neutrino energy spectra at the T2K far detector at various choice of off-axis angles, along with the probability of ν_μ disappearance and ν_e appearance as a function of neutrino energy. The third plot shows the neutrino spectrum as a function of angle at the far detector. Figure taken from [47] with permission.

efficiency. The OD serves as a veto for incoming particles for the ID, as well as providing passive shielding from neutrons and other particles.

The ID is the main detector volume for SK, with dimensions of 33.8 m in diameter and 36.2 m tall with a total volume of 32 kton of water. It is instrumented with inwards-facing 11,146 PMTs of 50 cm diameter which are mounted on a 70 cm grid[49]. To achieve an effective photocoverage of 40%, 7650 PMTs are located on the sides of the ID, 1748 on the top, and

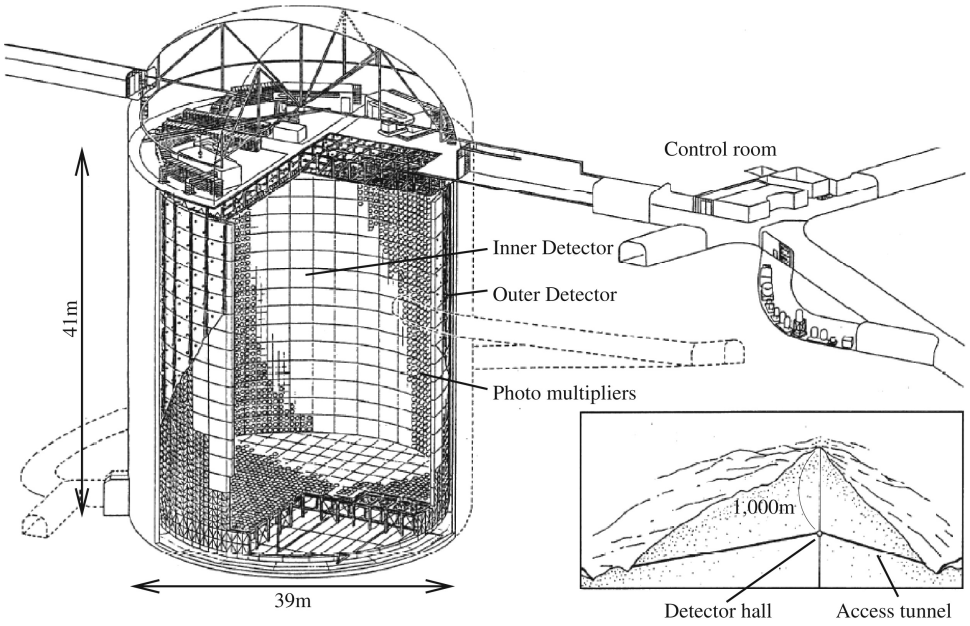

Figure 2.4: Diagram of the SK detector and facility. Figure taken from [45] with permission.

1748 on the bottom. Unlike the OD, the area between the ID PMTs is lined with opaque black sheets in order to minimize the number of reflected photons detected, as this can impact event reconstruction. The ID is used for the T2K oscillation analysis and detects leptons produced from neutrino interactions in the inner volume.

2.3.2 Event Reconstruction and Selection

The SK event selection used in the oscillation analysis looks for charged leptons produced by charged-current quasielastic neutrino interactions: μ for ν_μ interactions and e for ν_e interactions. The event selection is based around correctly identifying these leptons. To do this, the SK detector is designed to detect Cherenkov radiation produced by these particles. Cherenkov radiation is produced when a charged particle moves through a medium such as water at a speed greater than the speed of light in that medium. This is given as $v > \frac{c}{n}$, where v is the speed of the particle, c the speed of light and n the index of refraction. This light is emitted at an angle $\cos\theta = \frac{c}{nv}$ relative to the direction the particle is traveling. This produces a light cone around the particle, which can then be detected and reconstructed in the SK detector as a

ring-shaped hit pattern.

The event selection at SK looks for CCQE interactions from ν_μ and ν_e events. Due to detector design and lack of magnetic field, there is no simple way to differentiate between neutrino and antineutrino events at the SK detector. The event selection looks at events which are fully contained in the SK inner detector, as the event selection and oscillation analysis rely on the reconstructed neutrino energy and it is difficult to correctly reconstruct that energy for events where the produced particles leave the detector volume. Events are considered to be fully contained if there are less than 16 hit PMTs in the OD, indicating that the event deposited no energy outside the ID volume. The reconstructed event vertex must also be at least 200 cm from the ID walls for all selected events.

The primary signal channel at SK is the CCQE interaction, described in Section 1.4. As this produces a single lepton and proton for the final state, CCQE events should only have one detectable Cherenkov ring in the ID, as the proton will be below the Cherenkov threshold. This means the event selections for both ν_e and ν_μ events require that there is only one reconstructed ring in the event. Selected events are then separated based on the particle ID of the single reconstructed ring; muons are heavier and scatter less than electrons as they travel through the detector volume. This produces a sharply defined ring as compared to the fuzzier Cherenkov ring from an electron, which scatters more easily due to its lower mass and also induces electromagnetic showers as it travels. For the ν_e event selection, the cuts are:

1. The single reconstructed ring must be identified as electron-like by the SK particle identification.

2. $E_{vis} > 100$MeV. E_{vis} is the total visible light from the reconstructed rings in the event. This removes background from NC processes and Michel electrons from other particle decays, as the CCQE signal process is unlikely at low energies.

3. There must be no decay electrons detected. These show up as secondary events shortly after the primary neutrino interaction, and indicate the presence of a μ or π.

4. The reconstructed neutrino energy must be less than 1250 MeV. Detected ν_e with higher energies are likely to be contamination from the beam due to the lower energy peak and spread of the off-axis beam.

5. π^0 identified events are rejected based on a comparison of the likelihoods for ν_e and π^0 particle ID hypotheses.

The ν_μ event selection cuts are:

1. The single reconstructed ring must be identified as muon-like by the SK particle identification.

2. The reconstructed muon momentum must be greater than 200 MeV/c, in order to remove low energy background.

3. There must be one or no decay electrons in the event, as events with 2 or more are predominantly CC non-QE events, while some CCQE events will have no detected decay electrons.

2.4 The T2K Near Detectors

The T2K near detectors sit 280 m from the beam source at J-PARC, and consist of two separate parts: the Interactive Neutrino GRID (INGRID) Detector and the Near Detector at 280m (ND280). Unlike the SK detector and ND280, INGRID is situated on-axis, while ND280 is set at 2.5° off-axis.

2.4.1 The Interactive Neutrino GRID Detector

The Interactive Neutrino GRID (INGRID) detector at J-PARC is centered around the neutrino beam axis and is primarily used to monitor the beam direction and intensity. The INGRID detector is composed of 16 separate identical modules arranged as shown in Figure 2.5 and samples the beam in a 10 m $\times$ 10 m transverse section where the center of INGRID corresponds

to the neutrino beam center[45]. Each module is composed of 9 iron plates, which provide the target material, and 11 tracking scintillator planes arranged in a sandwich structure. The total iron target mass is 7.1 tons per module. Each module has veto scintillator planes placed around it for reducing external background.

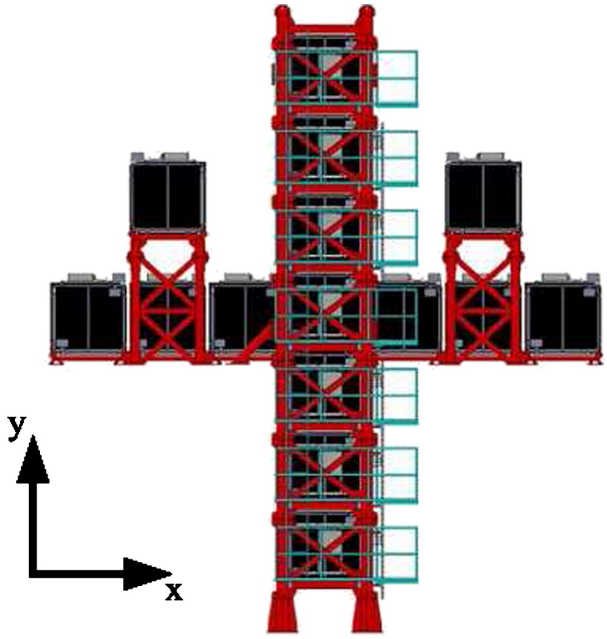

Figure 2.5: The INGRID detector. Figure taken from [45] with permission.

2.4.2 The ND280 Detectors

The near detector (ND280) for T2K is situated 280 meters from the T2K beam target and is 2.5° off-axis. As mentioned at the start of this chapter, this gives a narrower energy spectrum for neutrinos, and matches the off-axis angle at SK. ND280 is composed of five different detectors, which are used together to perform the ND280 analysis. The main section used for analysis is called the tracker, which is made of three time projection chambers (TPCs) and two Fine Grain detectors (FGDs). The two FGDs are the primary target volume for ND280, and are described in more detail in Section 2.5. Upstream from the track, closer to the beam source, is the Pi-0 Detector (P0D), for measuring the π^0 background from neutral current interactions. The P0D and the tracker are situated in a 6.5 m $\times$ 2.6 m $\times$ 2.5 m metal frame. The frame is surrounded by an electromagnetic calorimeter (ECal), which is in turn surrounded by the

recycled UA1 magnet. This magnet was previously used by the UA1/NOMAD experiment at CERN, and provides a 0.2 T dipole magnetic field for ND280, which is near constant in the detector volumes. The magnetic field allows for accurate momentum measurements and particle charge identification in the near detectors. This field is generated by a 2900 A current passed through the water-cooled aluminum coils that make up the magnet[45]. The inner dimension of these coils is 7.0 m $\times$ 3.5 m $\times$ 3.6 m, and they are surrounded by 16 flux return yokes, arranged in pairs, with outer dimensions of 7.6 m $\times$ 5.6 m $\times$ 6.1 m with a total weight of 850 tons. The coils and yoke are divided into two mirror-symmetric halves to allow for opening and closing the magnet to access the detectors. The magnet is additionally instrumented with scintillator to function as a muon range detector (SMRD).

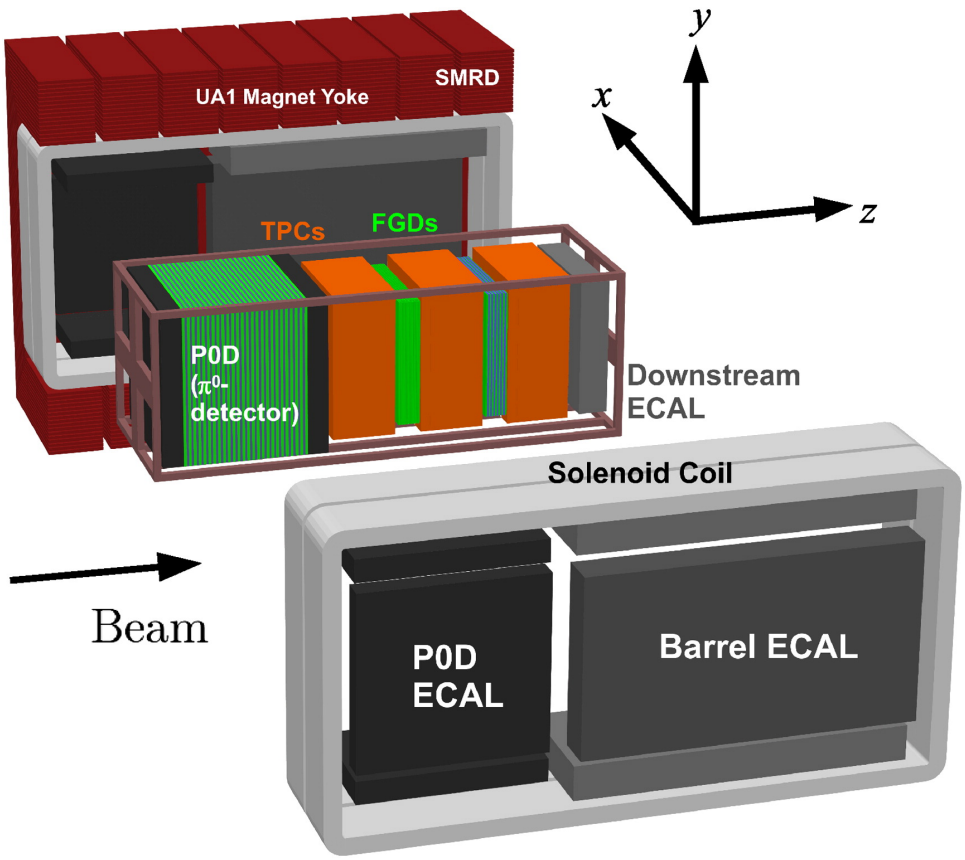

Figure 2.6: Picture of the ND280 layout. Figure taken from [45] with permission.

The Pi-0 Detector

The Pi-0 Detector (P0D) is designed to measure the neutral current process $\nu_\mu + N \rightarrow \nu_\mu + N + \pi^0 + X$ on water, and uses the same material as the target at SK. To do this, the P0D is composed of scintillator modules alternated with fillable water target bags and lead and bronze sheets. The water bags can be filled or left empty during running; this allows for subtraction analysis to determine the water cross-sections. There are 40 scintillator modules, each composed of an X and a Y layer of triangular scintillator bars with wavelength shifting (WLS) fibers through the middle of each bar. There are 134 vertical bars and 126 horizontal bars in each module. The total active target volume is 2103 mm $\times$ 2239 mm $\times$ 2400 mm, and has a total mass of 16.1 tons with the water bags filled, and 13.3 tons with the water bags empty [50].

The Side Muon Range Detector

The Side Muon Range Detector (SMRD) is not part of the inner detectors in ND280, but instead is incorporated with the magnet yoke that surrounds the rest of ND280. It serves several purposes: the detection of escaping high-angle muons relative to the beam direction, cosmic ray trigger and veto for particles entering the ND280 volume, and identifying beam interactions from the surrounding magnet and detector pit. The SMRD is not set up separately from the magnet yoke but is instead installed in the air gaps between the steel plates that make up the flux return yoke. Each yoke has 15 air gaps in the radial direction, where the SMRD layers are placed. The detector consists of 440 scintillator modules, with two kinds of module, as the horizontal and vertical gaps are of different sizes: horizontal, which are composed of four scintillation counters, and vertical, which are composed of five scintillation counters. The counters themselves are optimized to maximize the active area in each gap. There are three layers of scintillator modules on the top and bottom of all flux return yokes. There are 3 layers of scintillator modules on the sides of the first five flux return yoke pairs, four layers on the sides of the sixth pair and six layers of scintillator modules on the last two pairs of flux return yokes.

The Electromagnetic Calorimeters

The Electromagnetic calorimeter (ECal) is a sampling electromagnetic calorimeter which surrounds the TPCs, FGDs and the P0D. It provides near-complete coverage for particles exiting the inner detector volume, by detecting photons and measuring their energy and direction. The ECals can also provide reconstruction of π^0s produced inside the tracker, as unlike the P0D, the tracker is not designed to detect these. To do this, the ECal is made up of various configurations of layers of scintillator bars and layers of lead, which provide a neutrino-interaction target and additionally act as a radiator to produce electromagnetic showers.

There are three types of modules in the ECal: six Barrel ECal modules, which are placed around the sides of the tracker volume parallel to the beam axis, one Ds-ECal module, positioned downstream at the exit of the tracker volume and six P0D-ECal modules around the P0D parallel to the beam axis[51]. The Barrel ECal modules consist of 31 layers with 50 scintillator bars each, interspersed with 1.75 mm thick lead sheets. The Ds-Ecal module is similar to the Barrel ECal module, with 34 layers of scintillator interspersed with 1.75 mm thick lead sheets. The P0D-ECal modules have only six scintillator layers each, which alternate with five 4 mm thick lead sheets, as the P0D is designed for initial π^0 detection and the ECal serves to provide additional energy information.

The Time Projection Chambers

The Time Projection Chambers (TPCs) provide several important functions for the ND280 tracker, and are an integral part of the near detector analysis. They provide 3-D tracking for charged particles, as well as particle identification, which is important for identifying neutrino interactions originating from the neighboring detectors with more target mass. Additionally, the magnetic field the near detectors sit in allows the TPCs to make measurements of particle momentum and charge, as well as aiding particle identification. This is a key part of the ND280 analysis and allows ND280 to differentiate between neutrino and antineutrino events. There are three TPCs, all of the same design. The TPCs are placed around the FGDs, so that TPC 1

sits upstream of FGD 1, TPC 2 between FGD 1 and FGD 2 and TPC 3 downstream of FGD 2.

Each TPC consists of an inner chamber filled with an argon-based drift gas and an outer chamber filled with CO_2 for insulation[52]. The inner and outer walls of the inner box are composite panels with copper clad skins. The panels have a 11.5 mm pitch copper strip pattern, giving a uniform electric drift field in the active volume of the TPC in conjunction with a central cathode panel in the middle of the inner box[52], as shown in Figure 2.7, which is a simplified diagram of the TPC structure. When a charged particle passes through a TPC, it produces ionization electrons in the gas, which drift in the electric field towards the readout planes at the ends of the detector away from the central cathode. The readout planes are composed of 12 micromegas modules, which sample and multiply the electrons [52].

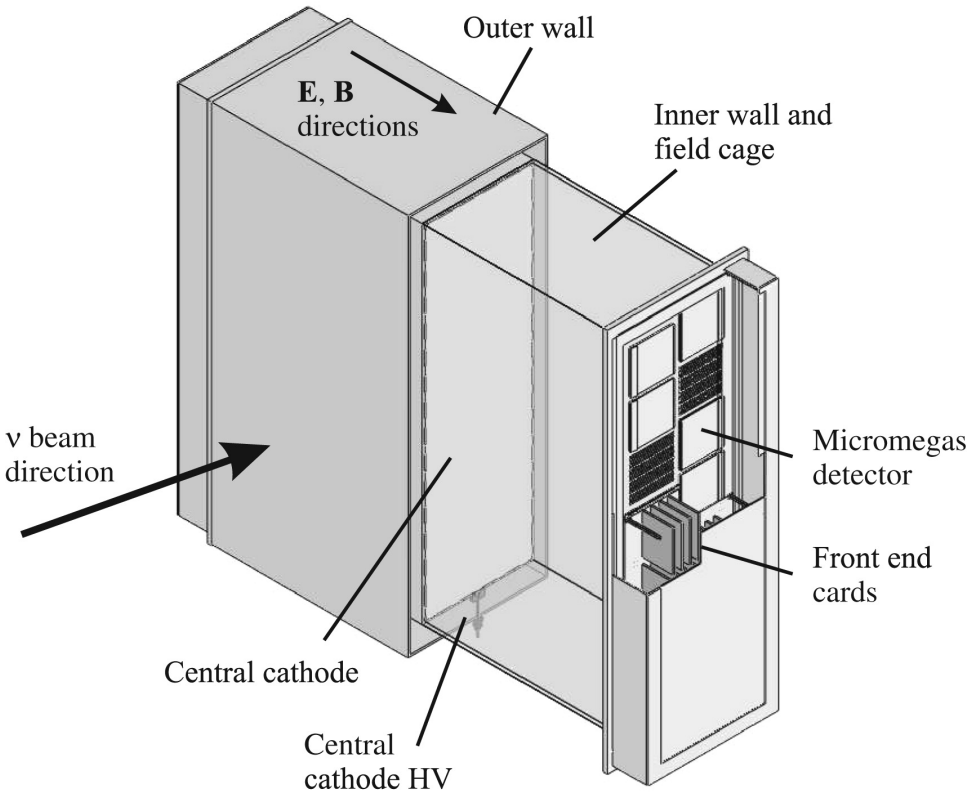

Figure 2.7: Simplified diagram of an individual TPC. Figure taken from [45] with permission.

The Fine Grained Detectors

The Fine Grained Detectors (FGDs) are two scintillator based detectors that serve as the main neutrino target for ND280 and provide vertexing and tracking for events. There are two FGDs: FGD 1, which functions as the carbon-only target volume, and FGD 2, which provides both carbon and oxygen targets. The FGDs are described in more detail in the following section.

2.5 The Fine-Grained Detectors

2.5.1 Overview

The T2K tracker, which consists of the three TPCs and two FGDs, is designed to measure the charged current neutrino interactions, particularly the CCQE interaction process as it is the most common interaction at the T2K beam energies. As described in Section 1.4.2, the energy from these interactions can be reconstructed from the outgoing lepton momentum and angle alone, making it convenient for determining the neutrino energy spectrum. While the TPCs provide momentum measurements, charge identification and particle identification, they are insufficiently dense to function as a neutrino target. Instead, the FGDs provide the main target materials for ND280.

As the main target volume for ND280, the FGDs are designed to fulfill several analysis requirements. To be useful in measuring neutrino interactions, the FGDs must be able to detect all charged particles at the neutrino interaction vertex, and also be thin enough that the charged leptons can travel to the adjacent TPCs for particle identification and momentum measurements. The FGDs are also designed to be able to perform basic particle identification using the dE/dx of particles contained in the FGD volume. Additionally, as the ND280 target volume, the FGDs must be able to provide measurements of neutrino interaction on water, the same target material as at SK.

The basic functional unit of the FGDs is the scintillator module, referred to as an XY module, made up of two layers of 192 scintillator bars each. These layers are perpendicular

to the beam, with one layer horizontal and the other vertical, giving each module the total dimensions of 186.4 cm $\times$ 186.4 cm $\times$ 2.02 cm. The scintillator bars have a square 9.6 mm cross section, as shown in Figure 2.8. Each bar has a reflective TiO_2 coating on the outside, and a wavelength shifting (WLS) fiber through the center of the bar. To improve light collection, one end of the fiber is mirrored and the other mechanically coupled to a photosensor. The scintillator itself is made out of polystyrene and provides the carbon-based target material for the FGDs [53]. There are 15 scintillator modules in FGD 1 and 7 in FGD 2.

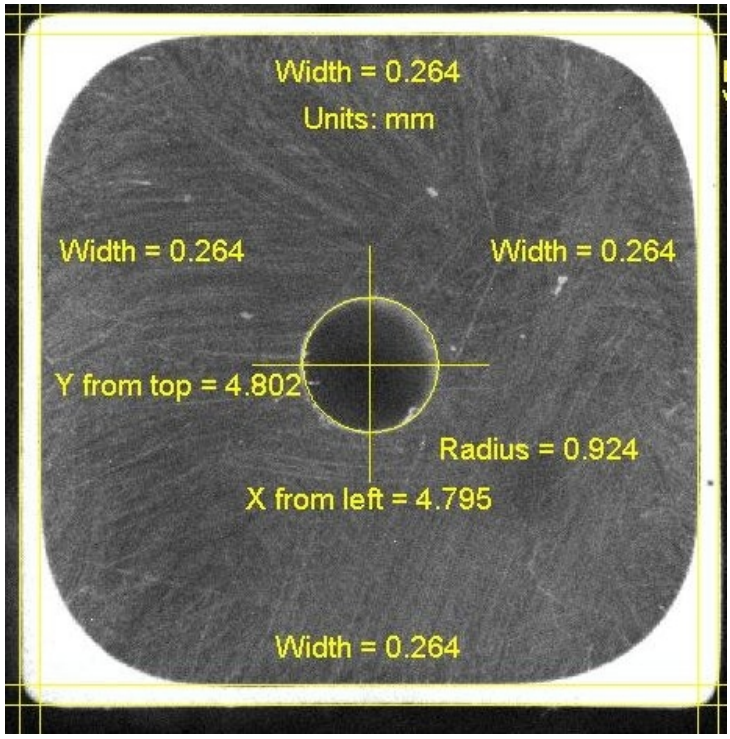

Figure 2.8: Cross-section of a scintillator bar used in the FGDs. Figure taken from [53] with permission.

Unlike FGD 1, which is only composed of scintillator modules, FGD 2 must include a water target mass and therefore includes separate water modules. There are six water modules in FGD 2, alternated with the scintillator modules so that FGD 2 starts and ends with an scintillator module. This is because while the scintillator modules function as both active detector material and a carbon target simultaneously, the water modules are uninstrumented. This also means that FGD 2 has less active material, which has an impact on track reconstruction in FGD 2. The

water modules are each 25.4 mm thick and 1809 mm wide and are build from rigid, hollow polycarbonate panels with an internal structure to maintain panel shape when filled with water. The internal structure of a water panel is shown in Figure 2.9. In addition, the oxygen content of the polycarbonate used allows each panel's elemental composition to match the composition of a water and scintillator mixture. The polycarbonate composition is $C_{16}H_{14}O_3$, which is effectively $C_{16}H_8$ plus water. To match the C:H ratio of this remainder to that of polystyrene in the scintillator, two 0.8 mm thick sheets of polypropylene, CH_2 are attached to the front and back surfaces of each water panel. The end result is that the water module composition is equivalent to 490 mg/cm^2 of scintillator[1] and 2297.2 mg/cm^2 of water, enabling subtraction analysis for measurements on water[53].

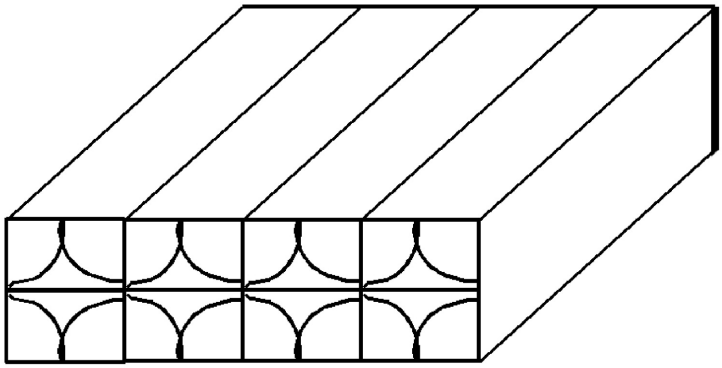

Figure 2.9: Diagram of structure of FGD water module. Not to scale. Figure taken from [53] with permission.

FGD 2 has an additional water system to maintain the pressure in the water modules as well as monitor the flow rates for potential leaks. This system maintains an operating pressure of 300 mbarA. This is below atmospheric pressure in order to prevent water emission in the case of leaks; instead, air will enter the system in the case of a leak, which does not have as much impact on effective operation of the FGDs. The water level in the modules is monitored through the upwards flow rates into the modules, as there was insufficient space for sensors in the panels themselves. The water levels are maintained by a closed loop with a pump that returns water to an overhead reservoir. Each panel has its own independent flow loop that draws on the same

[1] Valid assuming a negligible amount of Ti, as the water modules do not contain any.

reservoir, so that each panel can be drained or filled separately from each other, such as in the case of a major leak. The water used in the panels contains a small amount of antimicrobial and anticorrosive agents in order to prevent biological growth in the water system. This composes 0.25% by volume of the water and has little impact on the target composition.

The scintillator modules for FGD 1 and the water panels and scintillator modules for FGD 2 hang in a light-tight box that provides the structural framework for the FGD. Each box is 2300 mm $\times$ 2300 mm $\times$ 365 mm, and also contains the photosensors attached to the scintillator bars. The electronic readout cards are outside this volume, and are attached to the photosensor busboards through twenty-four backplanes mounted on the four sides of the dark box. These backplanes then attach to the minicrates that house the FGD readout electronics.

2.5.2 Electronics

The electronics in the FGDs are designed to take a snapshot of the detector activity, include before and after a beam spill. Each beam spill is composed of 6 - 8 bunches, with 580 ns separation between them and 3 s between beam spills. As the FGD also needs to be able to look for delayed activity related to pion decays, the FGD electronics must be active between bunches and for several μs after a spill. To achieve this, the FGD electronics trigger on beam spills and record for a total of around 10 μs. For the vertex reconstruction, there must also be a timing resolution of $<$ 3 ns for each hit.

In order to detect optical signals from charged particles, the FGDs use Multi-Photon Pixel Counters (MPPCs) as the readout. These photosensors are able to count photons at the level of a few photoelectrons, and are small enough to be used as readout for the scintillator bars. Additionally, MPPCs are not affected by strong magnetic fields like the field at ND280, while PMTs like those used at SK have reduced sensitivity in magnetic fields. Because of this, MPPCs are used both for the two FGDs and for the other scintillator detectors in ND280.

The MPPCs are pixelated avalanche photodiodes (APD) with an outer dimension of 5 mm $\times$ 6 mm and active area of 1.3 mm $\times$ 1.3 mm, and are attached to the WLS fibers in the scin-

tillator bars with a custom coupler in order to minimize light loss. Each MPPC has 667 APD pixels, which each operate independently with an applied voltage slightly above the breakdown voltage so that the output charge of the pixel is independent of the number of produced photo-electrons in the pixel itself. Because of this, the number of incident photons from a WLS fiber will be roughly proportional to the number of observed discharged pixels, so long as there are many fewer incident photons than pixels in the MPPC, allowing it to be an effective photon counter. To read out and digitize the data, the MPPCs are attached to busboards which aggregate the signals from the MPPCs in order to pass the data to the readout electronics that sit outside of the dark box. Each busboard is connected to 16 MPPCs, and also provides temperature and humidity sensors to monitor the dark box. The busboards are then connected by ribbon cables to the electronics backplanes which provide the interface between the inside and outside of the dark box. There are fifteen busboards connected per backplane in FGD 1, and seven per backplane in FGD 2 due to lower numbers of MPPCs [53].

The FGD readout electronics are situated outside the dark box, and connect to the MPPCs and busboards via the electronics backplane. The electronics are placed in minicrates and contain the frontend boards (FEBs), the light pulser boards (LPBs) and the crate master boards (CMB). There are four FEBs in each FGD 1 minicrate, and two for FGD 2. Each minicrate also contains one CMB, with an Field-Programmable Gate Array (FPGA) to control the readout procedure, and LPB for calibration. The LPB controls LEDs mounted on the busboards, which are used for testing WLS fiber integrity and calibrating the MPPC gains.

The FEBs take the MPPC signals from the busboards and digitize them, as well as providing the MPPCs with power. Each FEB contains two AFTER ASICs[54], with 32 MPPCs read out per ASIC. The AFTER ASIC provides a preamplifier and shaper to amplify the electrical pulses from the MPPCs and extend the pulse lengths, and can record both low-gain and high-gain signals. The ASIC also provides a switched capacitor array (SCA) which can store analog samples of the shaped MPPC pulses. The SCA has a sampling frequency of 50 MHz, with a total readout time of 10.1 μs. Using the ASICs allows for a lower sampling frequency versus

directly digitizing the MPPC signals. Once an event is triggered, the contents of the SCA are then digitized by a 12-bit flash ADC, which runs at 20 MHz[53], and transferred from the FEB to the CMB.

The CMBs handles the trigger signal processing, the LPB triggering and setting the configuration of the ASICs on top of controlling the data acquisition for the FGDs. This is done using an FPGA, which controls the record and readout phases of the attached ASICs in the minicrate. The digitized data from the SCAs is stored on the CMB in a pair of SRAMs. The readout process takes around 2 ms, which does not make a significant contribution to the total FGD readout time[53]. The data on the CMBs is then transmitted through an optical link to the Data Concentrator Cards (DCCs) outside the minicrates, which provide the interface between the FGD electronics and the rest of the ND280 control systems.

2.5.3 Operation

The triggering for ND280 is controlled by the master clock module, so called because it provides the global clock signal for the ND280 detectors. The primary trigger type is the beam spill trigger, which does not depend on activity at ND280 and is produced outside the ND280 system. This provides the trigger for the ND280 beam data, which is used for the near detector analysis. Other types of trigger are Trip-T cosmic trigger and the FGD cosmic trigger. The Trip-T cosmic trigger comes from coincidence in the ECal, P0D and SMRD, which are all run by the Trip-T readout electronics. The FGDs and TPCs do not use the Trip-T system. As the rate of cosmics triggered by the Trip-T detectors is low, the FGD also provides a trigger for cosmic events.

The FGD uses FGD 1 – FGD 2 coincidence to trigger on cosmic rays, which can be used for various measurements, calibration studies and systematic studies. To do this, the FGD electronics look for coincident activity in both FGD 1 and FGD 2. For the trigger, the MPPCs in each minicrate are grouped in sets of 8 and the signals from these 8 MPPCs are summed. These analog sum groups (ASUM) are considered to have fired when the signal sum exceeds a

set threshold, which is tuned for each individual group of MPPCs. If two or more of the ASUM groups in a minicrate fire, the minicrate is also considered to have fired. To have coincidence between FGD 1 and FGD 2, the trigger looks for two crates firing in FGD 1 coincident with two crates firing in FGD 2. This ensures that these cosmic events have energy deposits in FGD 1 and FGD 2, as well as at least one TPC track.

2.5.4 Calibration

There are two main tasks for the FGD calibration: calibration of measured charge and calibration of measured time. The charge calibration converts the raw pulse height (PH) measured of the digitized waveform from an MPPC to a normalized value that represents the energy deposited in the scintillator bar. The timing calibrations provide corrections to resolve differences between timing on different FEBs and the CMB timings, as well as account for the travel time of light in the WLS fibers. This gives the FGD a timing resolution of < 3 ns between hits in a single FGD, and a resolution on the timing between hits in FGD 1 and FGD 2, discussed in later chapters.

There are many steps in the charge calibration chain, several of which are temperature-dependent effects. Calibration starts with high- and low-gain channel response calibration, to find the MPPC response independent of which channel was used. The high-gain and low-gain channel responses have a linear relationship, measured for each MPPC using cosmic rays triggered in the FGDs. These pulse height values are then normalized using the average pulse height from a single pixel firing. This is measured using the pulse height distribution of the MPPC dark noise, which is where a pixel spontaneously fires due to electrons thermally generated in the pixel. This effect depends on the temperature, which can vary by up to $\pm 2^{\circ}$C. This temperature variation also affects the breakdown voltage of the MPPCs. An additional temperature-dependent calibration effect is the average numbers of pixels firing for a given number of photons incident on an MPPC. This depends on photodetection efficiency, cross talk and after-pulsing probabilities, all of which have some temperature dependence. This ef-

fect was studied at TRIUMF using an electron beam[53]. The MPPC response is also corrected for the effects of MPPC pixel saturation, where the measured pulse heights eventually saturate at increasing light levels due to multiple photons incident on individual pixels.

Other charge calibration corrections come from the scintillator bars, rather than the MPPCs. As there can be minor variations in things such as the MPPC to fiber coupling, the exact position of the WLS fiber in the scintillator bar, and minor variations in the scintillator material, the calibration uses an additional correction constant specific to each bar which modifies the efficiency of energy deposition to photons incident on the MPPC. Additionally, as there is some light loss along the fiber, measured by cosmic ray studies, there is a correction to account for the position of the particle track relative to the MPPC, as there can be up to a 25% loss at the far end. All these calibration steps yield a number proportional to the number of photons produced in the scintillator, which is then corrected using Birks' formula[53] with an additional efficiency normalization to yield the deposited energy, which is stored as a hit for that channel and can be used in the ND280 reconstruction.

2.6 Limitations of the T2K Analysis

Part of the T2K oscillation analysis, as detailed in the following chapter, uses selected events in ND280 to improve the overall uncertainty on the results. However, so far the near detector component of the oscillation analyses has only used neutrino interactions occurring in FGD 1, which only provides a carbon target. As the difference in target material between ND280 and SK limits how well ND280 can be used to understand the neutrino cross-section on water at SK, this puts a limit on how much the ND280 contribution can reduce the uncertainties at SK. While FGD 2 was designed specifically to provide an oxygen-based target to avoid this issue, neutrino interactions in FGD 2 have not been used before for a few reasons.

As described in the previous section, the water modules in FGD 2 are not active, and are designed to be used as part of a subtraction analysis to isolate information about the water cross-section in conjunction with FGD 1 rather than using FGD 2 on its own. This allows the

carbon target in FGD 1 to be used to improve the measurements on water in FGD 2. However, this introduces the issue of possible detector systematic correlations between the two detectors, as only using FGD 2 would not give a better reduction in uncertainty. Not only would detector systematics need to be remeasured for a second detector but there would need to be some studies and understanding of how each systematic source correlates. Additionally, the selection, described in Chapter 4, was initially only designed and tested for FGD 1; as the amount of active material differs between the two FGDs, the selection could potentially need changes to account for reconstruction differences. For these reasons, the initial near detector selections and analysis only used events occuring in FGD 1. The intent of this thesis is to extend the previous T2K analyses to include FGD 2 along with FGD 1, in order to directly determine interaction rates on water.

Chapter 3

Oscillation Analysis at T2K and the ND280 Fit

3.1 The T2K Oscillation Analysis Structure

3.1.1 General Overview

The primary goal of the T2K experiment is to measure neutrino oscillations at the far detector. As oscillation parameters are not directly measurable, T2K instead fits the neutrino oscillation parameters using the number and energy spectrum of observed events at the far detector. The T2K oscillation fit is a maximum likelihood fit on the data measured at the Super-Kamiokande detector, which compares the predicted event distribution to the observed event distribution at SK. Predicting the event rate requires three main components: a calculation of the flux, a parameterization of the cross-section, and a model of the detector efficiencies. The fit itself fits both the oscillation parameters and these other parameters, which have prior constraints and can be regarded as nuisance parameters in the result. Selected ν_μ and ν_e event rates are used to fit the oscillation parameters while marginalizing over the various nuisance parameters. These are the parameters that describe the flux from the neutrino beam at SK, the various cross section parameters that govern neutrino interactions with oxygen nuclei and the detector systematics

from SK itself and are used to tune the initial predictions at SK. The detector systematics can be characterized using SK information alone, while constructing prior constraints for flux and cross section parameters is more complicated. The initial set of inputs come from experiments and information external to the near and far T2K detectors. The nuisance parameters in our oscillation fit are the neutrino interaction cross section parameters and the parameters governing the beam flux at Super-Kamiokande (SK) from J-PARC and the prior mean values and uncertainties are calculated from external experiments such as NA-61[55] and MINERνA[56].

3.1.2 Motivation

The primary source of uncertainty on the predicted number and energy distribution of events at SK comes from the flux and cross-section, which are some of the nuisance parameters in the SK oscillation fits. Without using the data at the near detector, reducing uncertainty on the flux and cross-section parameters relies on using external inputs such as measurements of hadron production and neutrino interaction cross-section measurements. Additionally, this means that there is no correlation between the flux and cross-section inputs, as the priors are constructed completely independently. Adding in data from the near detector allows for the simultaneous constraint of the T2K beam flux and the cross section. This allows a global likelihood for the oscillation parameters to be constructed using the external data (for constraining nuisance parameters), the ND280 data, and the SK data. This depends on the nuisance parameters from the flux and cross-section models, as well as detector systematics at the near and far detectors. As maximizing this global likelihood is computationally impractical, sequential likelihood maximization is used instead. This allows each set of data to be handled as separate likelihoods, greatly decreasing the complexity of each individual fit.

The sequential likelihood maximization has essentially three separate steps, one each for the external, ND280 and SK data:

1. The external data is analyzed to produce the prior constraints on the various parameters. For the detector parameters, this is in the form of various studies on the systematic

uncertainties, described for ND280 in Chapter 5.

2. The ND280-specific likelihood is fit using the near detector data, which can be maximized separately from the oscillation fit at SK and is described in more detail this section. This uses the prior constraints found in the previous step as the prior constraint terms. The fit output is the fitted flux and cross section parameters, along with their covariance, to be used as a prior at SK.

3. The fitted values from the ND280 fit are then used as part of the constraint term for the oscillation likelihood which uses the SK data.

The uncertainty on the predicted number of events at SK is shown in Table 3.1 and Table 3.2 for the previous FGD-1 only analyses[57]. The uncertainty improvement to the flux and ND280-constrained cross-section parameters for the $\bar{\nu}_\mu$ event rate is due to significant improvements in the flux model and prediction – where the $\bar{\nu}_\mu$ prediction had a 9.2% uncertainty from the flux and ND280-constrainable cross-sections pre-ND280 fit, the ν_μ prediction has an uncertainty of 21.8% from the same source. However, both the ν_μ and $\bar{\nu}_\mu$ predictions show significant improvement to the overall uncertainty once the ND280 constraint is included. This prediction comes from the improved constraints provided by the near detector fit, as the ND280 fit constrains the convolution of the flux and cross-section as a function of energy and this constraint can be carried over to SK due to similar energy spectra[1].

However, even with the ND280 constraint to the flux and some cross-section parameters, there remains a large contribution that cannot be reduced with the near detector. This gives an uncertainty of 5.0% for the ν_μ prediction and an uncertainty of 10% for the $\bar{\nu}_\mu$ prediction, larger than the contribution from the ND280 constrained parameters. This is due to the effect of oxygen-only cross section uncertainties, which could not be constrained with the previous near detector fits due to differences in target material. For these parameters, relatively large uncertainties based on theoretical predictions and external experimental measurements are used

[1]Even for the $\bar{\nu}_\mu$ prediction, where the flux uncertainty is significantly reduced prior to the ND280 fit, the additional constraint provided by the near detector fit gives an significant improvement on the prediction.

	no ND280 Constraint	With ND280 Constraint
ND280-Constrained Parameters	21.8%	2.7%
ND280-Unconstrained Parameters	5.0%	
SK FSI + SI	3.0%	
SK Systematics	4.0%	
Total	23.5%	7.7%

Table 3.1: Fractional error on the prediction for the number of ν_μ events at SK, with and without the ND280 constraint from the previous neutrino mode analysis in 2014. Uncertainties shown are calculated from the RMS of the event rates when 10000 parameter variations are thrown[58]. ND280-unconstrained parameters are the 2p-2h, p_F, E_B, CC coherent, Isospin=$\frac{1}{2}$ Background and ν_e/ν_μ cross-section parameters. ND280-constrained parameters are the flux parameters and all other cross-section parameters.

	no ND280 Constraint	With ND280 Constraint
ND280-Constrained Parameters	9.2%	3.4%
ND280-Unconstrained Parameters	10.0%	
SK FSI + SI	2.1%	
SK Systematics	3.8%	
Total	14.4%	11.6%

Table 3.2: Fractional error on the prediction for number of $\bar{\nu}_\mu$ events at SK, with and without the ND280 constraint from the previous antineutrino mode analysis in 2015. Uncertainties shown are calculated from the RMS of the event rates when 10000 parameter variations are thrown [59]. ND280-unconstrained parameters are the 2p-2h, p_F, E_B, CC coherent, Isospin=$\frac{1}{2}$ Background and ν_e/ν_μ cross-section parameters. ND280-constrained parameters are the flux parameters and all other cross-section parameters.

instead to set the uncertainty and prior values. The major change for the analysis presented here is the ability to fit the oxygen-only cross-section parameters by way of samples that include oxygen as a target material in order to reduce that uncertainty.

3.1.3 Oscillation Fit At Super-Kamiokande

There are two main oscillation analysis methods in use at SK: a hybrid frequentist-Bayesian method to deal with nuisance parameters, and MaCh3, which is a fully Bayesian analysis and uses Markov chain Monte Carlo[60]. MaCh3 fits the near and far detector data simultaneously and will not be discussed here, as it does not use the sequential ND280 fit – SK fit method that

is the main focus of this thesis. This Markov chain fit was developed later than the original near-to-far extrapolation method discussed here and must use the hybrid method for validation due to computational reasons. While this method fits a global likelihood rather than sequential likelihoods, this does not have a significant impact on the fit results. Additionally, the FGD 2 selections described in this thesis have been incorporated in to the MaCh3 fit as well.

The SK fits use the 1-ring e-like sample for the ν_e appearance fits and the 1-ring μ-like sample for ν_μ disappearance fits. As the SK selection does not distinguish between neutrino and antineutrino events, the samples are also split into FHC and RHC subsamples. The SK data itself can be binned in two ways: in E_{reco}, the reconstructed neutrino energy, and θ_l, the reconstructed lepton angle, or p, the lepton momentum, and θ, the scattering angle with respect to the beam direction.

The oscillation fit maximizes a binned likelihood:

$$L(N_e^{obs}, N_\mu^{obs}, \vec{o}, \vec{f}) = L_{main}(N_e^{obs}, N_\mu^{obs}, \vec{o}, \vec{f}) \times L_{sys}(\vec{f}) \tag{3.1}$$

where $\vec{o}$ are the oscillation parameters ($\sin^2(\theta_{23})$, $|\Delta m^2_{32}|$, $\sin^2(2\theta_{13})$ and δ_{CP}) and $\vec{f}$ are the nuisance parameters – this encompasses the various cross-section model parameters, the flux parameters, the SK detector systematics, and final state interaction and secondary interaction model uncertainties. The likelihood is separated into two parts, where L_{main} is the term comparing the data with the event rates predicted with the oscillation and nuisance parameters and L_{sys} is a Gaussian penalty term that only depends on the nuisance parameters. The actual minimized quantity in the fit is $-2\ln L$, separating the two likelihood contributions.

In the hybrid fit approach, the nuisance parameters are marginalized by integrating the likelihood over the nuisance parameter values. In practice, this means creating 10000 throws of the nuisance parameters according to their priors and fitting these to produce a grid of likelihoods for the various parameter sets. The fit is then marginalized by picking the set of parameters with the lowest χ^2. In addition to this, the oscillation parameters can be marginalized over,

Parameter	Prior Type	Bounds
$\sin^2\theta_{23}$	Uniform	$[0.3;0.7]$
$\sin^2 2\theta_{13}$ reactor	Gaussian	0.085 ± 0.005
$\sin^2 2\theta_{13}$ T2K	Uniform	$[0;0.4]$
$\sin^2 2\theta_{12}$	Gaussian	0.846 ± 0.021
$\lvert\Delta m^2_{32}\rvert$ (NH) or $\lvert\Delta m^2_{13}\rvert$ (IH)	Uniform	$[2;3] \times 10^{-3}$ eV^2/c^4
Δm^2_{21}	Gaussian	$(7.53 \pm 0.18) \times 10^{-5}$ eV^2/c^4
δ_{CP}	Uniform	$[-\pi;+\pi]$
Mass Hierarchy	Fixed	NH or IH

Table 3.3: Priors used for oscillation parameters when marginalizing. From [61].

in order to produce 2D intervals. In that case, the oscillation parameters being marginalized are thrown according to the parameter type and range given in Table 3.3 with the exception of mass hierarchy, which is instead fixed to either normal or inverted hierarchy. Once the nuisance parameters have been marginalized over, the $\Delta\chi^2$ for the marginalized likelihood is minimized to fit the best fit oscillation parameters.

As the nuisance parameters are marginalized, there is no exact set of best fit parameters that correspond to the best fit spectra. Instead, the best fit spectra is produced using the thrown nuisance parameters:

$$N^j_{marg} = \frac{\sum_{i=1}^{n} L(N^{obs}_i, \vec{o}, \vec{f}_i) \cdot N^j_{pred}(\vec{\theta}_{bf}, \vec{f}_i)}{\sum_{i=1}^{n} L(N^{obs}_i, \vec{o}_{bf}, \vec{f}_i)} \tag{3.2}$$

where n is the number of nuisance parameter throws, $\vec{o}_{bf}$ is the best fit oscillation parameters, and $\vec{f}_i$ is the ith set of thrown nuisance parameters..

3.2 The ND280 Fit

3.2.1 The Maximum Likelihood Fit Method

The near detector fit maximizes the likelihood for the flux, cross-section and detector parameters given the ND280 data. All parameters are fit simultaneously, which allows there to be correlations between the fitted flux and cross-section parameters. This uses a binned likelihood, where the ND280 data is separated into bins which depend on topological sample and the re-

constructed kinematics of an event. The samples used are described in detail in Chapter 4; there are three samples for neutrino mode data and four for antineutrino mode data. Within each sample, the data is binned by the reconstructed momentum, p, and the reconstructed angle, $\cos\theta$.

The ND280 data is binned by sample type, described in Chapter 4, and reconstructed kinematic variables p and $\cos\theta$, allowing the fit to constrain both the overall event rate at SK and the neutrino energy distribution. The p – $\cos\theta$ bins were chosen in order to ensure that each bin had sufficient statistics for a χ^2 fit and have finer binning in regions with a high event rate in order to obtain more shape information. For the individual p – $\cos\theta$ bins in the fit, the observed event rate for both data and MC is expected to follow a Poisson distribution. Therefore, the probability of observing N_i^{obs} events in a bin i, given a predicted event rate N_i^{pred} which depends on the flux, cross-section and observable normalization parameters is

$$P(N_i^{data}|N_i^{pred}) = \frac{(N_i^{pred})^{N_i^{data}} e^{-N_i^{pred}}}{N_i^{data}!} \tag{3.3}$$

The Poisson likelihood term is a product of this probability over all bins.

The flux, cross-section and detector normalization parameters are all modeled as multivariate Gaussian distributions, with the probability shown in Eq. 3.4, where $\vec{y}$ is the vector of parameter values, n is the number of parameters, V_y is the associated covariance matrix and $\Delta\vec{y}$ is the difference between current parameter value and nominal parameter values.

$$\pi(\vec{y}) = (2\pi)^{\frac{n}{2}} |V_y|^{\frac{1}{2}} e^{-\frac{1}{2}\Delta\vec{y}(V_y^{-1})\Delta\vec{y}} \tag{3.4}$$

As the flux, cross-section and detector parameters are all independent from each other, each type of parameter contributes a separate term to the likelihood.

The maximized quantity is the likelihood ratio, where the denominator is evaluated at

$N_i^{pred} = N_i^{data}$, as this corresponds to the maximum value for the numerator:

$$L^r_{ND280} = \frac{\pi(\vec{b})\pi(\vec{x})\pi(\vec{d})\prod_i [N_i^p(\vec{b},\vec{x},\vec{d})]^{N_i^d} e^{-N_i^p(\vec{b},\vec{x},\vec{d})}/N_i^d!}{\pi(\vec{b}_{nom})\pi(\vec{x}_{nom})\pi(\vec{d}_{nom})\prod_i [N_i^d]^{N_i^d} e^{-N_i^d}/N_i^d!} \tag{3.5}$$

where $\vec{b}$ is the flux parameters, $\vec{x}$ is the cross-section parameters, and $\vec{d}$ is the detector observable normalization parameters at ND280. This allows for comparison between the likelihood of the predicted values and the maximum possible value. Several of the terms in this ratio cancel out, such as the determinants of the covariance matrices in Eq. 3.4. The actual minimized quantity is $-2\ln(L^r_{ND280})$, which has an approximately χ^2 distribution and is referred to as $\Delta\chi^2_{ND280}$ in the near detector fit.

For ND280, this log likelihood is composed of two separate independent parts: a Poisson contribution from the fitted observables and a Gaussian contribution from the fitted parameters and their covariance. The full $\Delta\chi^2_{ND280}$ for the near detector, defined as 2 times the log likelihood with constant terms dropped is defined as:

$$\begin{aligned}\Delta\chi^2_{ND280} = 2\sum_i^{Nbins} N_i^{pred}(\vec{b},\vec{x},\vec{d}) - N_i^{data}\ln(N_i^{data}/N_i^{pred}(\vec{b},\vec{x},\vec{d}))+ \\ \sum_i^{E_\nu bins}\sum_j^{E_\nu bins}\Delta b_i (V_b^{-1})_{i,j}\Delta b_j + \sum_i^{xsec}\sum_j^{xsec}\Delta x_i (V_x^{-1})_{i,j}\Delta x_j + \\ \sum_i^{obsbins}\sum_j^{obsbins}\Delta d_i (V_d^{-1})_{i,j}\Delta d_j\end{aligned} \tag{3.6}$$

Here N_i^{obs} is the number of observed events in the ith $p-\theta$ sample bin, N_i^{pred} the predicted number of events in the ith $p-\theta$ bin, b_i the flux parameters, x_i the cross section parameters, and d_i the detector observable normalization parameters. Each parameter set has its own covariance matrix V from the prior inputs. N_i^{pred} is calculated from the nominal prediction for bin i using the detector observable normalization weights, the cross section response functions and the flux weights, which depend on the sample $p-\cos\theta$ bin, the neutrino interaction mode and the true neutrino energy.

The basic fitting routine uses the Minuit algorithm package[62] as part of the ROOT[63] framework. The near detector analysis uses the MIGRAD algorithm for minimizing the $\Delta\chi^2$ described in Eq. 3.6. The postfit uncertainties are estimated using the HESSE algorithm from Minuit, which computes the second derivatives of the parameters around the minimized values to construct the Hessian matrix. The inverse of this gives the covariance matrix for the fitted parameters.

3.2.2 Changes from Previous Fit

This fit has several differences relative to the old ND280 fit: most significant is the addition of the FGD 2 target samples for both neutrino and antineutrino mode selections. As described in Sec. 2.5, FGD 1 is comprised of only scintillator target, while FGD 2 is alternating scintillator and water modules, thus providing a target more similar to that at SK. The samples added for FGD 2 do not separate between the carbon and oxygen target interactions, as the water volumes are uninstrumented and non-statistical differentiation is difficult. Instead, the fit uses the carbon and carbon + oxygen target samples to effectively do a subtraction analysis to fit the oxygen cross section parameters. The purpose of this is to reduce the remaining cross section uncertainties in the previous analysis, as this is the largest source of uncertainty in the oscillation analysis as shown in Tables 3.1 and 3.2.

In addition to the new samples, the detector observable normalization parameters have had several changes, including updated detector systematic studies for FGD 2. Because the fit now includes two separate targets with potential systematic correlations, the detector parameters must include FGD 1 to FGD 2 correlation considerations. For the FGD 1 systematics, there have also been intra-systematic correlations added. While the previous analysis assumed that there were no correlations between $p - \theta$ or other binning choices within a given detector systematic, these have now been estimated and incorporated in the covariance matrix. These systematics and correlations will be described in more detail in Chapter 5.

The new oxygen target sample additions allow for some changes to the cross section inputs

as well. In the previous analysis, the fit results for any of the oxygen cross section parameters were not passed to the oscillation fits as SK, and also the 2p-2h parameter was not separated into different versions for oxygen and carbon targets. Because the fit is to effective cross section parameters, there could potentially be a difference in response between different target materials so for this analysis the 2p-2h parameter has been fit as two separate parameters depending on target. The model now also includes a 2p-2h $\bar{\nu}$ normalization parameter, motivated by several neutrino cross section models having different scaling for neutrino and antineutrino events.

3.3 Fit Parameters and Prior Constraints

The near detector fit parameters come from three sources: the T2K beam flux, the neutrino interaction cross-section model and the detector systematic parameters. Of these, the neutrino and antineutrino flux, as well as relevant cross-section parameters at SK, are passed on to the oscillation fits. This section describes the various inputs that are used in the analysis.

3.3.1 Flux Parameters

A key part of the near detector fit is its ability to constrain and measure the flux to improve the event rate predictions at SK. The flux itself depends on many factors, such as the beam direction and intensity, and proton and secondary particle interactions in the target volume; because of this, the beam flux simulation is complex and involves multiple steps. The beam flux prediction is based on the Monte Carlo simulation of the T2K beam, tuned with external information from the NA61/SHINE experiments. The beam simulation uses FLUKA 2011.2b for the hadronic interactions in the target[64] and JNUBEAM, a GEANT3 simulation of the T2K beam and near detectors[47] developed by T2K, for the rest of the simulation. JNUBEAM handles particle propagation and all interactions outside of the beam target volume, while FLUKA is used because it shows better agreement with NA61 data than the GEANT3 interaction model[64]. Hadronic interactions are then reweighted using thin target data for various pion and kaon

interactions, primarily from the NA61/SHINE experiments at CERN[55][65].

The uncertainties on the flux prediction come from uncertainties on the hadron models as well as uncertainty on the beam direction. For the flux at low energy, the dominant uncertainty comes from uncertainties on the production cross sections, pion production multiplicities and secondary nucleon production, while for high energies, the predominant uncertainties come from kaon production. The uncertainty on the secondary nucleon production is the largest contributor to the flux uncertainty at low energy. As the primary source of wrong-sign neutrinos in the RHC flux comes from interactions outside the target, the uncertainties on the secondary nucleon production are reduced by using the NA61/SHINE 2009 data[64]. The target scaling uses data from the HARP collaboration[66], which helps constrain the uncertainties on pion production for pion rescattering.

The near detector fit uses a flux model that is binned in neutrino energy and into ν_μ, $\bar{\nu}_\mu$, ν_e and $\bar{\nu}_e$ at ND280 and SK. As the beam power and beam conditions have differed over the T2K run time, the flux model predictions are also split by run period. The forward horn current flux and reverse horn current flux have separate flux parameters. In the fit, these are normalization parameters which allow the flux prediction to vary around the nominal value from the simulations and a covariance matrix constructed from the uncertainties and correlations of each flux normalization parameter. The flux model uses separate parameters for the flux at ND280 and the flux at SK to account for differences in the spectra between the near and far detector. ND280 is positioned close enough to the T2K beam source that the neutrino beam does not look like a point source, while SK is far enough away that it is reasonable to model the beam as one. There are correlations between the ND280 flux parameters and the SK flux parameters, allowing measurements of the flux at ND280 to change the flux at SK. The source of these strong correlations is that the uncertainties on the underlying production parameters, such as production cross-sections, affect the flux spectra at near and far detector in similar ways.

The flux parameters are binned in energy, with units of GeV, for each flavor and beam mode as follows[67][57] and truncate at 30 GeV for both ND280 and SK flux parameters. The bin

boundaries for the flux parameters are:

- FHC ν_μ and RHC $\bar{\nu}_\mu$: 0.0, 0.4, 0.5, 0.6, 0.7, 1.0, 1.5, 2.5, 3.5, 5.0, 7.0, 30.0
- FHC $\bar{\nu}_\mu$ and RHC ν_μ : 0.0, 0.7, 1.0, 1.5, 2.5, 30.0
- FHC ν_e and RHC $\bar{\nu}_e$: 0.0, 0.5, 0.7, 0.8, 1.5, 2.5, 4.0, 30.0
- FHC $\bar{\nu}_e$ and RHC ν_e : 0.0, 2.5, 30.0

There are 100 flux normalization parameters in total, with 50 for the flux at ND280 and 50 for the flux at SK. The correlations between flux energy bins is shown in Figure 3.1 – this shows the flux as highly correlated between neutrino and antineutrino as well as between fluxes at ND280 and SK. Predicted flux and fractional uncertainties on the flux at ND280 are shown in Figures 3.2 and 3.3. Predicted flux and fractional uncertainties for SK are shown in Appendix A.

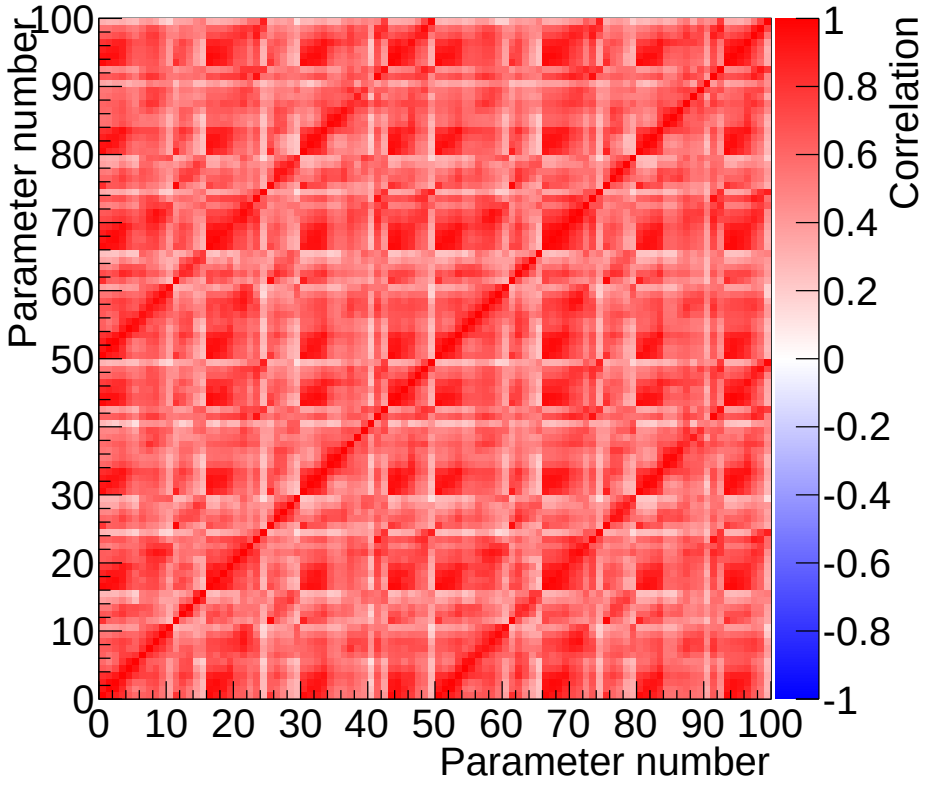

Figure 3.1: Correlations between the flux normalization parameters. The binning is: ND280 FHC ν_μ: 0 -10, ND280 FHC $\bar{\nu}_\mu$: 11 – 15, ND280 FHC ν_e: 16 – 22, ND280 FHC $\bar{\nu}_e$: 23 – 24, ND280 RHC ν_μ: 25 – 29, ND280 RHC $\bar{\nu}_\mu$: 30 – 40, ND280 RHC ν_e: 41 – 42, ND280 RHC $\bar{\nu}_e$: 43 – 49, SK FHC ν_μ: 50 – 60, SK FHC $\bar{\nu}_\mu$: 61 – 65, SK FHC ν_e: 66 – 72, SK FHC $\bar{\nu}_e$: 73 – 74, SK RHC ν_μ: 75 – 79, SK RHC $\bar{\nu}_\mu$: 80 – 90, SK RHC ν_e: 91 – 92, SK RHC $\bar{\nu}_e$: 93 – 99

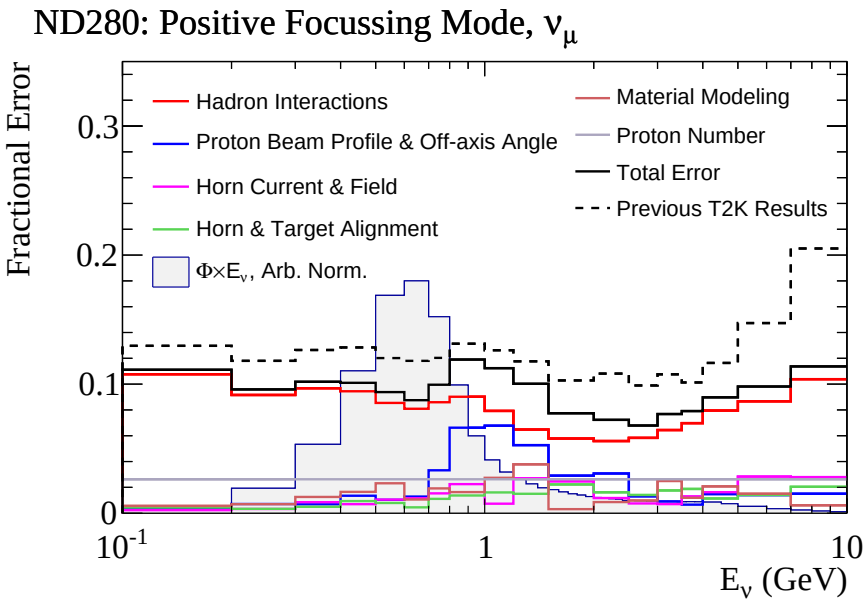

(a) ND280 FHC ν_μ flux uncertainty and prediction.

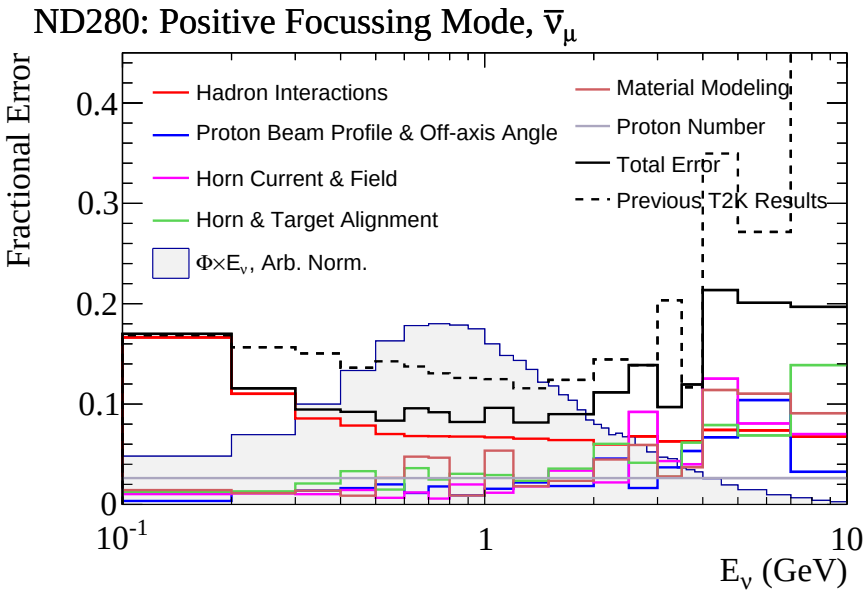

(b) ND280 FHC $\bar{\nu}_\mu$ flux uncertainty and prediction.

Figure 3.2: Predicted fractional uncertainties on the flux priors as a function of neutrino energy.

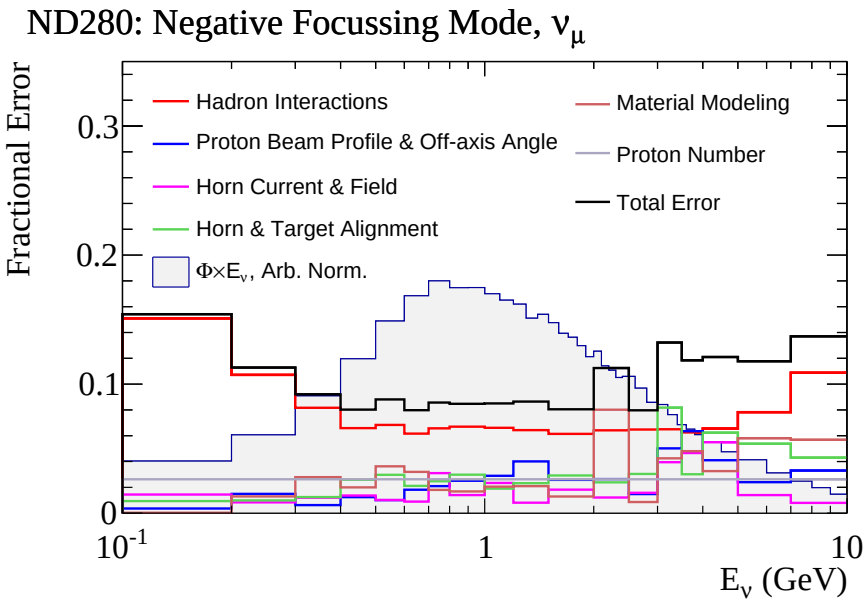

(a) ND280 RHC ν_μ flux uncertainty and prediction.[64]

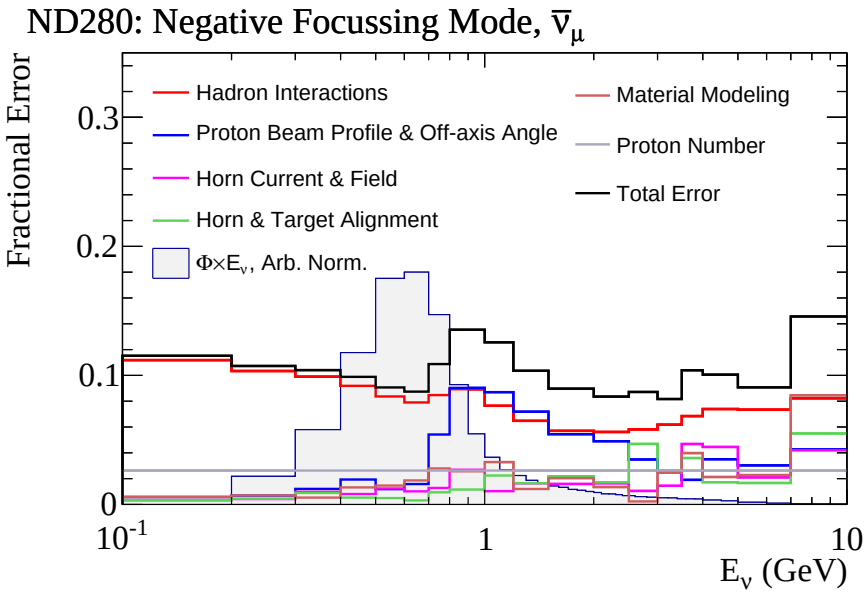

(b) ND280 RHC $\bar{\nu}_\mu$ flux uncertainty and prediction.

Figure 3.3: Predicted fractional uncertainties on the flux priors as a function of neutrino energy.

3.3.2 Cross Section Parameters

The cross section model parameters are implemented in two different ways: normalization parameters which apply a normalization weight to certain events, and response parameters, which can alter the particles produced in an interaction, and the p_μ and $\cos\theta_\mu$ distributions. The normalization parameters work much like the flux parameters – a multiplicative factor is applied to all events in the applicable interaction channel, without any dependence on energy or other observables. The response parameters are more complicated, as these are cross section parameters that are part of the theoretical cross section calculation. The most exact way to incorporate changes to the cross section calculations would be to rerun the entire T2K analysis structure, from generating neutrino interactions in NEUT to reconstruction and selection, for each event on each step of the fit minimization. This is of course not computationally feasible; instead weights for the parameters are calculated individually for each event and saved as cubic splines, with the weight as a function of the parameter value. This allows the computationally intensive part to be run prior to the fit itself and for the appropriate weights to be quickly interpolated from the saved splines during minimization.

The cross section parameters used in the T2K near detector fit are listed in Table 3.4. Parameters are listed along with their range of validity, NEUT nominal values and the prior values as calculated by the Neutrino Interaction Working Group on T2K[68]. The prior constraints and values on the CCQE and CC resonant parameters comes from fits to cross section data from MiniBooNE[69] and MINERνA[70][56], though the CCQE prior constraints are not used in the fit for reasons described below.

The final state interaction parameters control hadron transport within the nucleus after a neutrino interaction, which is simulated as a cascade where the pion is propagated through the nucleus in steps, allowing for multiple interactions before the particle exits the nucleus. These final state interactions (FSI) allow events to migrate between different topologies and for particle kinematics in the event to change. There are six FSI parameters used in the near detector fit for T2K, for pion final state interactions and are split into parameters that apply for high en-

Parameter	Validity Range	Prior Mean	NEUT Nominal	Error	Type
FSI Inel. Low E	all	0.0	0.0	0.41	response
FSI Inel. High E	all	0.0	0.0	0.34	response
FSI Pion Prod.	all	0.0	0.0	0.50	response
FSI Pion Abs.	all	0.0	0.0	0.41	response
FSI Ch. Exch. Low E	all	0.0	0.0	0.57	response
FSI Ch. Exch. High E	all	0.0	0.0	0.28	response
M_A^{QE} (GeV/c^2)	all	1.20	1.20	–	response
p_F ^{12}C (MeV/c)	200 - 275	217	217	–	response
2p-2h ^{12}C	all	100%	100%	–	norm
E_B ^{12}C (MeV)	12 - 42	25	25	9	response
p_F ^{16}O (MeV/c)	200 - 275	225	225	–	response
2p-2h ^{16}O	all	100%	100%	–	norm
E_B ^{16}O (MeV)	12 - 42	27	27	9	response
$C_A^5(0)$	all	1.01	1.01	0.12	response
M_A^{RES} (GeV/c^2)	all	0.95	0.95	0.15	response
Isospin=$\frac{1}{2}$ Background	all	1.30	1.30	0.20	response
CC ν_e/ν_μ	all	1.0	1.0	0.04	norm
CC $\bar{\nu}_e/\bar{\nu}_\mu$	all	1.0	1.0	0.04	norm
CC Other Shape	all	0.0	0.0	0.40	response
CC Coherent	all	1.0	1.0	0.30	norm
NC Coherent	all	1.0	1.0	0.30	norm
NC 1γ	all	1.0	1.0	1.00	norm
NC Other (near)	all	1.0	1.0	0.30	norm
NC Other (far)	all	1.0	1.0	0.30	norm
2p-2h $\bar{\nu}$	> 0	1.0	1.0	0.50	norm

Table 3.4: Cross section parameters used for the near detector fit, showing the valid range of the parameter, prior mean, nominal value in NEUT, and prior error as provided by the Neutrino Interaction Working Group (NIWG).[67] The type of systematic (response or normalization) is also shown. The CC-0π parameters (M_A^{QE} through E_B ^{16}O) use the NEUT nominal value for the nominal MC tuning and are fit without prior constraints, with the exception of the binding energy E_B.[67] Not all listed parameters are used in the fit at SK.

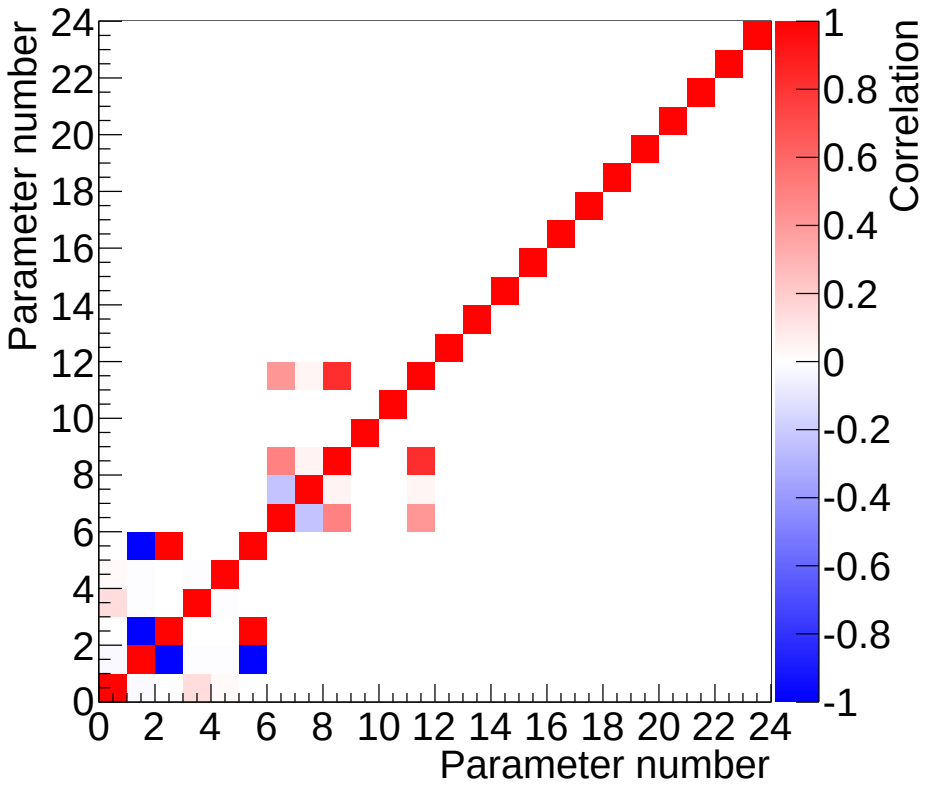

Figure 3.4: Correlations between cross section parameters listed in Table 3.4. Each bin corresponds to a single cross section parameter, and bins are in the order listed in Table 3.4.

ergy and ones that apply for low energy. These are implemented as response parameters which modify the various interaction cross-sections and are not used in the oscillation fits at SK[2]. The current implementation uses pion scattering data from the DUET experiment[71] to estimate the prior and prior constraints for each FSI parameter. The FSI parameters which apply in the high energy region are inelastic scattering (high energy), pion production and charge exchange (high energy). The low energy region uses the inelastic scattering (low energy), pion absorption, and charge exchange (high energy) parameters, as the charge exchange and scattering are tuned separately for the two regions.

- FSI Inelastic Scattering: final state has a single pion of the same charge as the initial pion. These parameters apply to both inelastic and elastic scattering, as the model used

[2]The FSI effects are instead dealt with as part of the SK detector covariance.

at T2K does not differentiate between these[72]. There are separate high energy and low energy versions for this parameter.

- FSI Charge Exchange: final state has a single pion of the opposite charge from the initial pion (π^+ from π^- and π^- from π^+) or a single π^0. There are separate high energy and low energy versions for this parameter.

- FSI Pion Absorption: Final state contains no pion. This parameter only applies to low energy interactions.

- FSI Pion Production: Final state includes 2 or more pions. This parameter only applies to high energy interactions.

The CCQE parameterization uses the relativistic Fermi gas nuclear model (RFG), and includes the Fermi momentum p_F and the binding energy E_b as response parameters. As p_F and E_b depend on the nuclear target, there are separate parameters for oxygen and carbon interactions. The CCQE model also includes the Nieves model for np-nh interactions[43][42]; the 2p-2h parameters for ^{12}C and ^{16}O are overall normalizations for these interactions; these are also split by interaction target. The 2p-2h ^{12}C parameter is used for all non-oxygen 2p-2h interactions. In addition, this analysis adds an extra normalization for antineutrino 2p-2h interactions[68]. Of the CCQE cross section parameters, the near detector fit passes M_A^{QE}, 2p-2h ^{16}O, p_F ^{16}O and E_b ^{16}O as inputs to the oscillation analysis, as the far detector does not contain carbon as a target material.

The CC-1π interactions are parameterized by three main parameters: M_A^{RES}, $C_A^5(0)$ and the Isospin $= \frac{1}{2}$ background scaling, all three of which are response parameters. The M_A^{RES} parameter is a correction to the axial mass for resonant 1π interactions and $C_A^5(0)$ is the dominant axial form factor for resonant pion production. The Isospin $= \frac{1}{2}$ background is the scaling of the nonresonant background for single pion processes which in NEUT is assumed to consist entirely of $I = \frac{1}{2}$ events. These parameters use prior constraints from the MiniBooNE and

MINERνA cross section data[68]. The near detector fit results for all three parameters are used in the oscillation fits at SK.

Of the cross section parameters that apply to interactions other than CCQE or CC-1π, only the CC other shape, from deep inelastic scattering, is implemented as a response parameter. The rest are normalization parameters for various interaction types. Unlike the CCQE and CC-1π model parameters, these do not have priors calculated from external data fits. Instead, the NEUT prior value is used and an uncertainty estimated for each parameter by the T2K neutrino interaction modelling working group. The CC Coherent normalization parameter is a normalization on carbon and oxygen CC coherent interactions; the prior uncertainty is derived from comparisons with MINERνA data[56]. Of the parameters listed in Table 3.4, the NC Other (far), NC 1γ, CC ν_e/ν_μ and CC $\bar{\nu}_e/\bar{\nu}_\mu$ parameters are included by the near detector fit, but due to lack of sensitivity there is no change in parameter values and widths. The NC Other (far) and NC Other (near) parameters are overall normalizations for NC interactions at SK and ND280 respectively. Due to differences in the NC Other contribution to samples at SK and ND280, the NC Other (near) fitted parameter is not propagated to the oscillation fit[68]. The NC1γ parameter is an overall normalization on the NC1γ interaction, separate from the CC Other normalization, and is a background at SK. The CC ν_e/ν_μ and CC $\bar{\nu}_e/\bar{\nu}_\mu$ parameters are included to account for potential differences in the ν_e/ν_μ cross-section ratio and $\bar{\nu}_e/\bar{\nu}_\mu$ cross-section ratio. The priors and uncertainties listed in the table are those used in the oscillation fits at SK.

Unconstrained Charged-Current Quasielastic Parameters

The external data fits using MiniBooNE and MINERνA provide constraints on the various cross section parameters. However, the constraints for the CC0π cross section parameters are not used in either the data fit or the various validation studies. The reasoning behind this is:

1. The MiniBooNE covariance matrix used in the external fits was incomplete due to lack of bin correlations in the data release, and changes to this covariance were found to cause

significant changes in the external fit.

2. The signal definitions for MiniBooNE and MINERνA were not consistent with each other, as MiniBooNE subtracts π-less Δ decay, a CC0π process, from the data using NUANCE while MINERνA does not.

3. There is poor agreement between the MiniBooNE and MINERνA data sets, and difficulty in consistently fitting both with the current models and parameters.

4. The $\bar{\nu}$ 2p-2h normalization parameter in the ND fit is not implemented in the external data fit and therefore cannot provide a prior.

Therefore, the CC0π cross section parameters M_{QE}^{A}, p_F ^{12}C, p_F ^{16}O , 2p-2h ^{12}C and 2p-2h ^{16}O are left unconstrained in the fit (that is, using a flat prior) and use the NEUT nominal values for calculating the nominal Monte Carlo rates. The $\bar{\nu}$ 2p-2h normalization parameter is also unconstrained in the fit and uses a nominal value of 1, corresponding to equal 2p-2h contributions for neutrinos and antineutrinos. When unconstrained, a parameter is allowed to vary in the fit, and is included in the covariance calculations after minimization but does not contribute to the overall $\Delta\chi^2$ term, allowing the parameter to vary across its entire valid range without penalty.

3.3.3 The Observable Normalization Matrix

The complex structure of the near detector and selection leads to a complicated set of detector systematic parameters; these must be accounted for and marginalized over in the near detector fit. These detector systematic parameters and their implementation are described in detail in Chapter 5. However, the current implementation of the detector systematic parameters is computationally expensive to fit on an event-by-event basis, where the various detector weights and variations for each individual event would need to be recalculated at every step of minimization. For this reason, the near detector fits a set of observable normalization parameters describing the effect of the systematic variations on the event rates for each sample.

The input consists of a set of normalization parameters for each fitted sample binned in p–θ and an associated covariance matrix describing the overall uncertainties and correlations on the observable normalization parameters. These normalization parameters and their covariance are calculated from 2000 variations of the detector systematic parameters and how these affect the event rates in each bin at ND280. The covariance also includes shape uncertainties from other sources that can be binned in p–θ, such as the Monte Carlo statistical error and a shape uncertainty for 1p-1h effects. Monte Carlo statistical errors are the uncertainty associated with the size of the generated Monte Carlo which is reweighted in the fit, due to the finite size of the Monte Carlo used in generating the matrix. These errors are added as independent error terms on the diagonal of the observable normalization covariance matrix. The previous near detector fit had a total of 290 detector observable normalization parameters, while the current fit has 580, due to the addition of the FHC ν_μ and RHC $\bar{\nu}_\mu$ and ν_μ samples for FGD 2. This has the effect of slowing down the fit simply due to the added difficulty of fitting such a large parameter space. The binning details are described later in Section 5.4.1.

The uncertainty on the model used for 1p-1h kinematics is also included as an additional independent covariance added to the observable normalization covariance matrix. This uncertainty covers the lepton kinematic model differences between the NEUT generator, which is what is used to generate the T2K Monte Carlo, and the Nieves generator. NEUT uses a Relativistic Fermi Gas (RFG) model to describe these interactions while Nieves uses a Local Fermi Gas model. Other models include Spectral Function and Relativistic Mean Field, as described in Section 1.4. In this case, the 1p-1h Nieves model was tested against the current model used for fitting at T2K. As fake data studies comparing the two different 1p-1h implementations have shown model choice to have a significant impact on the fit parameters at ND280 and in the oscillation fits[73], this model uncertainty is now incorporated into the normalization parameters as an additional shape covariance. The 1p-1h covariance was calculated as the bin-by-bin difference between the Nieves model prediction and the current NEUT model

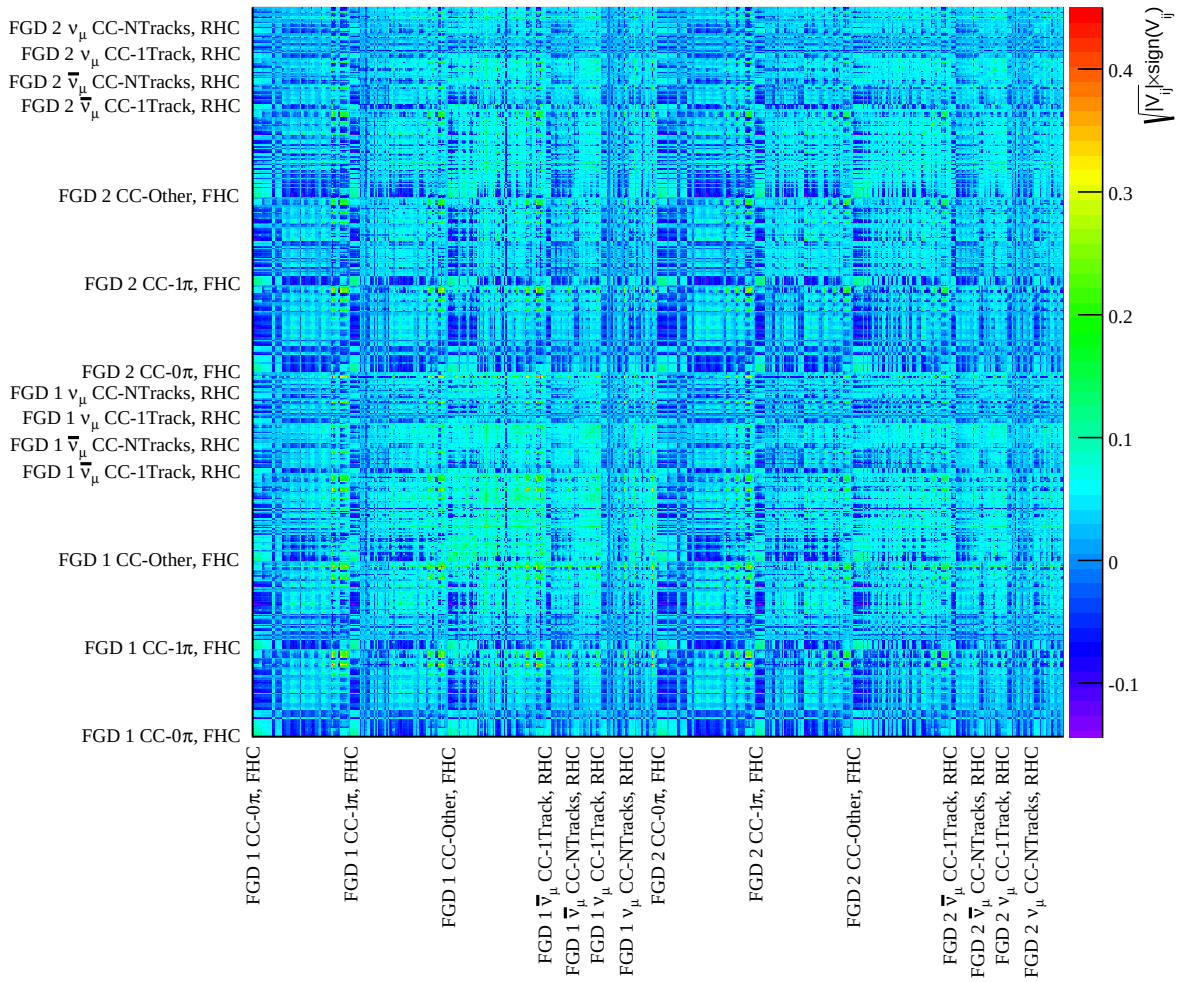

Figure 3.5: Detector covariance matrix, plotted as $\text{sign}(V_{ij})\times\sqrt{|V_{ij}|}$ for clarity. Maximum values are truncated at 0.45 for display purposes. Labels indicate where bins for a given sample start. The bins within each sample are ordered in increasing momentum intervals, each containing all angular bins from backward going to forward going.

prediction:

$$V_{1p-1h,ij} = (N_{Nieves,i} - N_{NEUT,i}) \times (N_{Nieves,j} - N_{NEUT,j}) \tag{3.7}$$

where $N_{Nieves,i}$ is the predicted event rate in bin i using the Nieves 1p-1h model, and $N_{Neut,i}$ is the predicted event rate in bin i using the nominal NEUT model.

Like the flux and cross section parameters, the observable normalization parameters are assumed to behave in a Gaussian manner and are included in the likelihood term shown in

Eq. 3.6, and are allowed to correlate with flux and cross section parameters in the fit. As the detector normalization parameters are constraints on the near detector event rates, these parameters are not used in the oscillation fits at SK. Instead, SK uses its own set of detector systematic parameters.

Chapter 4

The Tracker Selection

4.1 Introduction and Motivation

The strength of the near detector fit depends on the events selected at ND280, and how the neutrino interaction types can be identified. The primary signal for neutrino interactions at the T2K beam energies is the CCQE interaction, along with other charged current interactions such as CC Resonant and Deep Inelastic Scattering. To properly constrain the cross sections and the beam flux, being able to identify neutrino events and their interaction modes well is key. Unlike the SK event selections, ND280 is able to include specific samples for non-CCQE topologies as well as separate selections for neutrino and antineutrino events.

The selection used for the near detector fits is based on the tracker volume, comprised of the two FGDs and three TPCs. As described previously, the FGDs serve as the target volume, with FGD 2 providing oxygen targets similar to SK, and the TPCs allow for momentum and particle identification. The previous ND280 fit, used as the input for the previous $\bar{\nu}_\mu$ disappearance[74] and the joint ν_μ disappearance and ν_e appearance results[30], was FGD 1-only and did not have any selection for events occurring in FGD 2.

4.2 Data and Monte Carlo Inputs to the Selections

The data collected at T2K is separated by run period as well as detector configuration. For this analysis, neutrino beam data from Runs 2, 3, and 4 and antineutrino beam data from Runs 5 and 6 were used. Data from Run 1 had issues with calibration and is missing the top tracker ECal. As the ECal was originally intended to be used as part of this selection, this could present difficulties in using this data. Therefore data from this beam period is not used in the fit, as Run 1 only represents a small amount of statistics compared to later run periods and should have only a small impact on results.

The ND280 Monte Carlo is generated using the NEUT generator[75] for the neutrino interactions and simulated using the ND280 geometry in GEANT4. The MC is generated separately for each run period and P0D configuration, as the P0D water bags have been either filled with water or air at various points during ND280 running. As this increases the interaction rates in the P0D due to higher density, these must be simulated separately. There are two types of Monte Carlo events generated: ν_μ or $\bar{\nu}_\mu$ interactions in the magnet volume and sand muon events. Sand muon events are interactions of the neutrino beam with the sand surrounding the near detector. This is intended to simulate potential outside background events in the data.

Both the MC and the data are initially saved as files which contain the raw readout information from the detectors, real or simulated. Before reconstruction, gain calibration constants are applied, and dead and noisy channels removed from these files. The now calibrated files are then processed into ROOT file format compatible with the ND280 reconstruction software.

4.3 ND280 Detector Tracker Reconstruction

The ND280 reconstruction uses an external reconstruction toolkit, RecPack, for various fitting, propagation and matching routines[76]. RecPack provides two fitting algorithms, the least squares fit method and the Kalman filter method [77]. RecPack is designed to work with complex multi-volume geometries like ND280 and interfaces with the ND280 oaRecPack package, which provides RecPack with a simplified version of the ND280 geometry implemented in

Run Period	Data PoT	MC PoT
	FHC	
Run 2, Water In	4.2858e19	1.2015e21
Run 2, Water Out	3.55045e19	9.215e20
Run 3b, Water Out	2.146e19	4.48e20
Run 3c, Water Out	1.24821e20	2.63e21
Run 4, Water In	1.62818e20	3.499e21
Run 4, Water Out	2.84438e20	3.4965e21
	RHC	
Run 5c, Water In	4.29779e19	2.0825e21
Run 6b, Water Out	1.27374e20	1.4103e21
Run 6c, Water Out	5.02038e19	5.321e20
Run 6d, Water Out	6.39851e10	6.941e20
Total FHC PoT	5.82e20	1.22e22
Total RHC PoT	2.84e20	4.72e21

Table 4.1: Total protons on target (PoT) for data and Monte Carlo, broken down by run period and P0D water status. Monte Carlo PoT includes POT from sand muon Monte Carlo. Data PoT is after the basic data quality cuts described in Sec. 4.5.

ROOT. This simplified geometry models all volumes as boxes, and combines parts into single volumes where appropriate. The simple geometry also differentiates between active and dead material for reconstruction. The material properties used are the average properties in a given volume, so the FGD water module material would be an average of the material of the module itself and the properties of the water it is filled with.

The samples used in the near detector fit are designed using only information from the tracker volume at ND280 - the TPCs and FGDs. While the ND280 reconstruction does include information from other detectors such as the ECal and SMRD, these are not used in selections for the near detector fits and will not be described here.

4.3.1 Time Projection Chamber Track Reconstruction

The TPC track reconstruction starts by clustering hit waveforms in a TPC by way of connectivity within the Micro Mega (MM) pad columns or rows of a TPC. Each cluster is made up of hit waveforms that are consecutive in both position and time. TPC tracks consist of a series of these overlapping row or column clusters.

To identify TPC hit clusters, the reconstruction algorithm starts with the raw hit information in the form of waveforms, as a single hit is stored as a set of continuous charges on a TPC pad in time. Clusters are grouped by rows or columns of pads and are considered to be either horizontal or vertical clusters respectively. Clustering is done in XY planes, and hit waveforms are required to be overlapping in time and consecutive in position. To be considered to overlap in time, the ADC values above the pedestal threshold must be close in time. The hits must also be within a distance d of each other, which by default is the TPC pad pitch plus the gap between the pads in the cluster direction. This distance also takes into account whether or not waveforms are separated by the cathode, and is increased for clusters which already have a large spread. This allows clusters to pick up potentially isolated waveforms from longer tracks.

Once the clusters are grouped, TPC tracks are constructed using pattern recognition. First overlapping column or row clusters are matched into TPC segments. Segments are defined as a pair of clusters in two consecutive columns or rows; clusters are not required to be unique to segments and can be considered part of multiple segments. The reconstruction looks for consecutive clusters that are close in position to each other, and overlapping in time. For non-consecutive clusters, segments can be made from clusters with waveforms that overlap in time. Once segments have been constructed, the reconstruction attempts to pair segments by checking for segments that share clusters. This process can be extended to more than two segments, and produces the TPC tracks. Tracks made through combining segments often miss high angle tracks crossing the vertical gap between pads. For this reason, once the pattern matching has constructed shorter tracks out of the TPC segments, the RecPack Kalman filter algorithm is used to look for matches among the TPC tracks and construct longer ones. New tracks constructed this way are refit with the likelihood algorithm.

The TPC provides the main particle identification (PID) for the ND280 tracker and allows the selection to differentiate between muon, pion, electron and proton tracks, with muons and pions being difficult to differentiate in the TPCs[78]. To do this, the reconstruction uses the energy loss due to ionization of charged particles to provide a likelihood for each particle

hypothesis. Each track can consist of up to 72 clusters for a track that fully crosses a TPC and each cluster has a total energy computed from the sum of the charges of all hits in that cluster. The expected distribution of the energy for a cluster is very wide, with a long very high energy tail due to each TPC being thin. To account for this, the total energy is computed using a truncated mean consisting of the lower 70% of the clusters in that track[78][79]. In addition, a TPC track needs to have at least 18 nodes for this to be a reliable method of calculating the energy deposition. This total energy deposit is compared with the expected energy deposit for a given particle to create a particle ID likelihood for that particle. This takes track momentum into account and length into account. These likelihoods are used in the selection steps described later in this chapter.

4.3.2 Fine Grained Detector Reconstruction

The FGD reconstruction consists of two separate major parts: reconstructing tracks contained within the FGDs and reconstructing FGD tracks with a TPC component. For this reason, the FGD reconstruction is run after the TPC reconstruction is finished and the fitted TPC tracks are saved. This allows the FGD reconstruction routines to use the TPC tracks for matching FGD hits into TPC-FGD tracks.

The basic information in the FGD consists of saved hits, each with a time and XZ or XY position. The first step of the FGD reconstruction is to sort these hits into timebins, as described in more detail in Section 4.5.3. Each timebin consists of a set of FGD hits where each consecutive hit is less than 100 ns from the previous hit and are reconstructed independent from other time bins. This means that no hits are shared between time bins. Once the hits are all sorted into time bins, the FGD reconstruction steps are performed on each timebin individually, starting with the TPC-FGD matched track reconstruction. FGD-only reconstruction and particle identification are performed once the TPC-FGD reconstruction is finished.

The Time Projection Chamber – Fine Grained Detector Matched Reconstruction

The TPC-FGD reconstruction functions by looping over all reconstructed TPC tracks and attempting to incrementally match FGD hits to the TPC track to produce a FGD track segment. This uses the Kalman filter routine[77] provided by RecPack. To ensure that the FGD hits being matched are correct, the reconstruction checks that the initial time for the TPC track is within the time window of the FGD timebin. This initial time for the TPC track is determined in two ways, depending on whether the TPC track crosses the cathode or not. In the case that the TPC track crosses the cathode, T_0 can be calculated from the time of crossing and the maximal drift time. Otherwise, the initial TPC track time is found by comparing with hits in adjacent detectors using RecPack. If the initial time is outside that, the TPC-FGD matching is not performed for that track. If the track starts within the time window for that timebin, the TPC track is extrapolated back to the closest layer of hits in the FGD using RecPack.

The hit matching is processed layer-by-layer. Starting with the FGD hit with the lowest residual between the extrapolated TPC track and its position, the reconstruction computes a χ^2 using the distance between the extrapolated track and each hit using RecPack routines; this cutoff is the same for X and Y layers. Each time this calculated χ^2 is below a set cutoff value, the hit is matched to the TPC track, and the Kalman filter seed state recomputed with the new track information[76]. This is repeated for each hit in the layer, and repeats for the next FGD layer once done. The extrapolation continues even if there are no matched hits in a given layer. However, if two or more FGD layers have no matched hits in them, the extrapolation is terminated in order to avoid incorrectly matching hits from other particles. Once the extrapolation is finished either by termination or all hits have been examined, the final TPC track and the associated FGD hits are refit to give a consistent reconstructed output.

This does allow for a TPC 2 track to be matched to hits in both FGD 1 and FGD 2, creating an FGD 1 + TPC 2 + FGD 2 track. However, the hits matched with this track cannot be matched with tracks in any other TPCs. To allow for multi-TPC tracks, additional reconstruction must be performed.

The Fine Grained Detector-Only Reconstruction

While the primary track from a neutrino interaction in the FGDs is generally high enough momentum to leave the target volume and enter other detectors, this is not necessarily true for all secondary particles such as protons. The tracks left by these particles can be fully contained in the target FGD, with no TPC segments to match to. As there can be no dE/dx or curvature information from the TPCs, the FGD must be able to reconstruct all the needed information for these particles.

The input to the FGD-only reconstruction is the unmatched FGD hits from the timebin used in the TPC-FGD matched reconstruction stage. The initial step takes the unmatched hits and uses a pattern recognition method called SBCAT[76] to create XZ and YZ tracks from segments of hits in adjacent layers, similar to how clusters are matched in the TPC reconstruction. These reconstructed two-dimensional tracks are fit with straight lines and associated hits with high residuals are removed. In addition, tracks are checked to ensure no more than one consecutive layer is skipped, as with the TPC-FGD matched reconstruction. To match XZ and YZ track projections together to create a full three-dimensional FGD track, the reconstruction requires:

- The most upstream X and Y layers in each track must be adjacent.
- The most downstream X and Y layers from each track must also be adjacent.
- Both tracks must cross at least four layers.

Once an XZ and YZ projection are matched together, the resulting track is saved as an FGD-only track and the particle identification pulls are calculated.

For 3D tracks contained in the FGDs, particle identification pulls can be computed through comparing track length versus the total track energy [80]. As FGD 2 has less active material and therefore less complete information about energy deposition, this method is less effective than in FGD 1. First the track length is calculated for the 3D FGD-only track by fitting a straight line to each 2D projection (XZ or YZ). This differs slightly for FGD 1 versus FGD 2, as FGD 1 uses the middle of the scintillator bar for the z-position, while FGD 2 uses the

middle point of the scintillator bar and adjacent water layer for hit z-position. This is because the track could potentially have passed through the uninstrumented water layer next to the bar where the hit was seen. This gives a worse resolution for FGD 2 than for FGD 1. The total energy in the track is calculated from the sum of the charge deposited in the hits that make up the track, converted from photoelectron units (PEU) measured by the FGD readout to MeV, with corrections for WLS fiber attenuation and Birk's saturation. As with the track length estimation, FGD 2 is less accurate than FGD 1 in calculating the total charge, as energy is deposited in water layers but cannot be included in the calculation.

In general, the momentum estimation for FGD-only tracks is poor, and is not used for selection cuts. After these reconstruction steps, the tracks and associated information are saved and passed to the global tracker reconstruction.

4.3.3 Global Reconstruction and Charge Determination

The final reconstruction step allows for longer tracks than are created with the initial TPC-FGD reconstruction, as well as track direction correction. While the initial TPC-FGD reconstruction allows for hits in the FGDs to be matched with a track from a single TPC, there are many cases where higher energy particles can travel through multiple TPCs before exiting the ND280 volume. For example, the plain TPC-FGD reconstruction would miss tracks starting in one TPC and traveling through an adjacent FGD and TPC, which could be a potential background. To do this, the tracker reconstruction loops through sets of tracks in adjacent TPCs – tracks in TPC 1 and TPC 2, or TPC 2 and TPC 3 – and uses RecPack to extrapolate pairs of tracks. Tracks formed in this manner can have a single TPC track component in each TPC, along with associated FGD segements. After this step, the final TPC-FGD and FGD-only tracks are all refit using the Kalman filter from RecPack to ensure that all tracks use the energy-loss corrections from RecPack.

The final step in the tracker reconstruction is to apply FGD timing information to determine the matched TPC-FGD track direction. By default, both TPC and FGD tracks are assumed to

be downstream tracks, with tracks with FGD 1 and FGD 2 components starting from the FGD 1 volume. Using the average time of the hits in each FGD for tracks which cross both FGD 1 and FGD 2 volumes, a time difference can be computed:

$$\Delta t_{FGDs} = t_{avg,FGD1} - t_{avg,FGD2} \tag{4.1}$$

When $\Delta t_{FGDs} > 3ns$, the track is considered to be backwards-going and the saved reconstruction track is flipped. A difference of at least 3 ns is used to prevent accidental flipping of forward going tracks due to intrinsic timing resolution, as there are more forward going tracks than backwards. At this point, the tracker reconstruction is done and the reconstructed information is processed into the file format used in the selection and fit.

4.4 The ND280 Detector Tracker Selection

4.4.1 Selection Basics

All selected events and samples used in the fit share a few characteristics and are designed to select signal ν_μ and $\bar{\nu}_\mu$ interactions. Initially, Charged Current Inclusive (CC Inclusive) neutrino or antineutrino interactions are selected, removing all non-CC Inclusive identified events. These selected events are then sorted by final event topology – no additional events are removed from the selection at this point. The final event topology is defined as the set of particles that leave the interaction nucleus after the interaction. Event topology is chosen over event mode as it better matches what can be reconstructed in the near detectors, as ND280 only sees the final state that leaves the nucleus.

The main signal for the analysis, and the main signal interaction at SK is the CCQE interaction, due to the ease of energy reconstruction. As these types of events only have two outgoing charged particles, they have a relatively simple topology to look for as the proton is often not visible due to low energy. This topology is called the CC-0π topology, where one charged lepton track is seen and there are no visible secondary pions. Non-CCQE interactions

can also be detected and are categorized into the CC-1π, and CC Other, which includes all other topologies.

To perform the selection, evaluate systematics and store relevant event information, ND280 uses a specialized software tool called Psyche. Psyche was made specifically for use with ND280 events and uses the reconstructed event information and truth information from the Monte Carlo, and can also use the reconstructed data events. The selections only use reconstructed information from the events, while the systematic calculations can use true event information and are only used for Monte Carlo events. Psyche does not use any fitting routines itself but is designed to be used within the ND280 fit software in order to select events and is optimized for speed and low memory use.

Each event must have a muon-like track that starts in the defined fiducial volume in either FGD and passes into a neighboring TPC. Because of this, the efficacy of the selections depends on how well direction and vertex position can be reconstructed in the near detectors. Selections are divided by target FGD, neutrino mode and muon track sign. While the selection cuts used for forward horn current beam and reverse horn current mode are different, all selections share the same basic structure and similar CC Inclusive cuts.

For forward horn current, the ND280 selection differentiates between the CC0π, the CC1π and the CC Other topologies for ν_μ, while for reverse horn current (RHC) the selection there are two separate CC-Inclusive selections for the $\bar{\nu}_\mu$ signal and the wrong-sign ν_μ background. These are both separated into 1-Track and multi-track samples, as the lower antineutrino mode statistics for CC Inclusive and other reconstruction considerations make it difficult to separate between non-CC0π topologies.

- Forward Horn Current Selections:
  - CC Inclusive
    * CC0Pi
    * CC1Pi

        * Other Charged Current Interactions

- Reverse Horn Current
    - CC Inclusive Antineutrino Interactions
        * Charged Current Single Track Topologies
        * Charged Current Multi-track Topologies
    - CC Inclusive Wrong-sign Interactions
        * Charged Current Single Track Topologies
        * Charged Current Multi-track Topologies

Cuts used for each selection are shown in Tables 4.2, 4.3 and 4.4 and are described in detail in the following sections. The selected numbers of events in data and Monte Carlo for these selections are shown in Table 4.5. The numbers shown for the Monte Carlo are using the flux, PoT and cross section reweighting. CCQE weights use the NEUT nominal values.

Cut	FHC ν_μ	RHC $\bar{\nu}_\mu$	RHC ν_μ
Data Quality	Yes	Yes	Yes
Track Multiplicity	Yes	Yes	Yes
Fiducial Volume Cut	Negative track	Positive track	Negative track
Upstream Veto	Yes	Yes	Yes
Broken Track Cut	Yes	Yes	Yes
Muon PID	Negative track	Positive track, stricter criteria	Negative track, stricter criteria

Table 4.2: List of CC Inclusive Cuts for the three main selections. Major differences between cuts are listed here.

4.4.2 Fine Grained Detector 2 Considerations

While the two FGDs are very similar in their makeup and electronics, there are several differences in FGD 2 that impact event reconstruction and sample selections. The largest difference comes from the fact that FGD 2 contains water modules alternated with the XY scintillator modules, while FGD 1 only contains scintillator modules. While this allows for interactions

Cut	Cut Details		
TPC Positive Pion Tracks	n_1 = # of TPC-FGD π^+ Tracks		
Michel Electrons	n_2 = # of Michel electrons identified		
FGD-Only Pion Track	n_3 = # of FGD-Only Pion Tracks		
TPC Negative Pion Tracks	n_4 = # of TPC-FGD π^- Tracks		
TPC Electron & Positron Tracks	n_5 = # of TPC-FGD e^+ and e^- Tracks		
	CC 0π	CC 1π	CC Other
Sample Criteria	$\sum_{i=1}^{5} n_i = 0$	$\sum_{i=1}^{3} = 1$ and $n_4 + n_5 = 0$	$\sum_{i=1}^{3} > 1$ and/or $n_4 + n_5 > 0$

Table 4.3: List of the FHC multipion selection cuts and sample criteria.

Cut	Cut Details	
TPC-FGD Matched Track	n = # of TPC-FGD Matched Tracks	
	1-Track	Multi-Track
Sample Criteria	$n = 0$	$n > 0$

Table 4.4: List of the RHC multipion selection cuts and sample criteria. The multipion selection cuts are the same for the $\bar{\nu}_\mu$ and ν_μ, as there is no cut on the charge of the secondary tracks.

on oxygen in FGD 2, determining which events are on oxygen is not necessarily possible. The water modules in FGD 2 are uninstrumented and so can only act as target material. In addition, due to this reduction in vertex resolution, determining the exact start position of a track in FGD 2 is difficult - not only do tracks go through less active material, but any events occurring in the water volume will appear to have started in the closest scintillator layer. This means that the selection can only distinguish between carbon and oxygen events statistically rather than on an event-by-event basis. This reduction in active material also changes the efficiency of FGD-only reconstruction as short tracks will leave fewer hits.

One improvement that adding in the second FGD offers is inter-detector timing. While previous selections using only FGD 1 primarily used momentum reconstruction for determining the direction of tracks in order to select out backwards going events originating in FGD 2 and terminating in FGD 1, the hit timing between the two FGDs can be used instead. As the hit timing between the FGDs is precise to 3 ns, it is accurate enough to determine the direction of a track by comparing the time of the first hit in FGD 1 to the first hit in FGD 2. This allows

Sample	Data	ND280 prefit MC prediction
FGD1 ν_μ CC Inclusive (ν mode)	25558	25420.74
FGD1 ν_μ CC0π (ν mode)	17354	16950.81
FGD1 ν_μ CC1π (ν mode)	3984	4460.15
FGD1 ν_μ CC Other (ν mode)	4220	4009.78
FGD1 $\bar{\nu}_\mu$ CC Inclusive ($\bar{\nu}$ mode)	3438	3506.38
FGD1 $\bar{\nu}_\mu$ CC 1-Track ($\bar{\nu}$ mode)	2663	2708.65
FGD1 $\bar{\nu}_\mu$ CC N-Tracks ($\bar{\nu}$ mode)	775	797.73
FGD1 ν_μ CC Inclusive ($\bar{\nu}$ mode)	1990	1933.36
FGD1 ν_μ CC 1-Track ($\bar{\nu}$ mode)	989	938.13
FGD1 ν_μ CC N-Tracks ($\bar{\nu}$ mode)	1001	995.33
FGD2 ν_μ CC Inclusive (ν mode)	25151	24454.89
FGD2 ν_μ CC0π (ν mode)	17650	17211.71
FGD2 ν_μ CC1π (ν mode)	3383	3616.62
FGD2 ν_μ CC Other (ν mode)	4118	3626.56
FGD2 $\bar{\nu}_\mu$ CC Inclusive ($\bar{\nu}$ mode)	3499	3534.33
FGD2 $\bar{\nu}_\mu$ CC 1-Track ($\bar{\nu}$ mode)	2762	2729.88
FGD2 $\bar{\nu}_\mu$ CC N-Tracks ($\bar{\nu}$ mode)	737	804.45
FGD2 ν_μ CC Inclusive ($\bar{\nu}$ mode)	1916	1860.51
FGD2 ν_μ CC 1-Track ($\bar{\nu}$ mode)	980	943.90
FGD2 ν_μ CC N-Tracks ($\bar{\nu}$ mode)	936	916.61

Table 4.5: Observed and predicted event rates for the different ND280 samples in the ND280 fits. Predicted event rates include PoT, flux, detector and cross section reweighting.

both better removal of the background in FGD 2 for forward going FGD 1 events and inclusion of backwards going FGD 2 events in the selected samples.

4.4.3 Antineutrino Subsamples

For the antineutrino beam mode, there are two major considerations to take into account relative to neutrino beam mode selections. The first is that unlike the neutrino beam, the antineutrino beam at T2K is has a significant wrong-sign component from neutrinos. While ND280 is capable of using charge identification through curvature in the magnetic field, as described in Section 4.3, in order to distinguish between μ^+ and μ^- for the outgoing lepton, the selection at SK is insensitive to charge and relies on the near detector fit to properly constrain this wrong sign background. This means that a CC Inclusive selection for antineutrinos alone is not suffi-

cient for use in an oscillation analysis and instead there are two CC Inclusive selections used, one for signal $\bar{\nu}_\mu$ and the other for the wrong sign ν_μ events.

Additionally, reconstructing all the final state particles in an $\bar{\nu}_\mu$ interaction is not as easy as for a ν_μ interaction – while secondary particles from the ν_μ interactions are often high enough in energy to be reliably reconstructed and used in a cut, this is not always the case for antineutrino events. The RHC samples are instead separated into 1-track and multi-track topologies rather than CC-0π, CC-1π and CC Other topologies used for the FHC selection. For the RHC $\bar{\nu}_\mu$ selection, this is because while the FHC ν_μ samples use reconstructed π^+ to distinguish between topologies, the analogous π^- tend to be absorbed and are difficult to reconstruct in the FGDs. The wrong-sign ν_μ events in RHC could use the same selection as FHC ν_μ however the RHC $\bar{\nu}_\mu$ and ν_μ selections both use the same sample topologies to reduce systematic effects between the two selections.

4.5 Selection Cuts and Results

4.5.1 General Data Quality Cuts

The most basic cuts are common to all selections at ND280, and are not specific to beam mode, as their purpose is to verify that the events being used are from a time where beam and detectors were operational and have enough information to run the selection on.

Event Quality

This check applies only to events from data, as all MC events are assumed to have good beam and data quality. The main concerns are whether the beam was on and working correctly, and all ND280 detectors were operational. To check this, there are Boolean values saved in the raw data files which indicate beam status and data acquisition system status for each spill. This ensures that there are no potential data collection issues, either in the detectors or the data collection software, that could bias selected events.

Multiplicity Check

Because the majority of beam-triggered events saved have little to no reconstructible information, we cut out all events without reconstructed tracks. Events are required to have at least one reconstructed track in any of the three TPCs and in order to reconstruct a track in a TPC, there must be at least 5 nodes to use for the track. As the event selection depends on having a TPC-FGD matched track, events without any are not useful.

4.5.2 The Neutrino Mode Charged Current Inclusive Selection

The Charge Current Inclusive (CC Inclusive) cuts for the neutrino mode FGD 1 and FGD 2 samples are roughly the same, with most differences arising from geometry considerations. In addition, the Charged Current Inclusive selection cuts are very similar for all the selections used in the ND280 fit, with the main differences being track polarity and highest momentum track choice.

The Fiducial Volume Cut

The initial identifier for a CC Inclusive neutrino event is the reconstruction of a matched TPC-FGD track with negative curvature, where the highest momentum negative matched track is considered the lepton candidate for that event. In the case there are two neutrino interactions close in time enough to be reconstructed as one event, only the highest momentum one will be considered, effectively discarding the second, lower momentum event. The TPC segment of the lepton candidate is also required to have at least 18 nodes, rather than the minimum of 5 for basic reconstruction. While tracks can be reconstructed in the TPCs with fewer nodes, having at least 18 nodes gives more accurate momentum and particle identification.

This track is required to have its starting point in the fiducial volume of either FGD 1 or FGD 2, which is a subset of the total FGD volume. The fiducial volume for FGD 1 is defined in ND280 detector coordinates as :

- $|x| < 874.51$ mm

- $-819.51 < y < 929.51$ mm
- $136.875 < z < 446.955$ mm

The offset in the y-coordinate is due to the FGD XY modules being shifted off-axis by 55 mm relative to the ND280 detector coordinate system. This volume excludes the first layer of the initial XY module in FGD 1, and the outer 5 bars of a given XY module.

The fiducial volume for FGD 2 is defined as:

- $|x| < 874.51$ mm
- $-819.51 < y < 929.51$ mm
- $1481.45 < z < 1807.05$ mm

The fiducial volume for FGD 2 does not include the first scintillator module, but allows for interactions originating in the first water module to be selected, as forward-going interactions in the first water module will appear to have started in the second scintillator module. The fiducial volume cut is used as the first pass to remove interactions that occur outside of the FGD volumes, such as cosmic muons or interactions in the TPCs or ECALs.

The Upstream Veto Track Cut

The second cut for the FHC mode selection uses the highest momentum global track that has a segment in a TPC, but is not the lepton candidate described for the previous cut, referred to as the veto track. The reconstruction can sometimes fail to properly link tracks, for example a muon that starts in the P0D or TPC and goes through FGD 1 and TPC 2 may fail to link back and instead will be reconstructed as two separate tracks, one in TPC 1 and FGD 1, and another in FGD 1 and TPC 2. For this reason, the selection cuts on high-momentum upstream tracks. For both FGD 1 and FGD 2, events are removed from the selection if the veto track start position is more than 150 mm upstream from the muon candidate start position. The FGD 2 selection also cuts events which have the veto track starting in the FGD 1 fiducial volume

in order to remove potential upstream background from FGD 1 which might make topology separation difficult.

Broken Track Cut

This cut is used to reject another class of broken track events where the reconstruction breaks a potential candidate track into two separate tracks. Here the target is tracks which are broken into a short track fully contained in an FGD, and a FGD-TPC matched track starting in the last layers of the FGD. Such events would both have incorrectly reconstructed overall momentum as well as potentially be classified as the wrong topology due to an apparent FGD-only track originating from the selected vertex. To remove such events, this cut requires that an event with a candidate muon track and a reconstructed FGD-only track must have the muon candidate start position be less than 309.05 mm away from the upstream edge of the relevant FGD, removing any events where the muon candidate starts in the last two layers of the FGD. This distance is the same in FGD 1 and FGD 2 and there are no additional requirements for FGD 2.

Muon Particle Identification Cut

The final cut for the FHC CC Inclusive selection is the μ particle identification cut, where the candidate highest momentum negative track is required to be identified as a muon through reconstruction. The particle identification (PID) procedure uses dE/dx measurements from the TPC modules, as different particle types, such as muons, electrons or protons, will leave different energy deposits. The reconstruction calculates the pulls, shown in Eq. 4.2 for various different particle hypothesis using the measured energy deposits; for these calculations, only segments which pass the TPC track quality cuts contribute to the measured dE/dx. The likelihood for a given particle i is defined as in Eq. 4.3.

$$Pull_i = \frac{dE/dx_{meas} - dE/dx_{expected,i}}{\sigma_{dE/dx_{meas} - dE/dx_{exp}}} \tag{4.2}$$

$$L_i = \frac{e^{-Pull_i^2}}{\Sigma_j e^{-Pull_j^2}} \tag{4.3}$$

and j is all particle hypotheses.

For the muon hypothesis, there are two specific requirements imposed in order to remove electrons, protons and pions using PID. The electron cut requires :

$$\frac{L_\mu + L_\pi}{1 - L_p} > 0.8 \tag{4.4}$$

for tracks with $p < 500\text{MeV/c}$, as higher momentum tracks are less likely to be electrons. Finally, all candidate tracks must have a sufficiently high muon pid likelihood:

$$L_\mu > 0.05 \tag{4.5}$$

Similar particle identification methods are also used for cuts on secondary tracks for the FHC topologies.

Forward Horn Current Charged Current Inclusive Results

The event reduction for each cut is shown in Table 4.6. The CC-Inclusive selection is effective at cutting out non-CC Inclusive events for both FGDs, with a final CC Inclusive purity of 90.54% in FGD 1 and 89.29% in FGD 2. Momentum and $\cos\theta$ distributions are shown in Figs. 4.1 and 4.2 for MC and data, with a breakdown by event topology. Total composition by event topology is shown in Table 4.7. For FGD 2, Fig. 4.2b shows that the selection contains backwards-going muon events, unlike the FGD 1 selection. This is enabled by using the timing differences between FGD 1 and FGD 2 to identify the track direction. As there is no equivalent for FGD 1, there is instead a backward track veto. This is due to poorer timing resolution between the P0D and FGD 1 than between FGD 1 and FGD 2.

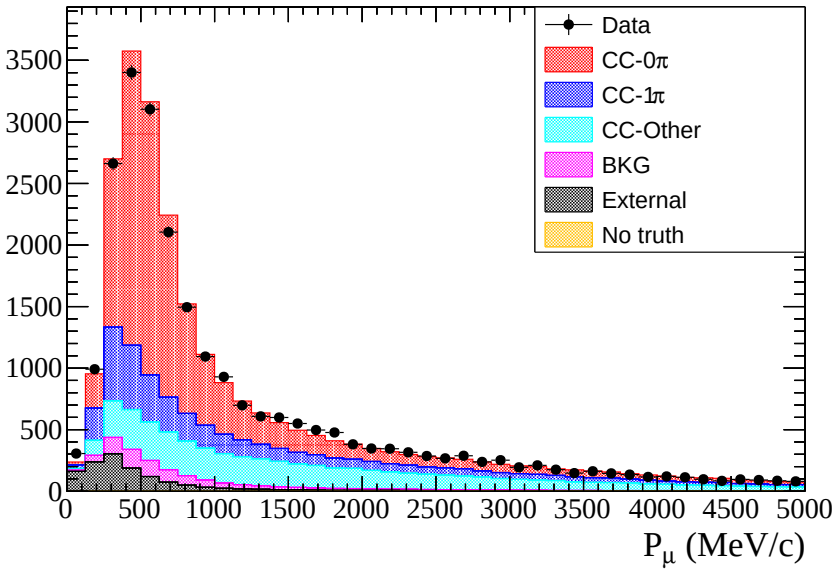

(a) Momentum distribution

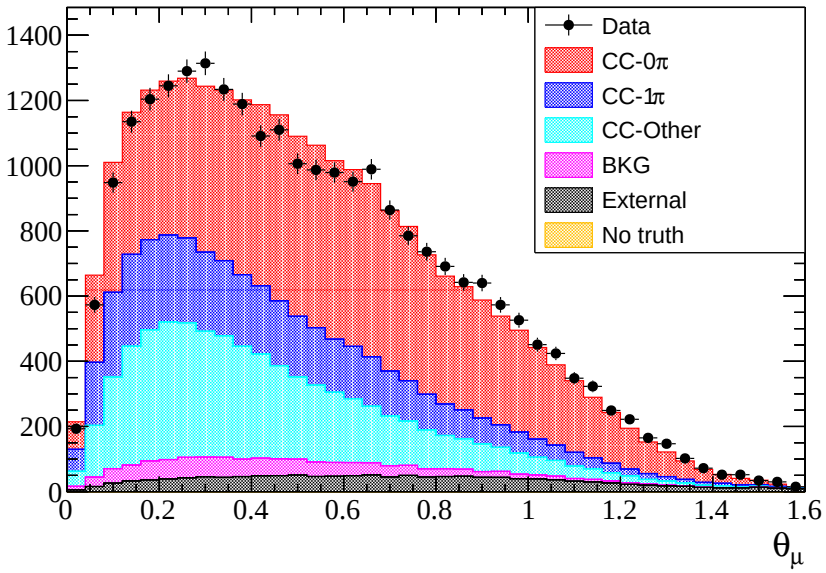

(b) θ_μ distribution

Figure 4.1: Momentum and θ_μ distributions for data and Monte Carlo, broken down by true topology, for the FGD 1 FHC CC Inclusive selection before the ND280 fit tuning[81]. The "No Truth" category indicates cases where there was no specific truth information associated with the selected vertex.

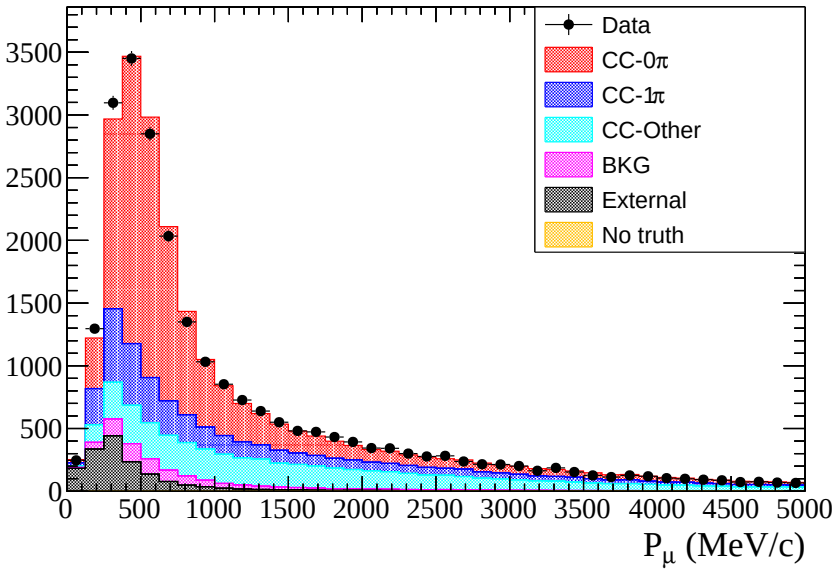

(a) Momentum distribution

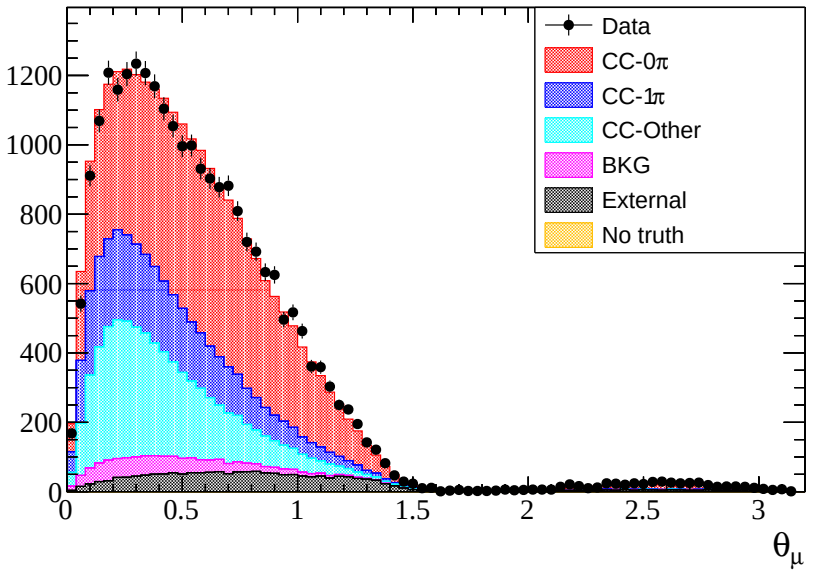

(b) θ_μ distribution

Figure 4.2: Momentum and θ_μ distributions for data and Monte Carlo, broken down by true topology, for the FGD 2 FHC CC Inclusive selection before the ND280 fit tuning[81]. The "No Truth" category indicates cases where there was no specific truth information associated with the selected vertex.

Cut Level	FGD 1	FGD 2
Quality and fiducial cut	100%	100%
Upstream veto cut	77.6%	70.4%
Broken track cut	76.5%	69.5%
Muon PID cut	56.4%	50.7%

Table 4.6: Event reduction fractions for each cut step for both FGD 1 and FGD 2[81]

Event topology	FGD 1	FGD 2
CC-0π	49.47%	49.26%
CC-1π	17.91%	17.57%
CC-Other	23.16%	22.46%
In-FV Background	4.09%	4.00%
Out of FGD FV Background	5.73%	6.69%

Table 4.7: Fractional breakdown of the CC-Inclusive sample by true topology for both FGD 1 and FGD 2[81]

4.5.3 The Neutrino Mode Multipion Selection

Once the CC Inclusive events are selected, they are separated by interaction topology into three different samples. At this point, no events leave the selection as all events should belong to one of the defined topologies: CC0π, CC1π and CC Other.

The key to selecting these topologies is pion identification and detection of secondary tracks. Like the CC Inclusive cuts, the information used in the selection comes from the TPCs and FGDs. Unlike the long high momentum tracks used to define the muon candidate track, secondary tracks are shorter and more difficult to reconstruct and understand. These topologies are defined as:

- The CC 0π Sample: This sample is characterized by no observed secondary pions; this corresponds closely with the CCQE interaction vertex and the signal definition at SK. It contains no TPC-identified pion, electron or positron tracks and does not have any Michel electrons or charged pions contained in the FGD.

- The CC 1π sample: This sample is characterized by a negative muon and a single π^+ with no other pions (π^0 or π^-). To select these, we require that there be either a single

reconstructed Michel electron and zero positive pion tracks in the TPC or no Michel electrons and a single reconstructed positive pion in the TPCs or FGD. Additionally, there must be no reconstructed negative pion tracks in the event as well as no electron or positron tracks in the TPC, which identify π^0 through their decay.

- The CC Other Sample: This sample includes all the selected CC Inclusive events that do not meet the criteria defined above for the CC0π or CC1π samples. These events have a single negative muon, and either at least one π^0 or π^- or more than one π^+. This also includes any topologies with other particles such as kaons.

The cuts used in separating the samples are the Michel electron cut, the FGD-contained reconstructed track cut and the TPC secondary track PID cut. All cuts are extended to the FGD 2 selection and modified where appropriate. The $p - \theta$ binning for these samples, as used in the fit, is given as:

- FHC CC-0π sample bin edges for the fit:
  p (MeV/c) : 0, 300, 400, 500, 600, 700, 800, 900, 1000, 1250, 1500, 2000, 3000, 5000, 30000
  $\cos\theta$: -1.0, 0.6, 0.7, 0.8, 0.85, 0.90, 0.92, 0.94, 0.96, 0.98, 0.99, 1

- FHC CC-1π sample bin edges for the fit:
  p (MeV/c) : 0, 300, 400, 500, 600, 700, 800, 900, 1000, 1250, 1500, 2000, 5000, 30000
  $\cos\theta$: -1.0, 0.6, 0.7, 0.8, 0.85, 0.90, 0.92, 0.94, 0.96, 0.98, 0.99, 1

- FHC CC-Other sample bin edges for the fit:
  p (MeV/c) : 0, 300, 400, 500, 600, 700, 800, 900, 1000, 1250, 1500, 2000, 3000, 5000, 30000
  $\cos\theta$: -1.0, 0.6, 0.7, 0.8, 0.85, 0.90, 0.92, 0.94, 0.96, 0.98, 0.99, 1

where the FGD 1 and FGD 2 samples use the same binning.

Time Projection Chamber Pion Track Cuts

The TPC pion track cuts use the pulls and likelihoods calculated from measured dE/dx as defined in Eq. 4.2 and Eq. 4.3. However, for the pion track cuts, the relevant tracks are defined as secondary tracks in the event that start in the same FGD fiducial volume as the selected muon candidate, and have a matched TPC segment with at least 18 clusters in the TPC, similar to the muon candidate cuts. Instead of checking the electron and muon pull hypotheses, the three particle types used in the cuts are pion, positron and proton for positive tracks. For negative tracks, the pion and electron hypotheses are considered instead.

For charged pion identification, the selection considers a secondary FGD-TPC track to be a pion if

$$\frac{L_\mu + L_\pi}{1 - L_p} > 0.8 \tag{4.6}$$

if $p < 500$ MeV/c, and

$$L_\pi > 0.3 \tag{4.7}$$

for all other cases.

Fine Grained Detector Isolated Reconstruction Track Cut

The FGD isolated reconstruction cut applies to tracks originating in the same FGD fiducial volume as the candidate muon track, but do not leave the FGD. This cut serves to identify secondary π^+ that stop in the FGDs. The definition of fiducial volume used to define track containment is slightly different from the general fiducial volume definition used in the CC-Inclusive cuts:

- $-887 < x < 888$ mm
- $-834 < y < 942$ mm
- z-position between the first active layer and last active layer in the FGD

FGD-only tracks must both start and end within this volume. As described in Sec. 4.3.2, the FGD-only track reconstruction can calculate a particle ID pull using the energy deposited as a function of track length. Like the TPC PID pulls, this is used to identify the most probable particle for that track. To be considered a contained positive pion track, the FGD-only track must have $\cos\theta > 0.3$ due to reconstruction efficiencies and a pion pull greater than -2 and less than 2.5.

Determining the Michel cut

Along with the other updates to various parts of the selection, the Michel electron cut must be defined for both FGD 1 and FGD 2 selections, as it is used to differentiate between the CC0π sample and CC1π sample for both detector selections. The intention is to select out events that have a delayed Michel electron originating from decaying pions that were produced by neutrino interactions. As not all pions produced in such a way will have sufficient energy to reach a neighboring detector, thus stopping within the volume of the FGD, these events can lead to contamination of the CC0π sample. In the case of Michel electrons, these particles often do not deposit enough energy to be reconstructed as an FGD-only track as described for the previous cut. Therefore, an additional cut that does not use reconstructed tracks is required.

To identify these Michel electrons, the basic procedure is to look for delayed activity in the FGD containing the muon track, with delayed activity being defined as occurring at least 100 ns after the initial neutrino interaction for that event. As shown in Fig. 4.3, the majority of selected CC Inclusive events do not have any delayed time bins. For events with at least one delayed time bin, there is a larger fraction of non-CC0π events than for the events with none.

Hits in the FGDs are sorted into FGD time bins by distance in time between each concurrent hit. To be considered to be in the same FGD time bin, a hit must be have a incident time difference less than 100 ns from the last hit seen in the FGD; if the difference is greater than 100 ns, the hit is then placed in the next FGD time bin, as shown in Fig. 4.4. The main purpose of this sorting, along with being used for the Michel tagging as described here, is to separate

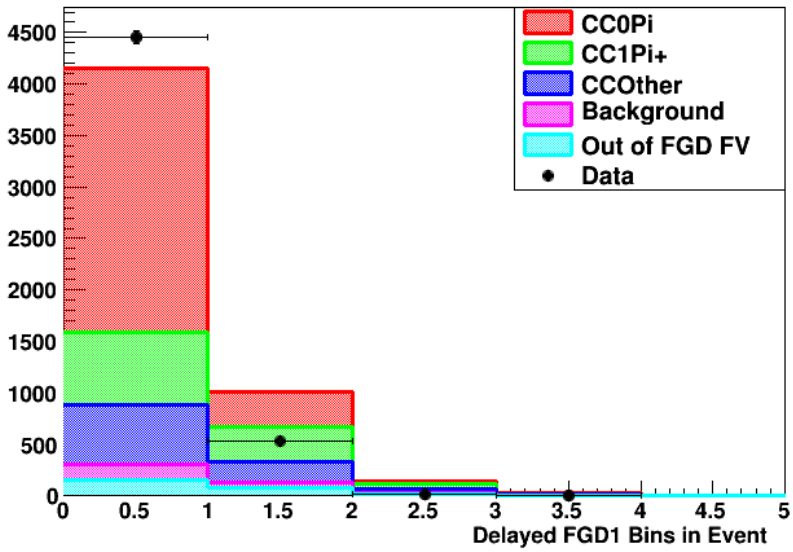

(a) FGD1

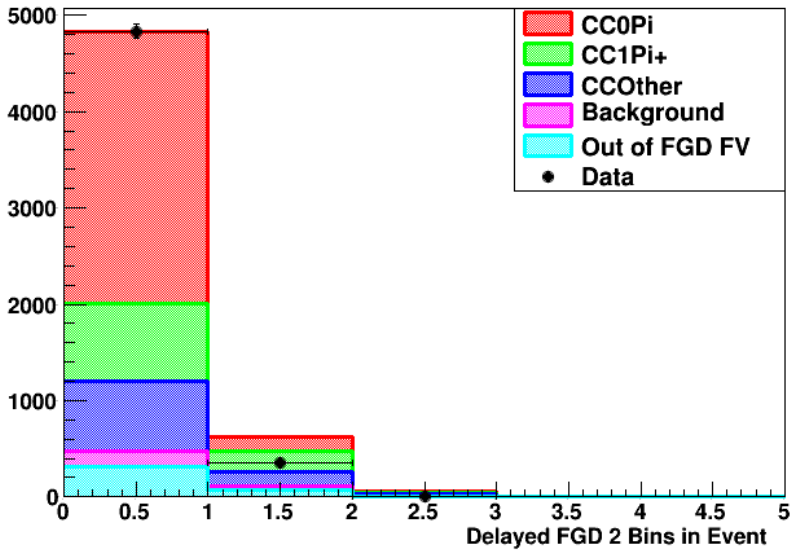

(b) FGD 2

Figure 4.3: Total number of delayed out-of-bunch FGD timebins in selected CC Inclusive events. Plots are normalized to data POT, and were created for a subset of the run 4 data.

neutrino interactions in different bunches from each other. As the muon decay lifetime is on the order of 2.2 μs, particles such as pions and Michel electrons should be sorted into time bins separate from their generating neutrino interaction. In addition to this, the delayed FGD timebin must not occur during any beam bunch windows, to be considered for a Michel electron candidate, as there is no way to separate the Michel activity from similar beam-induced activity in the FGD.

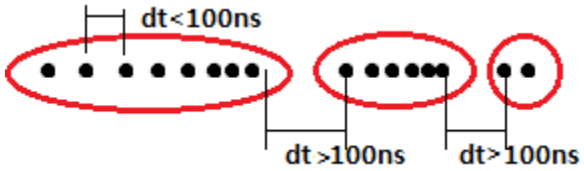

Figure 4.4: Example diagram of how FGD hits are grouped into timebins. The horizontal axis is time and each point represents the time of an individual FGD hit. Each red ellipse represents an FGD time bin and encompasses hits placed into it.[82]

The original Michel electron cut used in the FHC FGD 1 samples uses the total charge in the candidate time bin to determine whether or not the event had a Michel candidate; in FGD 1, due to the fully instrumented volume, there is a clear cutoff between background and charge deposits left by true Michel electrons. However, the charge deposition has less separation for FGD 2 events, as shown in Fig. 4.5. Instead, the cut now looks at number of hits in the delayed timebin, shown in Fig. 4.6. This allows for a higher Michel electron identification rate in FGD 2 and FGD 1 compared to the previous charge-based cut, shown in Table 4.8. While there is still more difficulty in selecting FGD 2 Michel e^-, due to the less instrumented geometry, a hit-based cut gives significantly higher efficiency. One feature that shows up in both implementations of the cut is the discrepancy between data and MC at low hits. At low numbers of hits or amount of charge deposited, there is a significant excess in MC consisting of background events, while the data is lower by a factor of 5. This indicates that there is some over-simulation of background and is discussed further in Section 5.3.12. This excess in simulated background limits the power of the Michel cut and would need to be understood to further improve it.

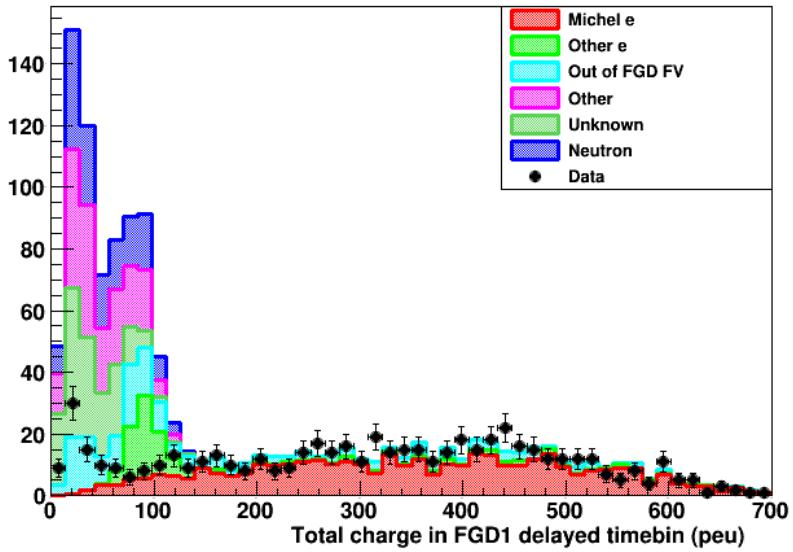

(a) FGD1

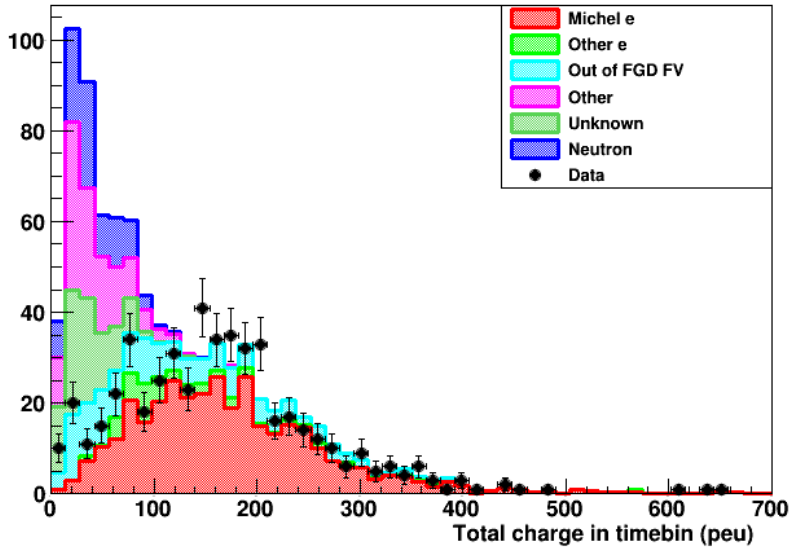

(b) FGD 2

Figure 4.5: Total charge seen in out-of-bunch timebins for selected CC Inclusive events. Plots show the breakdown by true particle associated with the delayed time bin. Plots are normalized to data POT, and were created for a subset of the run 4 data.

Michel Cut Definition	FGD 1	FGD 2
Previous Cut on Total Charge $>$ 200 photoelectrons	80.6%	31.9%
Current FGD-Specific Hit Cut	83.9%	52.7%

Table 4.8: Fraction of correctly identified Michel electrons with hits in delayed timebins.

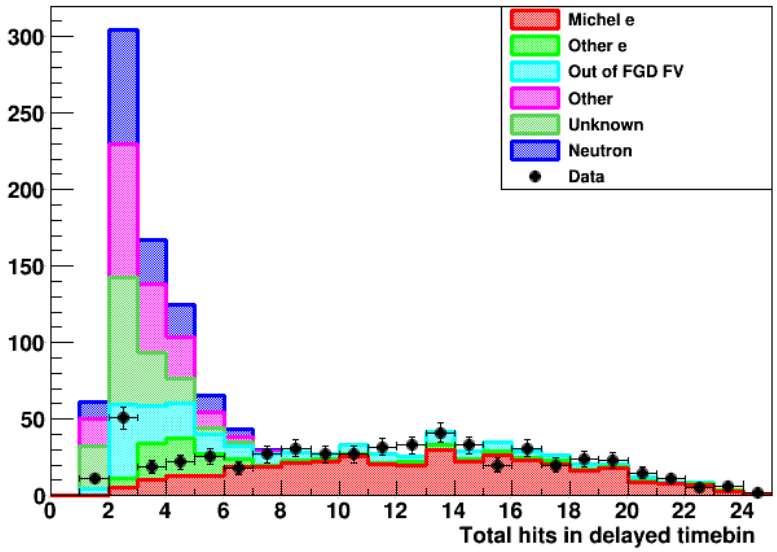

(a) FGD1

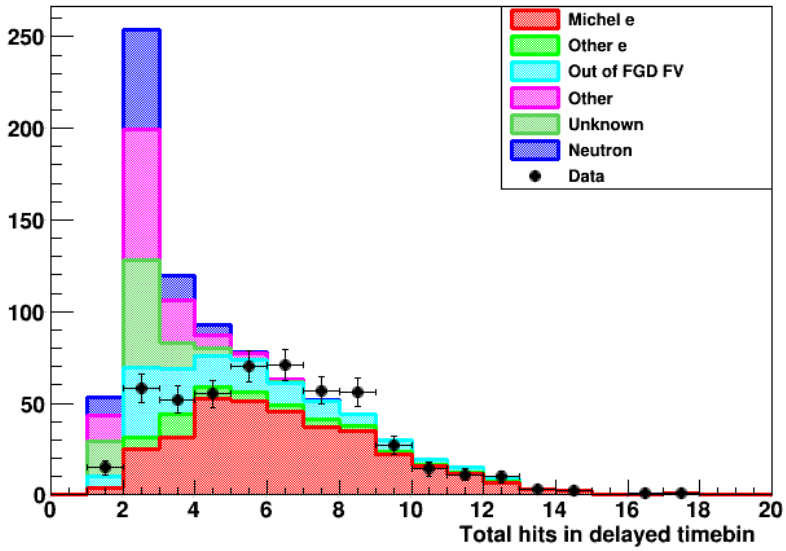

(b) FGD 2

Figure 4.6: Number of hits seen in out-of-bunch timebins for selected CC Inclusive events. Plots show the breakdown by true particle associated with the delayed time bin. Plots are normalized to data POT, and were created for a subset of the run 4 data.

Forward Horn Current Multipion Selection Results

The selected momentum and $\cos\theta$ distributions for the data and nominal MC are shown in Figs. 4.7, 4.8, 4.9 and 4.10; the "No Truth" category indicates cases where there was no specific truth information associated with the selected vertex. Overall purities and efficiencies for each sample in the respective signal topology are shown in Table 4.9. Of the three samples, the CC-0π sample has a significantly higher efficiency than the others. This is due in part to the fact that failure to correctly tag the non-CC-0π events will place those events in other samples even when selected as CC Inclusive. As the efficiency is calculated on a per-sample basis for the multipion selection, this can lower the efficiency for those samples. As CC-0π events are less likely to be misidentified, this has less impact on that sample's overall efficiency. The efficiencies and purities for each sample are roughly similar for FGD 1 and FGD 2, with the exception of CC-1π. This sample has a lower efficiency in FGD 2 due to the reduced active volume, which lowers the efficacy of FGD-only reconstruction and the Michel electron cut.

Sample	Efficiency	Purity
FGD1 ν_μ CC0π (ν mode)	47.61	70.4
FGD1 ν_μ CC1π (ν mode)	27.5	54.1
FGD1 ν_μ CC Other (ν mode)	27.61	72.9
FGD2 ν_μ CC0π (ν mode)	48.45	67.4
FGD2 ν_μ CC1π (ν mode)	23.69	53.5
FGD2 ν_μ CC Other (ν mode)	28.23	72.8

Table 4.9: Efficiencies and purities for the FHC CC-0π, CC-1π and CC-Other samples for both FGDs[81].Efficiencies shown are with respect to the total number of generated true events with that topology.

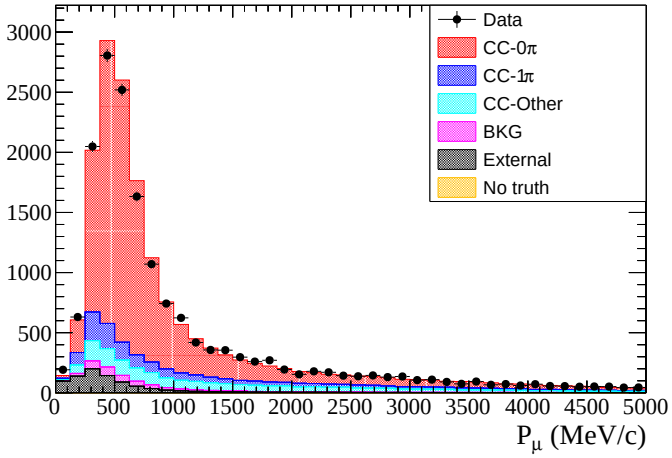

(a) FGD 1 CC-0π selection.

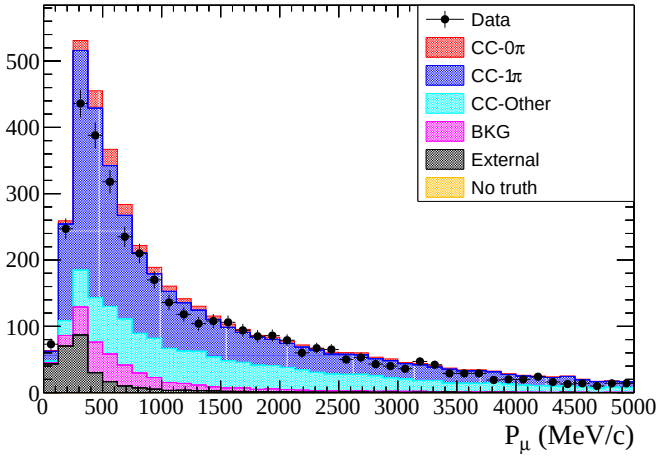

(b) FGD 1 CC-1π selection.

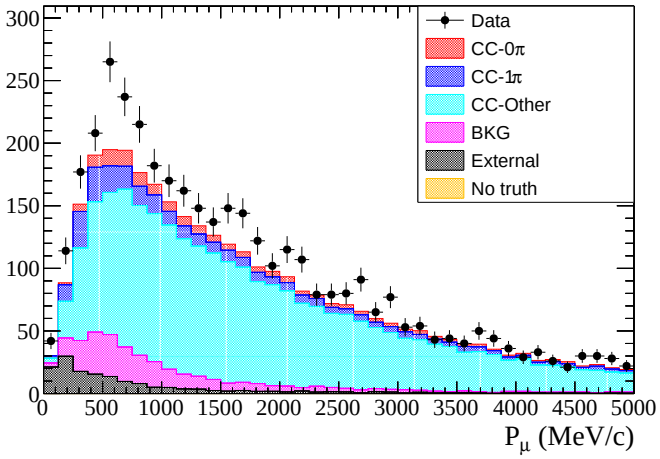

(c) FGD 1 CC-Other selection.

Figure 4.7: Momentum distributions for each of the three FHC samples broken down by true topology for FGD 1[81]. Distributions shown use the T2K Monte Carlo before the ND280 fit tuning. The "No Truth" category indicates cases where there was no specific truth information associated with the selected vertex.

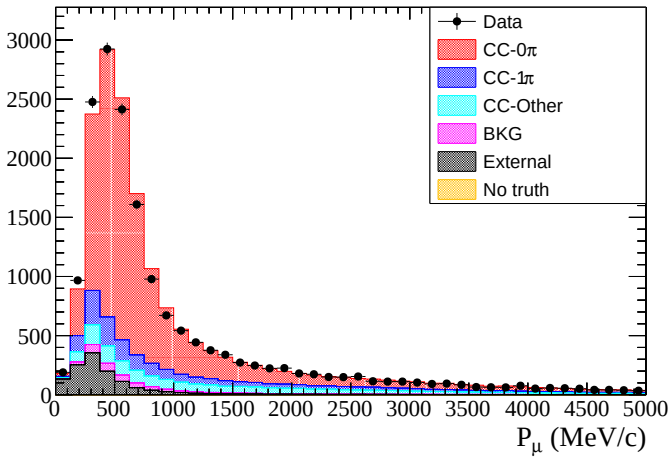

(a) FGD 2 CC-0π selection.

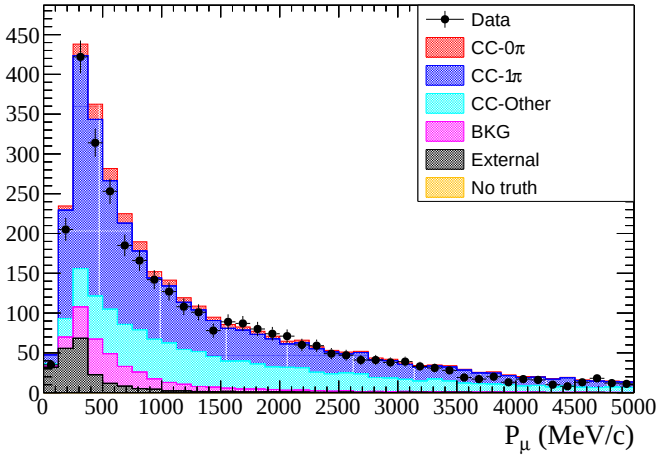

(b) FGD 2 CC-1π selection.

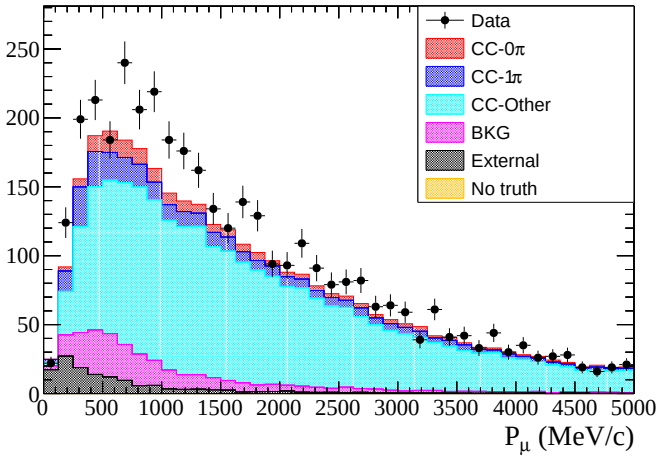

(c) FGD 2 CC-Other selection.

Figure 4.8: Momentum distributions for each of the three FHC samples broken down by true topology for FGD 2. Distributions shown use the T2K Monte Carlo before the ND280 fit tuning.

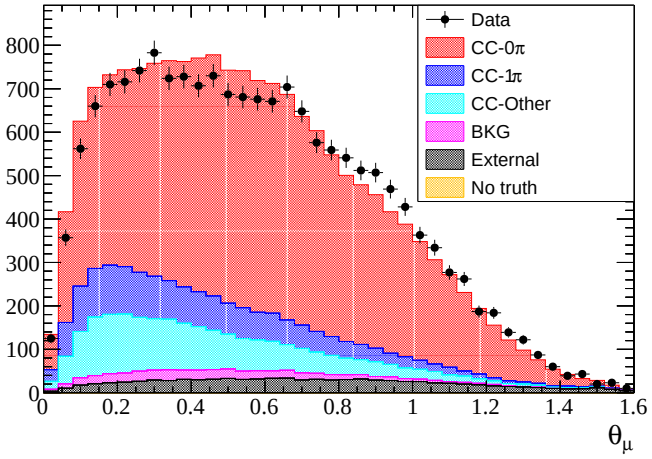

(a) FGD 1 CC-0π selection.

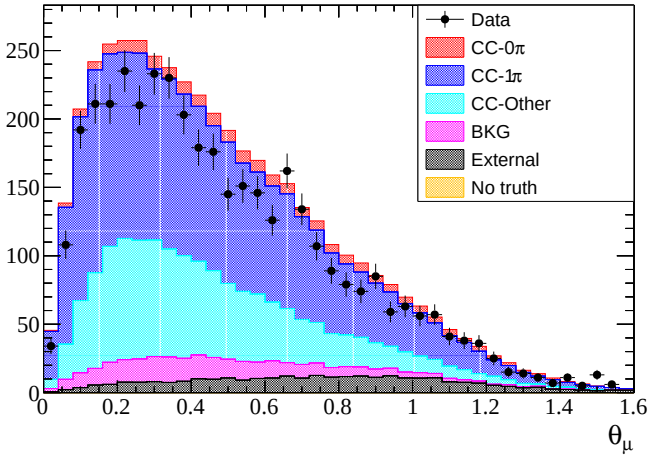

(b) FGD 1 CC-1π selection.

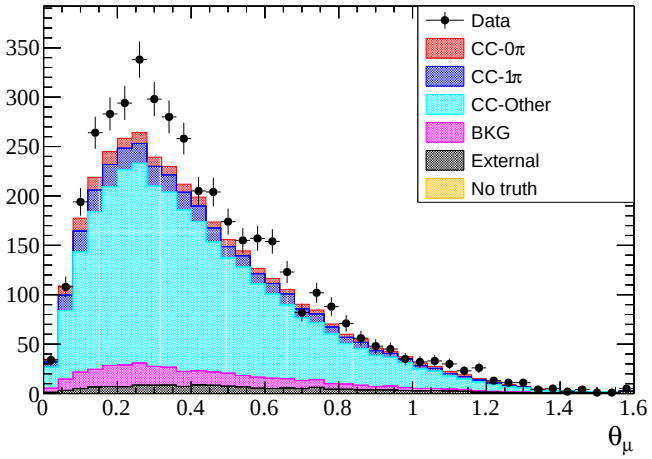

(c) FGD 1 CC-Other selection.

Figure 4.9: $\cos\theta$ distributions for each of the three FHC samples broken down by true topology for FGD 1[81]. Distributions shown use the T2K Monte Carlo before the ND280 fit tuning.

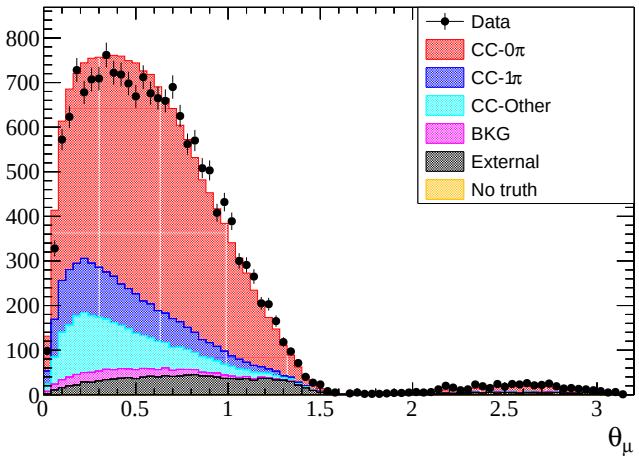

(a) FGD 2 CC-0π selection.

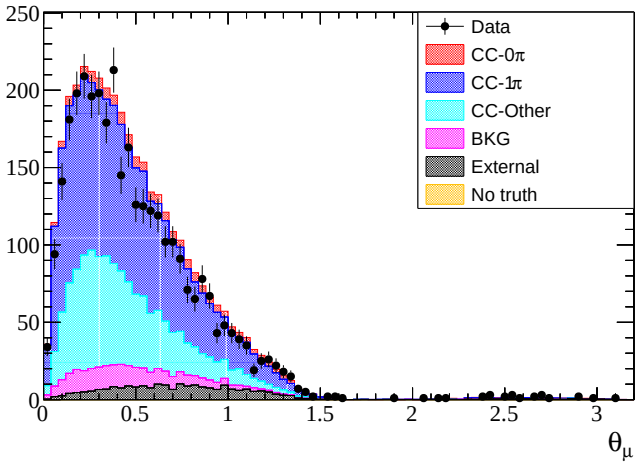

(b) FGD 2 CC-1π selection.

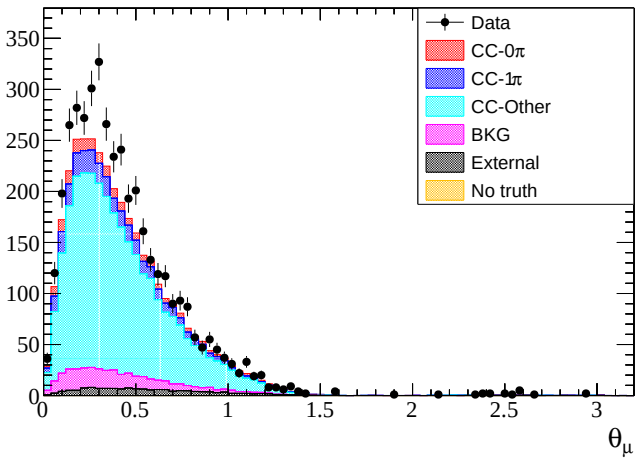

(c) FGD 2 CC-Other selection.

Figure 4.10: $\cos\theta$ distributions for each of the three FHC samples broken down by true topology for FGD 2[81]. Distributions shown use the T2K Monte Carlo before the ND280 fit tuning.

4.5.4 Reverse Horn Current Antineutrino Charged Current Inclusive Selection

The antineutrino CC Inclusive selection starts with the same initial quality cuts as the FHC samples, and is used to identify the signal $\bar{\nu}_\mu$ interactions in the FGDs when operating in antineutrino beam mode. The main difference in the $\bar{\nu}_\mu$ preselection from the cuts described in Section 4.5.2 is that where the ν_μ selection looks for a μ^-, antineutrino interactions will produce μ^+. So instead of requiring the highest momentum track in the event to be negative, the $\bar{\nu}_\mu$ selection requires the highest momentum track to have a positive charge.

In addition, the μ PID cut is slightly different: the selection still checks for a muon candidate, but requires stricter PID pull cuts on the highest momentum positive track in the event. The bounds on the pulls are :

$$\frac{L_\mu + L_\pi}{1 - L_p} > 0.9 \tag{4.8}$$

if $p < 500$ MeV and

$$0.1 < L_\mu < 0.7 \tag{4.9}$$

for all candidate tracks. The upper bound on L_μ serves to remove misidentified low energy μ^- tracks to reduce the ν_μ contamination, as these are frequently reconstructed with the wrong charge. As the $\bar{\nu}_\mu$ fraction in the FHC beam flux is insignificant, this upper limit is not required for the FHC selections.

Reverse Horn Current Antineutrino Charged Current Inclusive Results

The CC Inclusive antineutrino selection has an overall purity of 81.3% in FGD 1 and 80.7% in FGD 2, with topology breakdown shown in Table 4.10, and momentum and $\cos\theta$ distributions shown in Appendix B. FGD 2 has a higher overall efficiency than FGD 1 due to the ability to select backwards-going events in FGD 2, as mentioned in Section 4.5.2. The lower overall purity of the RHC $\bar{\nu}_\mu$ selections compared to the FHC ν_μ CC Inclusive events is due to

background contamination by wrong-sign ν_μ events. As the FHC beam flux does not have a significant fraction of $\bar{\nu}$, this effect is much smaller.

Event topology	FGD 1	FGD 2
CC-0π	59.7%	59.7%
CC-Multiple π	21.6%	21.0%
ν_μ Background	10.6%	11.0%
Other In-FV Background	1.9%	2.2%
Out of FGD FV Background	6.2%	6.1%

Table 4.10: Fractional breakdown of the RHC $\bar{\nu}_\mu$ CC-Inclusive sample by true topology for both FGD 1 and FGD 2[83].

4.5.5 Reverse Horn Current Antineutrino Charged Current Multitrack Selection

Although the CC Inclusive selection for antineutrino events is similar to the CC Inclusive selection for FHC neutrino events, the CC Multitrack selection for RHC $\bar{\nu}_\mu$ does not split events into the CC-0π, CC-1π and CC Other samples. Instead, a simpler set of cuts are used to sort events into two topological samples:

- The CC 1-Track Sample: This sample is characterized by no observed secondary pions or other particles; this is considered a CCQE-enhanced sample. It contains no secondary FGD-TPC matched tracks, but may contain events with short FGD-only tracks or with delayed Michel electrons leading to reduced purity compared to the CC-0π sample in FHC.

- The CC N-Tracks Sample: This sample is characterized by events containing observed secondary particles; unlike the CC-1π and CC-Other samples from the FHC selection, it does not contain any events where there are FGD-only tracks, but no secondary FGD-TPC tracks. For this reason this is considered to be a charged-current non-quasielastic-enhanced sample, where the fraction of non-quasielastic events is increased..

The single track selection for $\bar{\nu}_\mu$ is similar to the CC-0π selection for the FHC ν_μ, and is designed to primarily select CC-0π events. However, due to the difficulty of reconstructing the

short range π^-, this sample imposes a single additional cut on top of the CC Inclusive selection. For an antineutrino event to be considered a 1-Track event, there must only be a single TPC-FGD matched track. In addition, all TPC-FGD matched tracks are counted as secondary tracks, as there is no additional PID requirements. As the μ^+ candidate is a TPC-FGD matched track, this effectively requires that there are no secondary tracks that reach the TPCs for an event to be in the CC 1-Track sample.

Unlike the FHC selection, there are no cuts on FGD-only track multiplicity, as it is more difficult to reconstruct the contained secondary tracks due to low energy. When low energy π^- are produced from $\bar{\nu}_\mu$ interactions, they are quickly absorbed and therefore are not easily reconstructed. As non-CC-0π events with Michel electrons or other short-range secondary particles are not separated out, this is therefore considered to be a CCQE-enhanced sample.

The multi-track sample for RHC $\bar{\nu}_\mu$ contains all selected charged current $\bar{\nu}_\mu$ events that do not pass the 1-Track cut. When using in the ND280 fit, each sample has 20 $p-\theta$ bins in total:

- RHC 1-track sample bin edges for the fit:
  p (MeV/c) : 0, 500, 900, 1200, 2000, 10000
  $\cos\theta$: -1.0, 0.8, 0.92, 0.98, 1

and

- RHC N-tracks sample bin edges for the fit:
  p (MeV/c) : 0, 600, 1000, 1500, 2200, 10000
  $\cos\theta$: -1.0, 0.8, 0.9, 0.97, 1

As with the FHC samples, the FGD 1 and FGD 2 selections use the same binning.

Results

The overall efficiencies for the RHC $\bar{\nu}_\mu$ samples are shown in Table 4.11, along with the RHC ν_μ efficiencies. The efficiencies are similar to those for the FHC samples, taking CC-1π and CC-Other together. As these samples are used to understand the overall composition of the

RHC flux at SK, it is useful to know the fraction of ν_μ contamination in each sample, shown in Tables 4.12 and 4.13. These tables also show the overall purities for the samples, and as no $\bar{\nu}_\mu$ cuts depend on FGD-only tracks, the purities for FGD 1 and FGD 2 are similar for both the 1-track and multitrack samples. The CC 1-Track sample has low wrong-sign ν_μ contamination in both FGDs, while around 1/3 of the $\bar{\nu}_\mu$ CC N-Track sample is comprised of background ν_μ events. This results in a much lower purity for the CC N-Tracks sample. The selected momentum and θ distributions for the data and nominal MC are shown in Figs. 4.11, 4.12, 4.13 and 4.14.

	RHC $\bar{\nu}_\mu$		RHC ν_μ	
Selection	FGD 1	FGD 2	FGD 1	FGD 2
CC 1-Track	66%	68%	46.3%	46.4%
CC N-Tracks	29%	31%	36.5%	36.7%

Table 4.11: Efficiencies for the RHC samples for both FGD 1 and FGD 2[83] [84]

Event topology	FGD 1	FGD 2
CC-0π	74.4%	74.5%
CC-Multiple π	14.5%	13.8%
ν_μ Background	4.1%	4.2%
Other In-FV Background	1.3%	1.4%
Out of FGD FV Background	5.7%	6.1%

Table 4.12: Fractional breakdown of the RHC $\bar{\nu}_\mu$ CC-1 Track sample by true topology for both FGD 1 and FGD 2[83]. Distributions shown use the T2K Monte Carlo before the ND280 fit tuning.

Event topology	FGD 1	FGD 2
CC-0π	8.8%	9.4%
CC-Multiple π	46.4%	45.6%
ν_μ Background	32.9%	34.4%
Other In-FV Background	4.1%	4.4%
Out of FGD FV Background	7.9%	6.2%

Table 4.13: Fractional breakdown of the RHC $\bar{\nu}_\mu$ CC-N tracks sample by true topology for both FGD 1 and FGD 2[83]. Distributions shown use the T2K Monte Carlo before the ND280 fit tuning.

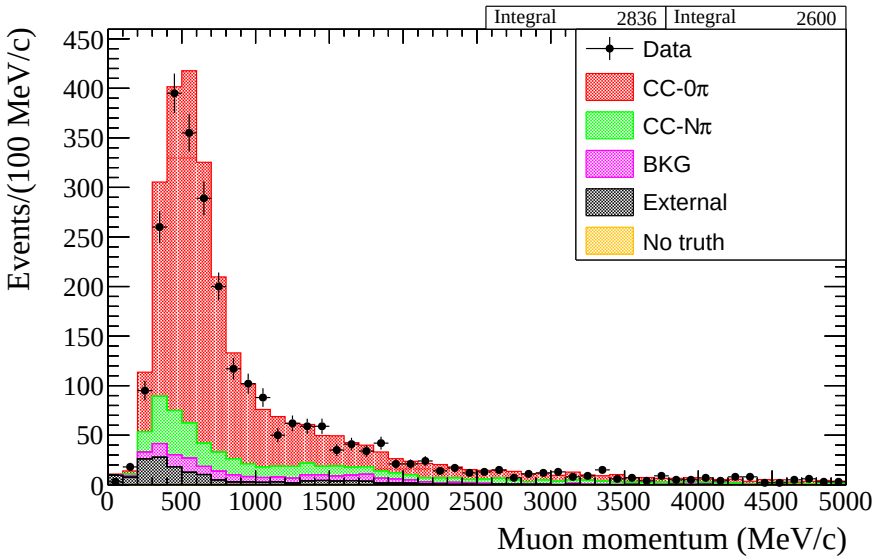

(a) Momentum distribution

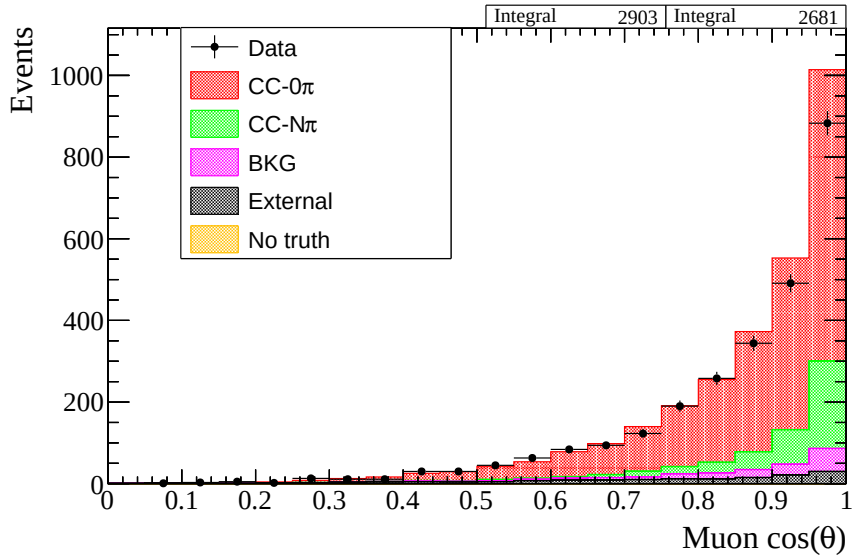

(b) $\cos\theta_\mu$ distribution

Figure 4.11: Momentum and $\cos\theta_\mu$ distributions for data and Monte Carlo, broken down by true topology, for the FGD 1 RHC $\bar{\nu}_\mu$ CC 1 Track selection[83]. Distributions shown use the T2K Monte Carlo before the ND280 fit tuning. The "No Truth" category indicates cases where there was no specific truth information associated with the selected vertex.

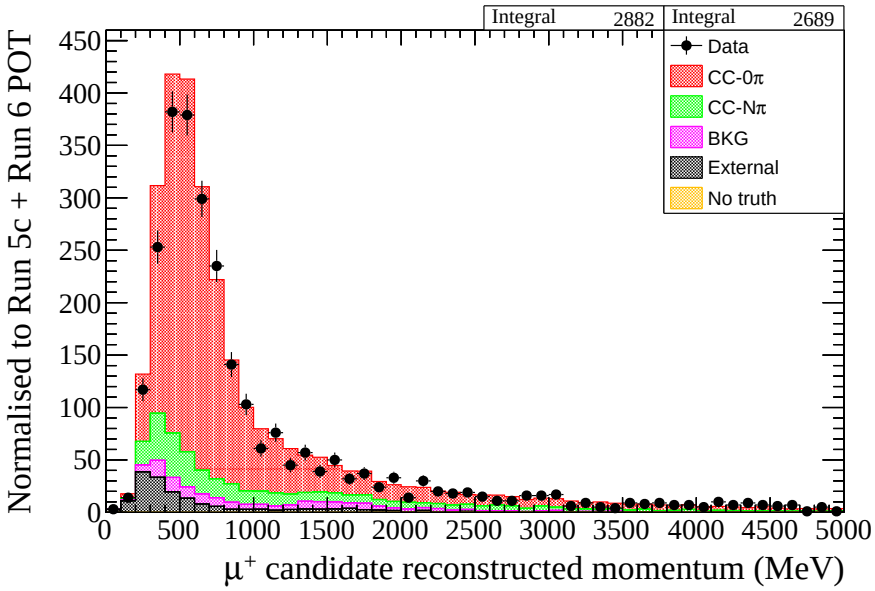

(a) Momentum distribution

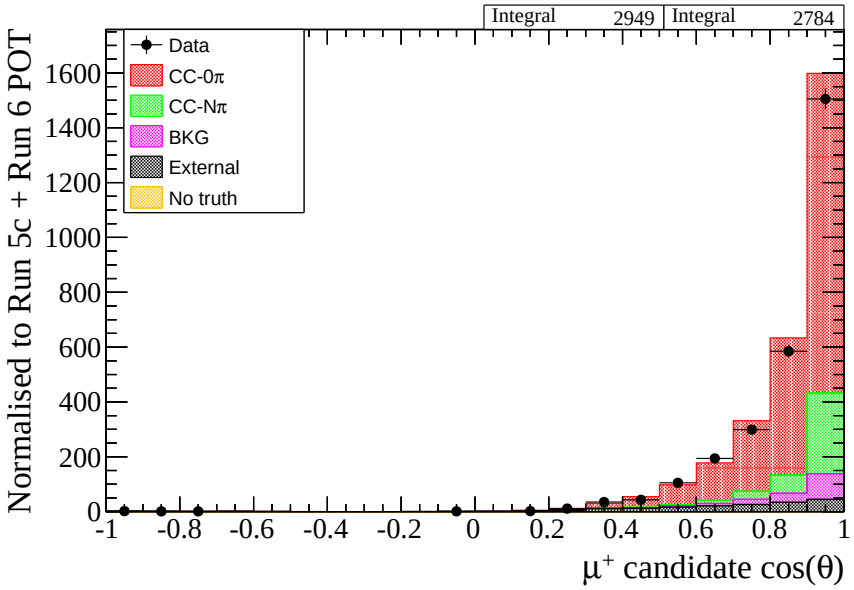

(b) $\cos\theta_\mu$ distribution

Figure 4.12: Momentum and $\cos\theta_\mu$ distributions for data and Monte Carlo, broken down by true topology, for the FGD 2 RHC $\bar{\nu}_\mu$ CC 1-Track selection[83]. Distributions shown use the T2K Monte Carlo before the ND280 fit tuning. The "No Truth" category indicates cases where there was no specific truth information associated with the selected vertex.

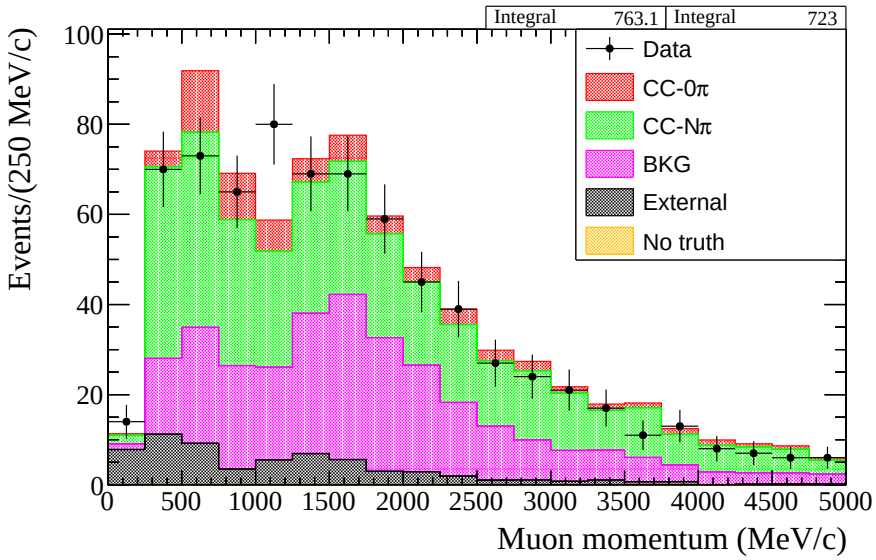

(a) Momentum distribution

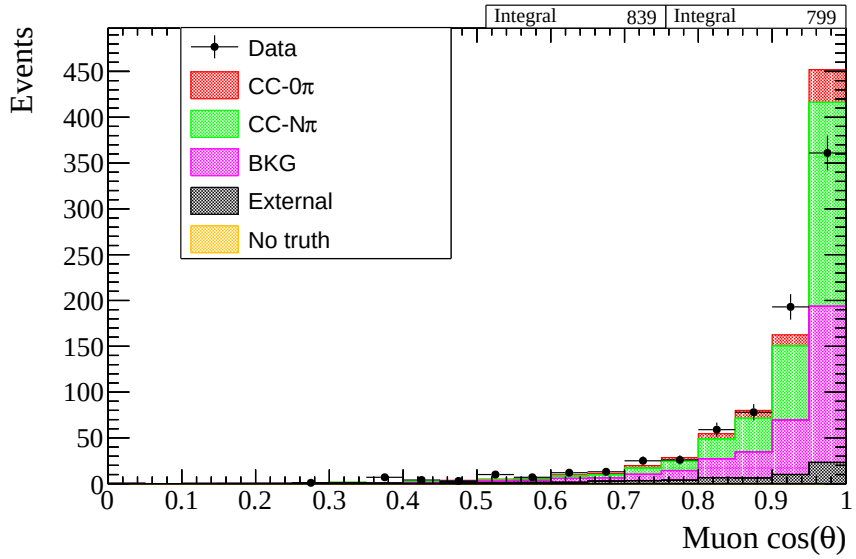

(b) $\cos\theta_\mu$ distribution

Figure 4.13: Momentum and $\cos\theta_\mu$ distributions for data and Monte Carlo, broken down by true topology, for the FGD 1 RHC $\bar{\nu}_\mu$ CC N-Track selection[83]. Distributions shown use the T2K Monte Carlo before the ND280 fit tuning. The "No Truth" category indicates cases where there was no specific truth information associated with the selected vertex.

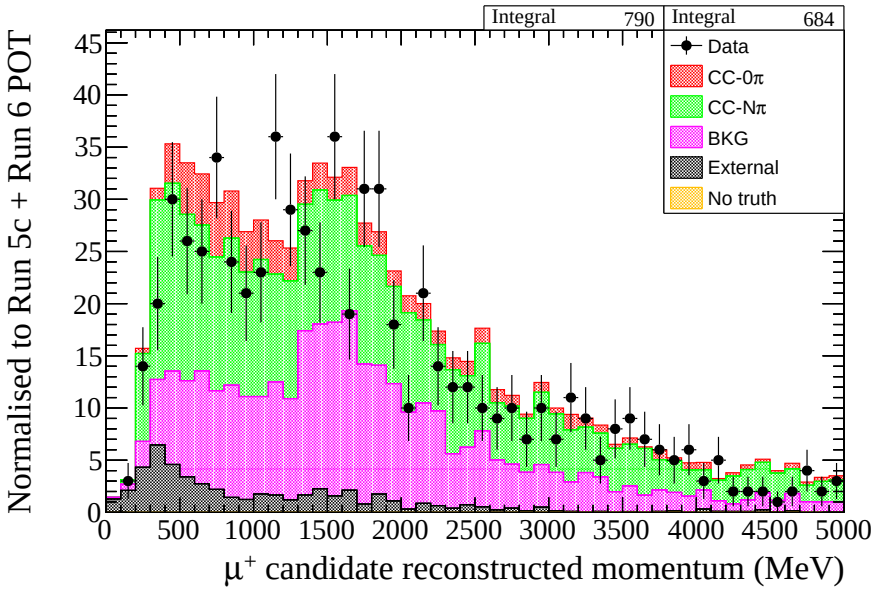

(a) Momentum distribution

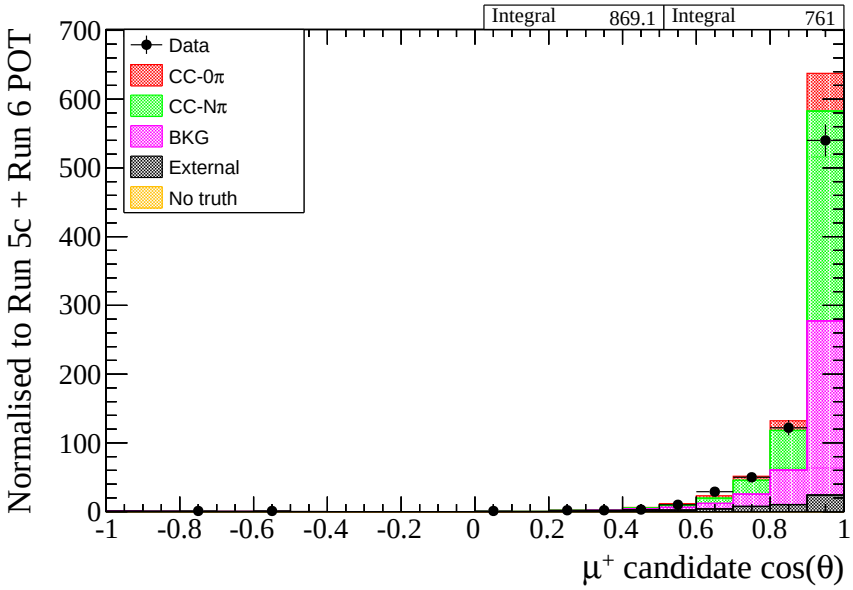

(b) $\cos\theta_\mu$ distribution

Figure 4.14: Momentum and $\cos\theta_\mu$ distributions for data and Monte Carlo, broken down by true topology, for the FGD 2 RHC $\bar{\nu}_\mu$ CC N-Track selection[83]. Distributions shown use the T2K Monte Carlo before the ND280 fit tuning. The "No Truth" category indicates cases where there was no specific truth information associated with the selected vertex.

4.5.6 Wrong Sign in Reverse Horn Current Charged Current Inclusive Selection

As with the previously described CC Inclusive selections, the ν_μ in $\bar{\nu}_\mu$ mode CC Inclusive selection requires the basic quality cuts. In order to reduce the effect of systematics on understanding the ν_μ contamination in the $\bar{\nu}_\mu$ beam, the wrong-sign selection uses mostly the same cuts as the antineutrino mode $\bar{\nu}_\mu$ selections, described in the previous subsection, but with the main muon track required to be negative as in the FHC selection. In addition, the muon PID cut now requires:

$$\frac{L_\mu + L_\pi}{1 - L_p} > 0.7 \tag{4.10}$$

for tracks with $p_\mu < 500$ MeV/c. This is to reduce the fraction of background e^- in the overall selection. The threshold is set slightly lower than the FHC selection, in order to avoid cutting out signal events. In addition, rather than requiring the condition in Eqn. 4.5 a more strict cut on the muon PID pull is used:

$$0.1 < L_\mu < 0.8 \tag{4.11}$$

This helps reject both protons and low energy μ^+ from antineutrino interactions that are reconstructed with the incorrect charge, similar to the cuts used for the $\bar{\nu}_\mu$ selection.

Results

This gives an efficiency of 55.17% in FGD 1 and 54.6% in FGD 2 for CC Inclusive ν_μ events. As with the RHC $\bar{\nu}_\mu$ and FHC ν_μ CC Inclusive selections, FGD 1 and FGD 2 select roughly the same number of events. The CC Inclusive wrong-sign ν_μ selection has a purity of 80.0% for FGD 1 and a purity of 79.2% for FGD 2. This is lower than the purities seen for the FHC ν_μ CC Inclusive sample and similar to the purities for the RHC $\bar{\nu}_\mu$ CC Inclusive selection. This comes from the increased $\bar{\nu}_\mu$ backgrounds compared to the FHC selection, with FGD 1 having a 10.6% $\bar{\nu}_\mu$ background and FGD 2 11.0%. As with the FHC selections, FGD 2 has a larger backwards-going component due to inter-FGD timing. Momentum and angle distributions for the RHC ν_μ selection are shown in AppendixB.

Event topology	FGD 1	FGD 2
CC-0π	33.0%	32.3%
CC-Multiple π	47.0%	45.8%
$\bar{\nu}_\mu$ Background	7.3%	8.5%
Other In-FV Background	3.7%	3.2%
Out of FGD FV Background	9.0%	10.2%

Table 4.14: Fractional breakdown of the RHC ν_μ CC-Inclusive sample by true topology for both FGD 1 and FGD 2[84].

4.5.7 Wrong Sign in Reverse Horn Current Charged Current Multitrack Selection

The wrong sign ν_μ events are split into two different track-multiplicity samples. The basic sample definition is the same as the samples used for the RHC $\bar{\nu}_\mu$ CC Inclusive events, but for events with a highest-momentum negative muon track.

- The CC 1-Track Sample: This sample is characterized by no observed secondary pions or other particles; this is considered a CCQE-enhanced sample. It contains no secondary FGD-TPC matched tracks, but may contain events with short FGD-only tracks or with delayed Michel electrons leading to reduced purity compared to the CC-0π sample in FHC.

- The CC N-Tracks Sample: This sample is characterized by events with observed secondary particles; unlike the CC-1π and CC-Other samples from the FHC selection, it does not contain any events where there are FGD-only tracks, but no secondary FGD-TPC track. For this reason this is considered to be a CCnQE-enhanced sample.

Both the sample definitions and the cuts used in distinguishing the samples are analogous to the cuts and definitions for RHC $\bar{\nu}_\mu$ events.

The RHC ν_μ 1-Track selection uses the same separation criteria as the $\bar{\nu}_\mu$ selection. This is intended to reduce the overall effects of the systematic errors on the fit predictions, as the ν_μ – $\bar{\nu}_\mu$ separation in the near detector is important for the antineutrino oscillation studies at SK.

Therefore this sample is defined as all selected CC Inclusive ν_μ events with a single TPC-FGD matched track and no requirements on FGD-contained secondary tracks.

The RHC ν_μ multi-track sample contains all selected RHC ν_μ CC Inclusive events that do not pass the track multiplicity cut for the 1-Track sample. These events all have at least two FGD-TPC matched tracks.

When using in the ND280 fit, each RHC ν_μ sample has 20 $p - \theta$ bins in total, and the binning is identical to the RHC $\bar{\nu}_\mu$ samples:

- RHC 1-track sample bin edges for the fit:
  p (MeV/c) : 0, 500, 900, 1200, 2000, 10000
  $\cos\theta$: -1.0, 0.8, 0.92, 0.98, 1

and

- RHC N-tracks sample bin edges for the fit:
  p (MeV/c) : 0, 600, 1000, 1500, 2200, 10000
  $\cos\theta$: -1.0, 0.8, 0.9, 0.97, 1

As with the FHC samples and the RHC $\bar{\nu}_\mu$ samples, the FGD 1 and FGD 2 selections use the same binning.

Results

Efficiencies for both samples are shown in Table 4.11 and purities in Tables 4.15 and 4.16. The CC-1 Track sample has a similar number of events selected to the CC-Multi Track sample for RHC ν_μ, unlike the RHC $\bar{\nu}_\mu$ 1-Track and the FHC ν_μ CC-0π samples which both select significantly more events than the other samples. The purity of the N-Tracks sample is higher for the RHC ν_μ selection than the RHC $\bar{\nu}_\mu$ CC N-Track sample due to higher energy secondary particles from the neutrino interactions being able to enter the TPCs. The selected momentum and $\cos\theta$ distributions for the data and nominal MC are shown in Figs. 4.15, 4.16, 4.17 and 4.18.

Event topology	FGD 1	FGD 2
CC-0π	50.5%	49.1%
CC-Multiple π	27.7%	26.2%
$\bar{\nu}_\mu$ Background	6.6%	7.4%
Other In-FV Background	2.9%	2.7%
Out of FGD FV Background	12.3%	14.6%

Table 4.15: Fractional breakdown of the RHC ν_μ CC-1 Track sample by true topology for both FGD 1 and FGD 2[84]

Event topology	FGD 1	FGD 2
CC-0π	15.3%	14.3%
CC-Multiple π	66.1%	67.0%
$\bar{\nu}_\mu$ Background	8.1%	8.6%
Other In-FV Background	4.4%	4.7%
Out of FGD FV Background	6.1%	5.4%

Table 4.16: Fractional breakdown of the RHC ν_μ CC-N tracks sample by true topology for both FGD 1 and FGD 2[84]

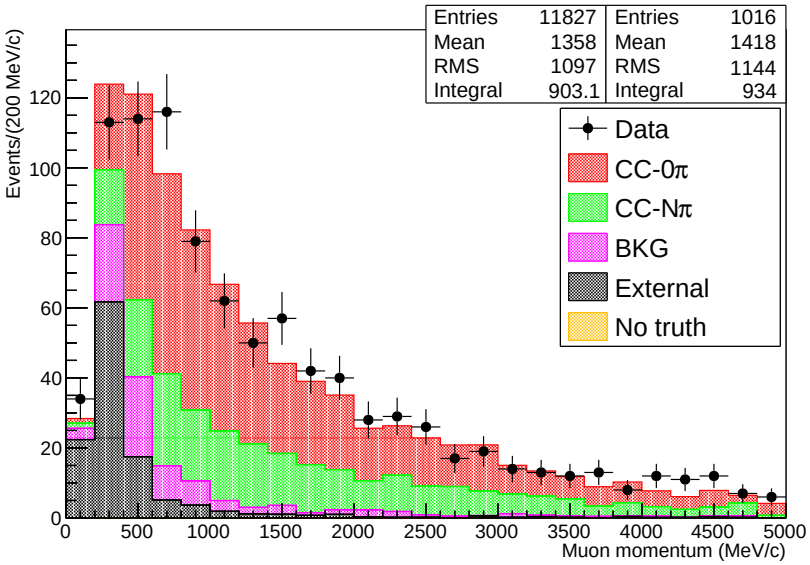

(a) Momentum distribution

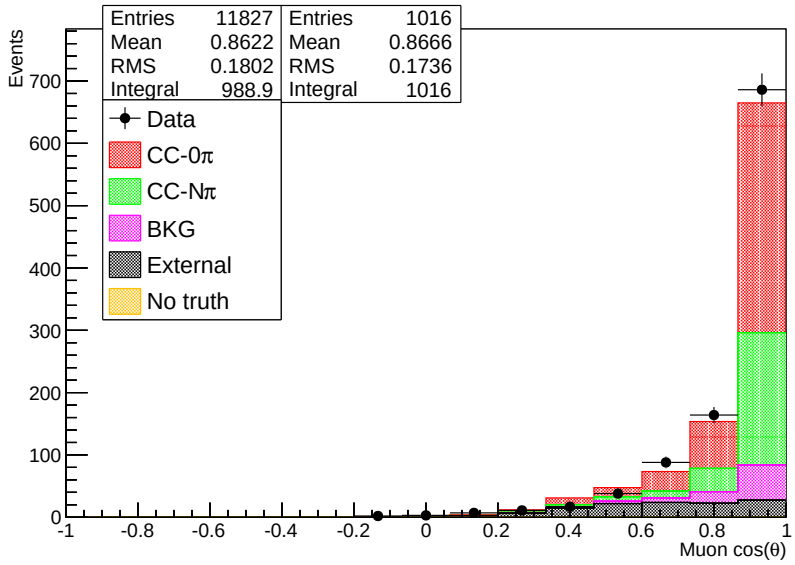

(b) $\cos\theta_\mu$ distribution

Figure 4.15: Momentum and $\cos\theta_\mu$ distributions for data and Monte Carlo, broken down by true topology, for the FGD 1 RHC ν_μ CC 1-Track selection[84]. Distributions shown use the T2K Monte Carlo before the ND280 fit tuning. The "No Truth" category indicates cases where there was no specific truth information associated with the selected vertex.

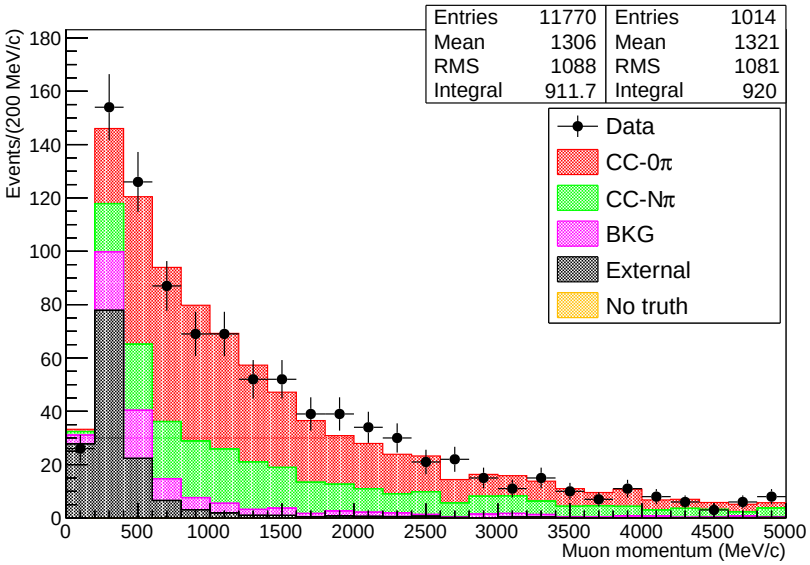

(a) Momentum distribution

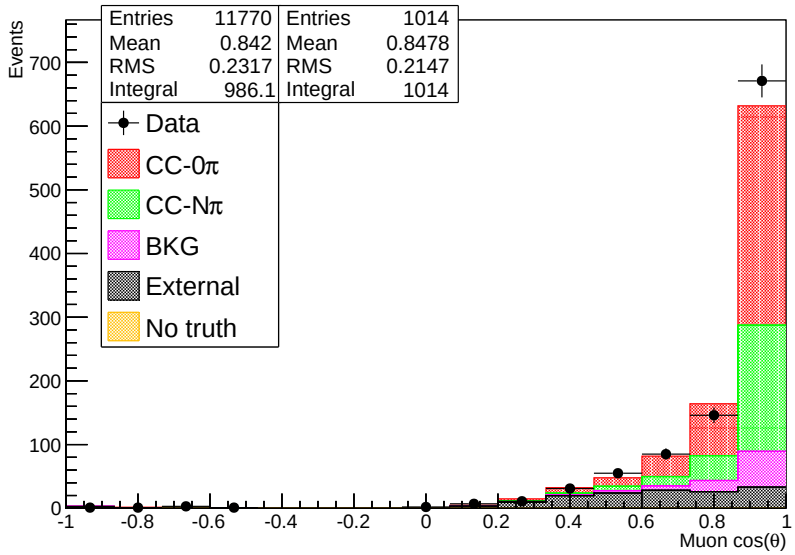

(b) $\cos\theta_\mu$ distribution

Figure 4.16: Momentum and $\cos\theta_\mu$ distributions for data and Monte Carlo, broken down by true topology, for the FGD 2 RHC ν_μ CC 1-Track selection[84]. Distributions shown use the T2K Monte Carlo before the ND280 fit tuning. The "No Truth" category indicates cases where there was no specific truth information associated with the selected vertex.

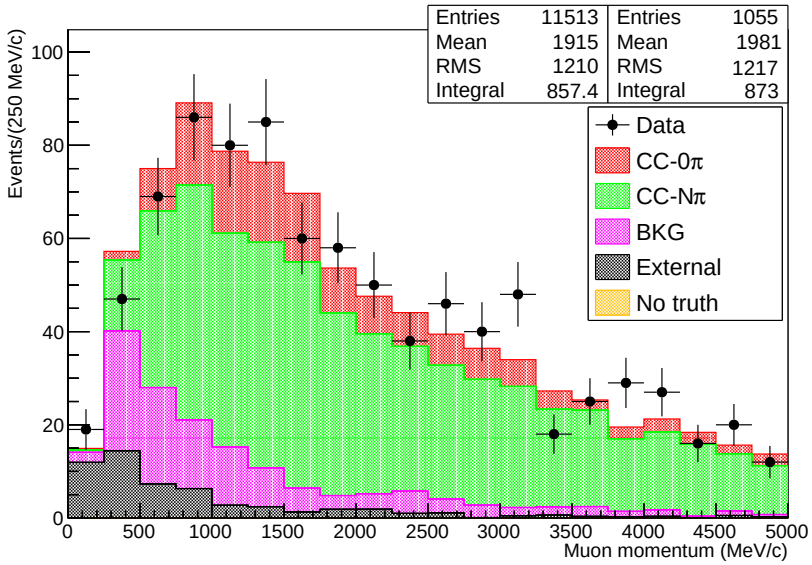

(a) Momentum distribution

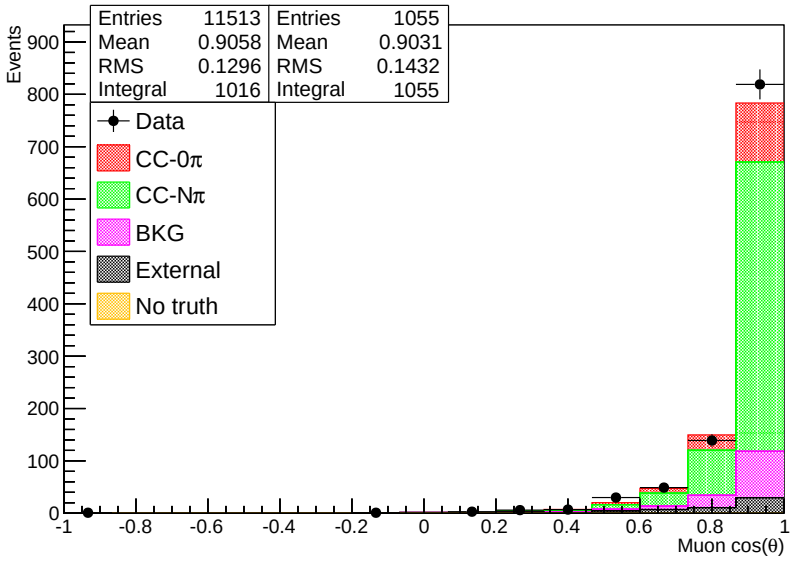

(b) $\cos\theta_\mu$ distribution

Figure 4.17: Momentum and $\cos\theta_\mu$ distributions for data and Monte Carlo, broken down by true topology, for the FGD 1 RHC ν_μ CC N-Track selection[84]. Distributions shown use the T2K Monte Carlo before the ND280 fit tuning. The "No Truth" category indicates cases where there was no specific truth information associated with the selected vertex.

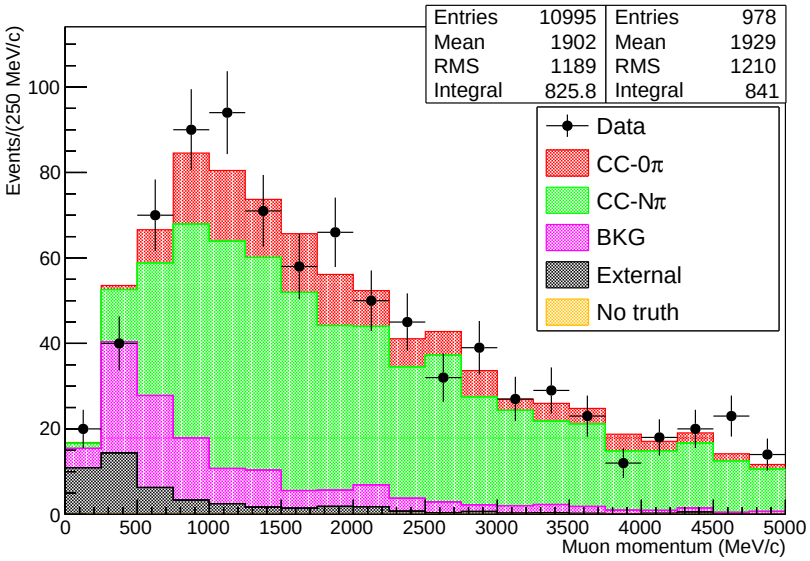

(a) Momentum distribution

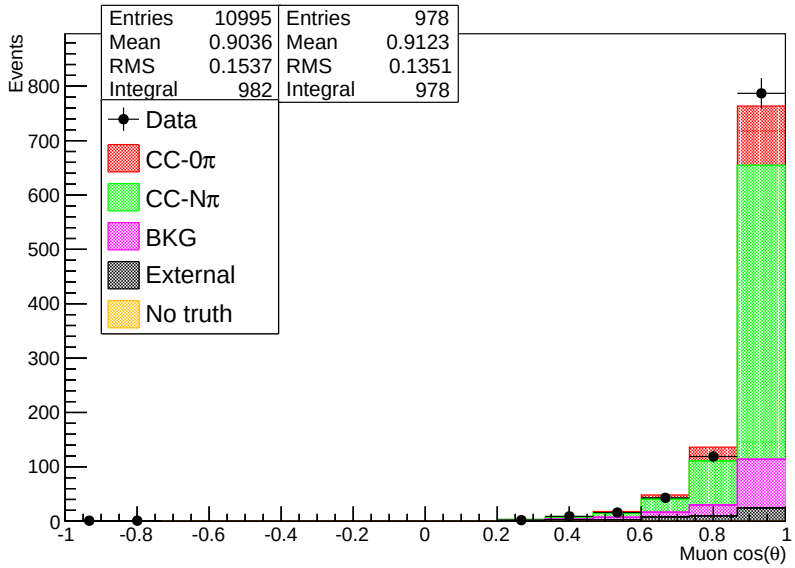

(b) $\cos\theta_\mu$ distribution

Figure 4.18: Momentum and $\cos\theta_\mu$ distributions for data and Monte Carlo, broken down by true topology, for the FGD 2 RHC ν_μ CC N-Track selection[84]. Distributions shown use the T2K Monte Carlo before the ND280 fit tuning. The "No Truth" category indicates cases where there was no specific truth information associated with the selected vertex.

Chapter 5

Systematics and Systematic Correlations

5.1 Overview of ND280 Detector Systematics

The uncertainty on the ND280 reconstruction and selected events comes from various underlying uncertainties on the properties of the near detector and the reconstruction methods used. These come from the various underlying physical properties of the detectors and are calculated as effective systematic effects on the Monte Carlo. These are generally characterized as the difference between the data and Monte Carlo simulation, such as the uncertainty in the measured target mass of the FGDs versus the implementation in Monte Carlo. These systematic uncertainties are used to produce the observable normalization weights and covariance matrix described in Chapter 3 and are a key part of constraining the cross section parameters with the near detector fit. This includes both the systematic uncertainties and associated corrections to the Monte Carlo.

While there are many different potential sources of uncertainty at the near detectors, the relevant detector systematics are those that relate to the event selections described in Chapter 4. The majority of the identified systematic effects apply to both the FHC and RHC samples, with the only exceptions being effects specific to the FHC ν_μ multipion selection due to using more cuts to define samples. Each systematic effect was identified and studied by various T2K collaborators for this analysis. In addition, a first estimation of the correlations between the

systematic uncertainties of the FGD 1 and FGD 2 selections was made based on knowledge of the physical sources for the systematic uncertainties. These correlations and detector systematic uncertainties were then used to generate the observable normalization parameter weights and covariance matrix used in the near detector fit.

5.1.1 List of Systematics

At ND280, the detector systematic uncertainties are implemented as two different types: variation detector systematics, which vary reconstructed quantities in events, and weight systematics, which apply a weight to each event without modifying the event itself, such as in the case of a detector efficiency. There are six variation systematics and eleven weight systematics. Within each category, there are different methods for applying systematics to events. The systematics related to tracks or other measured quantities in the FGDs, such as Michel electron efficiency and FGD Particle identification, are implemented to allow for separate systematic calculations for FGD 1 and FGD 2 where necessary. Table 5.1 lists these systematics, the type of systematic and the probability density function used for each systematic. Systematic uncertainty calculations and propagation are done using the Psyche software, described in Section 4.4.1.

5.1.2 Variation Systematics

Variation systematics are those detector systematics that can allow a selected event to migrate between different selected samples, or in rare cases in and out of the overall inclusive selection. These systematics modify reconstructed quantities such as track momentum and particle ID pulls, which can potentially change the highest momentum track in an event. When a variation systematic is applied, the relevant reconstructed observables are smeared and the event selection is rerun on the modified event. This smearing is implemented differently depending on the specifics of the systematic for each parameter. There are two main ways variation systematic parameters are applied at ND280 :

1. When the true observable for the systematic is known, the difference between the recon-

Systematic Source	Type	PDF
TPC Systematics		
Magnetic Field Distribution	Variation	Uniform
TPC Momentum Resolution	Variation	Gaussian
TPC Momentum Scaling	Variation	Gaussian
TPC Particle Identification	Variation	Gaussian
TPC Cluster Efficiency	Weight	Gaussian
TPC Track Reconstruction	Weight	Gaussian
Charge Confusion	Weight	Gaussian
FGD Reconstruction		
TPC – FGD Matching	Weight	Gaussian
FGD Particle Identification	Variation	Gaussian
Particle Time of Flight	Variation	Gaussian
FGD Hybrid Track Reconstruction	Weight	Gaussian
Michel Electron Detection	Weight	Gaussian
Selection Background		
Out of Fiducial Volume Events	Weight	Gaussian
Sand Muon Events	Weight	Gaussian
Event Pile-Up	Weight	Gaussian
Monte Carlo Modeling		
Pion Secondary Interactions	Weight	Gaussian
FGD Mass	Weight	Gaussian

Table 5.1: List of near detector systematic error sources and types for the T2K near detector selection.[81]

structed observable and its true value is rescaled as

$$x'_{rec} = x_{true} + (x^{MC}_{rec} - x_{true})(s + \alpha \times \delta s) \tag{5.1}$$

where s is a scale factor, δs its systematic error and α a Gaussian random variable with a mean of 0 and width of 1. Here s will always equal 1, unless there is systematic difference between MC and data.

2. When a correction is applied to the MC observable value using the mean difference between the data and Monte Carlo observable values, $\Delta\bar{x}$, the observable value becomes:

$$x'_{rec} = x^{MC}_{rec} + \Delta\bar{x} + \alpha \times \delta\Delta\bar{x} \tag{5.2}$$

where $\Delta\bar{x}$ is the mean difference between the data and Monte Carlo values for the observable, $\delta\Delta\bar{x}$ the uncertainty on that mean and α a Gaussian random variable with a mean of 0 and width of 1. In this case, the systematic uncertainty on the observable is added separately from the correction as its effect on the number of selected events differs between the nominal Monte Carlo and the corrected Monte Carlo.

The only exception to these are for the systematics derived from the magnetic field maps and are described along with the systematic details.

5.1.3 Weight Systematics

Weight systematics only have an effect on the overall event weight and do not modify any of the reconstructed values for an event. Because of this, they are implemented as weights applied to relevant events and can not cause sample migration for events as underlying reconstructed values do not change. There are two different implementation types for weight systematics: efficiency-like systematics and normalization systematics. Efficiency-like systematics are those that correspond to specific reconstruction or detection probabilities and normalization systematics are those that control overall normalizations for specific subsamples of the selection.

The efficiency-like systematics use studies comparing Monte Carlo predictions with data for well-understood event control samples. This allows an efficiency for data to be calculated as truth information is unnecessary. These control samples are specific subsets of events that fulfill specific requirements so that the feature being studied is well understood. An example of this would be using stopping cosmic events for looking at Michel electron efficiency [82]. These samples can also be constructed from beam triggered events as well. Control samples do not necessarily contain all the features that would be present in the T2K beam analysis, and may cover a more limited phase space. However, the control samples are designed to be sufficiently representative of the selection for use in finding systematic efficiencies [81].

In general, the efficiency on the data without taking control sample systematic error into

account is

$$\varepsilon_{data} = \frac{\varepsilon_{data}^{CS}}{\varepsilon_{MC}^{CS}} \varepsilon_{MC} \tag{5.3}$$

where the CS superscript denotes values calculated from the control samples[81]. As the control sample efficiencies have some statistical error on them, these must also be taken into account. There are two definitions for the individual event weights for the efficiency-like systematics, depending on whether applying an efficiency or inefficiency is appropriate:

$$w_{eff} = \frac{\varepsilon'_{data}}{\varepsilon_{MC}} \tag{5.4}$$

for efficiency[81] and

$$w_{ineff} = \frac{1 - \varepsilon'_{data}}{1 - \varepsilon_{MC}} \tag{5.5}$$

for inefficiency[81], where

$$\varepsilon'_{data} = (r^{CS} + \alpha \times \delta r^{CS}) \varepsilon_{MC} \tag{5.6}$$

where $r^{CS} = \frac{\varepsilon_{data}^{CS}}{\varepsilon_{MC}^{CS}}$ and δr^{CS} is the measured uncertainty on the ratio of the efficiencies measured using the control samples. As with the variation systematics, α is a Gaussian random variable with a mean of 0 and width of 1.

Normalization systematics are related to the overall event normalization and apply to specific subsamples of events. Like the efficiency-like systematics, these are applied as individual weights on each event. This weight is calculated as :

$$w_{event} = 1 + \alpha \times \delta e_{category} \tag{5.7}$$

where α is the random variable for the systematic variations and $\delta e_{category}$ is the systematic error for that category of events. A weight of 1 is applied when events are not part of the systematic category.

5.2 Systematic Correlations

The initial implementation of the detector systematics, and the implementation used in previous near detector fits, assumes there are no correlations between bins within systematics, and was only applied for FGD 1 samples. However, the systematics as implemented for ND280 are effective systematics – they depend on underlying physical quantities that may be shared. As the near detector fit now has been expanded to include FGD 2, a similar but not identical target to FGD 1, it is not immediately obvious how a systematic is correlated between events in FGD 1 and events in FGD 2. For detector systematics this means identifying which systematic parameters apply to measured quantities in the FGDs and how they are correlated between the two detectors. Allowing bins within a defined systematic uncertainty to be correlated with each other is also a new addition to the ND280 analysis and relies on the underlying physical quantities that contribute to the systematic, much like the FGD 1 – FGD 2 correlations. As this is the first implementation of FGD1 – FGD 2 correlations, all systematics are approximated to either be fully correlated ($\rho = 1$), fully anticorrelated ($\rho = -1$) or uncorrelated ($\rho = 0$). For the in-systematic correlations, bins are also assumed to fully correlated ($\rho = 1$), fully anticorrelated ($\rho = -1$) or uncorrelated ($\rho = 0$) with other bins in that systematic.

5.2.1 Correlations Between the Fine Grained Detector 1 and Fine Grained Detector 2 Selections

The CC Inclusive selections described in Chapter 4 are split into mutually exclusive FGD 1 and FGD 2 selections, which both take the various systematic uncertainties into account. As the near detector fit uses FGD 1 to constrain the carbon-specific parameters for FGD 2, understanding how the systematic uncertainties are correlated between the two selections is vital to correctly constraining the oxygen-specific parameters. For now, an understanding of the underlying physical quantities that contribute to a systematic are used as a rationale for choice of correlation; in the future more exact treatments of the underlying parameters and correlations should be done.

The primary concern for the FGD 1 – FGD 2 correlations are the FGD reconstruction systematic uncertainties. While there are correlations between other parts of the tracker volume, such as correlations between the three TPCs for certain systematics, these do not depend on choice of FGD for the target and are therefore considered to be fully correlated between the two selections.

5.3 Systematic Details

5.3.1 B Field Distribution

The magnetic field used in the ND280 reconstruction is taken from mapping data taken at the ND280 detectors [85], performed using Hall probes at the near detector. This mapping allows for magnetic distortions to be accounted for in the reconstruction, as the field is not constant throughout the magnet volume. The field map is applied to the cluster positions at reconstruction to evaluate change in y and z position[86]. In addition, the map validity is tested against the laser calibration system in the TPC, which uses the measured and expected positions of photo-electrons emitted by aluminum dots in the cathode which are illuminated by a laser. This testing is done both when the magnet is off and during normal running for ND280. A second correction to the distortion from these measurements is applied to the cluster positions as a function of drift distance [86].

These corrections were cross checked using the reconstructed momentum in TPC 2 and TPC 3, as TPC 1 is not expected to have large distortions in the B-field. The studies found that adding the initial B-field corrections reduces the relative momentum bias between TPCs, while the second correction increases it[86]. For this reason, the primary mapping correction is applied during reconstruction while the TPC calibration corrections are used as systematic uncertainty on the B field distortions. When the mappings for the magnetic field distortions are applied, the reconstructed momentum is recalculated as:

$$x'_{rec} = x^{MC}_{rec} + \alpha(x^{new}_{rec} - x^{MC}_{rec}) \tag{5.8}$$

where x_{rec}^{new} is the reconstructed momentum after the mapping changes. Unlike the other systematics, the variation α for the B field distortions has a uniform distribution between 0 and 1.

5.3.2 Time Projection Chamber Momentum Scale

The momentum scale is the second systematic uncertainty that arises from the measurements of the magnetic field at ND280. There are four Hall probes installed at ND280 to provide scaling factors for the magnetic field strength in the Monte Carlo, as the nominal MC B-field is significantly different from the measured mapping [85]. Changing the magnitude of the B-field can lead to changes in reconstructed TPC track momenta and migration between p – θ bins in the selections. The uncertainty on this scaling comes from several sources: the intrinsic resolution of the probes, potential relative misalignment between the probes, and non-linearities in the relationship between magnet current and field magnitude.

The systematic uncertainty for the momentum scaling can be accounted for as a simple scaling of the error on the momentum:

$$x'_{rec} = x_{rec}^{MC}(1 + \alpha \times \delta s) \tag{5.9}$$

where α is a Gaussian random variable with a mean of 0 and width of 1 and δs is the statistical error on the scaling, with $\delta x = x_{rec}^{MC}\delta s$ for the uncertainty on the momentum. The measured scaling factor comes from the B-field studies described in [85] and the final uncertainty used for systematic propagation is measured as 0.57% [81].

5.3.3 Time Projection Chamber Momentum Resolution

Due to factors such as the differences in magnetic field distortions and electric field distortions at the near detector, there is some uncertainty on the resolution of the momentum reconstruction in the TPCs. While there is a separate systematic for the B field distortions, the sources for the data – Monte Carlo discrepancy in resolution are not well understood and therefore the

conservative approach of including both errors is taken [81].

To study the TPC momentum resolution for data and Monte Carlo, a study has been performed using a control sample of events with tracks that cross multiple TPCs[87]; this allows the momenta of the two TPC tracks to be compared without using truth information. This is done by comparing the difference between the reconstructed momentum of the two TPC tracks with each other. The momentum resolution uncertainty is calculated for a single TPC segment; for global tracks, there is good agreement in the inverse momentum distributions between global tracks and single TPC segments. Therefore the same fractional differences are used for global tracks.

The Monte Carlo shows better TPC momentum resolution than data; this difference is accounted for by smearing the inverse momentum in the Monte Carlo to match that seen in data. This uses the fractional difference in momentum resolution between data and Monte Carlo, which is binned in x-position along the TPC[81][87]. While the scaling factor depends on x-position, an uncertainty of 0.1 was used for all scaling factors regardless of x-position. Additionally, this uncertainty has 100% correlation between different x-position bins, as a difference in position does not change the underlying physical source.

5.3.4 Time Projection Chamber Particle Identification

As described in Section 4.3.1, the TPC particle ID is calculated using a truncated mean of the charge collected in the TPC to calculated particle hypothesis pulls. There are two contributing data – Monte Carlo differences for the TPC particle ID: the difference between the mean pull values and the ratio between the pull widths. The uncertainties on these ratios is calculated for each particle type and TPC, and binned in particle momentum. The difference in pull means gives a estimation of the systematic bias and the ratio is used to estimate the smearing that needs to be applied to the Monte Carlo.

To measure the systematic uncertainties, samples of events with a high purity of muon, electron and proton tracks are selected. The selections are different for each particle type, with

Cluster Type	$(\varepsilon^{MC} - \varepsilon^{data})/\varepsilon^{MC}$	$\varepsilon^{data}/\varepsilon^{MC}$
Vertical	0.0011 ± 0.0002	0.9989 ± 0.0002
Horizontal	0.0007 ± 0.0001	0.9993 ± 0.0001

Table 5.2: Efficiency differences for the TPC cluster matching for data and Monte Carlo[81]. ε^{data} is the measured data cluster efficiency and ε^{MC} is the measured Monte Carlo cluster efficiency.

high purity for the muon and electron samples and lower purity for the proton sample [79].

The results from the muon studies are used for events identified as pions as well, as muons and pions have very similar energy loss. There is no correlation between particle type, while within the uncertainties for each particle, uncertainties for the momentum bins and TPCs are 100% correlated. Additionally the uncertainties on the pull mean is 100% correlated with the uncertainty on the pull width for each particle case.

5.3.5 Time Projection Chamber Cluster Efficiency

The systematic uncertainty on reconstructing a cluster in the TPCs comes from the difference in reconstruction efficiency in data and Monte Carlo. As the TPC track quality cut described in Chapter 4 uses the number of clusters, this can lead to differing fractions of Monte Carlo and data events passing the initial selection cuts. The efficiency and its uncertainty are measured for both horizontal and vertical reconstructed clusters. The uncertainty for horizontal and vertical clusters mostly comes from the underlying hit efficiency and therefore the systematic uncertainty is correlated between the horizontal and vertical clusters.

To evaluate the difference in cluster reconstruction efficiency, two control sample studies were performed. For the horizontal cluster efficiency, the control samples used consisted of cosmic trigger events with vertical tracks crossing TPC 2. For vertical cluster efficiency, a sample of CC inclusive events that originated in FGD 1 was used, to ensure mostly horizontal tracks that would be reconstructed with vertical clusters. The final cluster efficiencies are shown in Table 5.2.

	TPC 1	TPC 2	TPC 3
Data Efficiency	$99.9^{+0.1}_{-0.1}\%$	$99.7^{+0.2}_{-0.7}\%$	$99.3^{+0.5}_{-0.2}\%$
MC Efficiency	$99.6^{+0.2}_{-0.3}\%$	$99.5^{+0.3}_{-0.4}\%$	$99.8^{+0.1}_{-0.2}\%$

Table 5.3: Efficiencies for the TPC track reconstruction for data and Monte Carlo.[88]

5.3.6 Time Projection Chamber Track Reconstruction Efficiency

The event selection described in Chapter 4 uses TPC – FGD matched tracks for the basis of the selection. These tracks start as TPC-contained tracks, relying on only the TPC reconstruction methods. Incorrectly reconstructing these can lead to missing or incorrectly classifying the topology of events, and the main expected source of differences between data and Monte Carlo is extraneous hits from δ ray production. The systematic uncertainty on these TPC tracks is applied as an overall efficiency for successfully reconstructing a track in the TPC, which includes potential effects from the likelihood fit and other sources. The TPC track reconstruction efficiency is fully correlated between the TPCs.

The TPC track reconstruction efficiency is calculated using studies on control samples composed of through-going muons from the beam and cosmic events. Through-going cosmic muons are used along with the beam events to measure the reconstruction efficiency when there are no other tracks in the TPC. To study the effect of track length on reconstruction efficiency, the reconstruction efficiency of cosmic muons with barrel ECal tracks is used[81]. The efficiencies are computed separately for each TPC and the studies are described in [88]. The studies show high overall track reconstruction efficiencies and that there is no momentum or angle dependence. The efficiencies used for this analysis are listed in Table 5.3.

5.3.7 Charge Identification

The reconstruction uses global track information to identify the charge on tracks in the TPC, described in [89], using local charge identification in the TPC and information from the global track reconstruction to determine charge sign. There are two different sources of systematic uncertainty on the TPC track charge with some correlation between the two: the probability of

getting the local charge, or charge as determined from one TPC, incorrect, and the probability of the global charge identification incorrectly swapping the local charge sign. The correlation depends on the number of TPC segments, as the charge for each segment is used in the global charge determination. For this reason, the systematic uncertainty is calculated differently depending on if the global track has one, two or three associated TPC segments[89]. However, the three cases are considered to be correlated with each other, as the reconstruction still uses common information in each case. The efficiency is calculated as the probability that the global charge is different from the local reconstructed charge.

Systematic studies were performed on a control sample of tracks starting in the P0D and containing at least one TPC segment[89]. These studies show that the uncertainty on the charge identification depends on the reconstructed momentum error; the parameters used in calculating the uncertainty for the 1, 2 and 3 segment cases are listed in [89]. Because of this dependence, this systematic is considered 100% correlated between the different cases and 100% correlated between the FGD 1 and FGD 2 selections.

5.3.8 Time Projection Chamber – Fine Grained Detector Matching Efficiency

The TPC – FGD track matching in the reconstruction creates tracks by matching FGD hits to a reconstructed TPC track as described in Section 4.3.1. The efficiency of this reconstruction depends on both the efficiency of matching a TPC track to a single hit in an adjacent FGD, potentially failing to connect tracks to an FGD, and the efficiency for correctly matching a TPC – FGD track with a second TPC track, potentially incorrectly reconstructing the event vertex position[90]. The uncertainty from incomplete matching causing out of fiducial volume event migration is not included here and is part of the out of fiducial volume (OOFV) background systematic described later in this section

The systematic uncertainty was computed using a control sample of high angle cosmic events with one FGD 1 – TPC 2 – FGD 2 track in them. The systematics studies find that the efficiency for TPC – FGD matched tracks with more than two hits in the FGD to be 100%

	FGD 1	FGD 2
Data Efficiency	$96.9 \pm 0.8\%$	$96.5 \pm 0.85\%$
MC Efficiency	$97.6 \pm 0.45\%$	$97.6 \pm 0.50\%$

Table 5.4: Efficiencies for the TPC – FGD track matching for tracks with few reconstructed hits for data and Monte Carlo.[90]

for when the events also has a second TPC track . This holds for both FGD 1 and FGD 2. The systematic uncertainty for the TPC – FGD matching is applied to tracks with two or less matched hits in the FGDs, with the efficiencies and uncertainties shown in Table 5.4. Because the matching efficiency only pertains to the last two layers in each FGD, FGD 1 and FGD 2 share the same source of uncertainties on the matching efficiency from the uncertainty on the scintillator coating thickness and other scintillator bar properties. Therefore, this systematic is 100% correlated between FGD 1 and FGD 2.

5.3.9 Fine Grained Detector Particle Identification

The systematic uncertainty on the FGD particle ID described in Section 4.3.2 primarily comes from the difficulty in translating the measured deposited energy in an FGD into particle mass [91]. This results in an uncertainty on the measured particle pulls, which are derived from the measured energy deposits. Measuring that deposited energy in turn depends on uncertainty from the dead channels in the FGDs, the thickness of the scintillator coating and the charge reconstruction. Because the data to Monte Carlo charge reconstruction and scintillator coating thickness differences are the same for FGD 1 and FGD 2, this systematic uncertainty is considered to be correlated between the FGD 1 and FGD 2 selections. As there are no FGD-only track cuts in the RHC $\bar{\nu}_\mu$ and ν_μ selections, this systematic uncertainty does not apply.

The systematic studies for the FGD particle ID used control samples of events with single muon and proton tracks which stop in either FGD 1 or FGD 2[91]. The TPC particle ID is used to create the control samples and can be compared with the FGD particle ID to find the efficiency of correctly identifying a muon or proton. The systematic error on the charged pion identification uses the same numbers as measured for muons, as the FGD particle ID does not

strongly distinguish between the two. This systematic uses different uncertainties for tracks in FGD 1 and FGD 2.

5.3.10 Fine Grained Detector Time of Flight

The average hit time between FGD 1 and FGD 2 is used to determine the track direction and select which FGD volume the initial neutrino interaction occurred in. As described in Section 4.3.3, a track that crosses both FGDs is reconstructed as backwards-going when the average hit time in FGD 1 is at least 3 ns greater than the average hit time in FGD 2. The systematic uncertainty on this time of flight directly impacts whether an event is reconstructed as occurring in FGD 1 or in FGD 2.

To compute the systematic uncertainty, the standard neutrino interaction sample was used instead of a targeted control sample, selecting for events with tracks which passes through both FGD 1 and FGD 2. The final uncertainty on the time of flight is found to be $\delta\Delta t_{12} = 0.78$ ns. This systematic variation is added directly to the reconstructed time of flight as $\delta\Delta t_{12} \times \alpha$, where α is the random variable for the systematic variations. As this systematic uncertainty comes from the timing in FGD 1 and FGD 2, the time of flight is considered 100% correlated between the FGD 1 and FGD 2 selections.

5.3.11 Fine Grained Detector Hybrid Track Efficiency

The hybrid track efficiency is defined as the efficiency of reconstructing a true FGD-contained track in the presence of a TPC – FGD matched track, as all relevant FGD-contained tracks in the selection are accompanied by a TPC – FGD matched track. As the selection does not look for solitary FGD-contained tracks, that efficiency is not used. This systematic only applies to the FHC ν_μ selection as there are no FGD-contained track cuts in the RHC selections. As the selected FGD-only tracks are expected to be either protons or pions, the systematic uncertainty studies were performed separately for each case. The studies were only performed for the FHC running mode, as the RHC selections do not include any FGD-contained track cuts.

The control sample used to study the efficiency consists of events with either one recon-

structed track that enters a TPC, or two tracks which both enter a TPC. As these events do not contain any FGD-only tracks, instead stopping pion and proton tracks were generated using a particle gun in GEANT4 [91] for each event. These particles were generated as isotropic and with uniform energies, with further details in [91], with a lower momentum bound of 400 MeV for protons due to reconstruction limitations below that momentum. The hits from these tracks were injected into the control sample events, both data and Monte Carlo, and the FGD-only track reconstruction run. The efficiency is calculated as the ratio of the number of events with at least one reconstructed FGD-only track over the total number of selected events in the control sample. As the FGD track reconstruction has a strong dependence on the track angle, the efficiency is binned in $\cos\theta$, with θ being the true angle between the FGD-only track and the muon candidate. The efficiency and uncertainty are also calculated separately for pion and proton tracks [91], with overall systematic uncertainties on the track efficiency ratios being $<$ 8%.

Additionally, there is a significant difference in data – Monte Carlo efficiency differences between FGD 1 and FGD 2 due to geometry differences. The lower active volume of FGD 2 leads to both a lower track efficiency and to lower data – Monte Carlo differences than seen in FGD 1. As this is not currently well understood, there is no correlation between FGD 1 and FGD 2 for this systematic. However, as the tracking efficiency also depends on underlying uncertainties on the scintillator coating and overall hit efficiencies, there is 100% correlation implemented for all angular bins within each particle[81].

5.3.12 Michel Electron Efficiency and Purity

As described previously in Section 4.5.3, Michel electrons from π^+ decays ($\pi \to \mu \to e$) are identified by looking for sufficient delayed FGD hits after an interaction is seen. As this cut is only used in the FHC ν_μ selection, the systematic studies have only been performed for the neutrino mode running period. The Michel electron systematic is two separate systematics relating to the Michel electron cut that are applied together; one is the difference in efficiency

	FGD 1	FGD 2
Monte Carlo	$56.5 \pm 1.9\%$	$41.4 \pm 1.4\%$
Data	$56.4 \pm 1.6\%$	$42.8 \pm 1.1\%$

Table 5.5: Michel detection efficiencies for Monte Carlo and data[82].

of selecting the Michel electrons through this cut and the other the difference in the purity of delayed time bins selected by the Michel electron cut for data and Monte Carlo. In particular, the initial studies used to construct the Michel electron cut indicate there may be significant data and Monte Carlo differences in the purity.

Michel Electron Efficiency

The Michel electron detection efficiency depends on how likely a produced electron is to leave sufficient hits to pass the cut and therefore be detected. To study this, a control sample of cosmic muons stopping in FGD 1 and FGD 2 was used. As the high angle cosmic tracks do not necessarily pass through a TPC, a particle ID cut on the track length and momentum was used[82] to identify muons. This particle ID cut was based on studies of the muon lifetime and associated track lengths and momenta in the FGDs, as cuts using only the FGD particle ID muon pulls gave insufficiently pure muon samples.

The efficiency from these studies is defined as the probability of detecting an expected Michel electron given a known stopping muon in the FGD. The efficiencies are calculated separately using cosmic triggers from runs 2, 3 and 4 in data as the Michel purity is separated based on beam power. Because the cosmic samples do not depend on beam power, the average efficiency of these samples is used for data at all beam powers. The final efficiencies are shown in Table 5.5.

Michel Electron Purity

The primary source of background for identified Michel electrons in the Monte Carlo comes from out-of-FGD beam interactions in the near detector and magnet volumes, sand muon interactions, and cosmic muons. These particles can enter from outside of the FGD and leave

	FGD 1		FGD 2	
	MC ($\times 10^{-3}$)	Data ($\times 10^{-3}$)	MC ($\times 10^{-3}$)	Data ($\times 10^{-3}$)
Run 2	0.602 ± 0.008	1.61 ± 0.05	0.314 ± 0.006	1.21 ± 0.05
Run 3	0.714 ± 0.009	1.80 ± 0.04	0.397 ± 0.006	1.31 ± 0.03
Run 4	0.729 ± 0.009	2.00 ± 0.07	0.387 ± 0.006	1.50 ± 0.06

Table 5.6: False Michel electron identification rates for data and Monte Carlo. Rates are defined as the number of expected false Michel electrons per spill.

large enough energy depositions to be misidentified as a Michel electron. To isolate and study the external background, empty beam spills from the neutrino beam data were selected, rather than events. Spills were required to have no reconstructed tracks within the beam bunches in order to remove any true Michel electrons originating from beam ν_μ interactions in the FGDs. The same selection was used for both Monte Carlo and data, as no truth information is used.

There are significant differences in the simulated background for out-of-bunch particles, both at the high energy and low energy regions. The Monte Carlo does not simulate the high energy tail seen in the data – this is potentially due to coincident hits left by through going cosmics, which is not included as a background in the ND280 Monte Carlo. This can be seen where the simulated hit distributions stop at 30 for FGD 1 and 25 for FGD 2 (due to lower active volume) in Figure 5.1. These particles have roughly the same incidence rate in FGD 1 and FGD 2, and no dependence on the beam power. This can be seen in the rates in Table 5.6, where the rates for FGD 1 are around double those for FGD 2 for Monte Carlo, but much closer for data.

Additionally, the false identification rate in data depends on the beam power for both Monte Carlo and data. The Monte Carlo rates for run 3 and run 4 are expected to be similar, as the same beam configuration was used to simulate them. For data, the total protons on target per spill increases between run 3 and run 4 and thus shows an increase in false identification rate.

Excess Simulated Background

The primary background that affects the purity of the Michel electron identification is the high energy tail described previously, likely originating from cosmics. However, the external

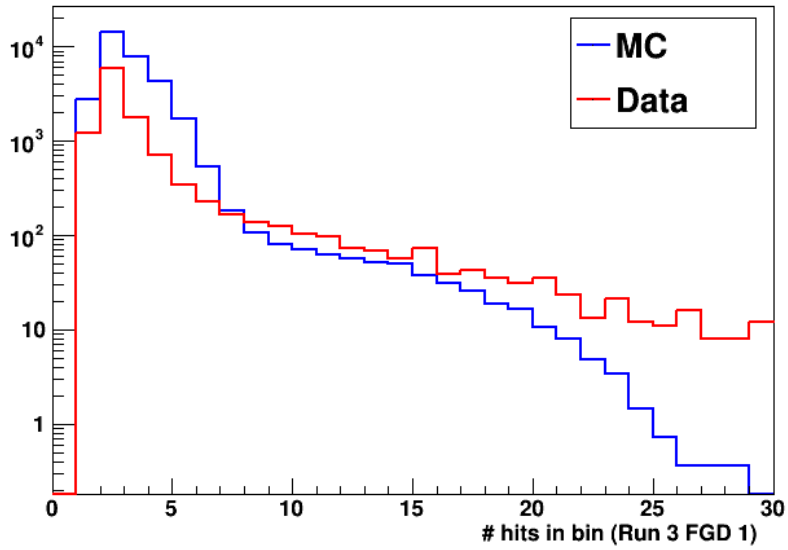

(a) FGD1

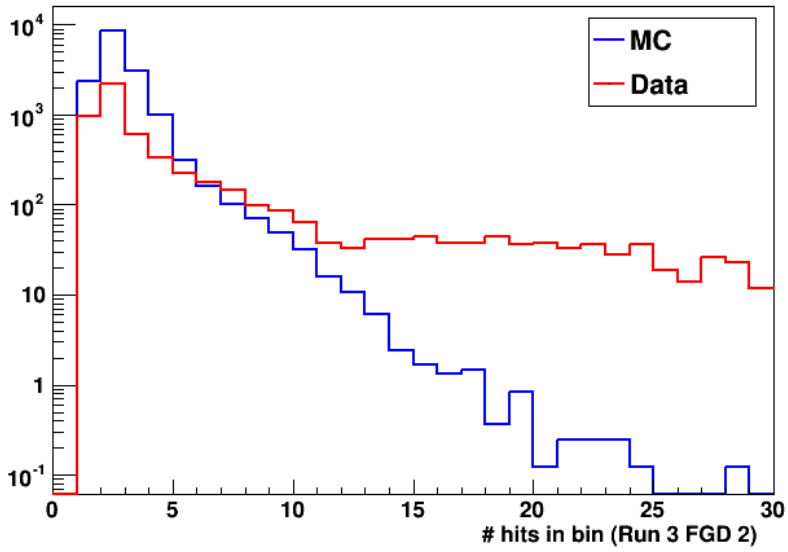

(b) FGD 2

Figure 5.1: Total number of hits in out-of-bunch timebins from empty spills. Plots are normalized to data POT, and were created for a subset of the run 3 data.

background studies for the Michel electron cut also reproduce the large excess in the simulated background at low numbers of hits seen previously in Section 4.5.3. There, it was a main factor in choosing the minimum number of hits to cut on due to this discrepancy between data and Monte Carlo.

As is shown in Fig. 4.6, and in Fig. 5.1, the shape of the simulated background at low hits is similar to that seen in data, but with a significant increase in magnitude. A large part of this excess comes from neutrons which produce γs which can be detected. Various other particles such as protons and pions contribute as well, though as the Monte Carlo did not save all relevant information for delayed hits it was not always possible to determine the simulated source of the delayed timebin hits. Because of this, it is difficult to understand exactly what part of the Monte Carlo is incorrectly tuned and therefore how to fix it. Until this is understood in more detail and can be fixed, this places an artificial lower limit on the Michel electron cut due to a lack of understanding of the actual cut purity below that point.

5.3.13 Sand Muons

The main ND280 Monte Carlo simulation only includes beam events that occur in the ND280 volume itself, including the surrounding magnet. However, neutrinos from the beam can interact with the sand surrounding the detector pit, and the walls of the pit where ND280 is situated. Tracks from these interactions can appear similar to neutrino interactions in the FGDs, and are a potential background for the analysis. As the primary source is from interactions with the surrounding sand, these background events are referred to as sand muons. Because these are not included in the main T2K Monte Carlo for the near detector, there is a separate dedicated Monte Carlo sample of sand muon events to estimate the effects on the analysis samples.

The sand muon Monte Carlo allows the total event rate from sand muons to be estimated for the analysis sample by running the selections described in Chapter 4 on the Monte Carlo and scaling to the data protons on target to get the predicted sand muon event rate. To estimate the systematic uncertainties on this background, the difference between rates in Monte Carlo and data is used for positive tracks and negative tracks separately. The uncertainty on the sand muon rate is 10% for neutrino mode and 30% for antineutrino mode [81] and is accounted for as a normalization systematic. As the interactions occur outside the detector volume, the underlying cause for uncertainties is the same for FGD 1 and FGD 2, with no correlations

between neutrino and antineutrino mode.

5.3.14 Event Pile Up

Event pile up occurs when an out of fiducial volume event is coincident with a in-fiducial volume CC Inclusive event in either FGD. These coincident events can lead to CC Inclusive events being removed from the selection sample by the external veto cut described in Section 4.5.2. For both the FHC and RHC selections, the primary source of this pile up comes from the sand muons [81]. This uncertainty depends on the beam intensity and horn current – within FHC or RHC, the source of the systematic uncertainty is similar for different intensities, but not necessarily between neutrino and antineutrino mode. Therefore a 100% correlation is used between beam intensity, and 0% correlation between FHC and RHC. Like the sand muon rate systematic, a correction is applied to the Monte Carlo to account for this.

Because there is a 10% uncertainty on the sand muon simulation for ν_μ and 30% uncertainty for $\bar{\nu}_\mu$, along with other possible differences between the sand muon simulation and data such as beam intensity, there is a systematic uncertainty on the correction. This systematic uses the difference between data and Monte Carlo, as calculated using a comparison of the number of TPC 1 or TPC 2 events per bunch in data and Monte Carlo.

5.3.15 Fine Grained Detector Mass

The FGD mass systematic is the uncertainty on the scintillator and water module areal densities due to differences in the simulated FGD volumes and the real detector volumes [92]. The uncertainty of the scintillator XY modules affects both FGD 1 and FGD 2, while the uncertainty on the water volume density is only applicable to FGD 2. These are implemented as uncertainties on the densities of modules, including coating for the scintillator modules and the polycarbonate water module vessels.

The uncertainty on an XY module is calculated from the data – Monte Carlo difference in mass, 0.41% [92] and the spread in direct mass measurements of all of the XY modules, 0.38%, giving an overall 0.6% systematic uncertainty on the XY modules in the FGDs. The water

module mass has a difference of 0.26% between data and Monte Carlo, and an uncertainty of the water module mass of 0.46% mostly from the masses of the plastic and glue [93], leading to an uncertainty of 0.55% on the FGD water module mass. The water and scintillator mass uncertainties are independent from each other, as the uncertainty is assigned based on the true vertex position[81]. As the source of the uncertainty on the scintillator mass is based on the module measurements and therefore the same for FGD 1 and FGD 2, the scintillator mass variation is considered to be 100% correlated between the FGD 1 and FGD 2 selections. The water mass variation is also considered to be 100% correlated between the FGD 1 and FGD 2 selections.

5.3.16 Pion Secondary Interactions

When pions are produced from interactions in ND280, they can interact elsewhere in the detector; this is referred to pion secondary interactions (SI) and can result in detection inefficiencies for pions in the FGDs. This can be through absorption, decay, quasi-elastic interactions and other methods[94]. As pion detection is used as the main criteria for topology definition and selection as described in Chapter 4, correctly modeling this in the Monte Carlo is important. The model using GEANT4 for the pion interactions does not agree well with existing data on pion interactions on nuclei[94] and so a correction weight is applied to the events. As the uncertainty depends on the target nuclei, this systematic is uncorrelated between target type but is considered 100% correlated between FGD 1 and FGD 2 for each target. The systematic uncertainty is calculated both from the studies comparing the ND280 Monte Carlo and data and uncertainties on the external data on pion interactions. The event weight is calculated as a product of the probabilities for each true pion trajectory in an event either interacting or not interacting for different cross section models. These probabilities are energy dependent and calculated every 0.1 mm along a given trajectory. The process is detailed in [94].

Background Origin	FHC ν_μ	RHC $\bar{\nu}_\mu$	RHC ν_μ
P0D	5.1%	8.4%	5.4%
ECal	11.6%	8.8%	6/7%
SMRD	4.9%	6.7%	4.8%
Other	13.6%	13.5%	24%

Table 5.7: Rate uncertainties for OOFV events by origin.[95]

5.3.17 Out of Fiducial Volume Background

Part of the background for CC Inclusive for both the FHC and RHC selections originates from outside of the FGD fiducial volume (OOFV). In these cases, an interaction has occurred somewhere else in the near detectors but has been reconstructed as starting in either the FGD 1 or FGD 2 fiducial volume. This also includes interactions in the first two layers of FGD 1 and the first layer of FGD 2. There are two main contributing types of uncertainty on the background OOFV rates: uncertainty on the interaction rates in the other detectors at ND280, and uncertainty on certain classes of reconstructed events in the FGDs.

The rate uncertainty is separated into four categories: interactions where the true vertex occurred in the P0D, the ECal, the SMRD or other near detector volumes. The relative difference for the interaction rate for data and Monte Carlo was studied using the neutrino beam data rather than control samples. The difference for each interaction source is used as the uncertainty on the interaction rate. The rate uncertainties are shown in Table 5.7. As these are from non-FGD sources, the underlying physical sources of uncertainties are the same for the FGD 1 and FGD 2 selections and this systematic is fully correlated between the two with no correlations between different background rate sources.

The reconstruction uncertainties are the probabilities that some part of the reconstruction, generally the TPC – FGD matching, has failed and an OOFV event has been reconstructed as occurring within the fiducial volume. The reconstruction uncertainties are split into several different categories depending on the true vertex location and type of reconstruction failure. Not all types of OOFV events have a significant reconstruction uncertainty even if they contribute to the overall background, such as events occurring in the FGD but outside the fiducial volume

Background Category	FGD 1	FGD 2
Downstream event	5%	5%
High Angle Event	33%	28%
Last Module Failure	35%	17%
Consecutive skipped layers	55%	82%
Hard scattering	32%	21%

Table 5.8: Reconstruction uncertainties (MC/data difference) for OOFV events by origin.[95]

or events originating in the upstream tracker. The OOFV background categories that do have some reconstruction uncertainty are events originating in the tracker components downstream of the FGD, high angle events, failure to match events with most hits missing in the FGD (referred to as last module failure), events which hard scatter in the FGD and events where no hits are deposited for two consecutive layers.

In general, the reconstruction rate and uncertainty do not depend on the track momentum so the systematic uncertainty is calculated for each category[95]; these categories are sufficiently different that there is no correlation between the categories. As these rely mainly on the hit efficiencies in the FGDs, each category is 100% correlated between FGD 1 and FGD 2. The reconstruction uncertainties are measured using events known to have started outside the FGD fiducial volume, such as cosmic events and comparing the reconstruction rate for data and Monte Carlo. The measured uncertainties are shown in Table 5.8; all other categories of OOFV events have a reconstruction uncertainty of 0%.

5.4 The Observable Normalization Covariance Matrix

As discussed in Section 3.3.3, the near detector fit does not directly use the underlying systematic parameters as implemented in the Psyche framework for computational resource reasons. Instead, the detector systematic parameters are fit in the form of a set of observable normalization parameters, binned in $p - \theta$ and separated by sample, and a covariance matrix that describes the uncertainties and correlations for these bins. The binning used for the observable normalization parameters and covariance is more coarsely binned than the binning used for the

FHC samples as described in Section 4.5.3, primarily for computational reasons. The selection binning is not sufficiently coarse to use in the fit, as it is designed to have all non-zero bins for the MC prediction, which would give 531 normalization parameters for the FGD 1 samples alone. When FGD 2 samples are included, this would lead to fitting 1062 parameters along with the flux and cross section. For this reason, the FHC samples for both FGD 1 and FGD 2 are rebinned to have ten bins in p and seven bins in $\cos\theta$ for each sample :

- FHC sample bin edges for the detector covariance:
  p (MeV/c) : 0, 300, 500, 600, 700, 900, 1000, 1500, 3000, 5000, 30000
  $\cos\theta$: -1.0, 0.6, 0.8, 0.85, 0.9, 0.94, 0.98, 1

This gives 70 bins for each FHC sample in FGD 1 and in FGD 2 and cuts off at a momentum of 30000 MeV. All FHC samples have the same binning. The binning for the RHC samples is not changed, as fewer bins are used for those samples in the fit selection and reducing these will have less effect on computational time. These bins are:

- RHC 1-track sample bin edges for the detector covariance:
  p (MeV/c) : 0, 500, 900, 1200, 2000, 10000
  $\cos\theta$: -1.0, 0.8, 0.92, 0.98, 1

and

- RHC N-tracks sample bin edges for the detector covariance:
  p (MeV/c) : 0, 600, 1000, 1500, 2200, 10000
  $\cos\theta$: -1.0, 0.8, 0.9, 0.97, 1

giving 20 bins in each RHC sample for both the $\bar{\nu}_\mu$ and ν_μ selections. In the case that multiple selection bins are covered by a single covariance matrix bin, the same observable normalization weight is used for all covered bins, as choice of bin depends on the reconstructed momentum and angle.

5.4.1 Systematic Variations

To generate the prior values and the detector covariance matrix using the systematics and correlations described in this section and Chapter 5, 2000 sets of variations of the detector systematic parameters are first thrown with a Gaussian distribution with mean 0 and standard deviation of 1. The correlations described previously are then applied using Cholesky decomposition[96]. As the analysis now includes samples from both FGD 1 and FGD 2, systematic correlations between the two detectors are somewhat complicated to correctly account for. To do so, two sets of detector systematic parameter variations are generated for each throw, with one set of variations applied for FGD 1 selected events and the other set of variations for FGD 2 selected events. In addition to the correlations between FGD 1 and FGD 2 samples, correlations between detector systematic parameter bins are now also applied. Bin-to-bin correlations are also new to this analysis, and are described along with the FGD 1 – FGD 2 correlations earlier in this chapter in Section 5.2.

The observable normalization values are calculated using the mean values for the $p-\theta$ bins as :

$$d_i^{nom} = \frac{N_i^{mean}}{N_i^{nom}} \tag{5.10}$$

and the observable normalization covariance matrix elements as:

$$(V_d)_{ij} = \frac{1}{1999}\Sigma\frac{(N_i^k - N_i^{mean})(N_j^k - N_j^{mean})}{N_i^{mean}N_j^{mean}} \tag{5.11}$$

This gives a correlated set of p–θ parameters to use in the fit. The observable normalization parameters and covariance are used in the fit with the assumption that the overall effect of variations in the systematics is Gaussian in all bins; this is roughly true for the $p-\theta$ bins with large numbers of events, while bins with less than 20 events on average show a more non-Gaussian shape. In addition to the detector systematics information, we also include a few other sources of uncertainties in the observable normalization parameter covariance matrix.

These are the Monte Carlo statistical uncertainties, from the finite size of the Monte Carlo, and an additional shape uncertainty from the 1p1h model differences, described in Section 3.3.3. The Monte Carlo statistical errors are included on the diagonal of the observable normalization matrix, and are calculated using the fit binning rather than the covariance matrix binning to avoid underestimating the uncertainties. This only affects the FHC samples as the binning is identical for RHC. The size of these is shown in Figure 5.2. The covariance is shown in Figure 5.3, without the Monte Carlo statistical errors on the diagonal.

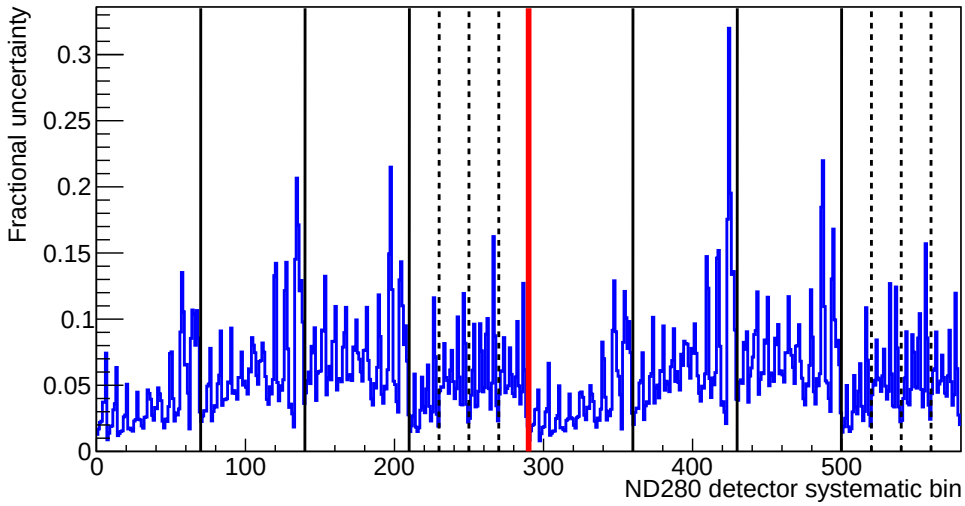

Figure 5.2: The fractional error due to the statistical uncertainty in the MC prediction for each of the ND280 detector systematic $p - \theta$ bins. The solid black lines separate the CC0π, CC1π and CC Other sample, the dashed lines separate the RHC $\bar{\nu}$ CC 1-Track, RHC $\bar{\nu}$ CC N-Tracks, RHC ν CC 1-Track and RHC ν CC N-Tracks samples, and the solid red line separates FGD1 and FGD2 samples[67].

5.4.2 Detector Correlations in the ND280 Fit

The addition of FGD 1 – FGD 2 selection correlations and bin-to-bin correlations has a significant effect on the observable normalization parameter covariance matrix used to model the detector systematics in the ND280 fit. The correlations between the $p - \theta$ bins for the selected samples are shown without the FGD 1 – FGD 2 and bin-to-bin correlations in Figure 5.4a and with the new correlations described previously in Figure 5.4b.

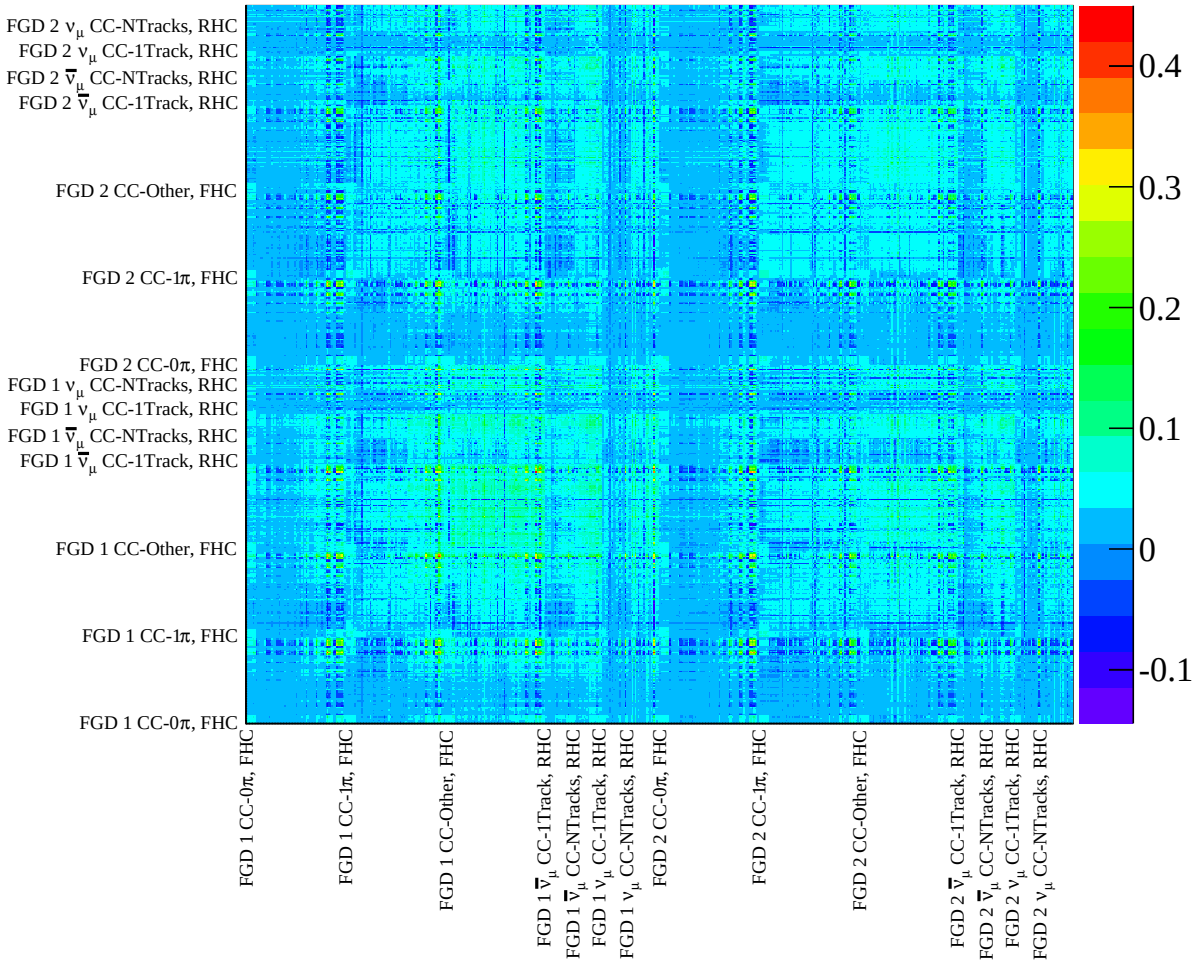

Figure 5.3: Detector covariance matrix calculated using the correlated systematic uncertainty variations. This does not include MC statistical errors, or the $1p-1h$ shape covariance.

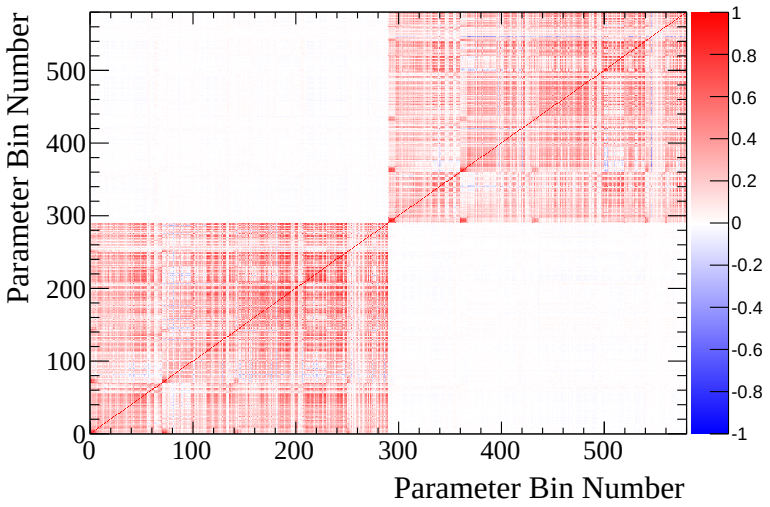

(a) Detector correlation matrix for all samples without bin-to-bin or inter-FGD correlations, without 1p-1h correlations.

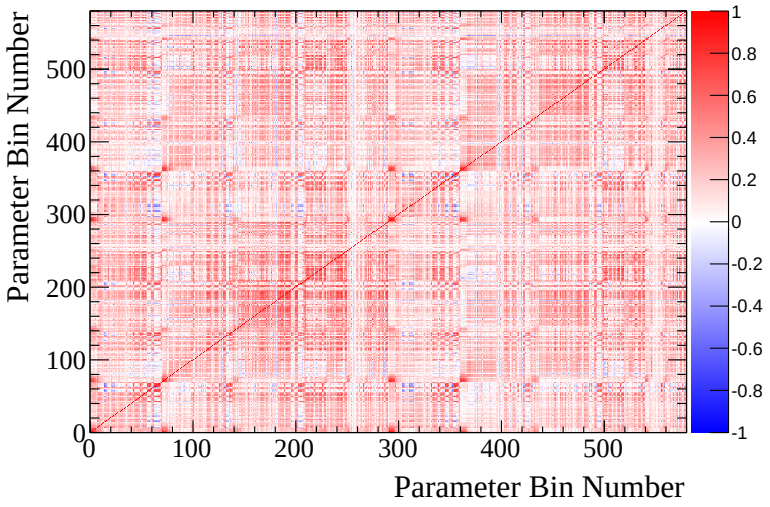

(b) Detector correlation matrix with updated correlations used, without 1p-1h correlations.

Figure 5.4: Detector correlation matrices without the 1p-1h errors included. This compares the current treatment of detector correlations with how detector correlations were implemented in the last analysis. Labels indicate the bin number; starting bins for each sample are: 0 - FGD1 CC0π, 70 - FGD1 CC1π, 140 - FGD1 CC Other, 210 - FGD1 RHC $\bar{\nu}$ CC 1-Track, 230 - FGD1 RHC $\bar{\nu}$ CC N-Tracks, 250 - FGD1 RHC ν CC 1-Track, 270 - FGD1 RHC ν CC N-Tracks, 290 - FGD2 CC0π, 360 - FGD2 CC1π, 430 - FGD2 CC Other, 500 - FGD2 RHC $\bar{\nu}$ CC 1-Track, 520 - FGD2 RHC $\bar{\nu}$ CC N-Tracks, 540 - FGD2 RHC ν CC 1-Track and 560 - FGD2 RHC ν CC N-Tracks. The bins within each sample are ordered in increasing momentum intervals, each containing all angular bins from backward going to forward going.

Chapter 6

Fitter Validation

Before passing the ND280 fit to data to the oscillation analysis at SK to use as an input, there is extensive validation of the fit machinery. This is done by performing multiple Monte Carlo studies and verifying the results from those. There are two types of validation studies done for the near detector fit:

1. Fits to Nominal Monte Carlo
2. Parameter Pull Studies

Each type of study aims to validate specific aspects of the overall fit machinery and methods. Fits to nominal Monte Carlo inputs serve to check potential issues with the fitter code as well as check the expected reduction in overall uncertainties. Finally, the parameter pull studies use an ensemble of toy fits to both check for potential code or input issues that were not seen in the nominal validation fit, as well as check fitted parameter biases. The parameter pull studies are also used to provide the p-value for the data fit to verify that the data fit $\Delta\chi^2$ falls within the expected distribution for the fit model used.

6.1 Nominal Monte Carlo Validation Fit

The initial validation study done is a fit to the nominal MC; this is a check that the fitter returns fitted parameter values identical to their input values. The nominal dataset is defined here as

the dataset where the fake data bin content is identical to the predicted bin content predicted by the ND280 fit with all parameters set to their nominal values. To ensure that the machinery is working, this should ideally return identical parameter values to within machine precision, and reduced errors on those parameters relative to their priors. The fitted errors indicate how much error reduction can be expected in the data fit.

The flux, cross section and detector observable normalization parameter inputs and priors used for this validation study are identical to those that will be used in the final data fit. In addition, the CCQE parameters are left unconstrained in this fit, as will be done for the data fit. The results of this study are shown in Figures 6.1, 6.2 and 6.3, and all flux, cross section and observable normalization parameters behave as expected. All fitted parameter values, including the unconstrained CCQE parameter values, are fitted to within 10^{-11} of their initial input values, which is close to machine precision. Overall uncertainties on parameters are reduced, and the fit introduces an overall anticorrelation between the flux and observable normalization parameters.

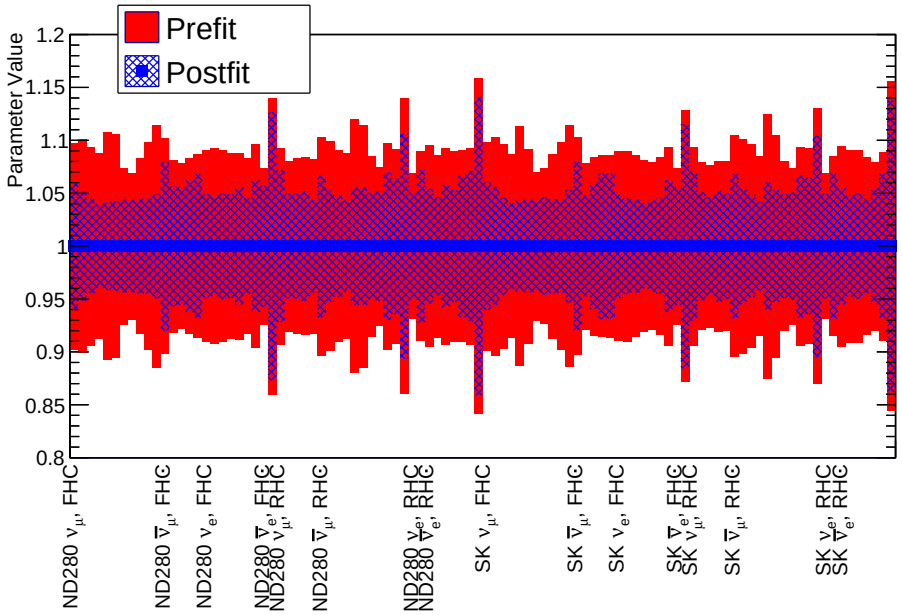

Figure 6.1: Nominal Monte Carlo dataset validation for the ND280 fit, showing flux parameters. Axis labels show the first bin of each category of flux parameters.

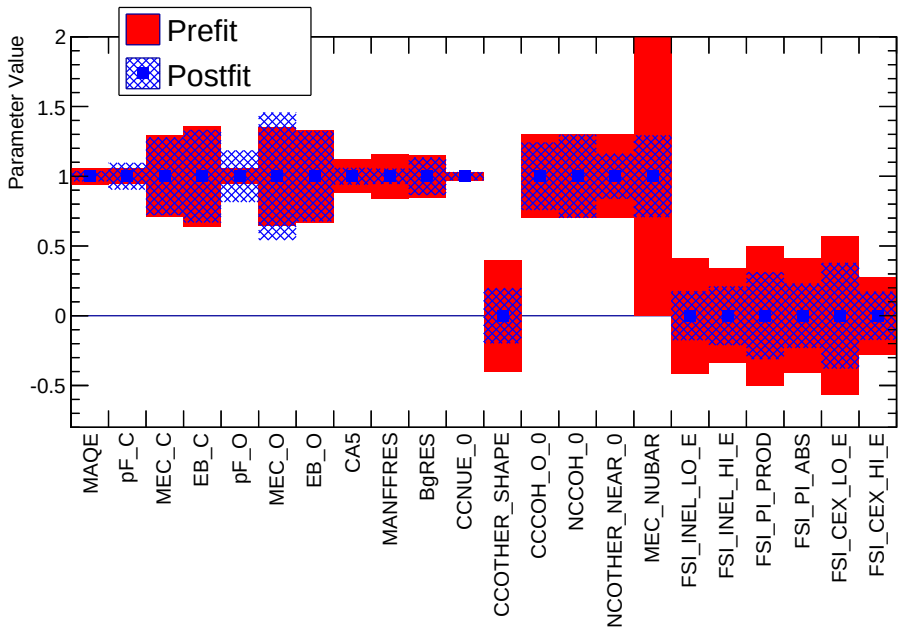

Figure 6.2: Nominal Monte Carlo dataset validation for ND280 fit, showing cross-section parameters. Axis labels show the name of each parameter; parameters are typically a ratio to NEUT nominal values, excepting the CC Other Shape parameter and the FSI parameters. There is no prior used in the fit for the CCQE parameters; the prior error bands shown for these parameters are the error bands produced as potential cross section inputs and are included here for comparison purposes only.

6.2 Parameter Pulls and p-value Calculation

In order to check that the fitted model is in agreement with the data, and to check for any parameter biases or other fitter issues, a large number of toy data sets are generated to cover possible parameter variations given the parameter priors and are fit using the same flux, cross section and observable normalization inputs as the final data fit. The main use for these toys is to conduct pull studies, where an ensemble of fitted parameter values can be compared with their priors to understand potential fit biases and other issues, and to construct a p-value for the final data fit from the $\Delta\chi^2$ distribution of these fits. The two types of studies use different toy data sets, but throwing the parameters works the same for both.

Parameter pulls are defined for a parameter x as

$$pull = \frac{x - \mu}{\sigma} \tag{6.1}$$

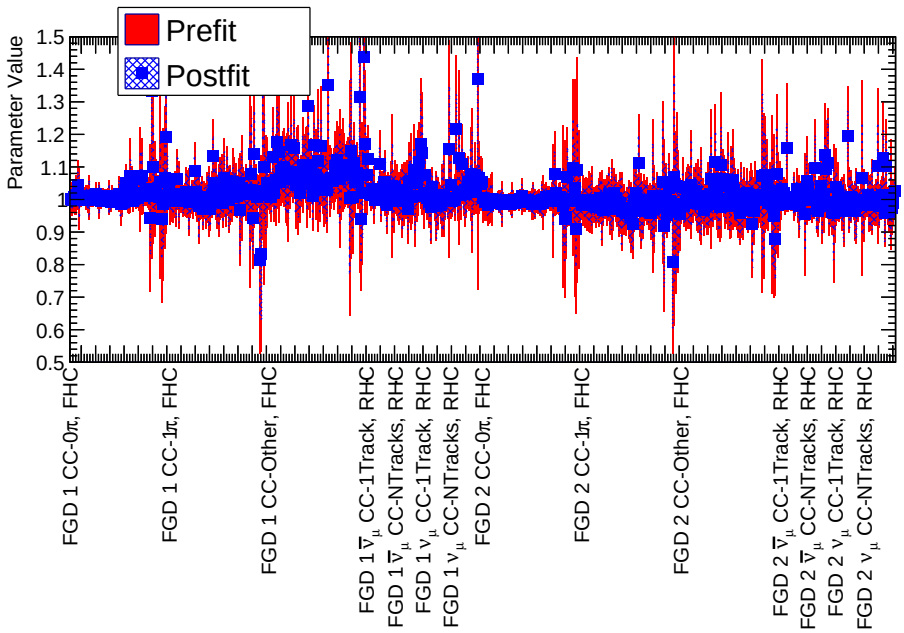

Figure 6.3: Nominal Monte Carlo dataset validation for the ND280 fit, showing detector normalization parameters. Axis labels show the first bin of each category of detector parameters. Values are fit to the normalization weights for each $p-\theta$ bin and are generally not expected to equal to 1.

and are valid when parameter value has been thrown as a Gaussian distribution with a mean μ and width σ [97]. For a fitted parameter value d, the pulls are calculated as

$$pull = \frac{d_{fit} - d_{nominal}}{\sigma_{fit}} \tag{6.2}$$

and thus calculated relative to this fixed prior toy value[97]. In this case the pulls compare the fitted values to the prior mean of the parameter distribution. In the case of parameters fit without a prior constraint, the pulls are calculated the same way. However, as there is no prior distribution to throw the parameter with, and the parameter does not contribute directly to the fit $\Delta\chi^2$, the nominal value is the fixed parameter value used in the toy throws.

The parameter pull values from a set of toy parameter fits should have a standard normal distribution with a mean value of 0, meaning the fitted parameter values were distributed around the prior constraint value, and a width of 1, matching the thrown distribution of these parameters. Parameters that are fit close to their physical boundaries or are poorly constrained

by the fit will often have a pull width of less than 1, and the mean may be shifted above 0. If the pull distribution means are offset from 0, this can indicate that there is a bias in that fitted parameter value. Pull distribution widths greater than 1 can also indicate that there are issues with toy fitter or ensemble. Pulls for parameters with no prior constraints are also expected to have a Gaussian distribution with a mean of 0 and width of 1.

The toy data set ensemble is generated by making Gaussian throws of the flux, cross section and detector systematic parameter variations according to their prior values and uncertainties. The exception to this are the CCQE parameters - as unconstrained parameters do not contribute to the overall $\Delta\chi^2$ term minimized in the fit, throwing these parameters should not have an impact on the overall p-value. Instead, the CCQE parameters are fixed at their NEUT nominal values shown in Table 3.4 when throwing. Additionally, while the detector systematic parameter variations described in Chapter 5 are each thrown using a Gaussian distribution, this does not necessarily translate to expected Gaussian distributions for the fitted detector observable normalization parameters. Because the detector systematic parameters are thrown using the Psyche framework, the 1p-1h shape uncertainty that is included in the observable normalization covariance matrix is thrown and applied as a separate shape covariance.

To make the Monte Carlo statistical throws, a Poisson throw with a mean of 1 is made and multiplied with each individual toy event weight after all parameter throws are made and accounted for. This changes the overall number of reweighted events in the $p - \cos\theta$ sample bins. The final generation step is to include the data statistical uncertainties, as the data is expected to follow a Poisson distribution for each bin and is accounted for in the ND280 likelihood. For each bin, a Poisson throw is made using the total toy event weight in that bin as the mean. The result from this throw replaces the total event weight in that bin.

While the treatment of the flux and cross section parameters is Gaussian in both the thrown variations and the fit itself, this is not true of the detector systematic parameters. As described in Section 3.3.3, the ND280 fitter uses a Gaussian covariance matrix binned in p–$\cos\theta$ to handle the observable normalization parameters for computational reasons. However, this does not

account for non-Gaussian behavior in the detector systematic parameters when varied; for this reason, we vary the detector systematic parameters separately in Psyche, rather than throwing from the observable normalization values and covariance. For these variations the correlations as described in Sec. 5.2 are used.

To perform the p-value studies, 500 toy data sets, each thrown independently from each other, are produced and fit with the ND280 fitting software. These toys consist of sets of fake data constructed using the thrown parameter values, which are then fit to the nominal prior used in the data fit. Of these 500 toy data sets, 461 fits successfully finished and converged for the pull studies, and 444 fits successfully finished and converged for the p-value study. This is partially due to computing issues, as these fits can potentially take over 48 hours to run, while the computing resources used for these studies have a runtime cutoff of 48 hours. This comes from the addition of the FGD 2 samples, doubling both the size of the Monte Carlo inputs and number of selected data events, and doubling the number of observable normalization parameters. For the toys that failed, there were no obvious features in either the thrown event rates or the thrown parameter values compared to successful toy fits.

A comparison of the $\Delta\chi^2$ from the toy data sets described previously with toy fits where the detector parameter variations are thrown using the observable normalization parameters instead of the underlying Psyche parameters is shown in Fig 6.4. This shows that the toys thrown from the detector covariance matrix do not reproduce the non-Gaussian tail seen in the $\Delta\chi^2$ distribution when Psyche detector systematic variations are thrown and that throwing the Psyche detector systematic variations is necessary to accurately represent the $\Delta\chi^2$ range for finding the p-value.

The parameter pulls are calculated using different toy data sets and priors that the $\Delta\chi^2$ distributions. In these toy data sets, parameters are varied in accordance to their prior values and uncertainties, and statistical uncertainty from data and Monte Carlo are accounted for in order to fully represent the model used for fitting and the uncertainties on the priors. This is in place of throwing the various parameters to produce toy data sets and fitting to the nominal

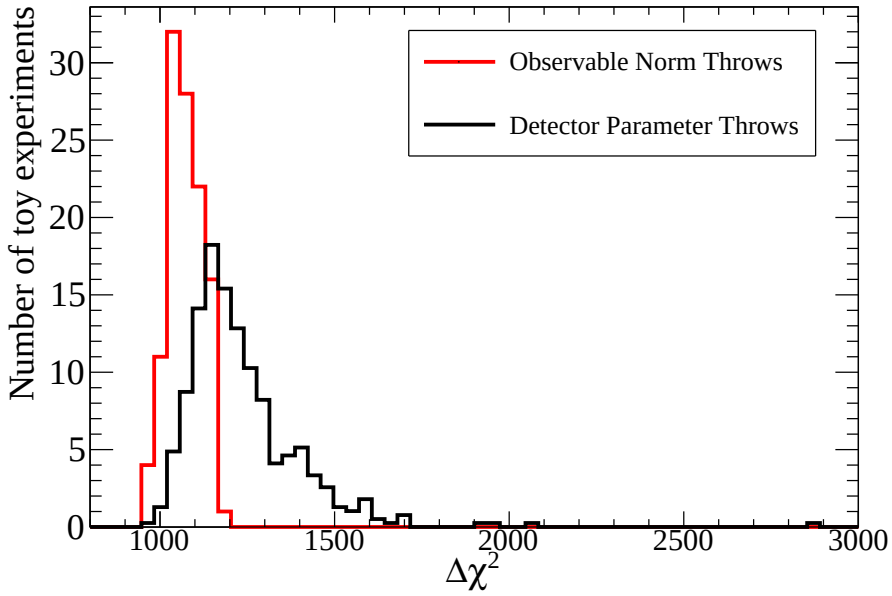

Figure 6.4: $\Delta\chi^2$ distributions for toys with observable normalization parameters thrown in red and Psyche detector systematic parameters thrown in black. The $\Delta\chi^2$ distribution for the observable normalization throws is from 114 toy fits and the distribution for the fits with Psyche throws has been scaled to match overall area.

prior.

Figures 6.5, 6.6 and 6.7 show the mean and width from a Gaussian fit to the individual parameter pull distributions. For these toys, instead of throwing the parameter values used in generating toy data sets, the fit prior values are thrown instead. The parameters are thrown identically to the parameters in the p-value toys, but are not applied to generate fake data. This corresponds with the definition of a robust pull study[97]. Unlike the toy fits for determining the p-value, the underlying detector systematic parameters are not thrown, as they are not used as priors in the fit. Instead, the observable normalization parameters are thrown – with the Monte Carlo statistical error and 1p-1h corrections in the covariance – and used as the prior for the toy fits. Each toy fit has its own set of thrown prior values, and is fit to the nominal Monte Carlo with data statistical throws applied.

Pull widths are distributed around 1 as expected for flux and detector normalization parameters. For cross section parameters p_F C and p_F O, a width less than 1 due to low constraint

power in the fit and a biased mean due to physical fit boundaries is expected. Similarly, MEC C and MEC O have fit boundaries that slightly affect the pull mean and width. Additionally, the pull means are distributed around 0, indicating that the model used for fitting has little or no bias. There is a slight increase in the pull means corresponding to an increase of 1% in the flux parameters; this may be due to some nonlinearities in the parameters but should not have a major impact on the validity of the data fit.

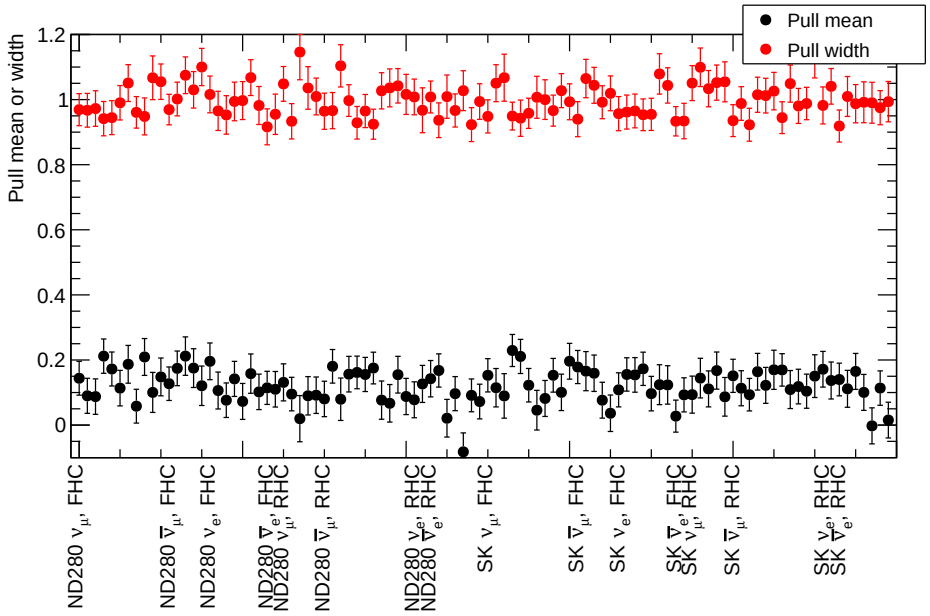

Figure 6.5: Pull means and widths for all flux parameters. The pull distributions are made from the results of fits to 461 toy datasets.

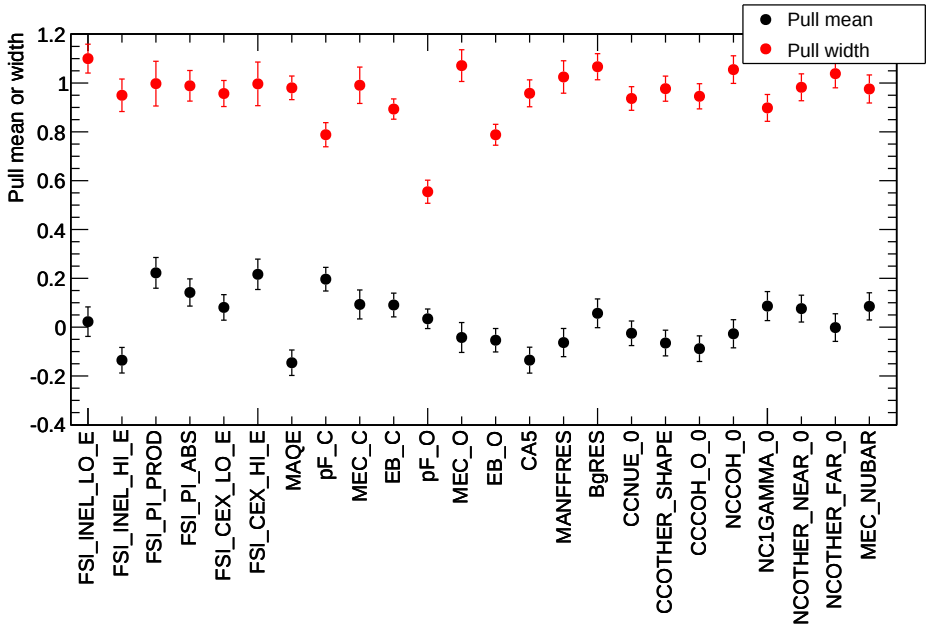

Figure 6.6: Pull means and widths for all cross section parameters. The pull distributions are made from the results of fits to 461 toy datasets.

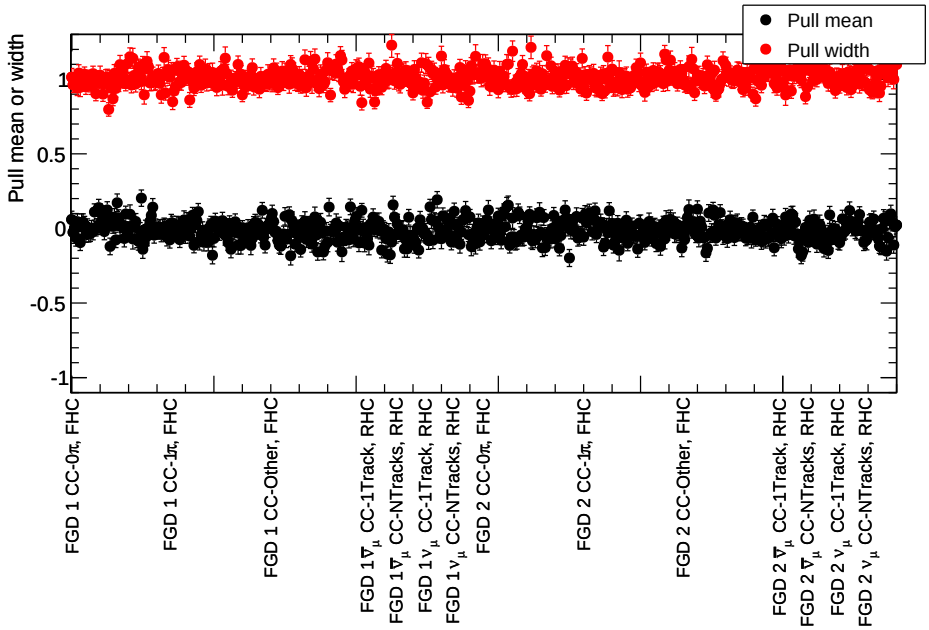

Figure 6.7: Pull means and widths for all observable normalization parameters. The pull distributions are made from the results of fits to 461 toy datasets.

Chapter 7

Final Fit Results at the ND280 Detector

7.1 Finalized Inputs

The final inputs to the data fit at ND280 are as described in Chapter 3, with flux and cross-section parameters using priors from external experiments and the detector observable normalization parameters using prior constraints from ND280 detector systematic studies. When fitting the ND280 samples, the flux, cross-section and detector observable normalization parameters are allowed to vary. All of the flux and detector observable normalization parameters are constrained by input priors; additionally, all cross-section parameters are also constrained using prior inputs with the exception of the CCQE parameters: M_{QE}^{A}, 2p-2h ^{12}Carbon, 2p-2h ^{16}Oxygen, p_F ^{12}Carbon, p_F ^{16}Oxygen and the 2p-2h $\bar{\nu}$ normalization. The rationale for this is explained in Section 3.3.2 – for these parameters, the data from other experiments is inconsistent, so only ND280 data is used to constrain them. These parameters are fit without a prior value or uncertainty and do not contribute to the minimized $\Delta\chi^2$. In the fit, data from the forward horn current and reverse horn current beam modes are considered simultaneously. The selections and samples described in Chapter 4 for FGD 1 and FGD 2 are used.

7.2 Results at the ND280 Detector

The selected data event totals, along with the prefit Monte Carlo and postfit Monte Carlo event totals, are shown in Table 7.1. Fitted parameters are shown in Figs. 7.1, 7.2, 7.3 and 7.4. Tables with the fitted parameter values are listed in Appendix C. The data fit shifts the fitted flux parameter values above their prior bounds for all parameters, by approximately 1.5 σ. This increased flux effect was seen in the previous analysis and does not appear to be related to the $\sim 1\%$ bias seen in the flux parameters in Chapter 6. Additionally, for all flux types aside from the FHC ν_μ and ν_e, the shape of the flux parameters shows a slight increase towards the higher energy flux bins for the flux at both SK and ND280.

The near detector fit at T2K finds an axial mass of $M_A = 1.1113 \pm 0.033$, which is consistent with previous T2K measurements of M_A as well the K2K measurement on oxygen with $M_A = 1.20 \pm 0.12$[98]. As with the K2K measurement, this is above the global average value of $M_A = 1.03 \pm 0.02$[24], and lower than that measured by MiniBooNE[69].

Sample	Data	ND280 prefit MC	ND280 postfit MC
FGD 1 ν_μ CC Inclusive (ν mode)	25558	25420.74	25607.36
FGD 1 ν_μ CC0π (ν mode)	17354	16950.81	17344.83
FGD 1 ν_μ CC1π (ν mode)	3984	4460.15	4112.98
FGD 1 ν_μ CC Other (ν mode)	4220	4009.78	4149.55
FGD 1 $\bar{\nu}_\mu$ CC Inclusive ($\bar{\nu}$ mode)	3438	3506.38	3424.03
FGD 1 $\bar{\nu}_\mu$ CC 1-Track ($\bar{\nu}$ mode)	2663	2708.65	2639.31
FGD 1 $\bar{\nu}_\mu$ CC N-Tracks ($\bar{\nu}$ mode)	775	797.73	784.72
FGD 1 ν_μ CC Inclusive ($\bar{\nu}$ mode)	1990	1933.36	1955.57
FGD 1 ν_μ CC 1-Track ($\bar{\nu}$ mode)	989	938.13	966.18
FGD 1 ν_μ CC N-Tracks ($\bar{\nu}$ mode)	1001	995.33	989.39
FGD 2 ν_μ CC Inclusive (ν mode)	25151	24454.89	25052.24
FGD 2 ν_μ CC0π (ν mode)	17650	17211.71	17638.36
FGD 2 ν_μ CC1π (ν mode)	3383	3616.62	3448.92
FGD 2 ν_μ CC Other (ν mode)	4118	3626.56	3964.96
FGD 2 $\bar{\nu}_\mu$ CC Inclusive ($\bar{\nu}$ mode)	3499	3534.33	3542.56
FGD 2 $\bar{\nu}_\mu$ CC 1-Track ($\bar{\nu}$ mode)	2762	2729.88	2728.34
FGD 2 $\bar{\nu}_\mu$ CC N-Tracks ($\bar{\nu}$ mode)	737	804.45	814.22
FGD 2 ν_μ CC Inclusive ($\bar{\nu}$ mode)	1916	1860.51	1924.22
FGD 2 ν_μ CC 1-Track ($\bar{\nu}$ mode)	980	943.90	987.12
FGD 2 ν_μ CC N-Tracks ($\bar{\nu}$ mode)	936	916.61	937.08

Table 7.1: Actual and predicted event totals for the different ND280 samples in the ND280 fit. The MC predictions are shown both before and after the ND280 fit.

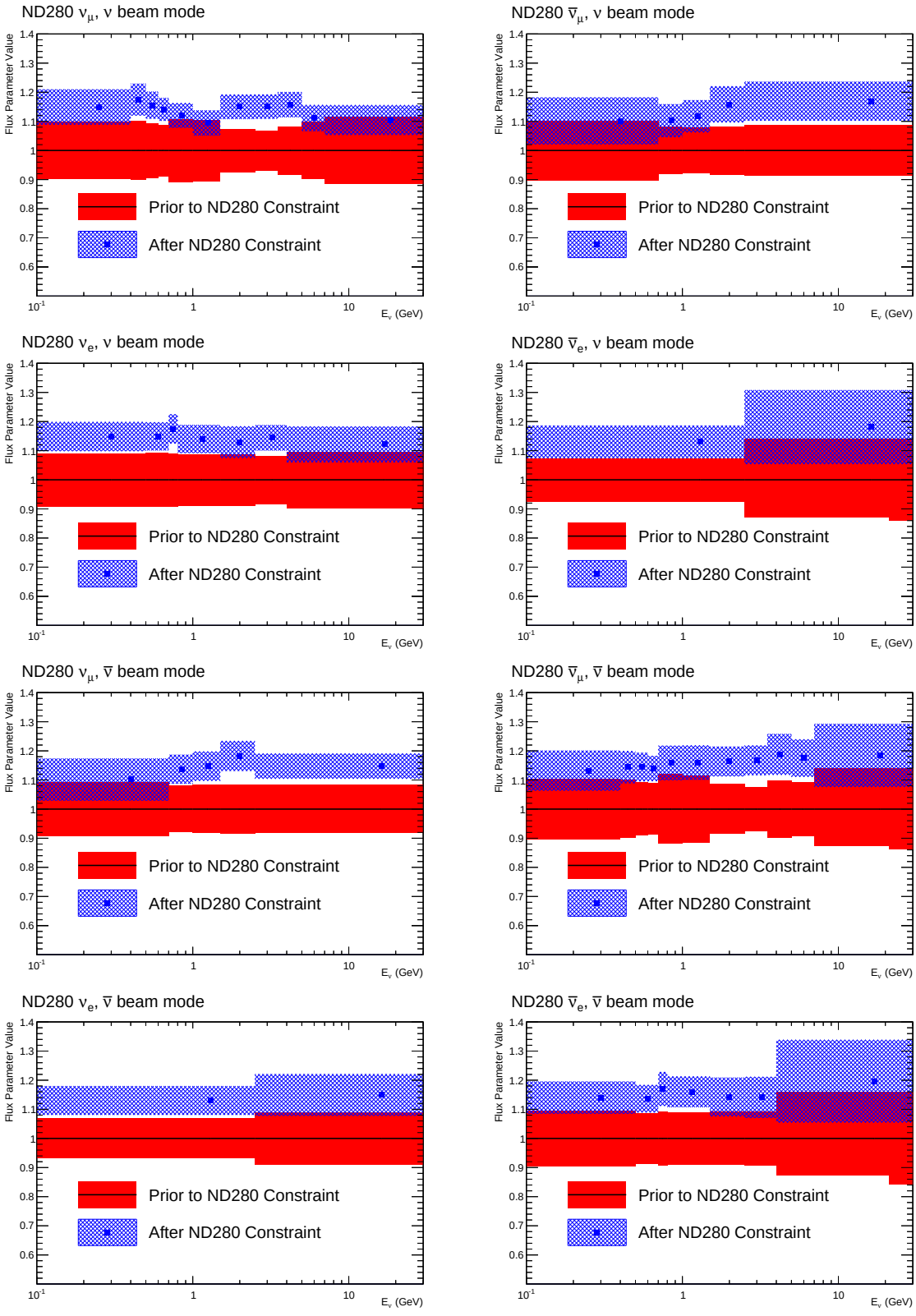

Figure 7.1: The pre-fit and post-fit ND280 flux parameters and their uncertainties.

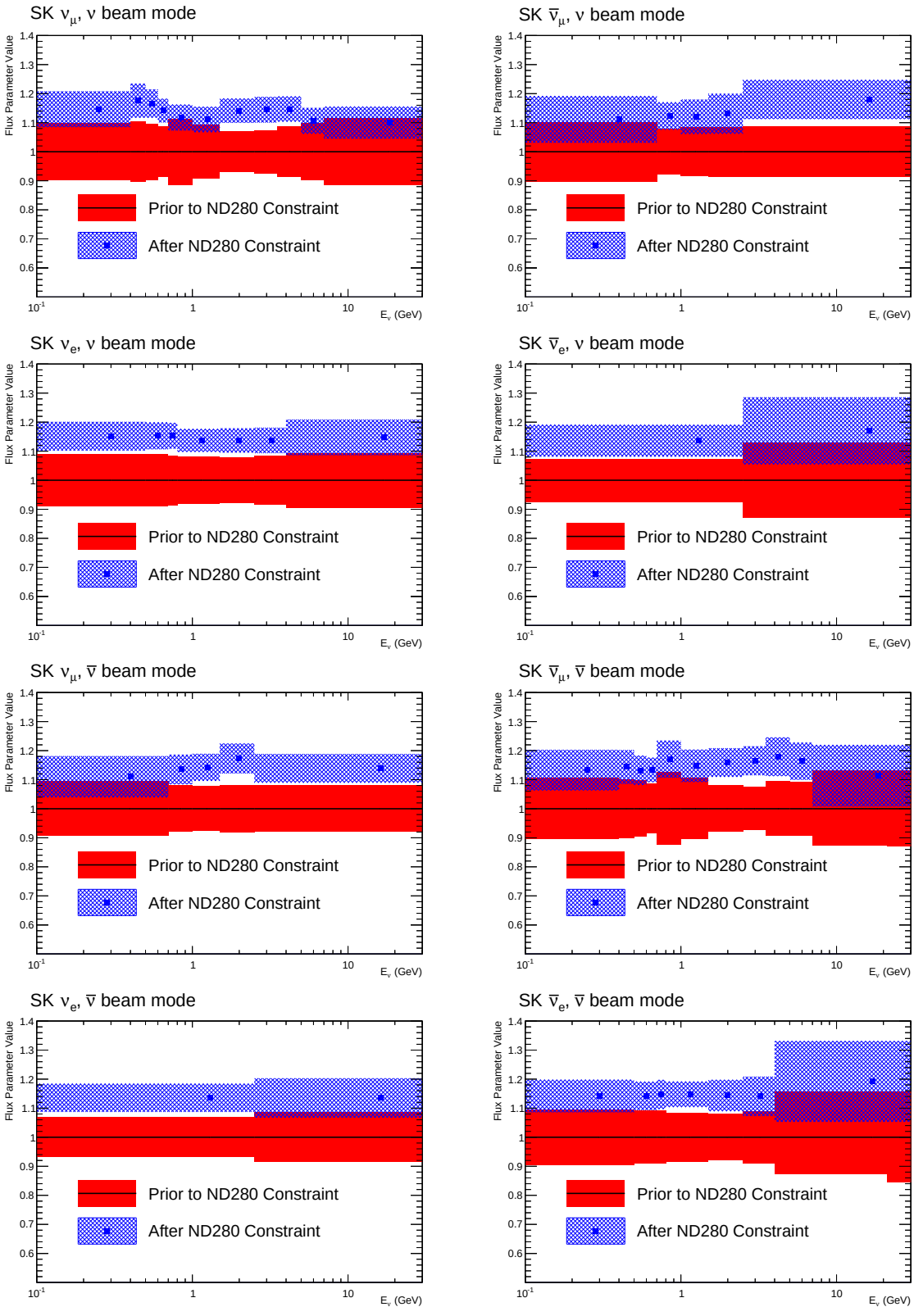

Figure 7.2: The pre-fit and post-fit SK flux parameters and their uncertainties.

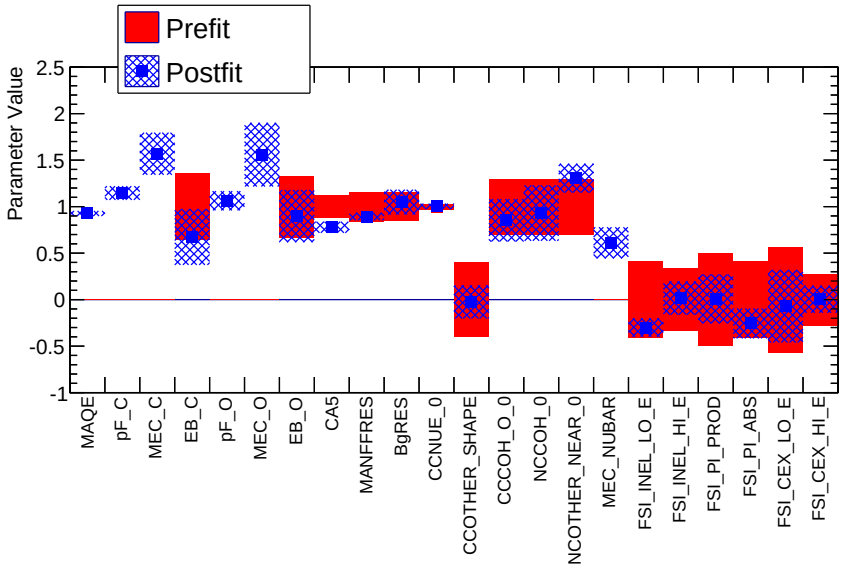

Figure 7.3: The pre-fit and post-fit cross section parameters and their uncertainties. Axis labels show the name of each parameter. Parameters are typically a ratio to NEUT nominal values, excepting the CC Other Shape parameter and the FSI parameters.

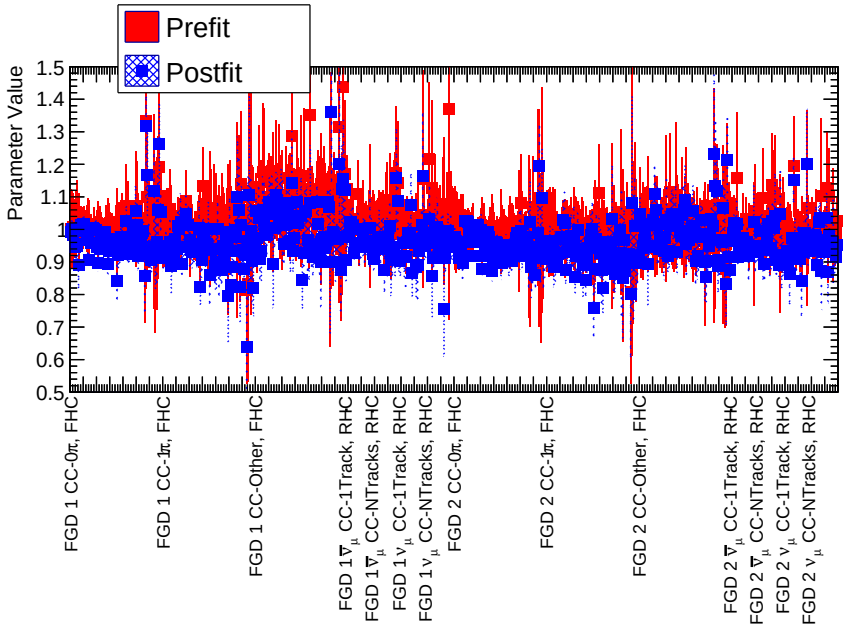

Figure 7.4: The pre-fit and post-fit observable normalization parameters and their uncertainties. Axis labels show the name of each parameter.

The parameter correlations prior to the fit and after fitting are shown in Figs. 7.5 and 7.6. The fit introduces correlations and anticorrelations between the flux and cross section parameters as intended as well as reducing the correlations between flux parameters.

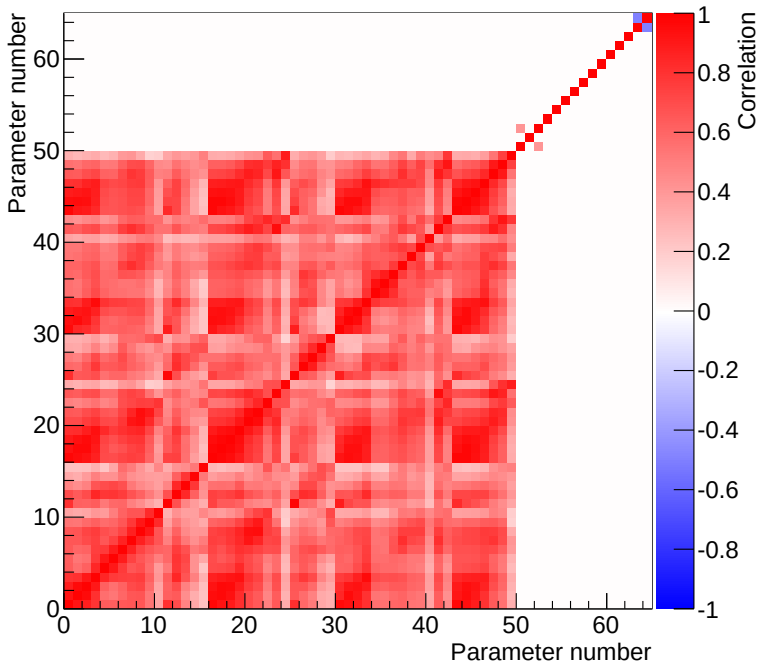

Figure 7.5: The parameter correlations prior to the ND280 fit. The parameters are 0-24 SK FHC flux, 25-49 SK RHC flux, 50 M_A^{QE}, 51 p_F ^{16}O, 52 MEC ^{16}O, 53 E_B ^{16}O, 54 $CA5^{RES}$, 55 M_A^{RES}, 56 Isospin=$\frac{1}{2}$ Background, 57 CC Other Shape, 58 CC Coh ^{16}O, 59 NC Coh, 60 NC 1 γ, 61 NC Other, 62 MEC $\bar{\nu}$ normalization, 63 σ_{ν_e}, 64 $\sigma_{\bar{\nu}_e}$

7.2.1 The p-value Calculation

The p-value for the data fit is calculated as the percentage of toy data fits with fitted $\Delta\chi^2$ greater than the observed $\Delta\chi^2$ from the data. A p-value of 0.05 or greater indicates that the fit model is considered sufficiently reasonable for fitting the data and the result can be passed to SK for the oscillation fits; this value is determined prior to fitting. The data fit gives a fitted $\Delta\chi^2$ of 1448.05 at the minimum, which when compared with the distribution of the $\Delta\chi^2$ from the toy data fits described in Section 6.2 gives a p-value of 0.086. As shown in Figure 7.7, the data

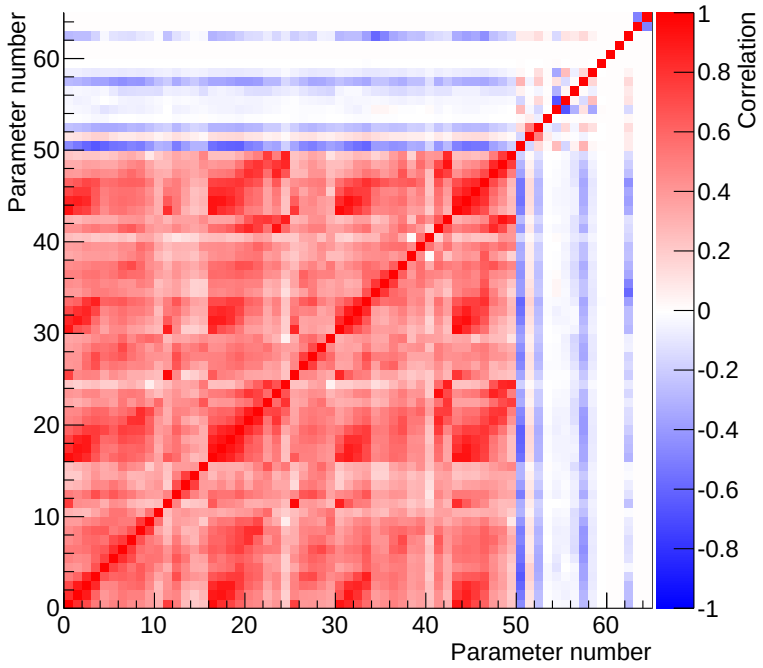

Figure 7.6: The parameter correlations included after the ND280 fit. The parameters are 0-24 SK PF flux, 25-49 SK NF flux, 50 M_A^{QE}, 51 p_F ^{16}O, 52 MEC ^{16}O, 53 E_B ^{16}O, 54 $CA5^{RES}$, 55 M_A^{RES}, 56 Isospin=$\frac{1}{2}$ Background, 57 CC Other Shape, 58 CC Coh ^{16}O, 59 NC Coh, 60 NC 1 γ, 61 NC Other, 62 MEC $\bar{\nu}$ normalization, 63 σ_{ν_e}, 64 $\sigma_{\bar{\nu}_e}$

$\Delta\chi^2$ is towards the upper tail of the distribution. Distributions for the $\Delta\chi^2$ contributions from the Poisson data terms and prior constraint terms are shown in Figures 7.8 and 7.9 respectively.

The primary source of tension between the data fit and the toys is from the $\Delta\chi^2$ contribution from the detector normalization parameters, as shown in Figures 7.10, 7.11 and 7.12. Both the flux and cross section contributions fall within the main part of their corresponding distributions and the overall sample contribution shown in Figure 7.8 does as well. This is not unexpected, as the detector observable normalization parameters use many approximations to the ND280 systematics in order to work in the fit, such as being modeled as Gaussian parameters.

7.3 Impact at Super-Kamiokande

The oscillation analysis at SK uses the ND280 fit result as the prior values and constraints for many parameters; as discussed in Chapter 3, the ND280 fit constrains the expected neu-

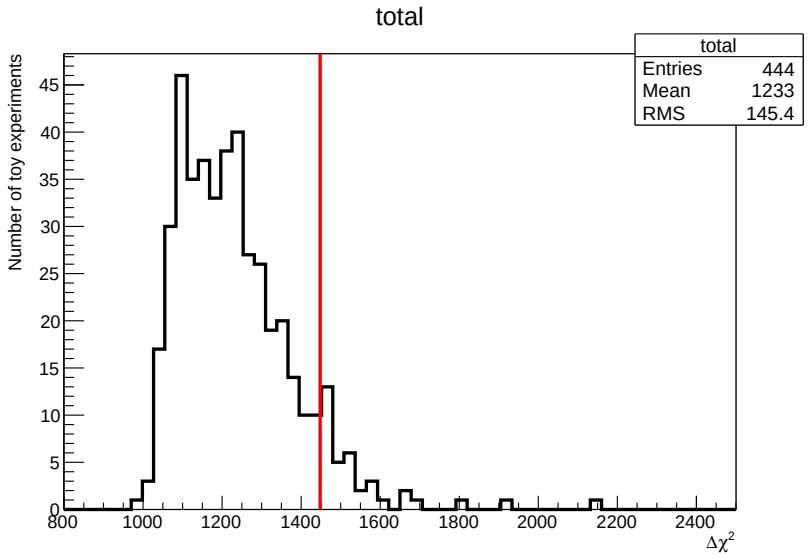

Figure 7.7: Total $\Delta\chi^2$ distribution for 444 toy fit results (black), with the value from the fit to the data superimposed in red. The total is the sum of the contribution from the Poisson data term and the contribution from the prior constraint term. The total $\Delta\chi^2$ from the fit to the data is 1448.05, which corresponds to a p-value of 0.086.

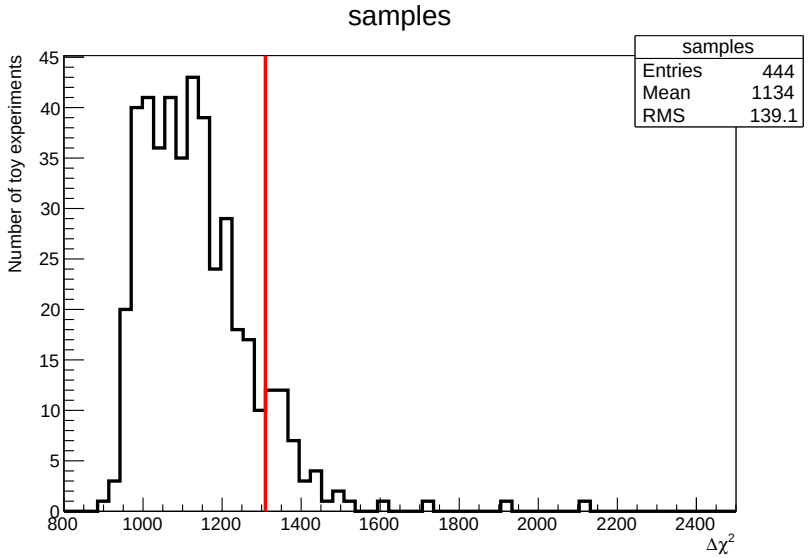

Figure 7.8: Contribution from the Poisson data terms to total $\Delta\chi^2$ distribution for 444 toy fit results (black), with the value from the fit to the data superimposed in red.

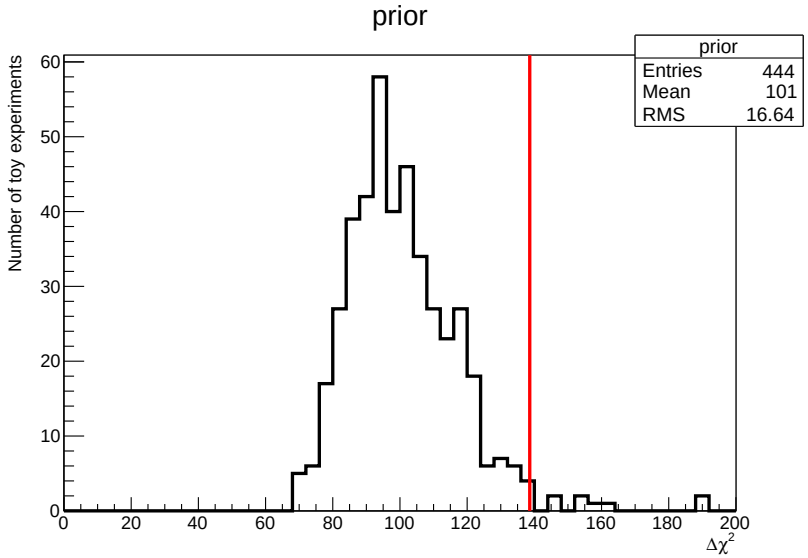

Figure 7.9: Contribution from prior constraint term to total $\Delta\chi^2$ distribution for 444 toy fit results (black), with the value from the fit to the data superimposed in red. This is the sum of the prior constraint terms from the flux, cross-section and detector parameters.

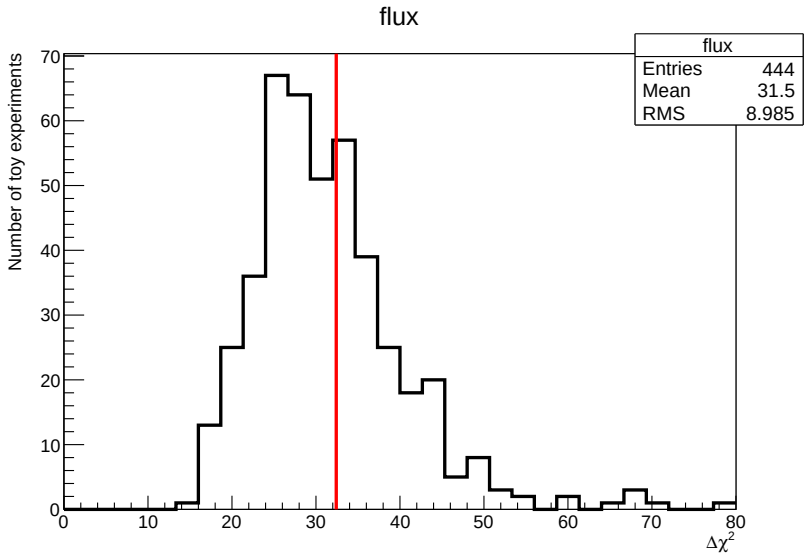

Figure 7.10: Contribution from flux constraint term to the prior constraint term $\Delta\chi^2$ distribution from 444 toy fit results (black), with the value from the fit to the data superimposed in red.

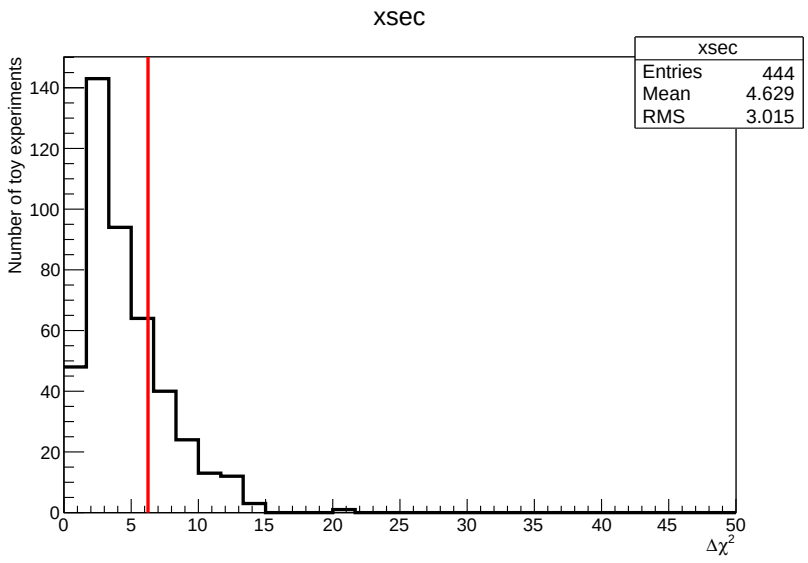

Figure 7.11: Contribution from cross section constraint term to the prior constraint term $\Delta\chi^2$ distribution from 444 toy fit results (black), with the value from the fit to the data superimposed in red.

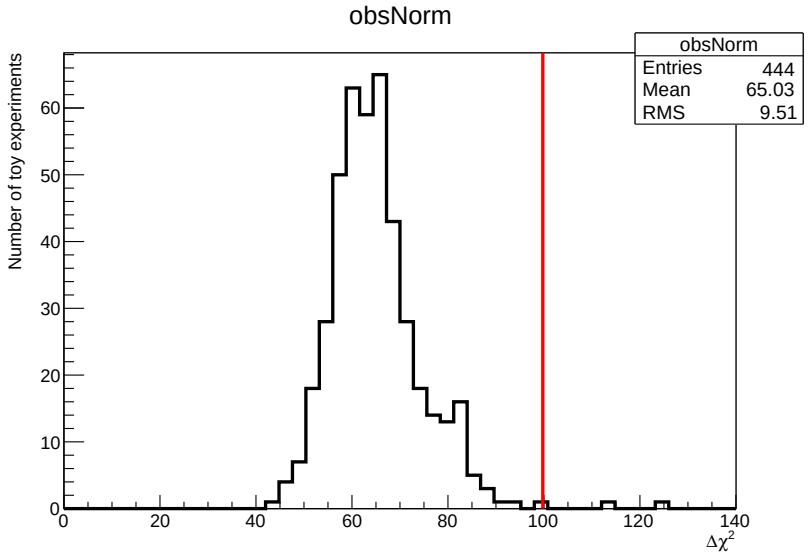

Figure 7.12: Contribution from detector constraint term to the prior constraint term $\Delta\chi^2$ distribution from 444 toy fit results (black), with the value from the fit to the data superimposed in red.

trino spectra at SK. Because of the addition of the FGD 2 sample containing events on water, the various oxygen cross section parameters used at SK (E_B, p_F and 2p-2h ^{16}O) can now be constrained with the near detector fit results. Table 7.2 shows the uncertainties on the prediction at SK using the previous FGD 1-only ND280 fitted constraint, and Table 7.3 shows the uncertainties on the prediction at SK using the new FGD 1 + FGD 2 ND280 constraint as described in this thesis, for the joint ν_μ – ν_e analysis. The addition of FGD 2 as a target in the ND280 fit gives an oxygen target at ND280, thus allowing oxygen target-specific cross-section parameters to be constrained using ND280.

	FHC ν_μ	FHC ν_e	RHC ν_μ	RHC ν_e
ND280-Constrained Parameters	2.7%	3.1%	3.4%	3.0%
ND280-Unconstrained Parameters	5.0%	4.7%	10.0%	9.8%
Flux × XSec (Post ND280)	5.7%	5.6%	10.6%	10.2%
SK FSI + SI	3.0%	2.4%	2.1%	2.2%
SK Systematics	4.0%	2.7%	3.8%	3.0%
Total	7.7%	6.8%	11.6%	11.0%

Table 7.2: Fractional error on the prediction for number of events at SK, broken down by source, using the FGD 1 only ND280 fit results. FHC numbers use data from Runs 1 – 4, and RHC numbers use data from Runs 5 – 6. Flux and cross-section are shown separately for the pre-ND280 case. Uncertainties shown are calculated from the RMS of the event rates when 10000 parameter variations are thrown[99] from the final ND280 fit covariance matrix.

As Table 7.2 shows, the largest source of uncertainty at SK when only FGD 1 is included in the ND280 fit comes from uncertainties on cross-section parameters with carbon-oxygen differences: E_B, p_F and the 2p-2h normalization (see row labeled "ND280-Unconstrained Parameters") . As the FGD 1 only analysis only contains a carbon target and extrapolation between target materials is not well understood, previous fits were not able to provide strong constraints on those cross-section parameters. In contrast, the FGD 1 + FGD 2 fit is able to constrain these target-specific cross-section parameters as shown by the reduced contribution from ND280-unconstrained parameters in Table 7.3. This leaves only a few cross-section parameters that cannot be constrained by the ND280 data: the NC γ normalization, the NC other normalization and the CC ν_e/ν_μ and CC $\bar{\nu}_e/\bar{\nu}_\mu$ cross-section ratio normalizations which are mentioned in

	ν_μ FHC	ν_e FHC	$\bar{\nu}_\mu$ RHC	$\bar{\nu}_e$ RHC
Flux (Pre-ND280)	7.6%	8.9%	7.1%	8.0%
XSec (Pre-ND280)	9.7%	7.2%	9.3%	10.1%
Flux × XSec (Post-ND280)	2.9%	4.2%	3.4%	4.6%
FSI + SI	1.5%	2.5%	2.1%	2.5%
SK Detector Syst	3.9%	2.4%	3.3%	3.1%
Total (Pre-ND280)	12.0%	11.9%	12.5%	13.7%
Total (Post-ND280)	5.0%	5.4%	5.2%	6.2%

Table 7.3: Fractional error on the prediction for number of events at SK, broken down by source. Pre-ND280 indicates that the ND280 fit result was not used as the prior, while post-ND280 indicates that the ND280 fit using FGD 1 and FGD 2 events as described in this thesis was used as the prior. Flux and cross-section are shown separately for the pre-ND280 case. Uncertainties shown are calculated from the RMS of the event rates when 10000 parameter variations are thrown[99] from the final ND280 fit covariance matrix.

	ν_μ FHC	ν_e FHC	$\bar{\nu}_\mu$ RHC	$\bar{\nu}_e$ RHC
ND280-Constrained Flux × XSec	2.82%	2.84%	3.27%	3.19%
CC ν_e/ν_μ + CC $\bar{\nu}_e/\bar{\nu}_\mu$	0.01%	2.60%	0.00%	1.51%
NC γ	0.00%	1.47%	0.00%	2.93%
NC Other	0.77%	0.16%	0.75%	0.33%

Table 7.4: Fractional error on the prediction for number of events at SK from cross-section and flux, broken down to show the contributions from parameters unconstrained by ND280. The combination of these uncertainties gives the flux × cross-section uncertainties shown in Table 7.3. Uncertainties shown are calculated from the RMS of the event rates when 10000 parameter variations are thrown[61].

Chapter 3. These have a much smaller contribution to the overall uncertainty than E_B, p_F and the 2p-2h normalization, as shown in Table 7.4.

All four samples – FHC ν_μ and ν_e and RHC ν_μ and ν_e – benefit from the improvement to the cross-section constraints. In the case of the FHC ν_μ samples, this reduces a flux × cross-section uncertainty of 2.7% and an ND280 unconstrained cross-section parameter uncertainty of 5%, which combines to give 5.7% flux × cross-section uncertainty as shown in row 3 of Table 7.2, to a single flux × cross-section uncertainty of 2.9% as shown in row 3 of Table 7.3. This allows the overall uncertainty on the prediction to be reduced from 7.7% using only FGD 1 in the ND280 fit, to 5%. The RHC samples show an even greater reduction in overall uncertainty, due to a larger contribution to the uncertainty from the oxygen-specific

cross-section parameters – 10% for ν_μ and 9.8% for ν_e respectively. With the ability to constrain oxygen cross-sections, this combines with the flux $\times$ cross-section uncertainties to give a total uncertainty 3.4% for ν_μ and 4.6% for ν_e from the flux and cross-section parameters. The uncertainty on the prediction as a function of the neutrino energy for the four samples can be seen in Figures 7.13, 7.14, 7.15 and 7.16. Outside of the high energy bins for the ν_e spectra, the uncertainty is significantly reduced for the entire energy range. These show that not only does the improvement to the ND280 constraint improve the overall uncertainties on the predictions but also improves the uncertainty across the neutrino energy spectrum.

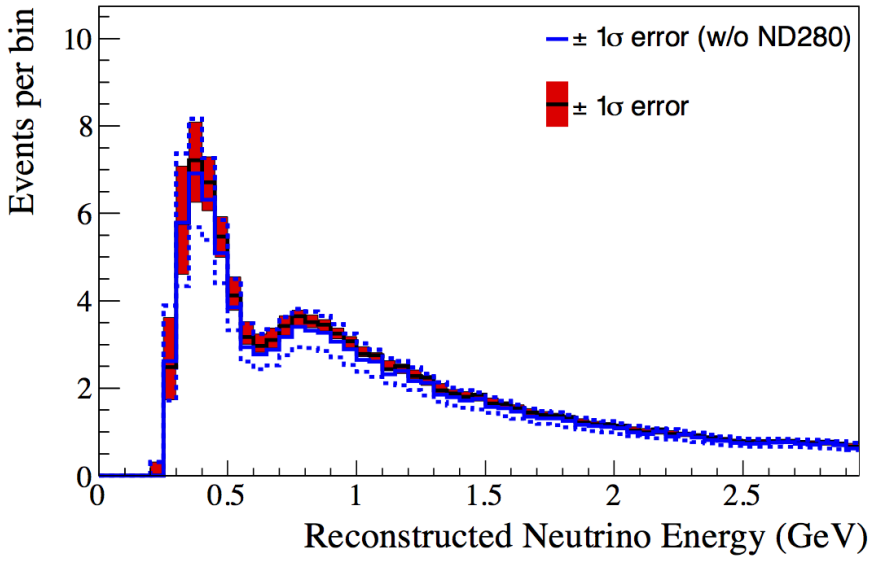

Figure 7.13: Predicted energy spectrum for FHC ν_μ events at SK, with and without ND280 constraints.

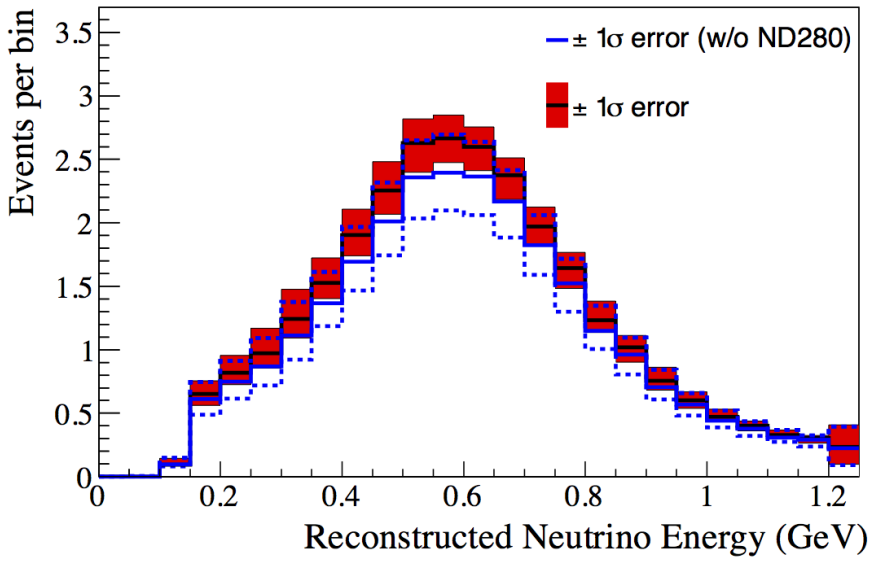

Figure 7.14: Predicted energy spectrum for FHC ν_e events at SK, with and without ND280 constraints.

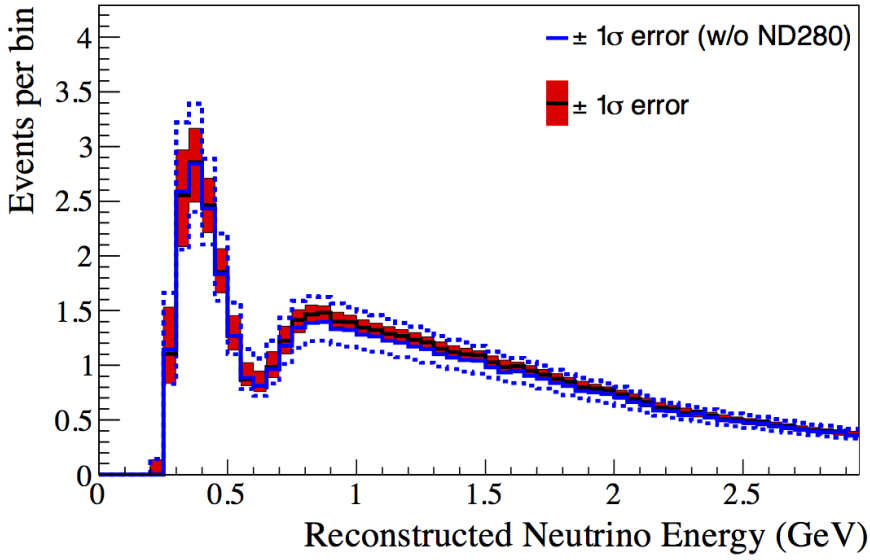

Figure 7.15: Predicted energy spectrum for RHC $\bar{\nu}_\mu$ events at SK, with and without ND280 constraints.

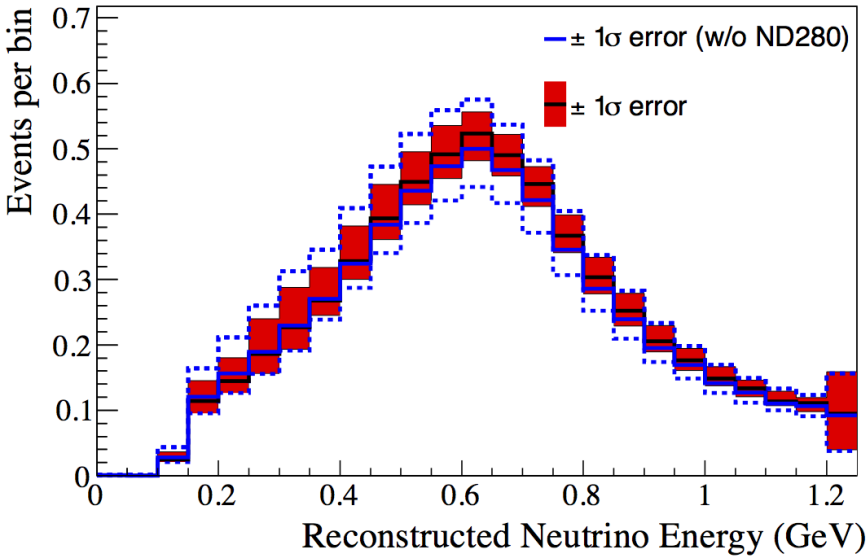

Figure 7.16: Predicted energy spectrum for RHC $\bar{\nu}_e$ events at SK, with and without ND280 constraints.

7.3.1 Oscillation Fit Results at Super-Kamiokande

The oscillation fit results shown here are the result of fitting both neutrino and antineutrino mode data looking at ν_μ disappearance and ν_e appearance and using the near detector fit results described in this thesis as the prior constraints for flux and cross section parameters in the fit. The fitted 2D contours for $\sin^2\theta_{13}$ vs δ_{CP} are shown in Figures 7.17, 7.18 for normal and inverted mass hierarchy respectively, and $\sin^2\theta_{13}$ vs Δm^2_{32} (Δm^2_{13} for IH) contours are shown in Figures 7.19 and 7.20. The other oscillation parameters are marginalized over according to the priors in Table 3.3. These plots show both the Run 1 – 7c analysis results (fitting neutrino and antineutrino mode data simultaneously), which are the latest T2K oscillation fit results and the first to use the FGD 1 + FGD 2 ND280 fit results described in this thesis, and the Run 1 – 4 joint oscillation fit results, which simultaneously fit ν_μ disappearance and ν_e appearance using neutrino mode data only[30]. The Run 1 – 4 fit uses the previous FGD 1-only ND280 results, as can be seen from the larger 68% and 90% CL contours, with a significant portion of the changes coming from overall increase in statistics at SK.

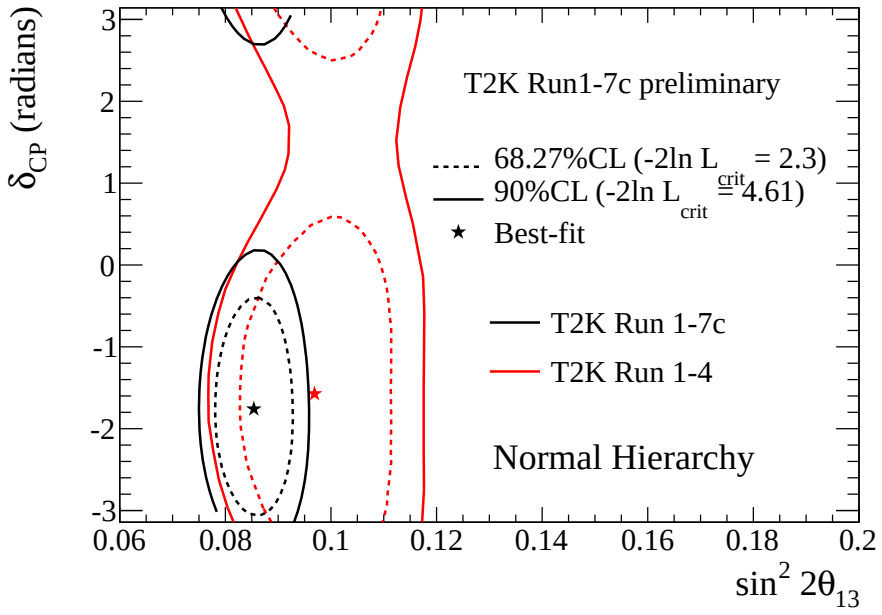

Figure 7.17: 2D contours for $\sin^2\theta_{13}$ and δ_{CP} for the Run 1 – 7c joint analysis and the Run 1 – 4 joint analysis for normal mass hierarchy. [61]

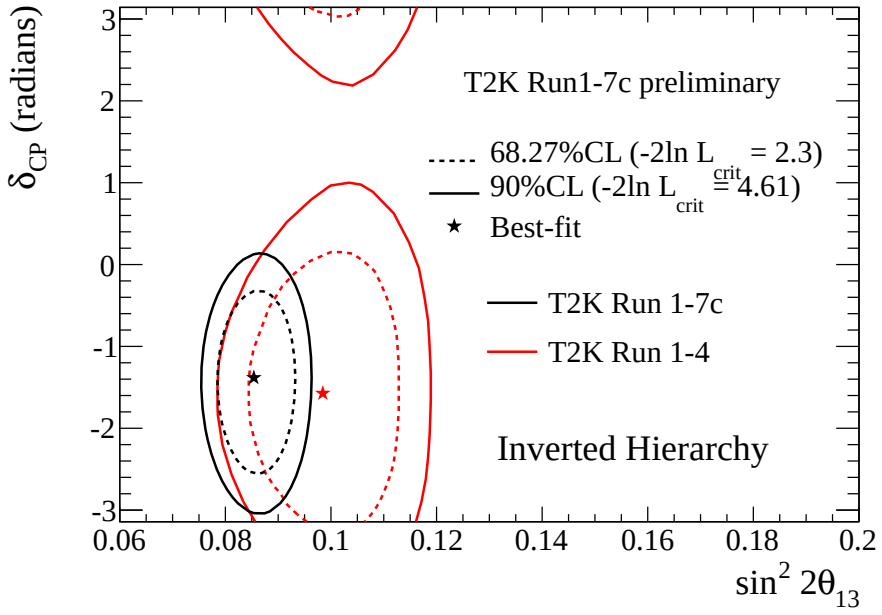

Figure 7.18: 2D contours for $\sin^2\theta_{13}$ and δ_{CP} for the Run 1 – 7c joint analysis and the Run 1 – 4 joint analysis for inverted mass hierarchy. [61]

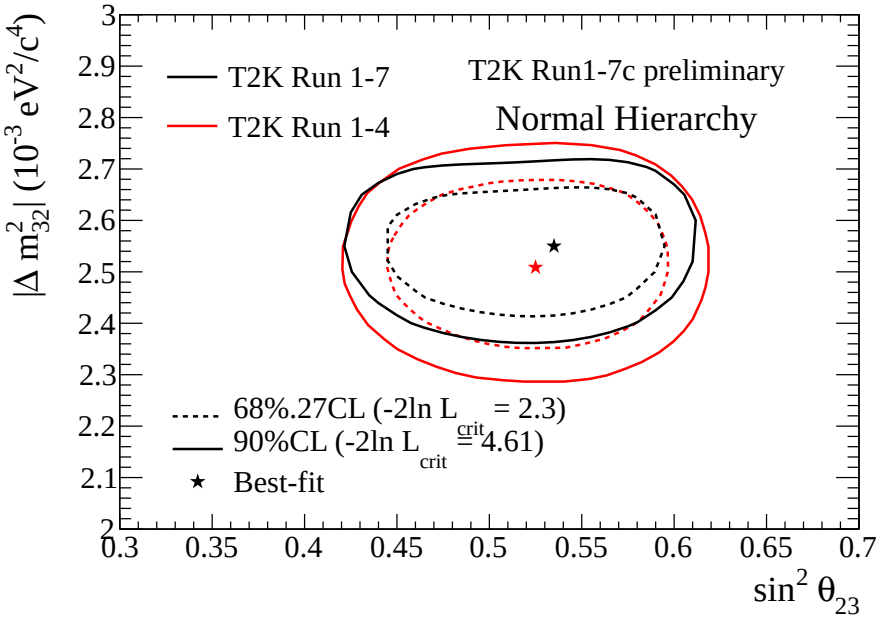

Figure 7.19: 2D contours for $\sin^2\theta_{23}$ and Δm^2_{32} for the Run 1 – 7c joint analysis and the Run 1 – 4 joint analysis for normal mass hierarchy. [61]

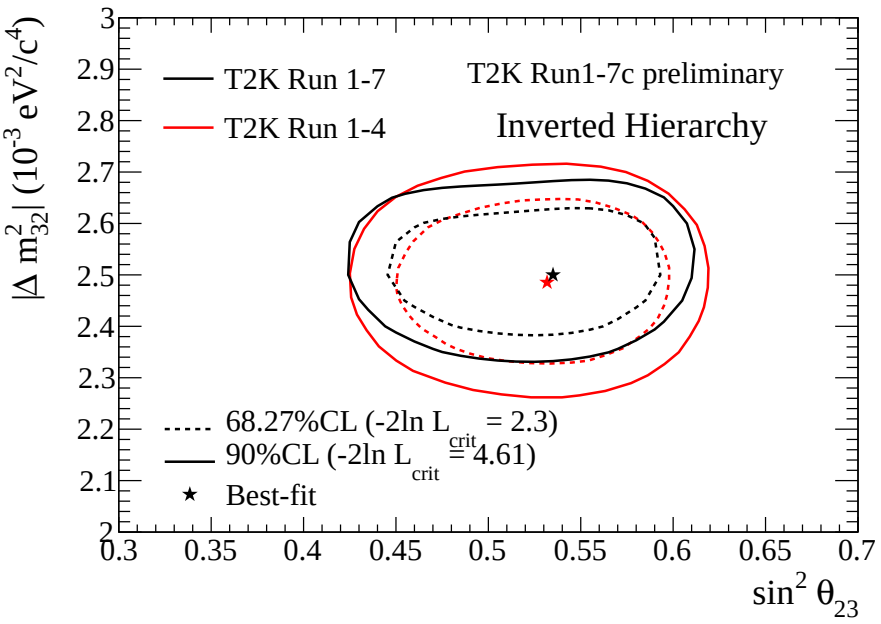

Figure 7.20: 2D contours for $\sin^2\theta_{23}$ and Δm^2_{13} for the Run 1 – 7c joint analysis and the Run 1 – 4 joint analysis for inverted mass hierarchy. [61]

In order to get a sense of how the improvements to the ND280 constraint impact the oscillation contours, it is useful to perform a simple estimation of the uncertainty on the contours in order to compare the previous FGD 1-only result, as described in Table 7.2 and the new FGD 1 + FGD 2 result shown in Table 7.3. However, the uncertainty in the contours comes from two sources: the systematic uncertainty on the SK rate prediction and the statistical uncertainty on the total number of events at SK, which scales with the total accumulation of protons on target. The statistical uncertainty is larger than that from systematics, particularly in the case of ν_e measurements, making it difficult to compare previous results. Instead, the overall uncertainties are best compared using the same SK statistics, as the systematics contribution is largely unaffected by the increase in statistics. As discussed earlier, the most significant difference in uncertainty on the rate prediction at SK comes from the unconstrained oxygen cross-section parameters, as previous to this analysis, the unconstrained cross-section uncertainties dominated the contributions from the SK detector systematics and flux.

Of the current T2K analyses, the least statistics-dominated is the ν_μ disappearance results

measuring θ_{23}. The current preliminary Run 1 – 7c results give an overall fractional uncertainty of $^{+0.086}_{-0.128}$ on the value of $\sin^2\theta_{23}$[61] for normal hierarchy. To estimate the uncertainty on θ_{23}, one can make a few simplifying assumptions: that the uncertainty on the expected number of events is an energy-independent normalization uncertainty, and that the oscillation probability for $\nu_\mu \rightarrow \nu_\mu$ can be approximated as

$$P(\nu_\mu \rightarrow \nu_\mu) \sim 1 - \sin^2 2\theta_{23} \tag{7.1}$$

where $\sin^2 2\theta$ is close to 1. The observed number of events N_{obs} can be expressed as

$$N_{obs} = \int \frac{dN}{dE}\left(1 - \sin^2 2\theta \sin^2\left(\frac{\Delta m^2 L}{E}\right)\right) dE \tag{7.2}$$

By then treating the error on the number of expected events as energy independent, this can be written as

$$N_{obs} = N_{exp}\left(1 - \sin^2 2\theta\left[\int\left(\frac{1}{N_{exp}}\right)\frac{dN}{dE}\sin^2\left(\frac{\Delta m^2 L}{E}\right) dE\right]\right) \tag{7.3}$$

The integral in the previous equation gives

$$\int\left(\frac{1}{N_{exp}}\right)\frac{dN}{dE}\sin^2\left(\frac{\Delta m^2 L}{E}\right) dE = 1 - \frac{N_{obs}}{N_{exp,unosc}} \tag{7.4}$$

and so the approximate error on $\sin^2 2\theta$ can be found:

$$\delta(\sin^2 2\theta) = \frac{1}{1 - \frac{N_{obs}}{N_{exp,unosc}}}\sqrt{\left(\frac{dN_{obs}}{N_{obs}}\right)^2 + \left(\frac{dN_{exp,unosc}}{N_{exp,unosc}}\right)^2} \tag{7.5}$$

with N_{obs} the observed number of ν_μ events, $N_{exp,unocs}$ the expected number of events assuming no oscillation, dN_{obs} being the Poisson statistical error on the observed number of events and $dN_{exp,unosc}$ being the systematic uncertainty on the predicted number of events at SK assuming no oscillation. While this formula does not account for the energy dependence in the analysis, this is nonetheless a useful tool to estimate the effect of the new constraint.

	FHC ν_{mu}	RHC $\bar{\nu}_\mu$
Using old ND280 Constraint	0.040	0.0939
Using new ND280 Constraint	0.035	0.0742

Table 7.5: Expected Fractional Uncertainty on $\sin^2 2\theta_{23}$ for Runs 1 – 7.

For the Run 1 – 7 ν_μ disappearance, SK observes 135 FHC ν_μ events and 66 RHC $\bar{\nu}_\mu$ events, with 521.8 and 184.8 events expected with no oscillations respectively[61]. Combined with the systematic uncertainties in Tables 7.3 and 7.2, an estimate of the overall uncertainty on $1-\sin^2 2\theta_{23}$ can be made using Run 1 – 7 statistics for both prior constraints. The fractional uncertainties are shown in Table 7.5. For FHC ν_μ signal, we expect roughly a 15% reduction in overall uncertainty on the contour due to the improved prior constraint. The uncertainty reduction for the RHC $\bar{\nu}_\mu$ is even greater, due to the larger impact from oxygen cross-section uncertainties. Here the uncertainty is reduced by $\sim$ 25% compared to using the FGD 1-only constraint. As an additional comparison, Figures 7.21 and 7.22 show the T2K oscillation contours from the Run 1 – 4 SK analysis, using the FGD 1-only Run 1 – 4 ND280 constraints, and the Run 1 – 7 SK data joint oscillation analysis, using the new ND280 fit which uses Runs 1 – 7 ND280 data, compared with Run 1 – 4 SK contours made using the new FGD 1 + FGD 2 ND280 fit constraints made with Run 1 – 7 ND280 data. This additional contour is shown as a blue line. Due to time constraints, the Run 1 – 4 SK contour using the FGD 1 + FGD 2 prior constraints is shown, rather than comparing FGD 1-only Run 1 – 7 SK fits; however, the effect of the systematics improvement is still visible. Additionally only the $\sin^2\theta_{23} - \Delta m^2_{13}$ contours are shown, as the other results use the reactor constraints, which are implemented differently for the fits with FGD 1-only constraints and the fits with the FGD 1 + FGD 2 constraints. This shows an overall improvement in the contour size for both normal and inverted hierarchy fits, with the FGD 1 + FGD 2 constrained SK Run 1 – 4 fit contours sitting much closer to the Run 1 – 7 contours. This shows that the new oxygen constraints from ND280 currently provide a noticeable reduction in the size of oscillation contours even at current statistics, and will show even greater impact as more statistics are collected.

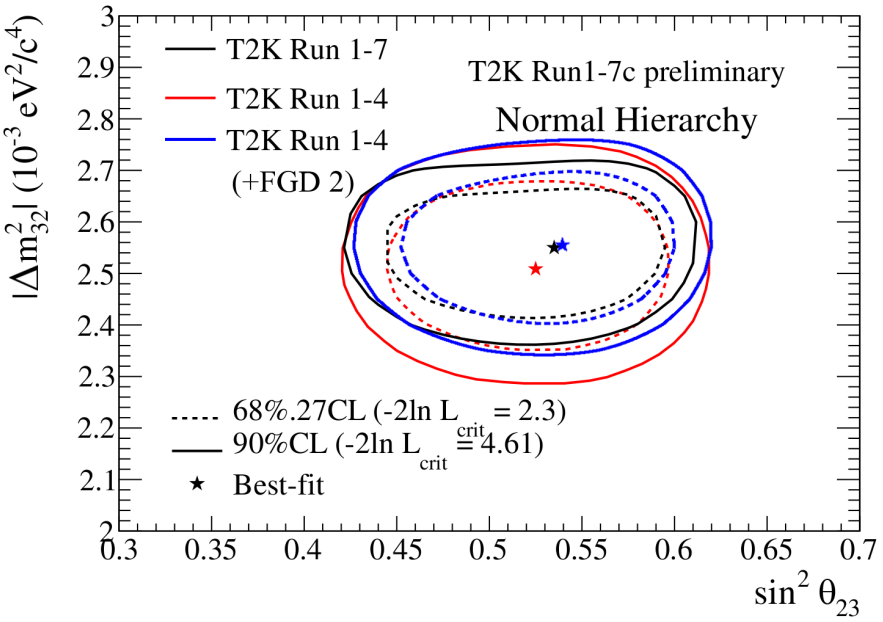

Figure 7.21: 2D contours for $\sin^2\theta_{23}$ and Δm^2_{32} for the Run 1 – 4 joint analysis for normal mass hierarchy using the FGD 1 + FGD 2 ND280 fit result compared with other T2K contours. 2D contours for $\sin^2\theta_{23}$ and Δm^2_{13} for the Run 1 – 7c joint analysis and the Run 1 – 4 joint analysis for normal mass hierarchy are taken from [61]. The difference between the red and blue contours shows the improvement due to the inclusion of the FGD 2 data in the ND280 fit, for an oscillation fit to the Run 1 – 4 SK data. The 1D $\sin^2\theta_{23}$ range is reduced by $\sim$3% and the 1D Δm^2_{13} range is reduced by $\sim$11%.

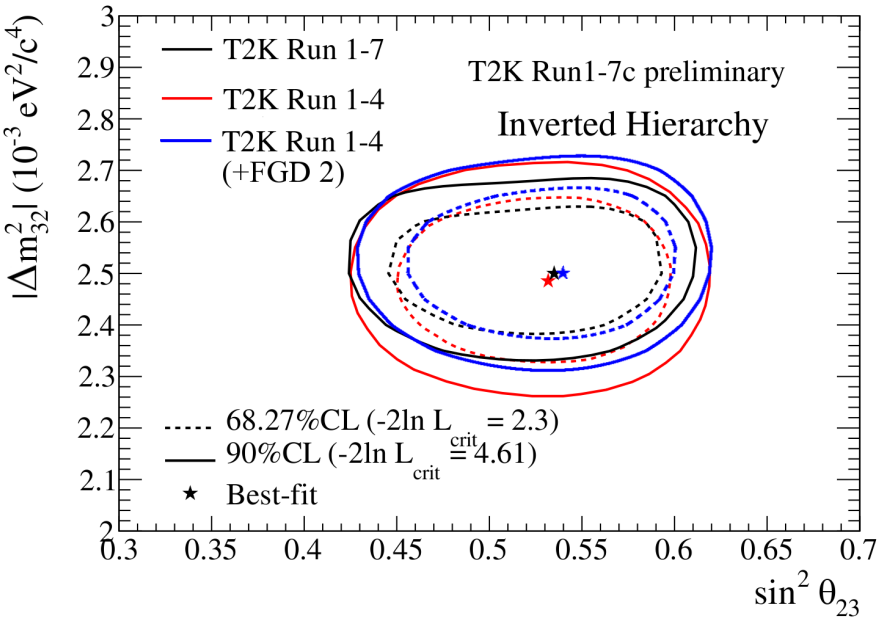

Figure 7.22: 2D contours for $\sin^2\theta_{23}$ and Δm^2_{13} for the Run 1 – 4 joint analysis for inverted mass hierarchy using the FGD 1 + FGD 2 ND280 fit result compared with other T2K contours. 2D contours for $\sin^2\theta_{23}$ and Δm^2_{13} for the Run 1 – 7c joint analysis and the Run 1 – 4 joint analysis for inverted mass hierarchy are taken from [61]. The difference between the red and blue contours shows the improvement due to the inclusion of the FGD 2 data in the ND280 fit, for an oscillation fit to the Run 1 – 4 SK data. The 1D $\sin^2\theta_{23}$ range is reduced by $\sim$2% and the 1D Δm^2_{13} range is reduced by $\sim$8%.

Chapter 8

Further Parameterization Studies

T2K currently splits several of the CCQE parameters into carbon and oxygen versions of the parameters for use in the analysis at SK, as discussed in Chapter 3 to account for nuclear effects and remove possible model dependencies. This allows such parameters specific to carbon targets to be strongly constrained using only FGD 1, as it only contains carbon as a target material, and then use the strong constraints on carbon to constrain the oxygen versions of those parameters in FGD 2, as it contains both carbon and oxygen as target materials. This additionally removes any dependence on modeling how these parameters scale from one nucleus to another. Splitting fit parameters by target is not directly equivalent to a cross-section study using the near detectors, as the fit is still a simultaneous constraint on the flux and cross section parameters. These parameters are the 2p-2h scaling, E_B and p_F parameters, all which primarily affect the CC-0π samples. Chapter 3 discusses the T2K implementation of the parameters in more detail, and a description of the neutrino interaction modeling is found in Chapter 1.

There is currently no strong physical reasoning for differences in the axial mass M_A^{QE} that depend on the target nucleus, as it only relates to the calculation of the neutrino-nucleon interaction form factors. While T2K cannot measure neutrino interactions on free nucleons and nuclear effects need to be accounted for, the nucleus-based parameters, such as the Fermi momentum, binding energy and the 2p-2h normalization, were introduced to account for such

effects and in a good model should absorb all such effects. However, the M_A^{QE} parameter used in the T2K fit is necessarily an effective one and may nonetheless have some dependence on the target nuclei that would otherwise be included in the 2p-2h parameters, as the 2p-2h model was introduced specifically to absorb nuclear effects that would otherwise affect M_A^{QE}. If 2p-2h has been well modeled, there should not be any difference between target nuclei for M_A^{QE}. In addition, the value of M_A^{QE} has a significant impact on the expected number of CCQE events at ND280, and the primary signal for the SK analysis. In this case, if our effective parameter was picking up nuclear effects that caused carbon and oxygen versions of the axial mass to have significantly different values, this could change the overall predicted rates at SK.

For CC-1π interactions, the effective parameters for $C_A^5(0)$ and M_A^{RES} described in Section 3.3.2 are the largest contributors to the resonant pion production at the T2K near detector. Like M_A^{QE}, these are nucleon-level parameters and in theory should not vary across nuclear targets. However, as neutrino – nucleus interactions are less well understood for pion production than for quasielastic processes, splitting these parameters into effective carbon and oxygen versions may allow potential interaction rate differences due to target be accounted for. Additionally, the near detector fit is more sensitive to those parameters, which is important for sufficiently constraining oxygen target parameters. In general, because the measurement of oxygen parameters must be done through subtraction, the fitted uncertainties will be larger than the uncertainties on their carbon counterparts.

Two separate studies were done to look for residual dependencies of effective cross-section parameters on the nuclear target, in order to probe the robustness of the cross-section model:

1. Splitting the quasielastic axial mass parameter M_A^{QE} by target.

2. Splitting the resonant pion production form factor $C_A^5(0)$ and the resonant axial mass parameter M_A^{RES} by target.

For both studies, all other parameters were implemented identically to the official near detector fit described in the previous chapters of this thesis. These studies are not part of the official

T2K analysis, but are an additional extension of the analysis to serve as a consistency check.

8.1 Fitting M_A^{QE} for Oxygen and Carbon Targets

We first investigate splitting a single cross-section parameter into two separate parameters, one on a carbon target and the other on oxygen. For this, the CCQE axial mass M_A^{QE} is chosen, as it affects the primary signal at T2K. A split version of this parameter might allow the near detector to more accurately represent how well the effective parameter is fit for use in the oscillation analysis, as well as pick up any nuclear effects not accounted for in the 2p-2h, binding energy or Fermi momentum parameters. From a technical standpoint, separate versions of the axial mass parameter are simple to implement in the fit, as this is done by separately reweighting carbon and oxygen events in the Monte Carlo in accordance to the new parameters. As we do not use external constraints for the CCQE cross section parameters in the near detector fit, there are no prior assumptions or correlations to take into account when creating a separate oxygen-based parameter. The same response splines described in Section 3.3.2 are used for both carbon and oxygen.

8.1.1 Additional Validation

Before running the data fit, several of the validation studies described in Chapter 6 were performed with the split M_A^{QE} parameters, as well as a few toy studies with the oxygen and carbon axial mass varied separately to ensure the parameters were correctly implemented. Like the standard near detector fit, parameters are fitted to their prior values with near machine precision. Both M_A^{QE} ^{12}C and M_A^{QE} ^{16}O parameters have fit to the value set for M_A^{QE} in the nominal MC, with M_A^{QE} ^{16}O having a larger uncertainty due to lower statistics on oxygen as expected. This indicates that the parameters are both being fit and do not have unexpected effects on other parameter values. Plots for these fits are shown in Figures 8.1, 8.2 and 8.3.

Two fake data fits have been performed in order to validate the performance of the parameter splitting code:

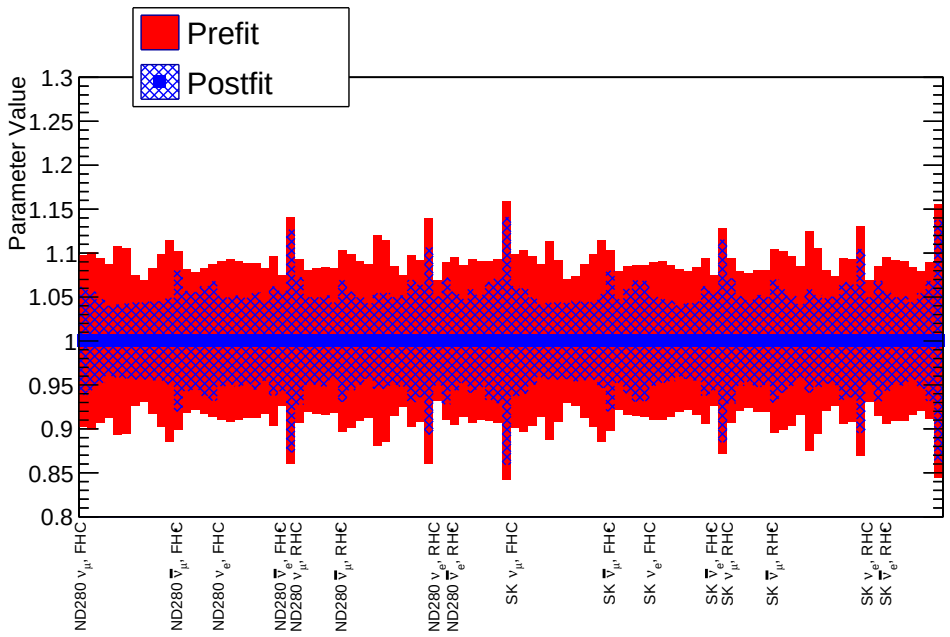

Figure 8.1: Fitted parameter values and uncertainties for the flux for the fit to the nominal MC with split M_A^{QE}.

1. M_A^{QE} ^{12}C $= 1$ GeV/c^2 and M_A^{QE} ^{16}O $= 1.2$ GeV/c^2

2. M_A^{QE} ^{12}C $= 1.2$ GeV/c^2 and M_A^{QE} ^{16}O $= 1$ GeV/c^2

where the nominal NEUT value is $M_A^{QE} = 1.2$. All other parameter values were set to nominal. As all previous fits were performed on fake data with a single set value for M_A^{QE}, these simple tests can verify that the fit machinery is able to correctly fit two separate values of M_A^{QE}. Plots of the fitted cross-section parameters for these are shown in Figures 8.4 and 8.5 and show that the parameters fit separately and correctly.

8.1.2 Results

The final $\Delta\chi^2$ for the M_A^{QE} carbon and oxygen fit was found to be 1447.9. This is very close to, though slightly lower than, the original $\Delta\chi^2$ for the data fit with a single M_A^{QE} parameter. Figure 8.6 show the cross section parameter fit values compared with the original data fit discussed in Chapter 7. These are shifted slightly compared to the original data fit, on the sub-$<1\%$ level

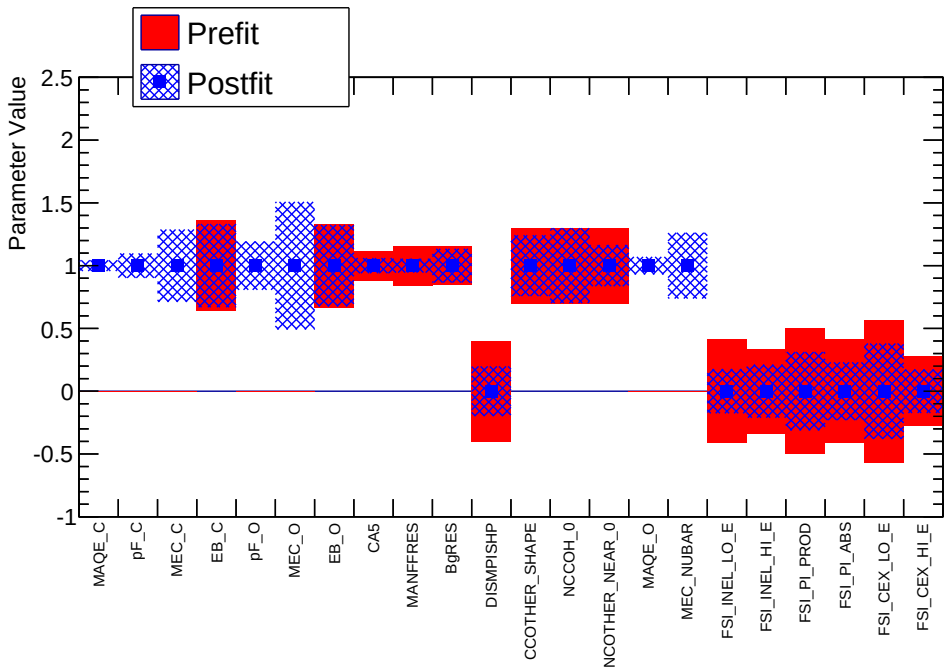

Figure 8.2: Fitted parameter values and uncertainties for the cross section parameters for the fit to the nominal MC with split M_A^{QE}.

– both the flux and observable normalization parameters show a small decrease. The fitted values are most easily compared using a simple paired test statistic to remove the correlated component of the uncertainties in order to evaluate significance. For a parameter P this is

$$\frac{P_{new} - P_{old}}{\sqrt{\sigma_{new}^2 - \sigma_{old}^2}} \tag{8.1}$$

where σ_{new} is the uncertainty on a given parameter from the new model-testing fit and σ_{old} is the uncertainty from the original fit, and $\sqrt{\sigma_{new}^2 - \sigma_{old}^2}$ is the uncertainty on the shift in parameter value.

The addition of a separate M_A^{QE} parameter for oxygen interactions has an impact on not only the fitted M_A^{QE} value but also the fitted value for the 2p-2h normalization on oxygen. While M_A^{QE} ^{12}C, shown in Table 8.1, is found to be slightly higher than the combined fit value for the axial mass, the M_A^{QE} ^{16}O parameter is decreased relative to the combined fit value to a

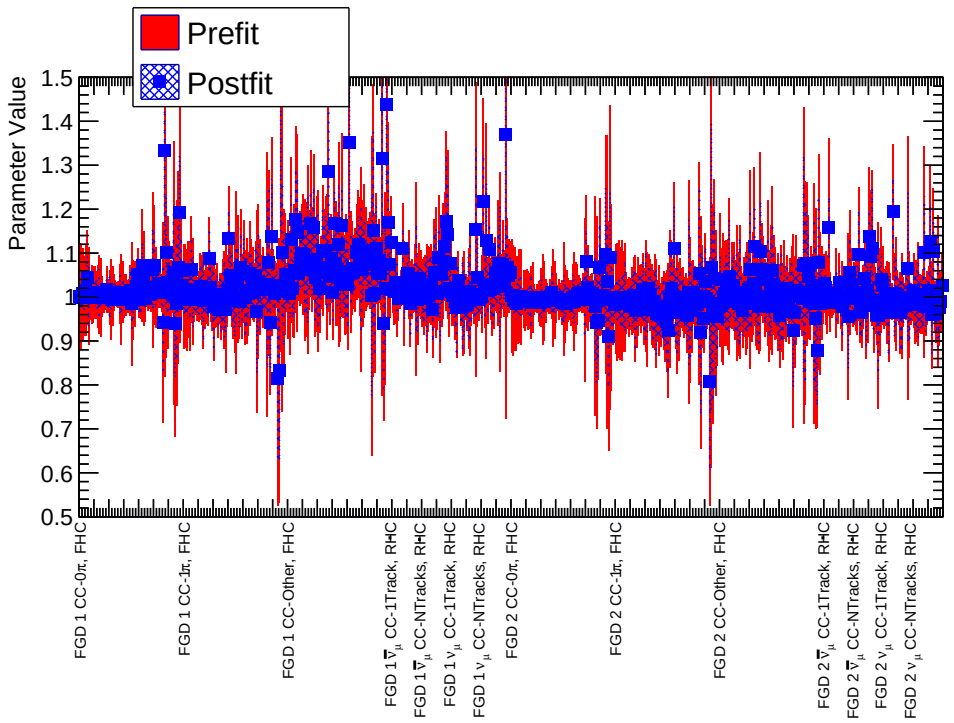

Figure 8.3: Fitted parameter values and uncertainties for the observable normalization parameters for the fit to the nominal MC with split M_A^{QE}.

value of 1.0747 ± 0.0590 from the original fit value of 1.1113 ± 0.0333 for the unsplit M_A^{QE} parameter, by less than 1 σ using Eq. 8.1. This is accompanied by a small overall increase of around 0.8 σ in the oxygen 2p-2h normalization, while the normalization on carbon does not change significantly. This shift in the oxygen 2p-2h normalization is to compensate for the lower observed CC-0π event rates due to the lower M_A^{QE} value for oxygen. As shown in Figure 8.7, the two M_A^{QE} parameters are nearly uncorrelated with one another. While this may be due to some nuclear effect on the event rates that can be absorbed by splitting the axial mass response parameter into separate versions for carbon and oxygen targets, the shift for the 2p-2h normalization and the M_A^{QE} values are not statistically significant and so there is no evidence that the M_A^{QE} parameter is absorbing unmodeled nucleus-dependent physics.

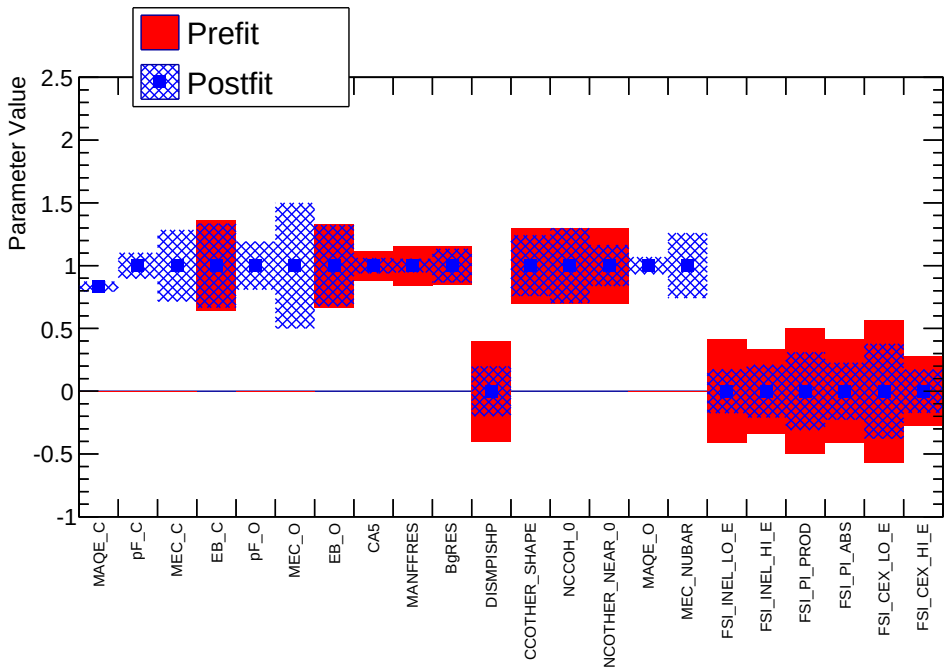

Figure 8.4: Fitted parameter values and uncertainties for the cross section parameters for the fake data fit with M_A^{QE} ^{12}C $= 1$ and M_A^{QE} ^{16}O $= 1.2$. Parameter values shown are relative to nominal, so M_A^{QE} ^{12}C is expected to fit to 1 and M_A^{QE} ^{16}O to 0.833.

8.2 Adding Carbon-Oxygen Separation for $C_A^5(0)$ and M_A^{RES}

Outside of the axial mass parameter, there are a few other cross section parameters that might see some effect from the target nucleus. In particular, we can also look at $C_A^5(0)$ and M_A^{RES} and split these into separate carbon and oxygen versions. Other cross section parameters such as the CC-other shape are not be expected to see any difference. Unlike M_A^{QE}, these two parameters do use a prior and prior uncertainty supplied by fits to external cross section measurements when fitting. This means that any separated version of the parameters should also have some prior - as $C_A^5(0)$ and M_A^{RES} are not correlated to other cross section parameters in the current version of the inputs, it is relatively simple to choose the priors for carbon and oxygen. Therefore the priors for M_A^{RES} ^{16}O and $C_A^5(0)$ ^{16}O have identical prior values to the original parameters and are assumed to be uncorrelated from their ^{12}C counterparts. These fits also split the M_A^{QE} parameter into oxygen and carbon versions as in the previous section.

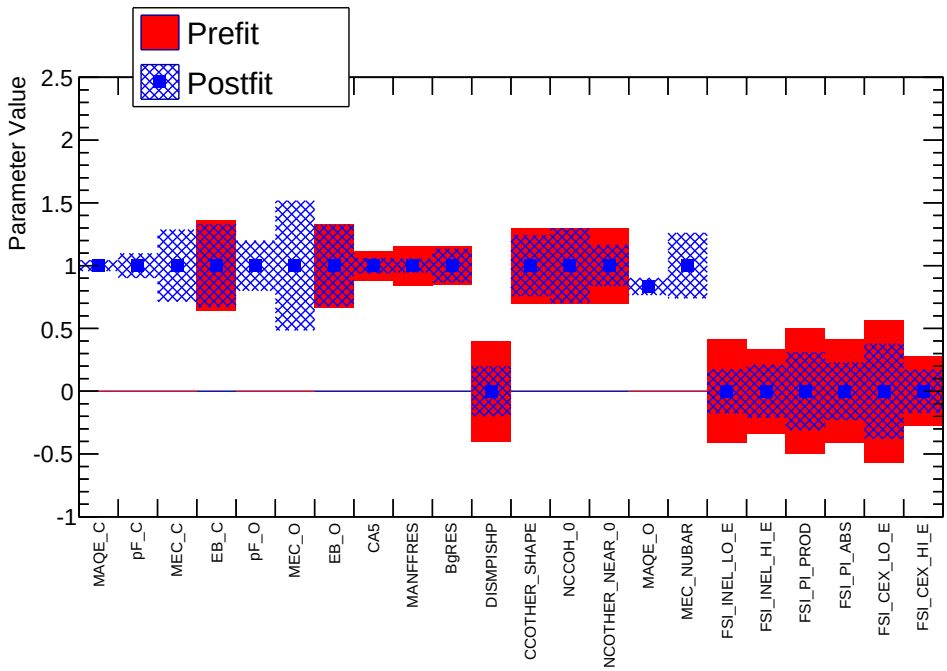

Figure 8.5: Fitted parameter values and uncertainties for the cross section parameters for the fake data fit with M_A^{QE} ^{12}C $= 1.2$ and M_A^{QE} ^{16}O $= 1$

8.2.1 Additional Validation

As with the M_A^{QE} carbon and oxygen fit, the near detector fit framework was revalidated to ensure the parameters were being fit properly. The original toy throws described in Chapter 6 were used to rerun the parameter pull studies for fits with the new parameters. While this essentially makes the assumption that the carbon and oxygen versions of the parameters are 100% correlated with each other, as a single $C_A^5(0)$ parameter is used where $C_A^5(0)$ ^{12}C and ^{16}O would otherwise be, this should not have an impact on the validation process. These studies show similar results as the M_A^{QE} carbon and oxygen validation fits and show no obvious issues with the fit machinery.

8.2.2 Results

The total $\Delta\chi^2$ from the data fit is 1449.86, slightly higher than both the original data fit and the M_A^{QE} fit described in the previous section due to the addition of two additional constrained

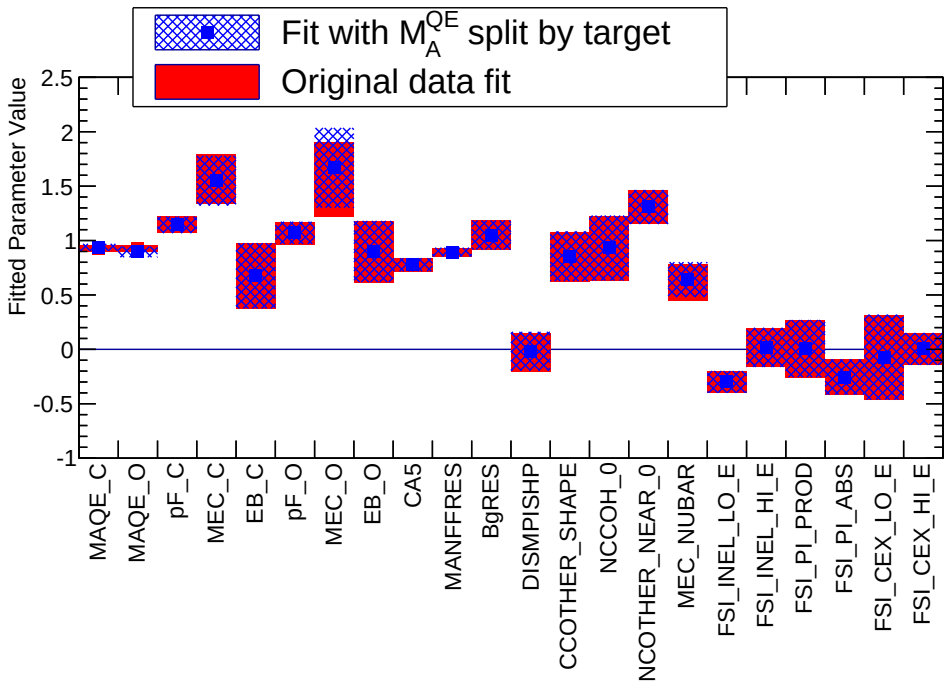

Figure 8.6: The post-fit cross section parameters from the M_A^{QE} carbon and oxygen fit and their uncertainties and the cross section parameters from the data fit described in Chapter 7. Axis labels show the name of each parameter. Parameters are typically a ratio to NEUT nominal values, excepting the CC Other Shape parameter and the FSI parameters. As the original data fit did not separately fit M_A^{QE} for carbon and oxygen targets, the same fitted M_A^{QE} value is shown for both targets.

parameters. The fitted M_A^{QE}, C_A^5 and M_A^{RES} values are shown in Table 8.1 along with the results from the other fits. Similar to the fit with only M_A^{QE} split, the flux and detector parameters are all lowered slightly compared to the original data fit, though less so than the fit with only M_A^{QE} split. For the flux parameters and most of the cross-section parameters, this shift was on the order of less than 1 σ from the original fit value, and not a statistically significant change. Figure 8.8 show the cross section parameter fit values compared with the original data fit discussed in Chapter 7.

Correlations between fitted cross section parameters are shown in Figure 8.9. As M_A^{QE} is split, the effects seen when only splitting M_A^{QE} appear in this fit, though M_A^{QE} ^{16}O has been decreased slightly less. As expected from the original fit, the $C_A^5(0)$ and M_A^{RES} parameters are anticorrelated with each other. Similar to the M_A^{QE} oxygen and carbon fit described earlier in

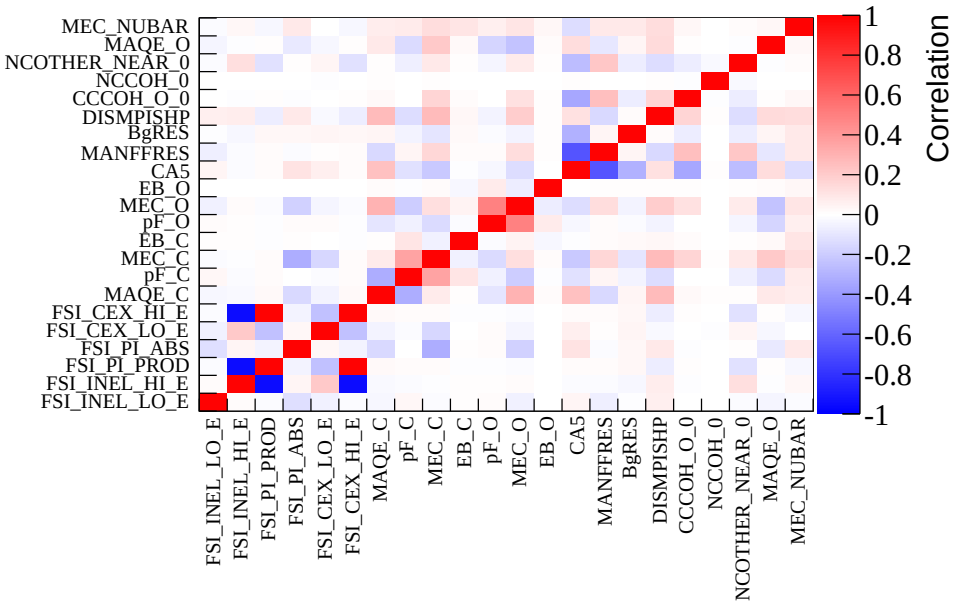

Figure 8.7: The postfit correlations between cross section parameters for the M_A^{QE} carbon and oxygen fit.

this chapter, M_A^{QE} ^{12}C and M_A^{QE} ^{16}O are only slightly correlated with each other. The M_A^{RES} ^{12}C and ^{16}O parameters are fit within 1 σ of the previously fit M_A^{RES} value, with a larger uncertainty on the ^{16}O parameter as expected, indicating that M_A^{RES} is not sensitive to target nuclei in the T2K near detector fit, unlike the M_A^{QE} parameter. The $C_A^5(0)$ parameters are an exception, in that they do show a difference between target materials, with the carbon version fit close to the $C_A^5(0)$ value from the standard data fit, while the oxygen parameter is increased by $\sim 1.5\sigma$ from the original fit value. $C_A^5(0)$ and M_A^{RES} remain anticorrelated with each other for both the oxygen and carbon parameters, as in the official fit. As with the fit with only M_A^{QE} split by target, most parameters did not show statistically significant changes when split by target, which indicates that there are no obvious nuclear effects being absorbed by these parameters. The single exception to this is C_A^5 ^{16}O, which does show a hint of a variation from the original fitted C_A^5 parameter. So unlike M_A^{RES}, there may be some unmodeled nuclear effect being seen here, as unlike CCQE cross-sections, there is no modelling of 2p-2h or other such effects for resonant pion production.

	Official	M_A^{QE} Split	M_A^{QE}, C_A^5 and M_A^{RES} Split
M_A^{QE} ^{12}C	1.1113 ± 0.0338	1.1256 ± 0.0384	1.1289 ± 0.0389
M_A^{QE} ^{16}O		1.0749 ± 0.0590	1.0802 ± 0.0593
$C_A^5(0)$ ^{12}C	0.7860 ± 0.0607	0.7854 ± 0.0606	0.7896 ± 0.0681
$C_A^5(0)$ ^{16}O			0.8943 ± 0.0879
M_A^{RES} ^{12}C	0.8491 ± 0.0384	0.8497 ± 0.0383	0.8405 ± 0.0457
M_A^{RES} ^{16}O			0.8652 ± 0.07207
2p-2h ^{12}C	156.90 ± 22.64	155.04 ± 22.86	156.59 ± 23.21
2p-2h ^{16}O	155.89 ± 34.24	166.80 ± 36.70	147.35 ± 39.57

Table 8.1: Fitted parameter values for the three different data fits for the tested parameters. If a listed fit did not have separate parameters for oxygen and carbon targets, the value from the general parameter is used as the entry for both.

8.3 Effect on the Predictions at Super-Kamiokande

As discussed in the previous sections, splitting the M_A^{QE} and $C_A^5(0)$ parameters into separate versions for carbon and oxygen targets leads to different fitted values depending on target material, while M_A^{RES} does not show this behavior. However, while it is useful to look at how individual parameter values change in the ND280 fit itself, the primary purpose of the ND280 fit is to provide flux and cross-section constraints for the oscillation analysis at SK and tune the predicted spectra and expected number of events. Splitting parameters by target material removes possible model dependence, even in the case where the parameter values do not change greatly. In the original fit output described in Chapter 7, only three parameters were split into separate carbon and oxygen versions – 2p-2h normalization, E_B and p_F – and the oscillation fit used the oxygen parameter values as the inputs. As there are now both more parameters that have an oxygen-specific version and see a difference in value from both the carbon version and the previous parameter values used for the fit, the next step is to test what impact this has on the predicted rates at SK. In particular, because parameters on oxygen targets in the ND280 fit have larger uncertainties than their carbon counterparts, it is important to look at the overall change in uncertainties on predicted spectra.

Table 8.2 shows the predicted number of events at SK given the official near detector fit and the two model dependence test fits described earlier in this chapter, for the FHC ν_μ, FHC ν_e,

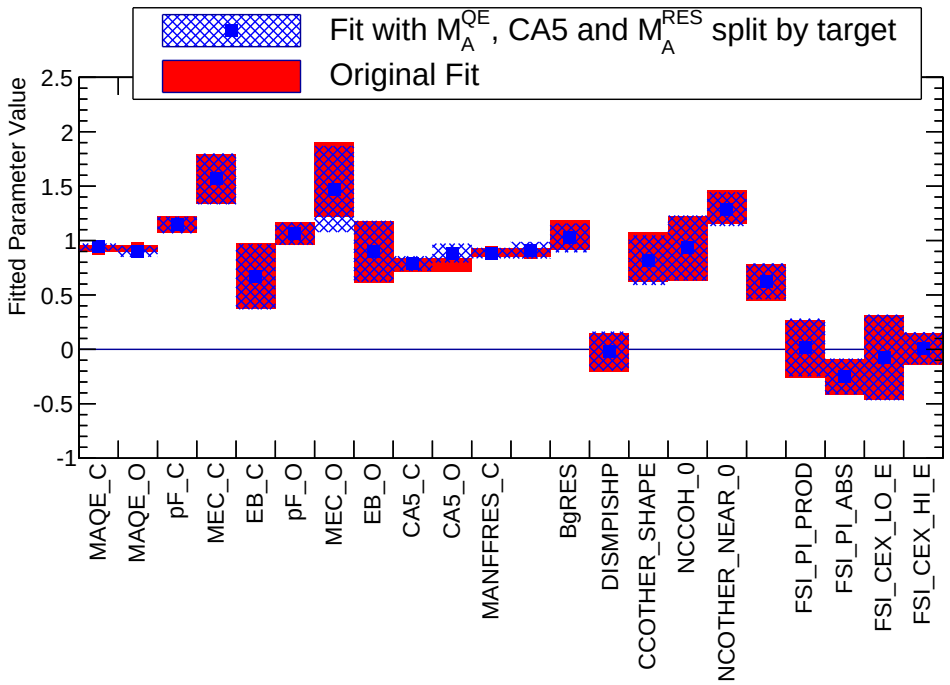

Figure 8.8: The post-fit cross section parameters from the M_A^{QE}, $C_A^5(0)$ and M_A^{RES} carbon and oxygen fit and their uncertainties and the cross section parameters from the data fit described in Chapter 7. Axis labels show the name of each parameter. Parameters are typically a ratio to NEUT nominal values, excepting the CC Other Shape parameter and the FSI parameters. As the original data fit did not separately fit M_A^{QE}, $C_A^5(0)$ and M_A^{RES} for carbon and oxygen targets, the same fitted M_A^{QE}, $C_A^5(0)$ and M_A^{RES} values are shown for both targets.

RHC ν_μ and RHC ν_e samples. The overall number of events predicted by the M_A^{QE} split fit is very close to that of the original fit, though all predictions are slightly higher. This is possibly due to the increase in the 2p-2h normalization on oxygen, which compensates for the reduced CCQE interactions in the observed CC-0π samples. In addition, splitting the M_A^{QE} parameter in the near detector fit causes and increase in the uncertainties for the FHC samples but shows little change in the RHC sample predictions. Such a small change is in line with the assumption that the axial mass M_A^{QE} should not pick up any strong dependence on nuclear target, as the change in predicted number of events is not statistically significant.

Unlike the fit with only M_A^{QE} split, the value of the 2p-2h normalization is lower relative to the original near detector fit for the M_A^{QE}, C_A^5 and M_A^{RES} split fit. Despite this, this fit shows

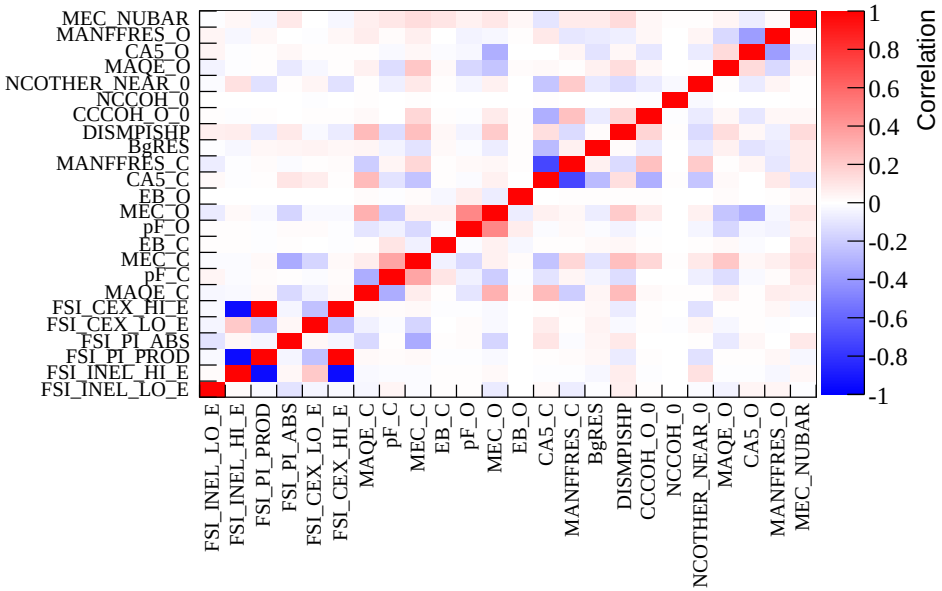

Figure 8.9: The postfit correlations between cross section parameters for the M_A^{QE}, $C_A^5(0)$ and M_A^{RES} carbon and oxygen fit.

a larger increase in the predicted number of events for all samples compared to just removing model dependence on M_A^{QE} alone, though the difference is still not statistically significant. This appears to be due to the large increase in the value of the C_A^5 form factor, and slight increase in the M_A^{RES} correction value. As these parameters control the background resonant pion production process, the increased rate is likely due to an increased non-CCQE background. In addition, the larger uncertainties from all three split parameters lead to a larger increase of the uncertainties on the prediction compared to both other fits. Plots of the predicted energy spectra at SK for each sample are shown in Figures 8.10, 8.11, 8.12 and 8.13.

In adding additional degrees of freedom to the ND280 fit in order to account for unmodeled nuclear effects, there is no significant indication that there are nuclear-target based inadequacies in the nominal T2K cross-section model. The axial mass M_A^{QE} and M_A^{RES} do not show significant change in the fit results, and there is no significant change in the overall predicted event rates for any of the samples at SK. This indicates that the current nominal cross-section model in use is sufficient for the main T2K results.

	FHC ν_μ	FHC ν_e	RHC ν_μ	RHC ν_e
Official	135.82 ± 6.79	28.687 ± 1.549	64.21 ± 3.34	6.004 ± 0.372
M_A^{QE} Split	136.9 ± 7.077	28.88 ± 1.637	64.69 ± 3.28	6.129 ± 0.379
M_A^{QE}, C_A^5 and M_A^{RES} Split	138.20 ± 7.49	30.12 ± 1.823	65.31 ± 3.48	6.474 ± 0.412

Table 8.2: Predicted number of events at SK using various ND280 postfit values and their uncertainties.

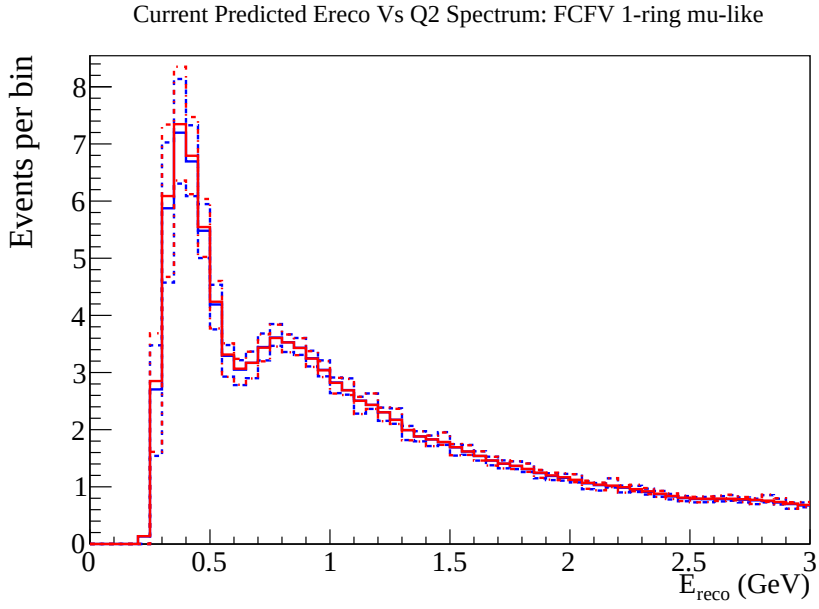

Figure 8.10: Predicted event spectrum for FHC ν_μ signal events at SK. Red lines show the prediction, as a solid line, and error envelopes, as dashed lines, from the near detector fit with M_A^{QE}, $C_A^5(0)$ and M_A^{RES} split by target, and blue lines show the prediction and error envelopes from the near detector fit with M_A^{QE} split by target.

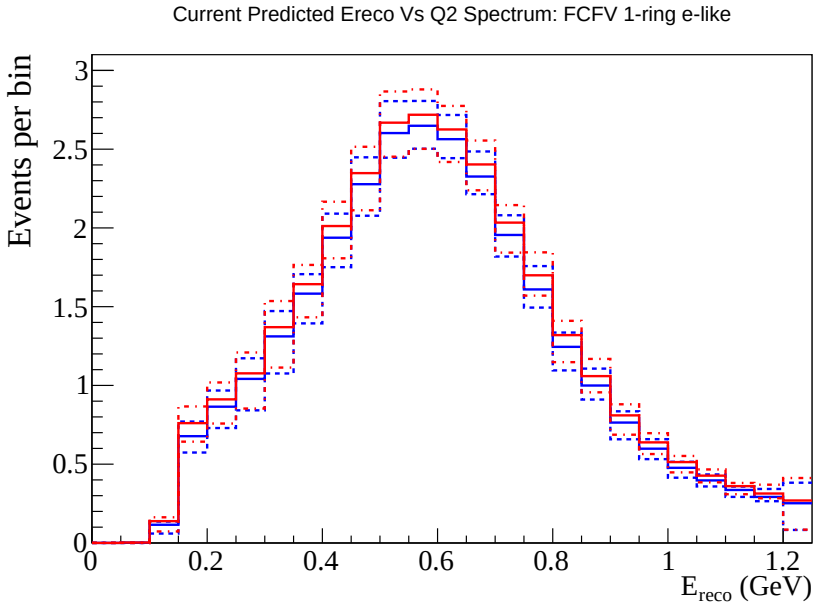

Figure 8.11: Predicted event spectrum for FHC ν_e signal events at SK. Red lines show the prediction, as a solid line, and error envelopes, as dashed lines, from the near detector fit with M_A^{QE}, $C_A^5(0)$ and M_A^{RES} split by target, and blue lines show the prediction and error envelopes from the near detector fit with M_A^{QE} split by target.

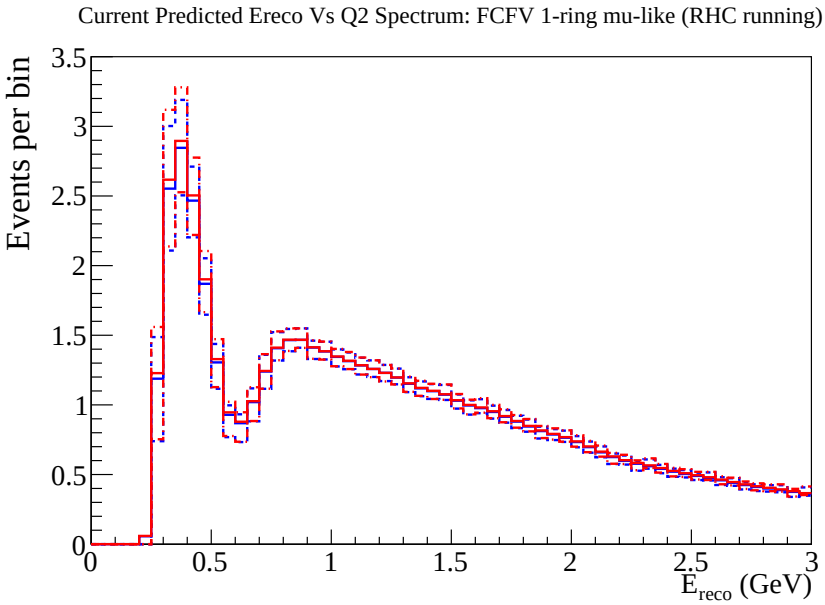

Figure 8.12: Predicted event spectrum for RHC ν_μ signal events at SK. Red lines show the prediction, as a solid line, and error envelopes, as dashed lines, from the near detector fit with M_A^{QE}, $C_A^5(0)$ and M_A^{RES} split by target, and blue lines show the prediction and error envelopes from the near detector fit with M_A^{QE} split by target.

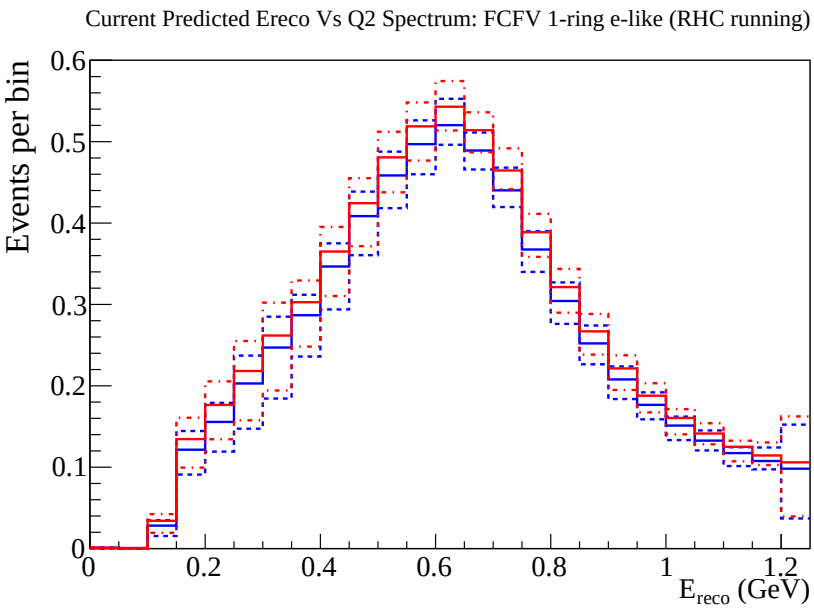

Figure 8.13: Predicted event spectrum for RHC ν_e signal events at SK. Red lines show the prediction, as a solid line, and error envelopes, as dashed lines, from the near detector fit with M_A^{QE}, $C_A^5(0)$ and M_A^{RES} split by target, and blue lines show the prediction and error envelopes from the near detector fit with M_A^{QE} split by target.

Chapter 9

Conclusions and Summary

Adding a water-carbon target to the T2K near detector maximum likelihood fit used to constrain the neutrino flux and cross-sections in the oscillation fits provides a method to significantly reduce the overall uncertainties on cross-sections at SK and thus the neutrino spectra predictions and oscillation measurements by providing constraints on oxygen-specific cross-section parameters. The various validation steps performed, such as pull studies, indicate that the fit is sufficiently unbiased with this addition, and both neutrino mode and antineutrino mode data was used in the fit.

This was accomplished by developing neutrino and antineutrino CC selections for FGD 2, to match the selections previously used in FGD 1. To do this, the CC inclusive selection cuts for neutrinos and antineutrinos were adapted to use FGD 2 as a target. In addition, the topology-based sample selections were adapted for FGD 2 and implemented as a separate set of cuts, as cuts are not identical due to differences in geometry and active volume. These new samples allow for subtraction analysis between the FGD 1 carbon target and the FGD 2 water-carbon target to measure oxygen interactions.

Along with the additional water-carbon samples, the near detector fit was updated with improved treatment of the detector systematics. As the systematics between the two detectors may have some correlations due to similar geometries, the fit now allows for correlations

between the two sets of samples for appropriate systematics. This translates to correlations between the angle and momenta bins used in the fit. Additionally, correlations were implemented within systematics, such as between momenta bins in order to more accurately model systematic effects.

The near detector fit, with the exception of the oxygen target parameters which were not fit in the previous analyses and new parameters added for this analysis, is in agreement with the results seen previously when fitting with only FGD 1. The fit gives an axial mass value of $M_A^{QE} = 1.113 \pm 0.033$, which is in agreement with the previous axial mass measurements at ND280.

The overall uncertainty on the neutrino spectrum predictions at SK, which includes uncertainties from the flux and SK-specific detector systematics as well, was reduced by around 2.5% for the neutrino mode spectra and by around 5% for the antineutrino mode spectra, giving an overall uncertainty of 5.0% for FHC ν_μ down from 7.7%, 5.4% for FHC ν_e down from 6.8%, 5.2% for RHC $\bar{\nu}_\mu$ down from 11.6% and 6.2% for RHC $\bar{\nu}_e$ down from 11.0%. This reduces the overall contribution from systematic sources to the uncertainty on the oscillation parameters significantly. Additionally, the 2D contours for $\sin^2\theta_{23}$ and Δm^2_{32} (Δm^2_{13} for IH) show improvements to the 1D contour ranges between fits using the FGD 1-only constrains and the FGD 1 + FGD 2 constraints described in the this thesis. The 1D $\sin^2\theta_{23}$ range is reduced by 3% for NH and 2% for IH, while the Δm^2 1D range is reduced by 11% for NH and 8% for IH.

Additional studies were performed using the T2K near detector fit to check the nuclear model dependencies in how cross-sections are modelled at T2K, as unaccounted-for nuclear effects could be absorbed by model parameters that are assumed to have no nuclear target dependence. To this end, the axial mass for CCQE interactions and the axial mass and C_A^5 form factor for resonant pion production were implemented as separate carbon and oxygen versions to test this.

These studies have shown that there is no significant change in the fitted parameter values

for these parameters when fit in a non-model dependent way, with the exception of the C_A^5 form factor, which shows a weak $\sim 1.5\sigma$ shift between carbon and oxygen. This indicates that the current neutrino-nucleus cross-section model used at T2K sufficiently models the nuclear effects such that the axial mass parameters do not pick up unaccounted-for effects, as the resonant pion production cross-section primarily contributes to background at SK.

In addition, using the results of these model dependency tests to construct the spectra predictions at SK shows no significant deviation in the predicted spectra from the original official predictions. The main difference in the predictions is the increase on the overall uncertainty on the prediction due to increased uncertainty on the new oxygen target parameters. This indicates that the current cross-section model used adequately models the nuclear target-dependent effects, and that additional uncertainties to account for deviations of this data from the model are not required.

While the studies performed and described here are for a few specific model parameters, there remain other cross-section parameters, such as those used to model final state interactions (FSI) that could benefit from similar model-dependency checking. Additionally, further investigation into the shift in C_A^5 when model dependencies are removed may be important, as while the SK analyses use CCQE as the signal with resonant pion production as background, future studies may wish to include a CC 1π signal as well. As less work has been done on modelling nuclear effects for resonant pion production than for quasielastic processes, further study is needed.

Bibliography

[1] David Griffiths. *Introduction to Elementary Particles*. Wiley-VCH, 2009.

[2] F. Reines and C. L. Cowan. Detection of the free neutrino. *Phys. Rev.*, 92:830–831, Nov 1953. doi:10.1103/PhysRev.92.830. URL http://link.aps.org/doi/10.1103/PhysRev.92.830.

[3] G. Danby, J-M. Gaillard, K. Goulianos, L. M. Lederman, N. Mistry, M. Schwartz, and J. Steinberger. Observation of high-energy neutrino reactions and the existence of two kinds of neutrinos. *Phys. Rev. Lett.*, 9:36–44, Jul 1962. doi:10.1103/PhysRevLett.9.36. URL http://link.aps.org/doi/10.1103/PhysRevLett.9.36.

[4] K. Kodama et al. Observation of tau neutrino interactions. *Physics Letters B*, 504(3): 218 – 224, 2001. ISSN 0370-2693. doi:http://dx.doi.org/10.1016/S0370-2693(01)00307-0. URL http://www.sciencedirect.com/science/article/pii/S0370269301003070.

[5] E. Komatsu et al. Seven-year Wilkinson Microwave Anisotropy Probe (WMAP) Observations: Cosmological Interpretation. *The Astrophysical Journal Supplement*.

[6] S. Schael et al. Precision electroweak measurements on the Z resonance. *Phys. Rept.*, 427:257–454, 2006. doi:10.1016/j.physrep.2005.12.006.

[7] W. N. Cottingham and D. A Greenwood. *An introduction to the standard model of particle physics*. Cambridge University Press, 2 edition, 2007.

[8] Michio Kaku. *Quantum field theory : a modern introduction*. Oxford University Press, 1 edition, 1993.

[9] G. G. Raffelt. Neutrino masses in astroparticle physics. *New Astronomy Reviews*, 46: 699–708, October 2002. doi:10.1016/S1387-6473(02)00239-7.

[10] Y. Fukuda et al. Evidence for oscillation of atmospheric neutrinos. *Phys. Rev. Lett.*, 81: 1562–1567, Aug 1998. doi:10.1103/PhysRevLett.81.1562. URL http://link.aps.org/doi/10.1103/PhysRevLett.81.1562.

[11] Q. R. Ahmad et al. Direct evidence for neutrino flavor transformation from neutral-current interactions in the Sudbury Neutrino Observatory. *Phys. Rev. Lett.*, 89: 011301, Jun 2002. doi:10.1103/PhysRevLett.89.011301. URL http://link.aps.org/doi/10.1103/PhysRevLett.89.011301.

[12] Joao Paulo Silva Gustavo Castelo Branco, Luis Lavoura. *CP violation*. Oxford University Press, 1999.

[13] J. Schechter and J. W. F. Valle. Neutrino masses in su(2) $\bigotimes$ u(1) theories. *Phys. Rev. D*, 22:2227–2235, Nov 1980. doi:10.1103/PhysRevD.22.2227. URL http://link.aps.org/doi/10.1103/PhysRevD.22.2227.

[14] K. A. Olive et al. Review of Particle Physics. *Chin. Phys.*, C38:090001, 2014. doi:10.1088/1674-1137/38/9/090001.

[15] A. Yu. Smirnov. The MSW effect and matter effects in neutrino oscillations. *Phys. Scripta*, T121:57–64, 2005. doi:10.1088/0031-8949/2005/T121/008.

[16] Raymond Davis, Don S. Harmer, and Kenneth C. Hoffman. Search for neutrinos from the sun. *Phys. Rev. Lett.*, 20:1205–1209, May 1968. doi:10.1103/PhysRevLett.20.1205. URL http://link.aps.org/doi/10.1103/PhysRevLett.20.1205.

[17] John N. Bahcall. Solar neutrinos. I: Theoretical. *Phys. Rev. Lett.*, 12:300–302, 1964. doi:10.1103/PhysRevLett.12.300.

[18] K. S. Hirata et al. Observation of a small atmospheric muon-neutrino / electron-neutrino ratio in Kamiokande. *Phys. Lett.*, B280:146–152, 1992. doi:10.1016/0370-2693(92)90788-6.

[19] M. Apollonio et al. Search for neutrino oscillations on a long base-line at the CHOOZ nuclear power station. *The European Physical Journal C - Particles and Fields*, 27(3): 331–374, 2003. ISSN 1434-6052. doi:10.1140/epjc/s2002-01127-9. URL http://dx.doi.org/10.1140/epjc/s2002-01127-9.

[20] P. Novella. Double Chooz: Searching for theta13 with reactor neutrinos. 2011.

[21] J. K. Ahn et al. Observation of reactor electron antineutrinos disappearance in the RENO experiment. *Phys. Rev. Lett.*, 108:191802, May 2012. doi:10.1103/PhysRevLett.108.191802. URL http://link.aps.org/doi/10.1103/PhysRevLett.108.191802.

[22] T. Araki et al. Measurement of neutrino oscillation with KamLAND: Evidence of spectral distortion. *Phys. Rev. Lett.*, 94:081801, Mar 2005. doi:10.1103/PhysRevLett.94.081801. URL http://link.aps.org/doi/10.1103/PhysRevLett.94.081801.

[23] F. P. An et al. Observation of electron-antineutrino disappearance at Daya Bay. *Phys. Rev. Lett.*, 108:171803, Apr 2012. doi:10.1103/PhysRevLett.108.171803. URL http://link.aps.org/doi/10.1103/PhysRevLett.108.171803.

[24] V. Lyubushkin et al. A study of quasi-elastic muon neutrino and antineutrino scattering in the NOMAD experiment. *The European Physical Journal C*, 63(3):355–381, 2009. ISSN 1434-6052. doi:10.1140/epjc/s10052-009-1113-0. URL http://dx.doi.org/10.1140/epjc/s10052-009-1113-0.

[25] A. Aguilar et al. Evidence for neutrino oscillations from the observation of $\overline{\nu}_e$ appearance in a $\overline{\nu}_\mu$ beam. *Phys. Rev. D*, 64:112007, Nov 2001. doi:10.1103/PhysRevD.64.112007. URL http://link.aps.org/doi/10.1103/PhysRevD.64.112007.

[26] A. A. Aguilar-Arevalo et al. A Search for Electron Antineutrino Appearance at the $\Delta m^2 \sim 1$ eV^2 Scale. *Phys. Rev. Lett.*, 103:111801, 2009. doi:10.1103/PhysRevLett.103.111801.

[27] M. H. Ahn et al. Measurement of Neutrino Oscillation by the K2K Experiment. *Phys. Rev.*, D74:072003, 2006. doi:10.1103/PhysRevD.74.072003.

[28] P. Adamson et al. Measurement of neutrino and antineutrino oscillations using beam and atmospheric data in MINOS. *Phys. Rev. Lett.*, 110:251801, Jun 2013. doi:10.1103/PhysRevLett.110.251801. URL http://link.aps.org/doi/10.1103/PhysRevLett.110.251801.

[29] P. Adamson et al. First measurement of electron neutrino appearance in NOvA. *Phys. Rev. Lett.*, 116(15):151806, 2016. doi:10.1103/PhysRevLett.116.151806.

[30] K. Abe et al. Measurements of neutrino oscillation in appearance and disappearance channels by the T2K experiment with 6.61020 protons on target. *Phys. Rev. D*, 91 (072010), 2015.

[31] T2K Collaboration (private communication). General plots/NIWG, 2016.

[32] C. H. Llewellyn Smith. Neutrino Reactions at Accelerator Energies. *Phys. Rept.*, 3: 261–379, 1972. doi:10.1016/0370-1573(72)90010-5.

[33] T. Leitner, L. Alvarez-Ruso, and U. Mosel. Charged current neutrino-nucleus interactions at intermediate energies. *Phys. Rev. C*, 73:065502, Jun 2006. doi:10.1103/PhysRevC.73.065502. URL http://link.aps.org/doi/10.1103/PhysRevC.73.065502.

[34] R. A. Smith and E. J. Moniz. NEUTRINO REACTIONS ON NUCLEAR TARGETS. *Nucl. Phys.*, B43:605, 1972. doi:10.1016/0550-3213(75)90612-4,10.1016/0550-3213(72)90040-5. [Erratum: Nucl. Phys.B101,547(1975)].

[35] B. Povh, M. Lavelle, K. Rith, C. Scholz, and F. Zetsche. *Particles and Nuclei: An Introduction to the Physical Concepts*. Springer Berlin Heidelberg, 2013. ISBN 9783662054321.

[36] E. J. Moniz, I. Sick, R. R. Whitney, J. R. Ficenec, R. D. Kephart, and W. P. Trower. Nuclear fermi momenta from quasielastic electron scattering. *Phys. Rev. Lett.*, 26: 445–448, Feb 1971. doi:10.1103/PhysRevLett.26.445. URL http://link.aps.org/doi/10.1103/PhysRevLett.26.445.

[37] Andrew Furmanski. Implementing the spectral function nuclear model in NEUT, and parametrizing systematic uncertainties. Technical Report 184, T2K, May 2014.

[38] J. Nieves, J. E. Amaro, and M. Valverde. Inclusive quasielastic charged-current neutrino-nucleus reactions. *Phys. Rev. C*, 70:055503, Nov 2004. doi:10.1103/PhysRevC.70.055503. URL http://link.aps.org/doi/10.1103/PhysRevC.70.055503.

[39] Cezary Juszczak, Jan T. Sobczyk, and Jakub Zmuda. On extraction of value of axial mass from MiniBooNE neutrino quasi-elastic double differential cross section data. *Phys. Rev.*, C82:045502, 2010. doi:10.1103/PhysRevC.82.045502.

[40] X. Espinal and F. Sanchez. Measurement of the axial vector mass in neutrino-carbon interactions at K2K. *AIP Conf. Proc.*, 967:117–122, 2007. doi:10.1063/1.2834461.

[41] S. Boyd, S. Dytman, E. Hernndez, J. Sobczyk, and R. Tacik. Comparison of models of neutrinonucleus interactions. *AIP Conference Proceedings*, 1189(1), 2009.

[42] J. Nieves, I. Ruiz Simo, and M. J. Vicente Vacas. Inclusive charged-current neutrino-nucleus reactions. *Phys. Rev. C*, 83:045501, Apr 2011. doi:10.1103/PhysRevC.83.045501. URL http://link.aps.org/doi/10.1103/PhysRevC.83.045501.

[43] R. Gran, J. Nieves, F. Sanchez, and M. J. Vicente Vacas. Neutrino-nucleus quasi-elastic and 2p2h interactions up to 10 GeV. *Phys. Rev. D*, 88:113007, Dec 2013. doi:10.1103/PhysRevD.88.113007. URL http://link.aps.org/doi/10.1103/PhysRevD.88.113007.

[44] M. Martini, M. Ericson, G. Chanfray, and J. Marteau. Unified approach for nucleon knock-out and coherent and incoherent pion production in neutrino interactions with nuclei. *Phys. Rev. C*, 80:065501, Dec 2009. doi:10.1103/PhysRevC.80.065501. URL http://link.aps.org/doi/10.1103/PhysRevC.80.065501.

[45] K. Abe et al. The T2K experiment. *Nuclear Instruments and Methods in Physics Research Section A: Accelerators, Spectrometers, Detectors and Associated Equipment*, 659(1):106 – 135, 2011. ISSN 0168-9002. doi:http://dx.doi.org/10.1016/j.nima.2011.06.067. URL http://www.sciencedirect.com/science/article/pii/S0168900211011910.

[46] T2K Collaboration (private communication). General and frequently updated plots/beam, 2016.

[47] K. Abe et al. T2K neutrino flux prediction. *Phys. Rev. D*, 87:012001, Jan 2013. doi:10.1103/PhysRevD.87.012001. URL http://link.aps.org/doi/10.1103/PhysRevD.87.012001.

[48] Sacha E Kopp. Accelerator neutrino beams. *Physics reports*, 439(3):101–159, 2007.

[49] S. Fukuda et al. The Super-Kamiokande detector. *Nuclear Instruments and Methods in Physics Research Section A: Accelerators, Spectrometers, Detectors and Associated Equipment*, 501(2–3):418 – 462, 2003. ISSN 0168-9002. doi:http://dx.doi.org/10.1016/S0168-9002(03)00425-X. URL http://www.sciencedirect.com/science/article/pii/S016890020300425X.

[50] S. Assylbekov et al. The T2K ND280 off-axis pizero detector. *Nuclear Instruments and Methods in Physics Research Section A: Accelerators, Spectrometers, Detectors and Associated Equipment*, 686:48 – 63, 2012. ISSN 0168-9002. doi:http://dx.doi.org/10.1016/j.nima.2012.05.028. URL http://www.sciencedirect.com/science/article/pii/S0168900212005153.

[51] D Allan et al. The electromagnetic calorimeter for the T2K near detector ND280. *Journal of Instrumentation*, 8(10):P10019, 2013. URL http://stacks.iop.org/1748-0221/8/i=10/a=P10019.

[52] N. Abgrall et al. Time projection chambers for the T2K near detectors. *Nuclear Instruments and Methods in Physics Research Section A: Accelerators, Spectrometers, Detectors and Associated Equipment*, 637(1):25 – 46, 2011. ISSN 0168-9002. doi:http://dx.doi.org/10.1016/j.nima.2011.02.036. URL http://www.sciencedirect.com/science/article/pii/S0168900211003421.

[53] P-A Amaudruz, M Barbi, D Bishop, N Braam, DG Brook-Roberge, S Giffin, S Gomi, P Gumplinger, K Hamano, NC Hastings, et al. The T2K fine-grained detectors. *Nuclear Instruments and Methods in Physics Research Section A: Accelerators, Spectrometers, Detectors and Associated Equipment*, 696:1–31, 2012.

[54] Pascal Baron, Denis Calvet, Eric Delagnes, Xavier de la Broise, Alain Delbart, Frederic Druillole, Eduardo Monmarthe, Estelle Mazzucato, Francois Pierre, and Marco Zito. AFTER, an ASIC for the readout of the large T2K time projection chambers. *IEEE Trans. Nucl. Sci.*, 55:1744–1752, 2008. doi:10.1109/TNS.2008.924067.

[55] N. Abgrall et al. Measurements of cross sections and charged pion spectra in proton-carbon interactions at 31 GeV/c. *Phys. Rev. C*, 84:034604, Sep 2011. doi:10.1103/PhysRevC.84.034604. URL http://link.aps.org/doi/10.1103/PhysRevC.84.034604.

[56] L. Fields et al. Measurement of muon antineutrino quasielastic scattering on a hydrocarbon target at $E_\nu \sim 3.5$ GeV. *Phys. Rev. Lett.*, 111:022501, Jul 2013. doi:10.1103/PhysRevLett.111.022501. URL http://link.aps.org/doi/10.1103/PhysRevLett.111.022501.

[57] Mark Hartz et al. Constraining the flux and cross section models with data from the ND280 detector for the 2014/15 oscillation analysis. Technical Report 220, T2K, May 2015.

[58] Costas Andreopoulos et al. T2K 6.57×10^{20}-POT joint 3-flavour oscillation analysis. Technical Report 175, T2K, March 2014.

[59] Takahiro Hiraki, Christophe Bronner, James Imber, and Hidekazu Tanaka. Muon anti-neutrino disappearance analysis with T2K run5+6 data (p-theta group). Technical Report 238, T2K, June 2015.

[60] Asher Kaboth, Richard Calland, and David Payne. A joint ND280-SK $1R_\mu$-SK $1R_e$ fit using MCMC. Technical Report 171, T2K, March 2014.

[61] Costas Andreopoulos et al. T2K neutrino and anti-neutrino 3-flavour joint analysis of run 1-6 (6.914×10^{20}-POT ν 4.011×10^{20}-POT $\bar{\nu}$), run 1-7b (7.002×10^{20}-POT ν 7.471×10^{20}-POT $\bar{\nu}$) and run 1-7c (7.482×10^{20}-POT ν 7.471×10^{20}-POT $\bar{\nu}$) data sets. Technical Report 266, T2K, July 2016.

[62] F. James and M. Roos. Minuit: A System for Function Minimization and Analysis of the Parameter Errors and Correlations. *Comput. Phys. Commun.*, 10:343–367, 1975. doi:10.1016/0010-4655(75)90039-9.

[63] R. Brun and F. Rademakers. ROOT: An object oriented data analysis framework. *Nucl. Instrum. Meth.*, A389:81–86, 1997. doi:10.1016/S0168-9002(97)00048-X.

[64] Megan Friend et al. Flux prediction and uncertainty updates with NA61 2009 thin target data and negative focussing mode predictions. Technical Report 217, T2K, June 2015.

[65] N. Abgrall et al. Measurement of production properties of positively charged kaons in proton-carbon interactions at 31 GeV/c. *Phys. Rev. C*, 85:035210, Mar 2012. doi:10.1103/PhysRevC.85.035210. URL http://link.aps.org/doi/10.1103/PhysRevC.85.035210.

[66] M. Apollonio et al. Forward production of charged pions with incident protons on nuclear targets at the CERN proton synchrotron. *Phys. Rev. C*, 80:035208, Sep 2009. doi:10.1103/PhysRevC.80.035208. URL http://link.aps.org/doi/10.1103/PhysRevC.80.035208.

[67] Mark Hartz et al. Constraining the flux and cross section models with data from the ND280 detector using FGD1 and FGD2 for the 2016 joint oscillation analysis. Technical Report 230, T2K, June 2016.

[68] M. Dunkman et al. Updated recommendation of the 2014-5 oscillation parameters. Technical Report 265, T2K, April 2016.

[69] A. A. Aguilar-Arevalo et al. First measurement of the muon antineutrino double-differential charged-current quasielastic cross section. *Phys. Rev. D*, 88:032001, Aug 2013. doi:10.1103/PhysRevD.88.032001. URL http://link.aps.org/doi/10.1103/PhysRevD.88.032001.

[70] G. A. Fiorentini et al. Measurement of muon neutrino quasielastic scattering on a hydrocarbon target at $E_\nu \sim 3.5$ GeV. *Phys. Rev. Lett.*, 111:022502, Jul 2013. doi:10.1103/PhysRevLett.111.022502. URL http://link.aps.org/doi/10.1103/PhysRevLett.111.022502.

[71] A. Bercellie et al. Cross section parameters for 2014 oscillation analysis. Technical Report 192, T2K, June 2015.

[72] Patrick de Perio, Yoshinari Hayato, and Roman Tacik. NEUT nuclear effects (FSI). Technical Report 33, T2K, March 2012.

[73] Sarah Bolognesi et al. Assessing the effect of cross-section model uncertainties on the T2K oscillation analyses with fake data studies using the BANFF, MaCh3 and VALOR fit frameworks. Technical Report 285, T2K, June 2016.

[74] K. Abe and others (T2K Collaboration). Measurement of muon antineutrino oscillations with an accelerator-produced off-axis beam. *Phys. Rev. Lett.*, 116(181801), 2016.

[75] Yoshinari Hayato. A neutrino interaction simulation program library NEUT. *Acta Phys. Polon.*, B40:2477–2489, 2009. Version 5.3.3 of the NEUT library is used that includes (i) the multinucleon ejection model of Nieves *et al.* [42] and (ii) nuclear long range correlations for CCQE interactions, treated in the random phase approximation [100].

[76] A. Hillairet, A. Izmaylov, B. Jamieson, and T. Lindner. ND280 reconstruction. Technical Report 072, T2K, November 2011.

[77] Rudolph Emil Kalman. A new approach to linear filtering and prediction problems. *Transactions of the ASME–Journal of Basic Engineering*, 82(Series D):35–45, 1960.

[78] Claudio Giganti and Marco Zito. Particle Identification with the T2K TPC. Technical Report 001, T2K, October 2009.

[79] S Bordoni, Giganti C, Hillairet A, and Sanchez F. The TPC particle identification algorithm with production 6B. Technical Report 221, T2K, April 2015.

[80] Caio Liccardi and Mauricio Barbi. Particle identification with the Fine Grained Detectors. Technical Report 103, T2K, January 2012.

[81] Pierre Bartet et al. ν_μ CC event selections in the ND280 tracker using Run 2+3+4 data. Technical Report 212, T2K, October 2015.

[82] Jiae Kim, Christine Nielsen, and Michael Wilking. Michel Electron Tagging in the FGDs. Technical Report 104, T2K, Jan 2015.

[83] V. Berardi et al. CC $\bar{\nu}_\mu$ event selection in the ND280 tracker using Run 5c and Run 6 anti-neutrino beam data. Technical Report 246, T2K, Oct 2015.

[84] V. Berardi et al. CC ν_μ background event selection in the ND280 tracker using Run 5c + Run 6 anti-neutrino beam data. Technical Report 248, T2K, October 2015.

[85] A. Frank, A. Marchionni, and M. Messina. B-field calibration and systematic errors. Technical Report 081, T2K, September 2011.

[86] C. Bojechko et al. Measurement and correction of magnetic field distortions in the time projection chambers. Technical Report 061, T2K, June 2011.

[87] A. Cervera and L Escudero. Study of momentum resolution and scale using tracks that cross multiple TPCs. Technical Report 222, T2K, November 2014.

[88] Yevgeny Petrov and Anthony Hillairet. ND280 TPC track reconstruction efficiency. Technical Report 163, T2K, February 2016.

[89] Federico Sanchez and John vo Medina. ND280 global charge identification systematic error. Technical Report 229, T2K, May 2016.

[90] A. Hillairet et al. ND280 tracker tracking efficiency. Technical Report 075, T2K, January 2016.

[91] Wojciech Oryszczak and Weronika Warzycha. FGD systematics: PID and IsoRecon hybrid efficiencies. Technical Report 223, T2K, April 2015.

[92] Kendall Mahn, Scott Oser, and Thomas Lindner. FGD mass checks. Technical Report 122, T2K, May 2012.

[93] Daniel Roberge. Elemental composition of FGD passive water modules. Technical Report 198, T2K, January 2010.

[94] Jordan Myslik. Determination of pion secondary interaction systematics for the ND280 tracker analysis. Technical Report 125, T2K, October 2013.

[95] F. Dufour, L. Haegel, T. Lindner, and S. Oser. Systematics on out-of-fiducial-volume backgrounds in the ND280 tracker. Technical Report 098, T2K, June 2015.

[96] Graham Upton and Ian Cook. *A Dictionary of Statistics*. Oxford University Press, 3 edition, 2014. ISBN 9780199679188.

[97] Luc Demortier and Louis Lyons. Everything you always wanted to know about pulls. Technical Report 5776, CDF, August 2002.

[98] R. Gran et al. Measurement of the quasi-elastic axial vector mass in neutrino-oxygen interactions. *Phys. Rev.*, D74:052002, 2006. doi:10.1103/PhysRevD.74.052002.

[99] James Imber et al. Four sample joint oscillation analysis with T2K run1-6 data. Technical Report 267, T2K, July 2016.

[100] J. Nieves, J. E. Amaro, and M. Valverde. Inclusive quasi-elastic neutrino reactions. *Phys. Rev. C*, **70**:055503, 2004. URL http://journals.aps.org/prc/abstract/10.1103/PhysRevC.70.055503. [Erratum-ibid. C **72** (2005) 019902].

Appendix A

Additional Flux Prediction Plots

This appendix contains plots of the flux predictions and uncertainties on the predictions for the neutrino fluxes at ND280 and SK, for both FHC and RHC beam modes. These plots were produced by the T2K beam group as described in Section 3.3.1 in Chapter 3.

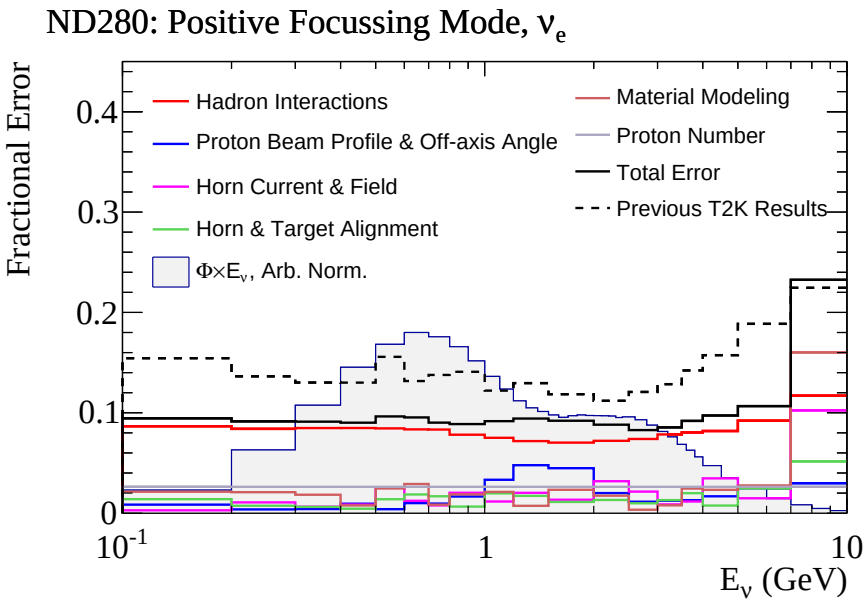

(a) ND280 FHC ν_e flux uncertainty and prediction.

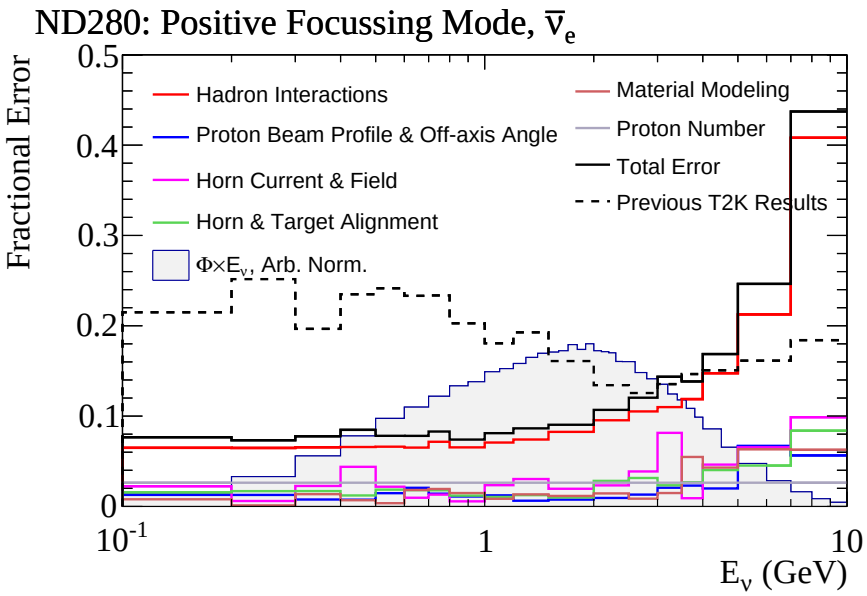

(b) ND280 FHC $\bar{\nu}_e$ flux uncertainty and prediction.

Figure A.1: Predicted fractional uncertainties on the flux priors as a function of neutrino energy.

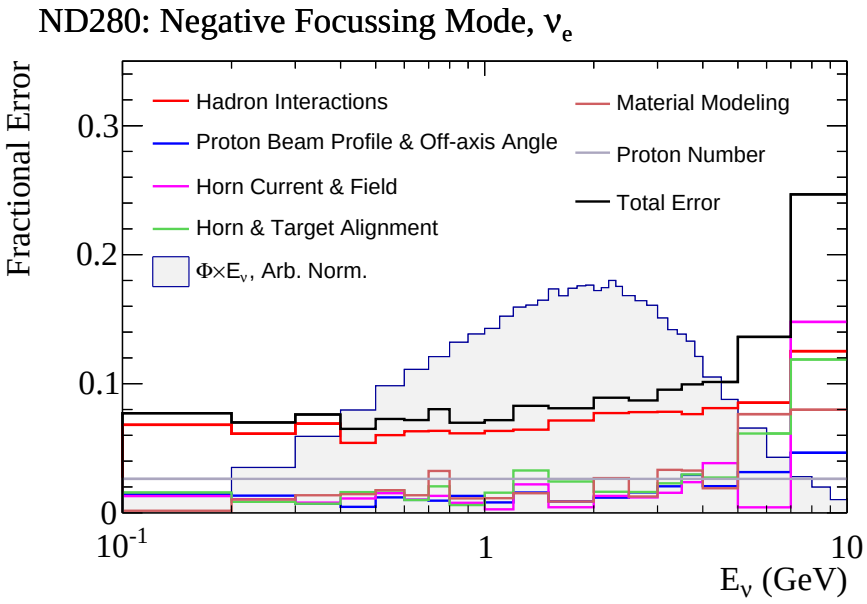

(a) ND280 RHC ν_e flux uncertainty and prediction.

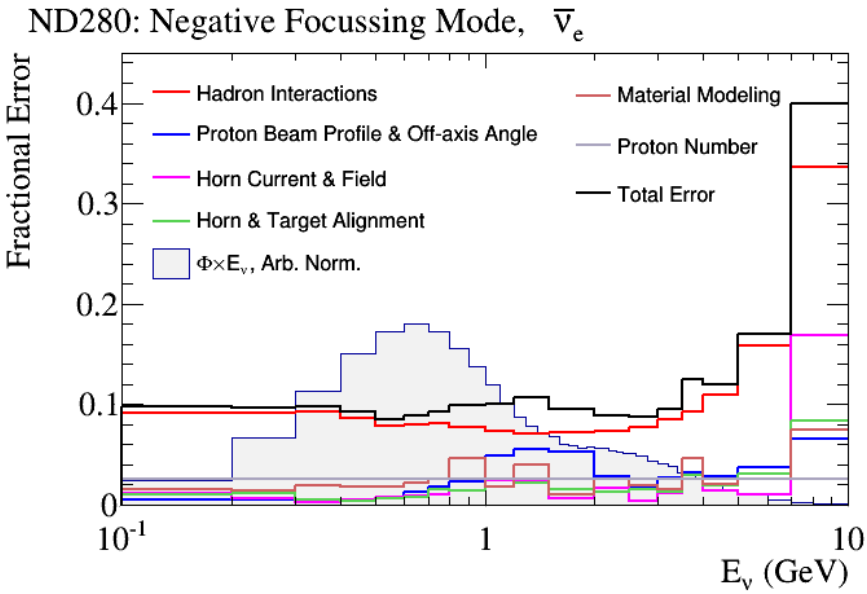

(b) ND280 RHC $\bar{\nu}_e$ flux uncertainty and prediction.

Figure A.2: Predicted fractional uncertainties on the flux priors as a function of neutrino energy.

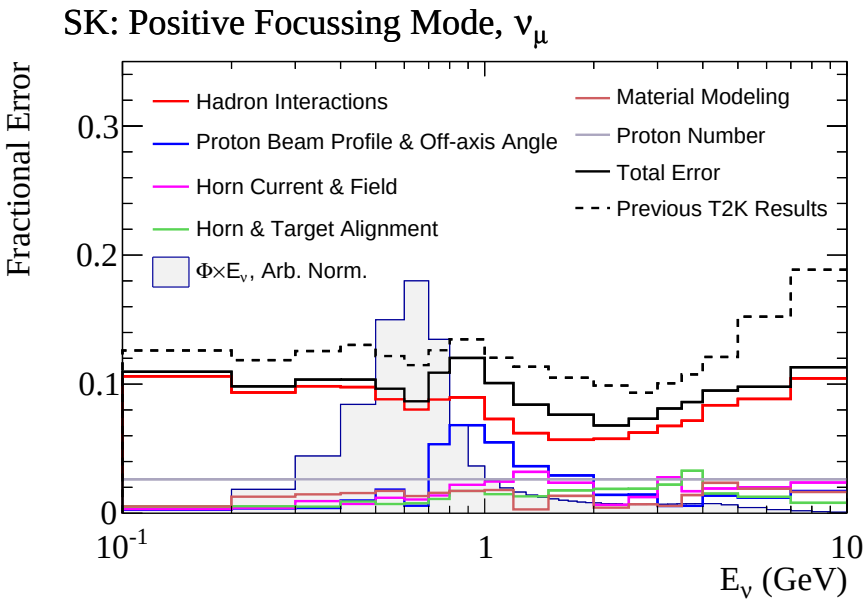

(a) SK FHC ν_μ flux uncertainty and prediction.

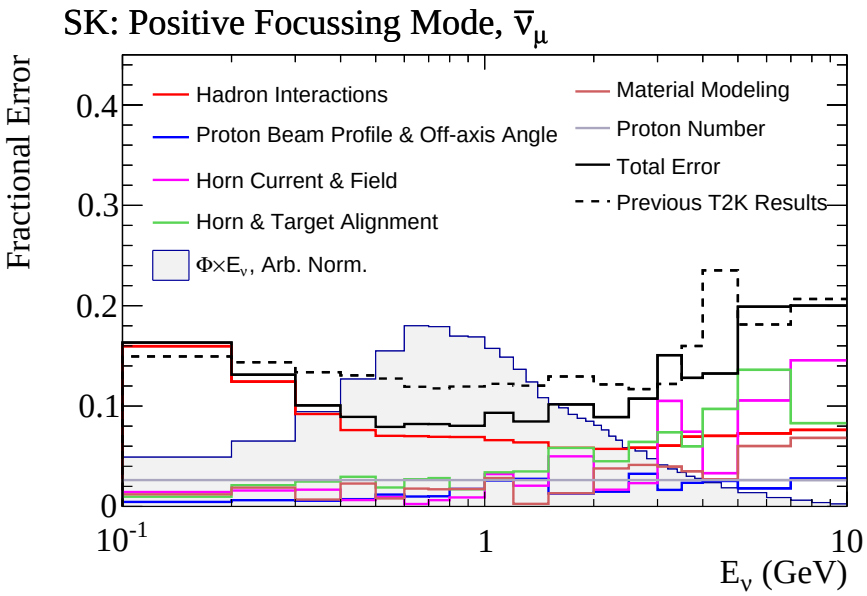

(b) SK FHC $\bar{\nu}_\mu$ flux uncertainty and prediction.

Figure A.3: Predicted fractional uncertainties on the flux priors as a function of neutrino energy.

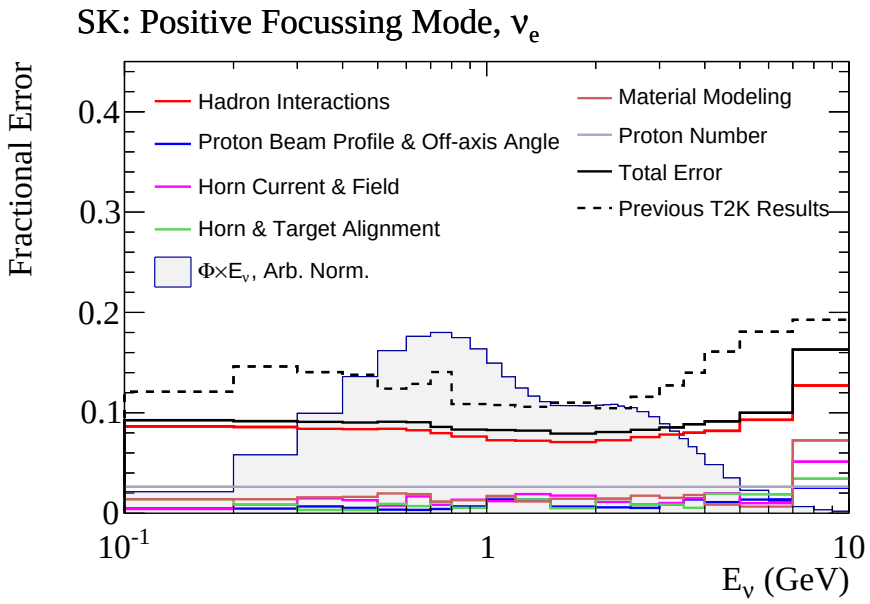

(a) SK FHC ν_e flux uncertainty and prediction.

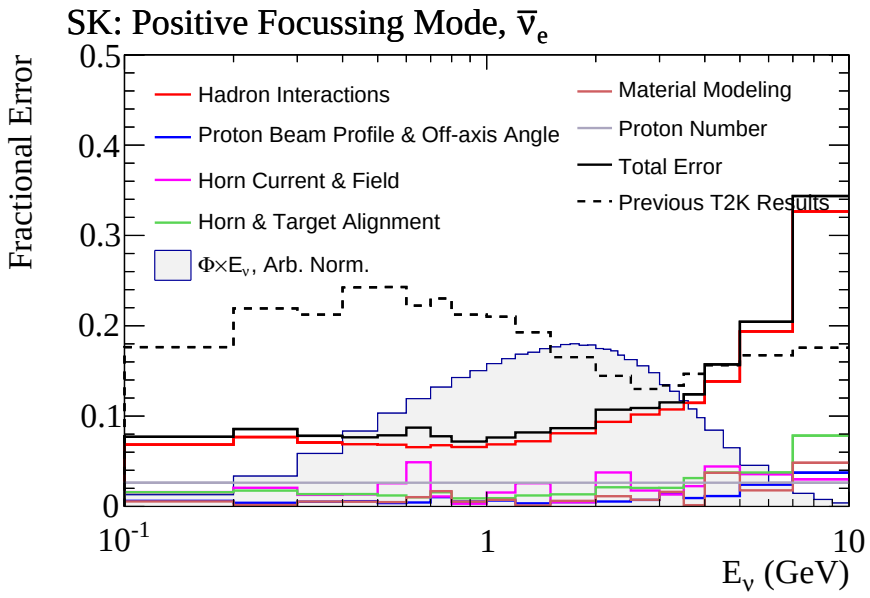

(b) SK FHC $\bar{\nu}_e$ flux uncertainty and prediction.

Figure A.4: Predicted fractional uncertainties on the flux priors as a function of neutrino energy.

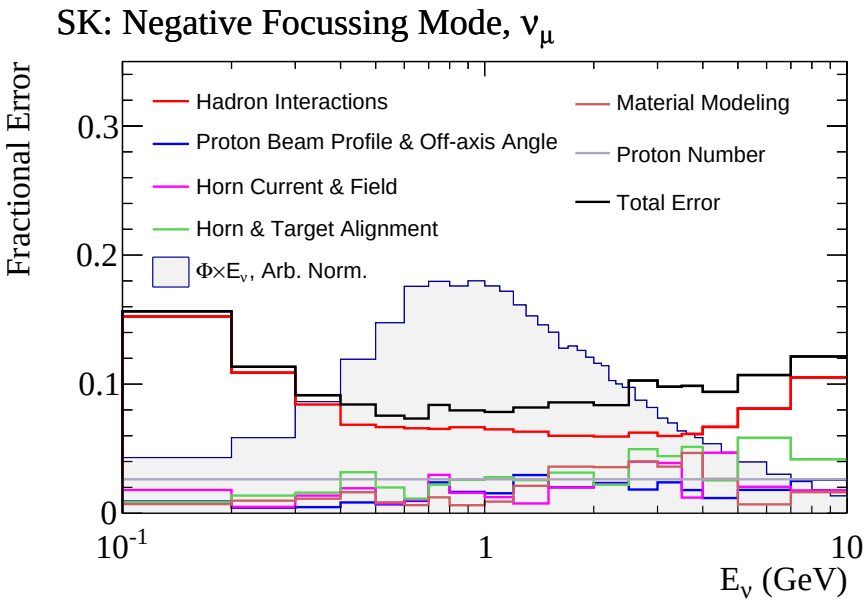

(a) SK RHC ν_μ flux uncertainty and prediction.

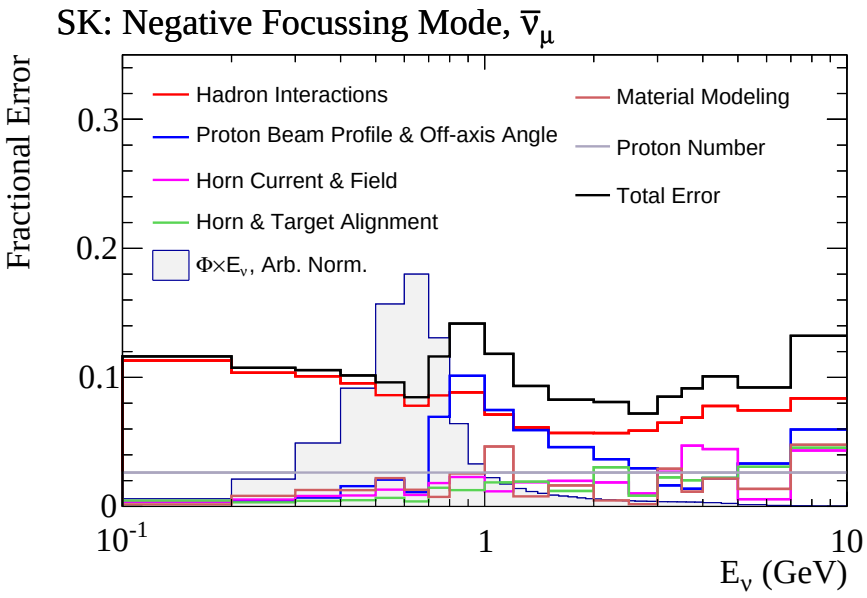

(b) SK RHC $\bar{\nu}_\mu$ flux uncertainty and prediction.

Figure A.5: Predicted fractional uncertainties on the flux priors as a function of neutrino energy.

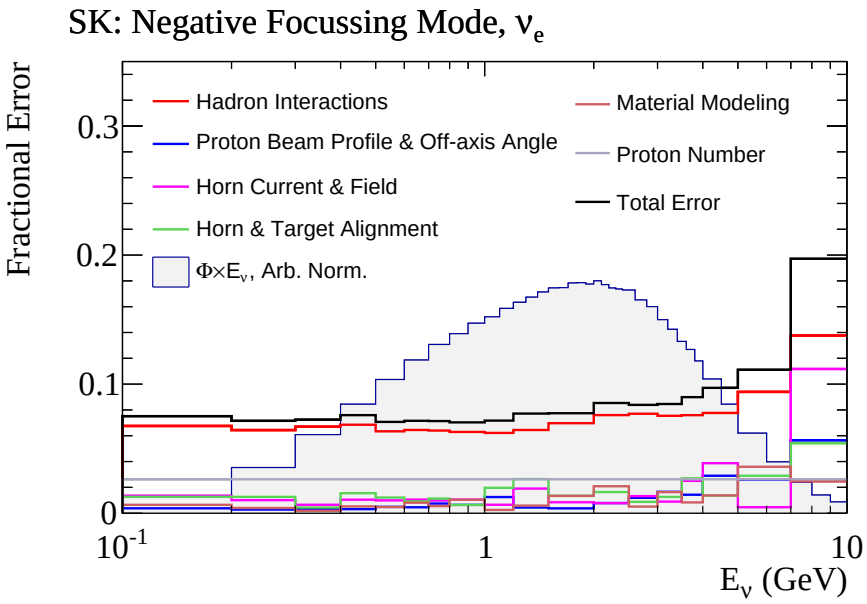

(a) SK RHC ν_e flux uncertainty and prediction.

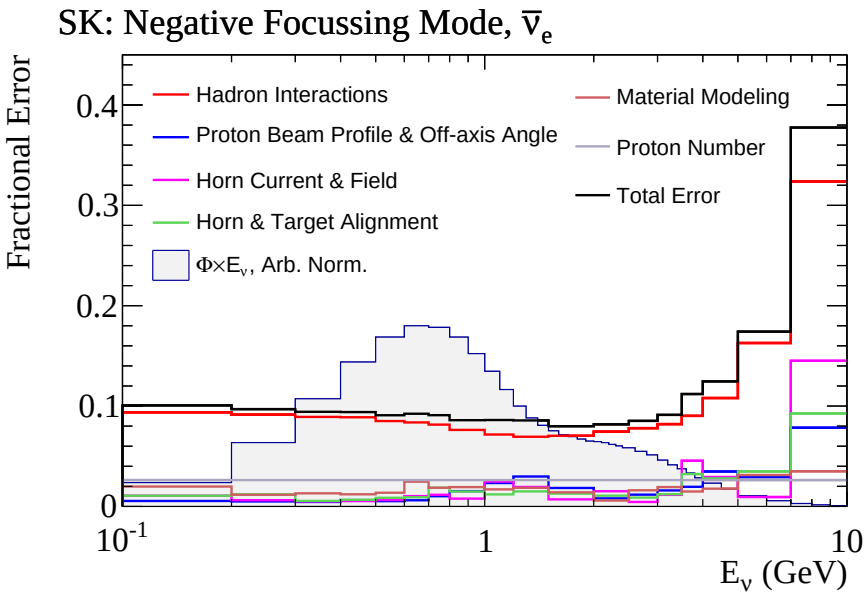

(b) SK RHC $\bar{\nu}_e$ flux uncertainty and prediction.

Figure A.6: Predicted fractional uncertainties on the flux priors as a function of neutrino energy.

Appendix B

Momentum and Angle Distributions for Selected ND280 Events

This appendix contains plots relevant to Chapter 4. These plots show the momentum and angular distributions for the RHC $\bar{\nu}_\mu$ CC Inclusive selection, described in Section 4.5.4, and the RHC wrong-sign ν_μ CC Inclusive selection, described in Section 4.5.6.

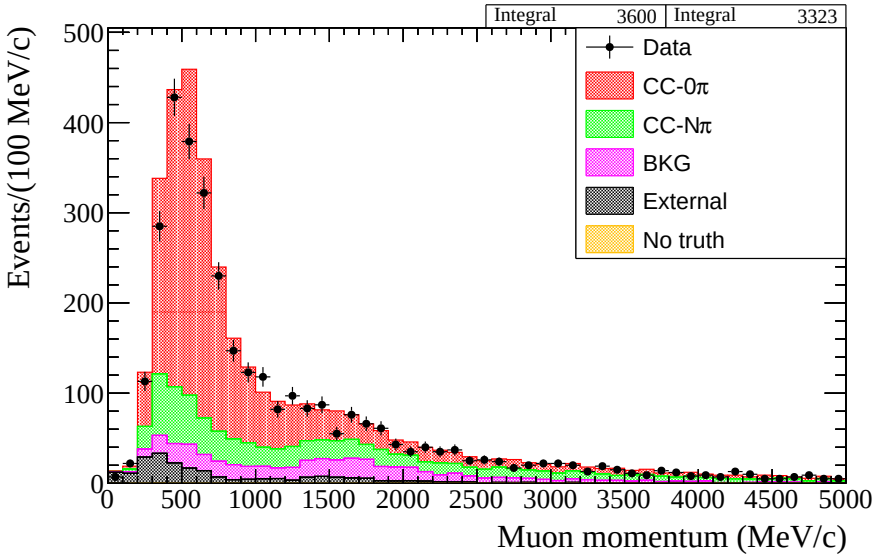

(a) Momentum distribution

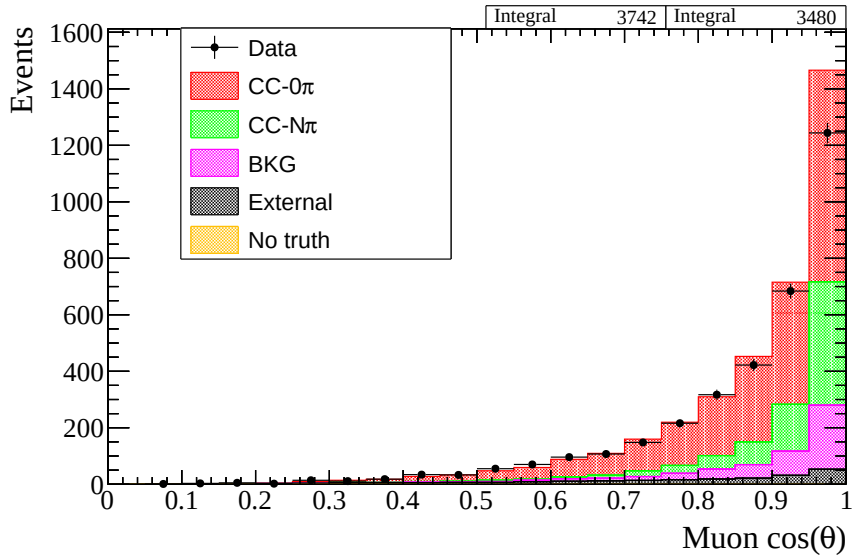

(b) $\cos\theta_\mu$ distribution

Figure B.1: Momentum and $\cos\theta_\mu$ distributions for data and Monte Carlo, broken down by true topology, for the FGD 1 RHC $\bar{\nu}_\mu$ CC Inclusive selection[83]. Distributions shown use the T2K Monte Carlo before the ND280 fit tuning.

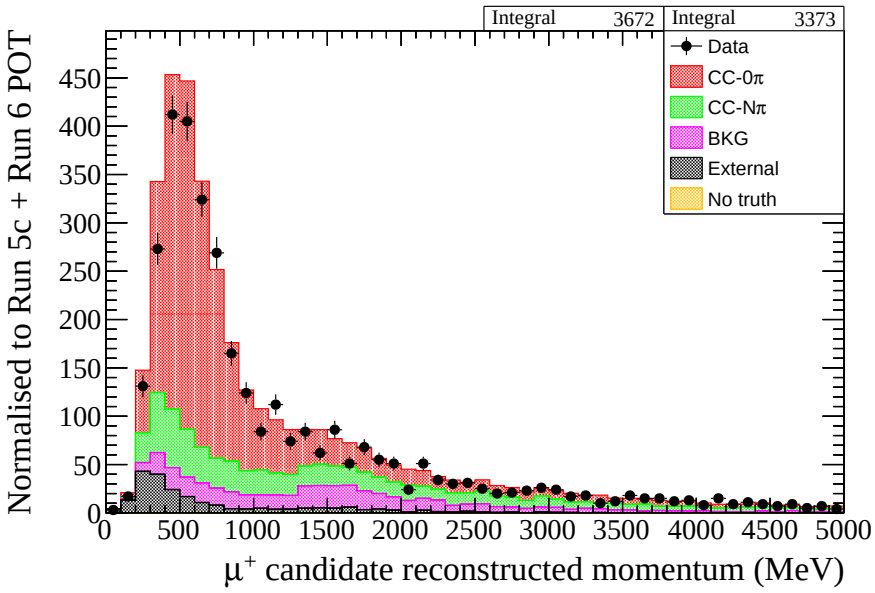

(a) Momentum distribution

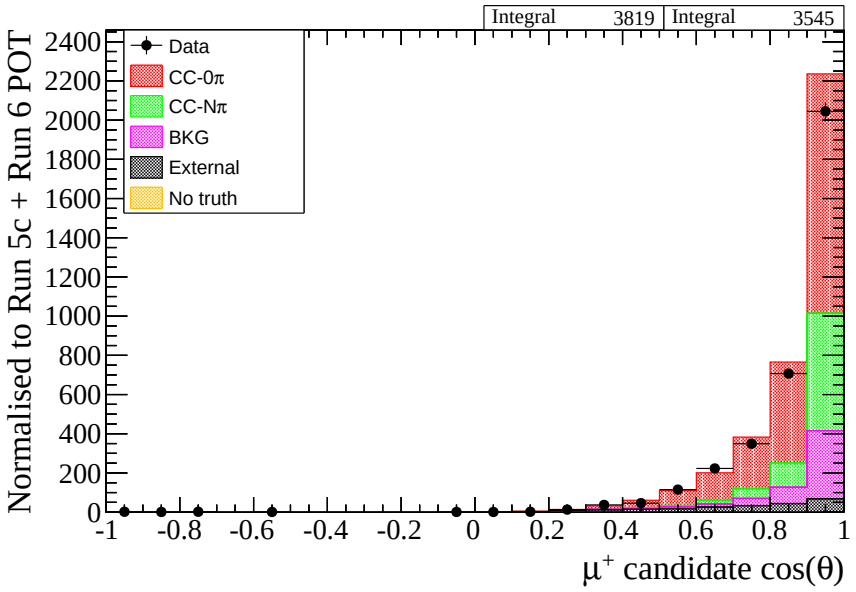

(b) $\cos\theta_\mu$ distribution

Figure B.2: Momentum and $\cos\theta_\mu$ distributions for data and Monte Carlo, broken down by true topology, for the FGD 2 RHC $\bar{\nu}_\mu$ CC Inclusive selection[83]. Distributions shown use the T2K Monte Carlo before the ND280 fit tuning.

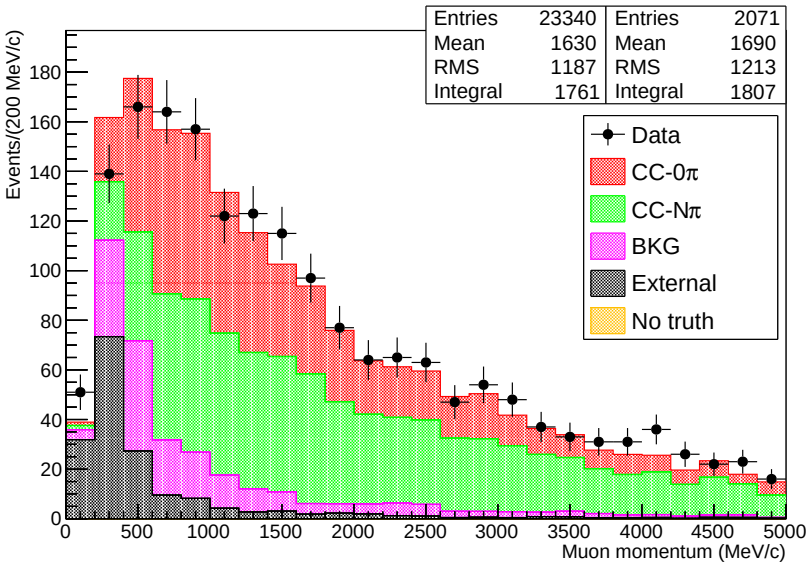

(a) Momentum distribution

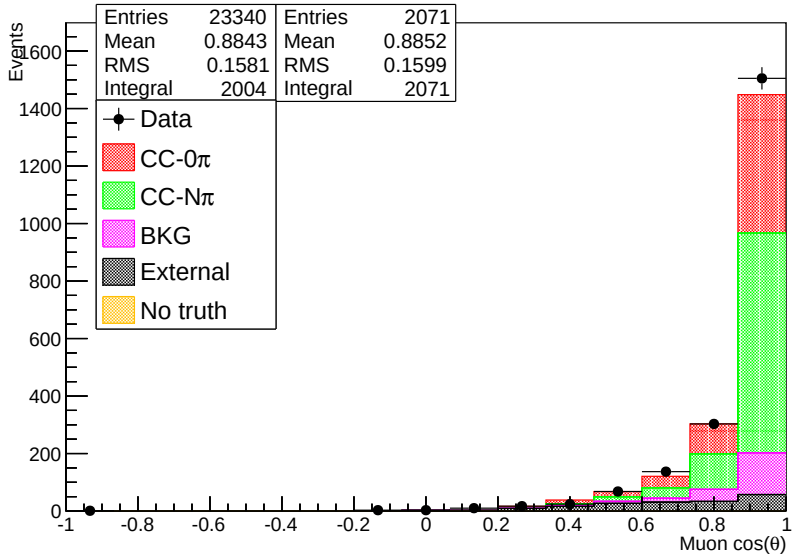

(b) $\cos\theta_\mu$ distribution

Figure B.3: Momentum and $\cos\theta_\mu$ distributions for data and Monte Carlo, broken down by true topology, for the FGD 1 RHC ν_μ CC Inclusive selection[84].

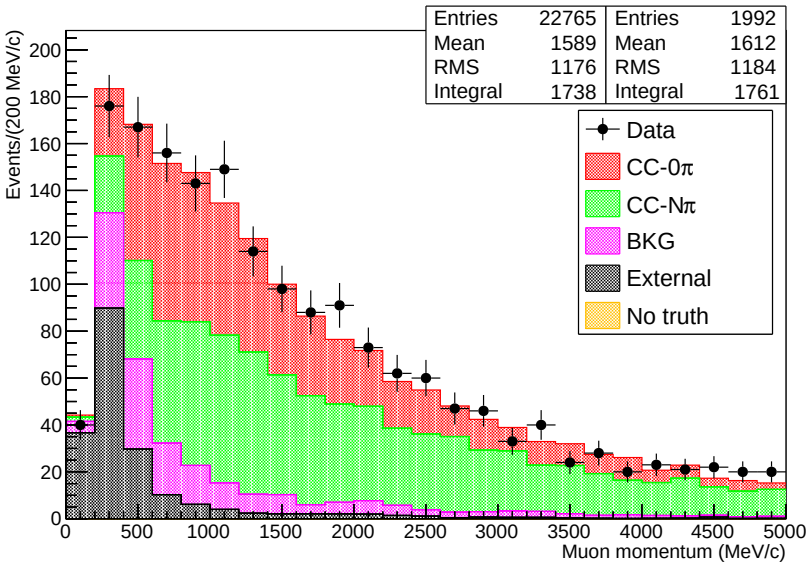

(a) Momentum distribution

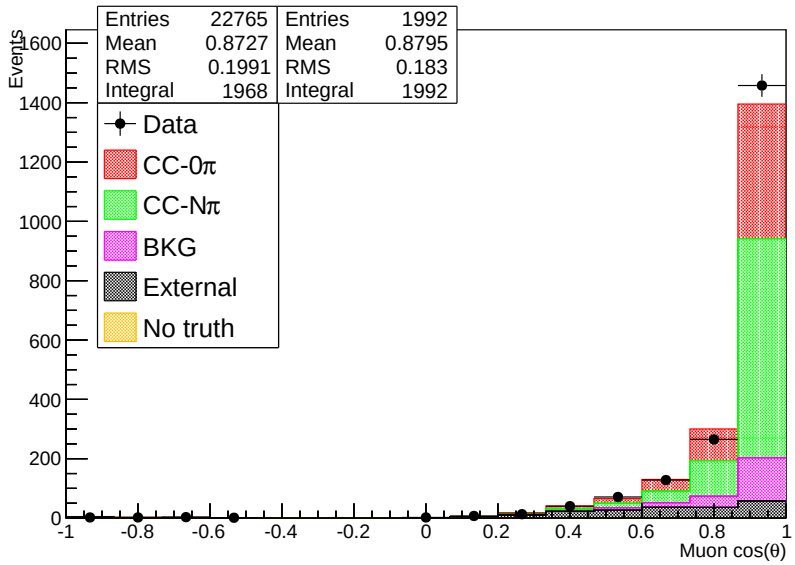

(b) $\cos\theta_\mu$ distribution

Figure B.4: Momentum and $\cos\theta_\mu$ distributions for data and Monte Carlo, broken down by true topology, for the FGD 2 RHC ν_μ CC Inclusive selection[84].

Appendix C

Tables of Fitted Parameter Values at ND280

This appendix contains tables of the fitted parameter values from the ND280 fit described in Chapter 7, for flux and cross-section parameters.

FHC flux parameter	Prefit	ND280 postfit
ND280 ν_μ Bin 0	1.0 ± 0.097467	1.1494 ± 0.060655
ND280 ν_μ Bin 1	1.0 ± 0.10102	1.1745 ± 0.055057
ND280 ν_μ Bin 2	1.0 ± 0.093831	1.1554 ± 0.046689
ND280 ν_μ Bin 3	1.0 ± 0.087563	1.1412 ± 0.039376
ND280 ν_μ Bin 4	1.0 ± 0.10743	1.1205 ± 0.042462
ND280 ν_μ Bin 5	1.0 ± 0.10542	1.0945 ± 0.043416
ND280 ν_μ Bin 6	1.0 ± 0.074043	1.15 ± 0.042205
ND280 ν_μ Bin 7	1.0 ± 0.069071	1.1505 ± 0.041948
ND280 ν_μ Bin 8	1.0 ± 0.082987	1.1574 ± 0.043407
ND280 ν_μ Bin 9	1.0 ± 0.098196	1.1112 ± 0.045209
ND280 ν_μ Bin 10	1.0 ± 0.1146	1.1046 ± 0.051429
ND280 $\bar{\nu}_\mu$ Bin 0	1.0 ± 0.10173	1.1015 ± 0.080716
ND280 $\bar{\nu}_\mu$ Bin 1	1.0 ± 0.08147	1.1024 ± 0.05676
ND280 $\bar{\nu}_\mu$ Bin 2	1.0 ± 0.078275	1.1175 ± 0.055378
ND280 $\bar{\nu}_\mu$ Bin 3	1.0 ± 0.082962	1.1584 ± 0.062253
ND280 $\bar{\nu}_\mu$ Bin 4	1.0 ± 0.086702	1.1694 ± 0.067138
ND280 ν_e Bin 0	1.0 ± 0.090449	1.1485 ± 0.050188
ND280 ν_e Bin 1	1.0 ± 0.092268	1.1492 ± 0.048532
ND280 ν_e Bin 2	1.0 ± 0.090296	1.1746 ± 0.05036
ND280 ν_e Bin 3	1.0 ± 0.087908	1.1399 ± 0.048494
ND280 ν_e Bin 4	1.0 ± 0.088004	1.1293 ± 0.054468
ND280 ν_e Bin 5	1.0 ± 0.082902	1.1442 ± 0.04385
ND280 ν_e Bin 6	1.0 ± 0.096231	1.1216 ± 0.061689
ND280 $\bar{\nu}_e$ Bin 0	1.0 ± 0.074039	1.13 ± 0.056243
ND280 $\bar{\nu}_e$ Bin 1	1.0 ± 0.14013	1.181 ± 0.12721

Table C.1: Prefit and ND280 postfit values for the ND280 FHC flux parameters. Flux values are relative to the nominal T2K flux prediction.

NF flux parameter	Prefit	ND280 postfit
ND280 ν_μ Bin 0	1.0 ± 0.092802	1.1014 ± 0.072527
ND280 ν_μ Bin 1	1.0 ± 0.080395	1.137 ± 0.05007
ND280 ν_μ Bin 2	1.0 ± 0.083051	1.1476 ± 0.050325
ND280 ν_μ Bin 3	1.0 ± 0.083992	1.1825 ± 0.051599
ND280 ν_μ Bin 4	1.0 ± 0.082472	1.1475 ± 0.043341
ND280 $\bar{\nu}_\mu$ Bin 0	1.0 ± 0.1034	1.1323 ± 0.068888
ND280 $\bar{\nu}_\mu$ Bin 1	1.0 ± 0.098917	1.144 ± 0.055399
ND280 $\bar{\nu}_\mu$ Bin 2	1.0 ± 0.090715	1.1444 ± 0.049222
ND280 $\bar{\nu}_\mu$ Bin 3	1.0 ± 0.087484	1.1394 ± 0.043408
ND280 $\bar{\nu}_\mu$ Bin 4	1.0 ± 0.11988	1.1587 ± 0.059233
ND280 $\bar{\nu}_\mu$ Bin 5	1.0 ± 0.11453	1.1597 ± 0.059095
ND280 $\bar{\nu}_\mu$ Bin 6	1.0 ± 0.085223	1.1637 ± 0.051206
ND280 $\bar{\nu}_\mu$ Bin 7	1.0 ± 0.075007	1.1675 ± 0.051101
ND280 $\bar{\nu}_\mu$ Bin 8	1.0 ± 0.097631	1.188 ± 0.070358
ND280 $\bar{\nu}_\mu$ Bin 9	1.0 ± 0.091953	1.1752 ± 0.064477
ND280 $\bar{\nu}_\mu$ Bin 10	1.0 ± 0.1395	1.1845 ± 0.10848
ND280 ν_e Bin 0	1.0 ± 0.068591	1.1303 ± 0.049596
ND280 ν_e Bin 1	1.0 ± 0.089673	1.1493 ± 0.071727
ND280 $\bar{\nu}_e$ Bin 0	1.0 ± 0.09542	1.1402 ± 0.055452
ND280 $\bar{\nu}_e$ Bin 1	1.0 ± 0.086103	1.1363 ± 0.047436
ND280 $\bar{\nu}_e$ Bin 2	1.0 ± 0.092835	1.1699 ± 0.058373
ND280 $\bar{\nu}_e$ Bin 3	1.0 ± 0.090264	1.16 ± 0.052849
ND280 $\bar{\nu}_e$ Bin 4	1.0 ± 0.090515	1.1423 ± 0.066818
ND280 $\bar{\nu}_e$ Bin 5	1.0 ± 0.092819	1.1409 ± 0.070634
ND280 $\bar{\nu}_e$ Bin 6	1.0 ± 0.1584	1.1966 ± 0.14206

Table C.2: Prefit and ND280 postfit values for the ND280 RHC flux parameters. Flux values are relative to the nominal T2K flux prediction.

PF flux parameter	Prefit	ND280 postfit
SK ν_μ Bin 0	1.0 ± 0.098732	1.1465 ± 0.061691
SK ν_μ Bin 1	1.0 ± 0.10349	1.1759 ± 0.05881
SK ν_μ Bin 2	1.0 ± 0.096444	1.1659 ± 0.048881
SK ν_μ Bin 3	1.0 ± 0.086696	1.1416 ± 0.040814
SK ν_μ Bin 4	1.0 ± 0.11305	1.1177 ± 0.04471
SK ν_μ Bin 5	1.0 ± 0.091748	1.111 ± 0.04374
SK ν_μ Bin 6	1.0 ± 0.070174	1.1415 ± 0.041818
SK ν_μ Bin 7	1.0 ± 0.07368	1.1446 ± 0.044229
SK ν_μ Bin 8	1.0 ± 0.087373	1.1471 ± 0.043473
SK ν_μ Bin 9	1.0 ± 0.097937	1.1065 ± 0.044603
SK ν_μ Bin 10	1.0 ± 0.11436	1.1003 ± 0.055456
SK $\bar{\nu}_\mu$ Bin 0	1.0 ± 0.10258	1.1114 ± 0.080454
SK $\bar{\nu}_\mu$ Bin 1	1.0 ± 0.078533	1.1232 ± 0.04736
SK $\bar{\nu}_\mu$ Bin 2	1.0 ± 0.084454	1.1204 ± 0.059361
SK $\bar{\nu}_\mu$ Bin 3	1.0 ± 0.085568	1.1308 ± 0.068884
SK $\bar{\nu}_\mu$ Bin 4	1.0 ± 0.086428	1.1799 ± 0.067391
SK ν_e Bin 0	1.0 ± 0.089698	1.1516 ± 0.049553
SK ν_e Bin 1	1.0 ± 0.089952	1.1529 ± 0.046389
SK ν_e Bin 2	1.0 ± 0.085965	1.153 ± 0.044459
SK ν_e Bin 3	1.0 ± 0.080918	1.1373 ± 0.039562
SK ν_e Bin 4	1.0 ± 0.078972	1.137 ± 0.041913
SK ν_e Bin 5	1.0 ± 0.08385	1.1371 ± 0.043819
SK ν_e Bin 6	1.0 ± 0.093894	1.1475 ± 0.061585
SK $\bar{\nu}_e$ Bin 0	1.0 ± 0.074028	1.1362 ± 0.055155
SK $\bar{\nu}_e$ Bin 1	1.0 ± 0.12842	1.1701 ± 0.11563

Table C.3: Prefit and ND280 postfit values for the SK FHC flux parameters. Flux values are relative to the nominal T2K flux prediction.

NF flux parameter	Prefit	ND280 postfit
SK ν_μ Bin 0	1.0 ± 0.093682	1.1102 ± 0.071174
SK ν_μ Bin 1	1.0 ± 0.079343	1.1353 ± 0.050959
SK ν_μ Bin 2	1.0 ± 0.076727	1.1426 ± 0.046598
SK ν_μ Bin 3	1.0 ± 0.080559	1.173 ± 0.051551
SK ν_μ Bin 4	1.0 ± 0.08029	1.139 ± 0.049424
SK $\bar{\nu}_\mu$ Bin 0	1.0 ± 0.10448	1.133 ± 0.069783
SK $\bar{\nu}_\mu$ Bin 1	1.0 ± 0.10153	1.144 ± 0.058132
SK $\bar{\nu}_\mu$ Bin 2	1.0 ± 0.096167	1.1323 ± 0.050464
SK $\bar{\nu}_\mu$ Bin 3	1.0 ± 0.084637	1.1337 ± 0.042324
SK $\bar{\nu}_\mu$ Bin 4	1.0 ± 0.12509	1.1708 ± 0.064084
SK $\bar{\nu}_\mu$ Bin 5	1.0 ± 0.10529	1.1478 ± 0.055719
SK $\bar{\nu}_\mu$ Bin 6	1.0 ± 0.079987	1.159 ± 0.049348
SK $\bar{\nu}_\mu$ Bin 7	1.0 ± 0.073938	1.1651 ± 0.049955
SK $\bar{\nu}_\mu$ Bin 8	1.0 ± 0.093992	1.179 ± 0.066625
SK $\bar{\nu}_\mu$ Bin 9	1.0 ± 0.092513	1.1637 ± 0.064092
SK $\bar{\nu}_\mu$ Bin 10	1.0 ± 0.13031	1.1138 ± 0.10591
SK ν_e Bin 0	1.0 ± 0.068881	1.1358 ± 0.048551
SK ν_e Bin 1	1.0 ± 0.084945	1.1352 ± 0.067841
SK $\bar{\nu}_e$ Bin 0	1.0 ± 0.094695	1.1419 ± 0.056154
SK $\bar{\nu}_e$ Bin 1	1.0 ± 0.091039	1.1425 ± 0.049143
SK $\bar{\nu}_e$ Bin 2	1.0 ± 0.091012	1.1472 ± 0.050225
SK $\bar{\nu}_e$ Bin 3	1.0 ± 0.083856	1.1478 ± 0.044191
SK $\bar{\nu}_e$ Bin 4	1.0 ± 0.079578	1.1436 ± 0.054013
SK $\bar{\nu}_e$ Bin 5	1.0 ± 0.089008	1.1409 ± 0.067854
SK $\bar{\nu}_e$ Bin 6	1.0 ± 0.15581	1.1922 ± 0.1391

Table C.4: Prefit and ND280 postfit values for the SK RHC flux parameters. Flux values are relative to the nominal T2K flux prediction.

Cross Section Parameter	Prefit	ND280 postfit
M_A^{QE} (GeV/c^2)	1.2 $\pm$ 0.069607	1.1113 $\pm$ 0.033281
p_F ^{12}C (MeV/c)	217.0 $\pm$ 12.301	248.71 $\pm$ 16.048
MEC ^{12}C	100.0 $\pm$ 29.053	156.9 $\pm$ 22.635
E_B ^{12}C (MeV)	25.0 $\pm$ 9.0	16.846 $\pm$ 7.5097
p_F ^{16}O (MeV/c)	225.0 $\pm$ 12.301	239.22 $\pm$ 23.246
MEC ^{16}O	100.0 $\pm$ 35.228	155.89 $\pm$ 34.243
E_B ^{16}O (MeV)	27.0 $\pm$ 9.0	24.262 $\pm$ 7.5922
$CA5^{RES}$	1.01 $\pm$ 0.12	0.78601 $\pm$ 0.060705
M_A^{RES} (GeV/c^2)	0.95 $\pm$ 0.15	0.84904 $\pm$ 0.038442
Isospin=$\frac{1}{2}$ Background	1.3 $\pm$ 0.2	1.3633 $\pm$ 0.17371
CC Other Shape	0.0 $\pm$ 0.4	-0.024697 $\pm$ 0.17809
CC Coh	1.0 $\pm$ 0.3	0.85333 $\pm$ 0.22835
NC Coh	1.0 $\pm$ 0.3	0.9308 $\pm$ 0.29816
NC Other	1.0 $\pm$ 0.3	1.3066 $\pm$ 0.15511
MEC $\bar{\nu}$	1.0 $\pm$ 1.0	0.6109 $\pm$ 0.1672
FSI Inel. Low E	0.0 $\pm$ 0.41231	-0.29976 $\pm$ 0.099264
FSI Inel. High E	0.0 $\pm$ 0.33793	0.017027 $\pm$ 0.17908
FSI Pion Prod.	0.0 $\pm$ 0.5	0.0077633 $\pm$ 0.26256
FSI Pion Abs.	0.0 $\pm$ 0.41161	-0.2558 $\pm$ 0.16117
FSI Ch. Exch. Low E	0.0 $\pm$ 0.56679	-0.071184 $\pm$ 0.39018
FSI Ch. Exch. High E	0.0 $\pm$ 0.27778	0.004313 $\pm$ 0.14587

Table C.5: Prefit and ND280 postfit values for the cross-section parameters